New Yb^{3+}-doped laser materials and their application in continuous-wave and mode-locked lasers

DISSERTATION

zur Erlangung des akademischen Grades
doctor rerum naturalium
(Dr. rer. nat.)
im Fach Physik

eingereicht an der
Mathematisch-Naturwissenschaftlichen Fakultät I
der Humboldt-Universität zu Berlin
von

Dipl. Phys. Peter Klopp
geb. 14.12.1968, Wiesbaden

Präsident der Humboldt-Universität zu Berlin
Prof. Dr. Christoph Markschies

Dekan der Mathematisch-Naturwissenschaftlichen Fakultät I
Prof. Thomas Buckhout, PhD

Gutachter:

1. Prof. Dr. Thomas Elsässer
2. Prof. Dr. Günther Huber
3. Prof. Dr. Achim Peters

Tag der mündlichen Prüfung: 16.05.2006

Abstract

Yb^{3+} laser media excel with high efficiency and relatively low heat load, especially in medium to high power laser oscillators and amplifiers. Mode-locking of Yb^{3+} laser systems can provide subpicosecond pulse durations at high average power. This work deals with two groups of the most promising novel Yb^{3+}-activated laser crystals: Yb^{3+}-activated monoclinic double tungstates, namely the isostructural crystals $Yb:KGd(WO_4)_2$ (Yb:KGW), $Yb:KY(WO_4)_2$ (Yb:KYW), and $KYb(WO_4)_2$ (KYbW), and Yb^{3+}-doped sesquioxides, represented by $Yb:Sc_2O_3$ (Yb:scandia). Spectroscopic data of KYbW were investigated as part of this thesis, finding an extremely short 1/e-absorption length of 13 micrometers at 981 nm. Continuous-wave (cw) and mode-locked laser performance of moderate-average-power lasers based on lowly Yb^{3+}-doped tungstates were examined. Ultrashort pulse generation with Yb:KYW, Yb:KGW, and Yb:glass was compared in a passively mode-locked laser. A relatively high mode-locked laser efficiency was achieved due to a tapered diode pump laser with excellent beam quality. Quasi-cw and cw lasing of Yb^{3+} in highly doped and stoichiometric tungstate crystals were investigated. These materials are interesting for microchip and thin-disk lasers. Important issues were crystal quality and heat generation at high Yb^{3+} concentrations. For the first time, laser operation of tungstates with a Yb^{3+} concentration >>20% and finally, with KYbW, cw lasing of a stoichiometric Yb laser material was achieved. Furthermore, with KYbW, the smallest laser quantum defect ever for a laser crystal was demonstrated, 1.6%. Using a $Yb:Sc_2O_3$ laser medium, for the first time mode locking of an oscillator using a sesquioxide laser crystal was realized. Laser regimes with non-solitonlike and solitonlike pulse shaping were investigated, using a Ti:Sapphire laser and a tapered laser diode as pump sources. With a Ti:Sapphire-laser-pumped Yb:scandia laser the highest conversion efficiency with respect to absorbed pump power for any mode-locked Yb^{3+}-based laser was achieved, 47%.

Keywords: Yb^{3+} lasers, ytterbium-activated tungstates, ytterbium-doped sesquioxides, mode-locked lasers

Abstract

Yb^{3+}-Lasermedien glänzen mit hoher Effizienz und relativ geringer thermischer Last, besonders in Laseroszillatoren und -verstärkern mittlerer bis hoher Leistung. Modenkopplung von Yb^{3+}-Lasersystemen ermöglicht Subpikosekunden-Pulse bei hoher mittlerer Ausgangsleistung. Diese Arbeit widmet sich zwei Gruppen der vielversprechendsten neuen Yb^{3+}-aktivierten Laserkristalle: den strukturell analogen, monoklinen Doppelwolframaten Yb:KGd(WO$_4$)$_2$ (Yb:KGW), Yb:KY(WO$_4$)$_2$ (Yb:KYW) und KYb(WO$_4$)$_2$ (KYbW) und den Yb^{3+}-dotierten Sesquioxiden, vertreten durch Yb:Sc$_2$O$_3$ (Yb:Skandia). Die spektroskopischen Daten von KYbW, darunter eine extrem kurze 1/e-Absorptionslänge von 13 Mikrometern bei 981 nm, wurden im Rahmen der Dissertation vermessen. Die Lasereigenschaften niedrig Yb^{3+}-dotierter Wolframate im Dauerstrich (cw)- und modengekoppelten Betrieb wurden in Lasern moderater Ausgangsleistung untersucht. Ultrakurzpuls-Erzeugung mit Yb:KYW, Yb:KGW und Yb:Glas wurde in einem passiv modengekoppelten Laser verglichen. Dabei wurde eine relativ hohe Lasereffizienz erreicht, Dank einer Trapezlaserdiode als Pumpquelle mit exzellenter Strahlqualität. Quasi-cw- und cw-Laserbetrieb von Yb^{3+} in hochdotierten und stöchiometrischen Wolframatkristallen wurden untersucht. Diese Materialien sind interessant für Mikrochip- und Scheibenlaser. Wichtige Fragestellungen waren die Kristallqualität und die Hitzeentwicklung bei hohen Yb^{3+}-Konzentrationen. Erstmals wurde Lasertätigkeit von Wolframaten mit Yb^{3+}-Konzentrationen >>20% und schließlich, mit KYbW, cw-Laserbetrieb eines stöchiometrischen Yb-Lasermaterials demonstriert. Weiterhin wurde mit KYbW der kleinste bisher für einen Laserkristall gemessene Laserquantendefekt erzielt, 1,6%. Unter Benutzung eines Yb:Sc$_2$O$_3$-Lasermediums wurde erstmals modengekoppelter Betrieb eines Oszillators mit Sequioxid-Laserkristall gezeigt. Betrieb mit nichtsolitonen- und solitonenartiger Pulsformung sowie mit Ti:Saphir-Laser oder Trapezlaserdiode als Pumplaser wurden untersucht. Mit einem Ti:Saphir-gepumpten Yb:Skandia-Laser wurde eine Konversionseffizienz von 47 % bezogen auf die absorbierte Pumpleistung erreicht, der bisher höchste Wert für einen modengekoppelten Yb^{3+}-basierten Laser.

Schlagwörter: Yb^{3+}-Laser, Ytterbium-aktivierte Wolframate, Ytterbium-dotierte Sesquioxide, modengekoppelte Laser

New Yb^{3+}-doped laser materials and their application in continuous-wave and mode-locked lasers

1. Introduction

Combining Yb^{3+} as the active ion and a suited glass or crystal host provides laser media with excellent optical and mechanical properties. For laser oscillators and amplifiers operating in the 1-µm-range, Yb^{3+}-based laser materials have the potential to substitute many Nd^{3+}-based materials, especially in medium to high power systems used for material processing. Here, Yb^{3+} laser media excel with high efficiency and relatively low heat load. Mode-locking of Yb^{3+} laser systems can provide subpicosecond pulse durations at high average power. Such short pulses can e.g. enhance the precision of drilling compared to Q-switched systems and permit the structuring of transparent materials [Chi96, Dra03, Min01, Pro95].

This work deals with two groups of the most promising novel Yb^{3+}-activated laser crystals: Yb^{3+}-activated monoclinic double tungstates, namely the isostructural crystals $Yb:KGd(WO_4)_2$ (Yb:KGW), $Yb:KY(WO_4)_2$ (Yb:KYW), and $KYb(WO_4)_2$ (KYbW), and Yb^{3+}-doped sesquioxides, represented by $Yb:Sc_2O_3$ (Yb:scandia). Highly efficient laser operation is demonstrated with lowly doped tungstate and scandia crystals in continuous-wave (cw) and mode-locked regimes. Highly doped KYW and stoichiometric KYbW are investigated. With KYbW, the first cw lasing of a stoichiometric Yb^{3+} laser material is achieved.

Motivation

A general advantage of Yb^{3+} lasers is that the conversion efficiency of pump light into laser output can be very high and heat production is relatively low, due to a small laser quantum defect (*lqd*) and the absence of excited state absorption, up- or downconversion mechanisms, which are a problem with many other laser active ions including Nd^{3+}. All Yb^{3+}-activated laser materials can be pumped by InGaAs diode lasers, which helps to build cheap, compact and reliable laser systems.

A disadvantage is that Yb^{3+} laser systems operate in a quasi-three- or quasi-four-level scheme at room temperature, since the lower laser level belongs to the ground state manifold $^2F_{7/2}$ and is considerably thermally populated. This leads to reabsorption of the emitted laser light and therefore to higher lasing thresholds and reduced efficiency. However, reabsorption can be saturated by high laser intensities and its strength varies with the splitting of the ground state manifold in the different hosts.

Several properties of Yb^{3+}-doped materials strongly depend on the host and make its choice a compromise: Generally, interaction of the Yb^{3+} electronic states with the crystal lattice is strong compared to other trivalent rare earth ions and leads to homogeneous broadening of the transition lines and to vibronic features, but interaction differs with the host. Inhomogeneous broadening will result from multiple sites for the active ion and is a strong mechanism in glasses and disordered crystals. Therefore, the shapes of the optical spectra and the values of the absorption and emission cross sections vary strongly. Broad spectra usually mean low maximum values and are often also paid for by low thermal conductivity. For a given bandwidth of the emission spectrum, higher cross sections correspond to a shorter Yb^{3+} upper-state lifetime. A larger ground-state splitting means less reabsorption at the main laser line, but also a larger *lqd*. Structural anisotropy is connected with anisotropic spectral and thermo-mechanical properties. In most hosts, structural mismatch or quenching due to impurities or defects limit the maximum useful Yb^{3+} concentration to low values.

Yb^{3+}-activated monoclinic double tungstates are anisotropic crystals, which exhibit very good spectroscopic and decent thermo-mechanical properties. They are an excellent choice for cw or mode-locked lasers and promise the highest efficiencies among all Yb^{3+}-activated hosts [Bre01b], if the pronounced quasi-three- or quasi-four-level character of their laser operation scheme is taken into account. This means minimizing reabsorption loss and exploiting the possible small laser quantum defect. For high-average power applications, efficient cooling of the Yb^{3+}-activated tungstate laser medium or a small thermal load per volume will be required. In this context, the high Yb^{3+} dopant concentrations realizable in $KY(WO_4)_2$ (KYW) and in the stoichiometric analog $KYb(WO_4)_2$ (KYbW) are of great interest. They offer amazingly high absorption and gain coefficients (KYbW: $1/e$-level absorption length of 13.3 μm at a pump wavelength of 981 nm) and promise the application of very thin crystal platelets in face cooled laser concepts. Furthermore, such platelets will enable single-frequency operation of microchip lasers, and material with high active-ion concentration can be combined with undoped material to create compound laser media. The small laser quantum defect achievable with $Yb:KY(WO_4)_2$, $Yb:KGd(WO_4)_2$, and $KYb(WO_4)_2$ is also advantageous with respect to a small heat load. The gain bandwidth of Yb^{3+}-activated tungstates permits minimum durations of mode-locked pulses below 100 fs. Alternative Yb^{3+}-doped crystals capable of producing pulses that short show less favorable spectroscopic and/or thermo-mechanical properties.

Yb^{3+}-doped Sc_2O_3 (scandia) exhibits good spectroscopic properties and is the Yb^{3+}-activated material that promises the highest achievable laser efficiencies, aside from the double tungstates. The great advantage of scandia is its excellent thermo-mechanical properties (thermal conductivity ≈50% better than that of yttrium aluminium garnet), reducing cooling requirements and predetermining it as the ideal Yb^{3+} host for high-power laser applications. If doping levels higher than 1% are desired, the analog sesquioxides $Yb:Y_2O_3$ and $Yb:Lu_2O_3$, though spectroscopically slightly inferior, may become more attractive due to higher thermal conductivities.

This work and its highlights

Theoretical background is given in chapters 2 to 4, dealing with the crystallography and the properties of Yb^{3+}-activated laser materials, the laser physics of quasi-three- and quasi-four-level laser media, and the theory of passive mode-locking. Spectroscopic data of KYbW were investigated as part of this thesis. Experimental results are presented in chapters 5 and 6, reporting on laser oscillators using Yb:tungstate and Yb:scandia media.

In chapter 5.1., we examine the continuous-wave (cw) and mode-locked laser performance of moderate-average-power lasers based on lowly Yb^{3+}-doped tungstates. The cw experiments show the potential with respect to achievable laser efficiencies. Ultrashort pulse generation with Yb:KYW, Yb:KGW, and Yb:glass is compared in a passively mode-locked diode-pumped laser. A relatively high mode-locked laser efficiency can be achieved due to the use of a tapered diode laser with excellent beam quality.

In chapter 5.2., quasi-cw and cw lasing of tungstates with high Yb^{3+}-concentration is investigated. Important issues are if high Yb^{3+} concentrations in a tungstate host still permit a good optical crystal quality and if the heat produced in the relatively small active volumina of highly doped crystals can be handled. For the first time, laser operation of tungstates with an Yb^{3+} concentration considerably higher than 20% and finally, with KYbW, cw lasing of a stoichiometric Yb laser material is achieved. While reducing thermal problems by pumping a KYbW laser crystal above the mean wavelength of fluorescence, we demonstrate the smallest laser quantum defect ever for a laser crystal, 1.6%.

In chapter 6.1., we examine the cw laser performance of Yb:Sc_2O_3 with Ti:Sapphire-laser pumping, achieving a slope efficiency of 65%.

In chapter 6.2., we demonstrate for the first time mode-locked operation of an Yb:Sc_2O_3 laser, and more general, mode locking of an oscillator using a sesquioxide laser crystal. Laser regimes with non-solitonlike and solitonlike pulse shaping are investigated, using a Ti:Sapphire laser and a tapered laser diode as pump sources. With a Ti:Sapphire-laser-pumped Yb:scandia laser we achieve the highest conversion efficiency with respect to absorbed pump power for any mode-locked Yb^{3+}-based laser.

2. Yb^{3+}-activated laser materials

2.1. Yb^{3+} as a laser active ion

The main advantages of trivalent Yb as an active ion, high possible efficiencies and low heat generation, can be referred to its very simple level scheme (chapt. 2.1.1.). Aside from the transitions between the two Stark manifolds, there are no additional channels of loss for pump or laser radiation, and a small laser quantum defect can be achieved. Yb^{3+} must be considered a low-loss laser ion, particularly compared to Nd^{3+}. Taking this into account and comparing also other properties and practical aspects of Yb^{3+} and Nd^{3+} laser materials (chapt. 2.1.2.), the ytterbium ion is often favorable for high-power and ultrashort-pulse laser systems.

2.1.1. Yb^{3+} level scheme

Ytterbium (Yb, element number 70) is a member of the lanthanides group (rare earths). The characteristic of these elements is their electron structure $[Xe]\ 4f^{x}\ 5d^{y}\ 6s^{2}$, where the *4f*-shell is filled with $0 \leq x \leq 14$ electrons ($x = 0$ for La) and $y = 0$ or 1. In chemical reactions they are electro-positive and their oxidation state is usually +3 or +2. The electron structure of Yb^{3+} is $[Xe]4f^{13}$. This means that the *4f*-shell is complete with the exception of one hole, which is responsible for the simple level structure.

There exist only two relevant Stark multiplets, $^2F_{5/2}$ and $^2F_{7/2}$ (Fig. 2.1.), which are separated by approximately 10000 cm^{-1}; the next excited configuration is located at ≈100,000 cm^{-1}. The upper state, $^2F_{5/2}$, is degenerated into three Stark levels (0´), (1´), and (2´), the lower state, $^2F_{7/2}$, into four Stark levels (0), (1), (2), and (3). The splittings of the Stark levels depend on the host and vary from ≈400 cm^{-1} to ≈1300 cm^{-1} for a whole multiplet [Auz01].

In the thermal equilibrium, the level populations are Boltzmann-distributed. In case of pumping and lasing, a considerable part of the active ions is found in the upper manifold. Fast intraband thermalization (phononic transitions, right hand side of Fig. 2.1.) leads to a separate distribution for each manifold, with most of the excited ions being in (0´). Therefore laser inversion is possible only here and laser emission will occur from (0´) leading into (1), (2), or (3), which is symbolized by the bold arrows in the middle of Fig. 2.1. It is difficult to realize the necessary high pump intensities and achieve inversion for the (0´)-to-(0) ("zero-line") transition; however, there are examples of an Yb^{3+}-doped fiber laser [Sel03] and a pulsed $Yb{:}Sr_5(PO_4)_3F$ laser emitting on this transition [Bay00]. The other emission lines (thin arrows) are displayed, as they, together with the laser-active lines, contribute to fluorescence.

The relevant transitions for optical pumping are also shown in Fig. 2.1. (absorption, bold arrows). In a "quasi-four-level laser scheme" the Yb^{3+} ions are pumped into (1´) or (2´), wheras "quasi-three-level laser scheme" means direct pumping into the upper laser level (0´). "Quasi" refers to the fact that the Stark levels within a multiplet are only "quasi-separate" and actually connected by a Boltzmann distribution. The definitions are further discussed in chapter 3.1.

Quasi-three-level and quasi-four-level lasers typically have low laser quantum defects, but suffer losses from reabsorption of the laser emission. The trivalent Yb ion does not show further multiplets which could serve for additional channels of loss. Such exist with many other laser active ions, especially with rare earths, including Nd^{3+}, and cause up- or downconversion or excited state absorption (see also appendix A.1.).

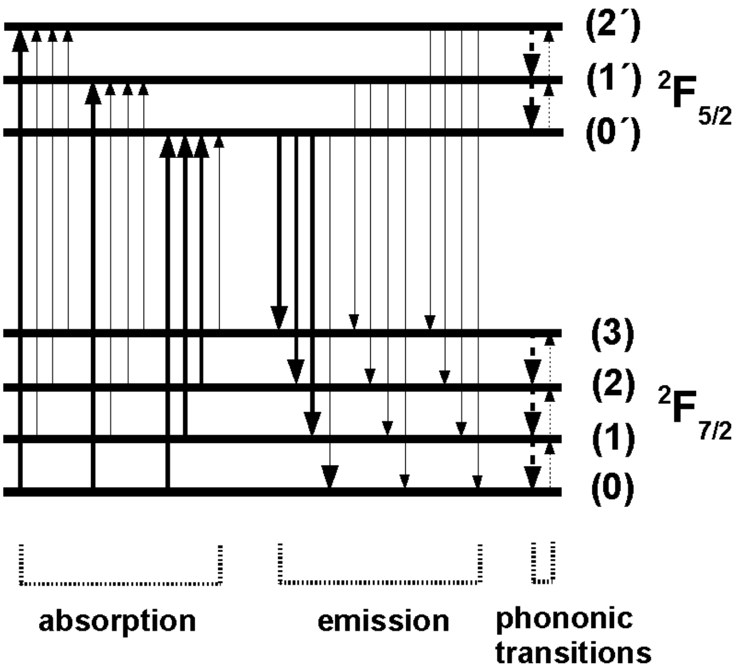

Fig. 2.1. Level scheme of Yb^{3+} and possible transitions (optical absorption and emission, phononic transitions). The upper manifold $^2F_{5/2}$ consists of three Stark levels, (0′) - (2′), the ground state $^2F_{7/2}$ of four, (0) - (3). Level splittings have been chosen arbitrarily. Bold arrows symbolize transitions relevant for optical pumping and for lasing. Phononic transitions lead to fast intraband thermalization, so that laser inversion can be achieved only at the (0′) level. Direct pumping into this level enables extremely low laser quantum defects. Due to the lack of further states, losses occur merely from spontaneous emission and from reabsorption caused by thermal population of the (1) - (3) levels.

2.1.2. Yb^{3+} versus Nd^{3+}

Low losses (aside from reabsorption) and low heat production are a clear advantage of Yb^{3+}-doped materials over Nd^{3+}-doped ones (for details, see the overview of loss processes in appendix A.1.). Other features may be advantageous, depending on the kind of optical source to be realized. Additionally, these properties are strongly influenced by the chosen host.

Maximum doping level

If active media with high dopant concentrations are desired, e.g. for thin-disk or microchip lasers, Yb materials should be preferred. Cross-relaxation problems with Nd^{3+} usually prevent higher dopant levels. Additionally, the size of the trivalent ytterbium ion is closer to that of Y^{3+}. Therefore, in many Y^{3+}-based hosts, any Yb^{3+} doping levels between 0% and 100% can be realized without compromising the optical quality (see chapt. 2.2.5.), while for still relatively low Nd^{3+} doping levels (a few %) optical degradation is observed [Lup02].

Spectroscopic properties

Doped into the same crystals or glasses, Yb^{3+} will generally show longer upper-state lifetimes, lower pump and emission cross sections and broader spectral lines than Nd^{3+}.

Energy storage

Long-lived excited states permit a high energy storage efficiency. Therefore, in Q-switched lasers or in amplifiers, Yb materials can be favorable for the generation of high pulse energies at low repetition rates [Fan92]. Furthermore, the lower gain cross sections and the reabsorption effect of Yb materials reduce the problem of amplified stimulated emission.

Diode pumping

Yb^{3+} does not offer pump bands suitable for flash lamp emission. However, laser diodes can be combined more easily with Yb^{3+} than with Nd^{3+} laser materials. Nd^{3+} transition lines are usually narrow compared to the diode emission bandwidth, reducing the effective absorption cross section [Bar90]; often exact wavelength tuning of the diode emission is necessary. When using low brightness diodes in longitudinal pumping schemes with Yb^{3+}, low absorption can be compensated by long, waveguiding media (e.g. fibers) or by short, highly doped crystals.

Gain

The small-signal gain of Nd^{3+} exceeds that of Yb^{3+}, due to larger products of emission cross section and upper-state lifetime for Nd materials (see eqs. 3.19. and 3.26.). With Yb^{3+}, reabsorption additionally reduces the small-signal gain.

Optical amplifiers require high positive gain. Yb^{3+}-doped materials will not be suitable, if only low pump powers are available and consequently signal intensities are low. In this case, the gain for both Yb^{3+} and Nd^{3+} and reabsorption for Yb^{3+} will not be saturated, so that the difference in the net gain persists. On the other hand, a large product of emission cross section and upper-state lifetime means a low gain saturation intensity (see eqs. 3.36. and 3.38.). Therefore, the gain advantage of Nd materials in amplifiers shrinks with increasing signal intensities; furthermore, the influence of reabsorption from Yb^{3+} decreases. Finally, the gain will be limited by the absorbed pump power alone. The lower small signal gain of Yb^{3+} can actually help to suppress background noise and prepulses.

Optical resonators enhance the signal intensities by enabling many passes through the active medium. Therefore, Q-switched Yb lasers usually do not show problems with too low a gain and inefficient pulse extraction. For a cw laser above threshold, the gain equals the losses, anyway, no matter how large the small-signal gain is. However, for an Yb^{3+} laser, the smaller product of emission cross section and upper-state lifetime will lead to a higher lasing threshold (see eqs. 3.69.b and 3.28.), which should be countered by a relatively low output coupler transmission and minimization of additional resonator losses.

Ultrashort-pulse generation or amplification

A larger emission bandwidth and therefore a broader gain enable the generation of shorter light pulses or their amplification with minor spectral narrowing. Yb^{3+}-doped active media regularly permit pulse durations below 1 ps (experimental record for Yb^{3+} in a crystalline host: 69 fs with Yb:BOYS [Dru02b]; Yb^{3+} in a glass host: 58 fs with Yb:phosphate [Hoe98]). Nd^{3+}-doped materials do not, with the exception of glass or some disordered crystals [Aus97, Obe92, Yan00], which exhibit only poor thermal properties. On the other hand, Nd materials provide better stability of passively mode-locked lasers against Q-switching, mainly due to higher emission cross sections (chapter 4.3. and [Hoe99]).

2.2. Crystals and glasses as hosts

2.2.1. Influence of the host on spectroscopic properties

While basic theory is explained in this paragraph, formulas, which are essential to determine spectroscopic properties from measured data, are collected in the appendix A.2.

Electronic transition intensities and Stark splitting

One-photon transitions between *4f* electron states (including the $^2F_{5/2}$ and $^2F_{7/2}$ manifolds of Yb^{3+}) are electric-dipole-forbidden, since the parity of the wavefunctions does not change. Therefore only magnetic dipole radiation should be observed, which is rather low in intensity; electric quadrupole transitions are negligible. Actually, we find much larger transition rates, in case of Yb^{3+} usually one to two orders larger than from magnetic dipole radiation alone [DeL93]. This can be explained by interaction of the rare earth ions with the crystal field, which mixes energetically higher-lying states of opposite parity (*5d*, *5g*, ...) into the *4f* states and thus enables electric-dipole transitions. The crystal field also breaks up the degeneracy in the *z*-component M_J of the total angular momentum J (Stark splitting). For an even number of electrons, the electronic levels are split up into $(2J+1)$-fold multiplets, otherwise – like for Yb^{3+} – into $(J+1/2)$-fold multiplets, which are two-fold Kramers degenerated.

Crystal field and Judd-Ofelt theory

There exist different approaches based on perturbation theory to calculate the electric-dipole transition rates and the spectral line patterns of the lanthanides; an overview is given e.g. in [Sme98]. The standard theory was developed by Judd and Ofelt [Jud62, Ofe62].

Usually, the semiempirical form of the Judd-Ofelt theory is used, where the influence of the crystal field on the *4f* energy levels of a specific rare earth ion can be expressed by three parameters (for anisotropic media: three for each polarization); with the help of these, the line patterns can be reproduced with good precision. The Judd-Ofelt parameters are gained by fitting to the observed spectra. In the Judd-Ofelt theory the crystal field is considered to be weak and therefore treated as a perturbation of the free ionic system, where the Hamilton operator is given by a central field, electron correlations, and spin-orbit coupling. Aside from a static contribution of the crystal field, there are also dynamic contributions, e.g. the coupling of the *4f* electronic levels with lattice vibrations, which enhance the transition intensity and split or broaden the spectral lines. The crystal field potential which describes the interactions between the active ion and the ligands can be expressed in the expanded form:

$$V_{CF} = \sum_{t,p} B_{tp} \sum_{i} r_i^t C_p^{(t)}(\theta_i, \phi_i) \qquad (2.1.)$$

Here r_i, θ_i, ϕ_i are the coordinates of the i-th *4f*-electron, p stands for the polarizations, $C_p^{(t)}$ are spherical tensor operators of rank t, and B_{tp} are the so-called crystal field parameters. The even terms ($t = 2, 4, 6, ...$) modify the energies of the electronic states, while the odd ones ($t = 1, 3, 5, ...$) provide the admixture of opposite-parity states and therefore contribute to the intensity of the electric-dipole transition. The set of B_{tp} parameters characterizes the strength and symmetry of the active-ion/host interaction and is individual for each laser material. The maximum Stark splitting of an electronic state of a rare-earth ion scales quasi linearly with the crystal field parameters [Auz02].

Effects determining the crystal field parameters

Shorter distances between the ligands and the *4f*-orbitals of the rare earth ions lead to larger values of the crystal field parameters. This means e.g. that for a given laser ion and crystal structure type the ground state splitting will increase with decreasing lattice constant [Bou02b]. In this context, also, the shielding of the *4f*-electrons by the *5s* and *5p* orbitals against the crystalline environment has to be mentioned. The *5s* and *5p* orbitals form a complete, optically inactive [Xe] rare gas shell, and as the outermost shell they define the ionic radius. They keep the neighbor ligands at a distance and reduce the Coulomb interaction of the *4f* electrons with these. For the *4f* electrons of Yb^{3+} this results in crystal field splittings which are one order smaller than the spin-orbit splitting.

The crystal field parameters increase with the effective charges of the ligands. In fluorides and oxy salts, the crystal field influence on the active ion is mainly given by the Coulomb interaction with the F^- or O^{2-} ligands. The effective charge is larger for F^- than for O^{2-}, since the electrons are localized tightly to the F^-, whereas O^{2-} often show a more covalent character in their bonds, especially if they are part of a chemical group (like in WO_4^{2-}) [Por98].

However, the most important influence is the crystal structure and its symmetry. Where the Yb^{3+} ion occupies a site of perfect cubic symmetry, the admixture of opposite-parity states is weak and the upper state lifetime is very long (e.g. 10.84 ms in Rb_2NaYF_6 [DeL93]). In many hosts containing chemical groups (BO_3, PO_4, WO_4, ...) as anions, the crystal fields are strongly distorted at the position of the active ions, causing a large transition amplitude and anisotropic spectroscopic properties. The Yb^{3+}-doped double tungstates $KLn(WO_4)_2$ (Ln = Y, Gd, Yb) may serve as an example, with excited state lifetimes in the region of 0.3 ms and cross sections that vary strongly for different polarizations.

In general, one cannot conclude that materials with short upper state lifetimes also show large ground state splittings; the behavior of the crystal field parameters assigned to odd parity field components and the behavior of those for even components can differ substantially.

Spectral linewidths

The spectral linewidths observed at room temperature are mainly the result of homogeneous broadening by electron-phonon coupling and, in many hosts, of inhomogeneous broadening by a varying crystal field. These influences often also cause substructures and add satellite lines to the electronic transitions. The contribution by the natural linewidth is negligible.

Line broadening leads to reduced absorption and emission cross sections in the line centers, since the transition intensity is spread over a wider band, while the broadening mechanisms usually are connected with no substantial increase of the transition intensity. Broad linewidths in combination with small Stark-splittings of ground and excited states mean broadly overlapping absorption and emission bands. Laser materials with such properties exhibit a pronounced quasi-three- or quasi-four-level character of their laser operation schemes, i.e. strong reabsorption effects are observed; on the positive side, usually very small quantum defects can be achieved (see also chapts. 5.2.1.3., 5.2.1.4., and A.1.).

Inhomogeneous broadening by crystal field variation

There are different reasons for varying crystal fields: The active ions may be introduced at different sites in the lattice, where they see different ligands or where they are located at varying distances from the ligands. Some hosts show structural disorder; an extreme example are glasses. Furthermore, local distortions of the crystal field by strain, defects, impurities, or other active ions in direct neighborship cause smaller effects.

Homogeneous broadening by electron-phonon coupling

Rare earth ions show a relatively weak coupling of the electronic *4f-4f* transitions to the lattice vibrations compared to the transitions of laser-active transition metal ions, whose spectra exhibit strong vibronic features [McC64b].[1] This behavior is a consequence of the shielding of the *4f* electrons by the *5s* and *5p* orbitals. However, the coupling strength varies within the lanthanide series, reaching maxima at the beginning and at the end of the series [Ell97]. This can be explained by two combined effects: The mean quadratic radii of the electron orbitals decrease from Ce^{3+} to Lu^{3+}, which is the so-called "lanthanide contraction".[2] It reduces the overlap of the *4f* orbitals with the orbitals of the ligands (weaker coupling). On the other hand, the shielding of the *4f* orbitals gets weaker from Ce^{3+} to Lu^{3+} (stronger coupling). Therefore, Yb^{3+} as the last but one in the series exhibits relatively strong homogeneous line broadening, and in many hosts pronounced vibronic features are observed in the spectra [Gau02, Ito04, Mon01, Puj02b, Web71].

Homogeneous line broadening can be referred mainly to two processes: one-phonon absorption and emission and Raman-scattering of phonons [Luo02]. During a radiative electronic transition, a phonon is absorbed from or emitted into the lattice. In this case, the energy of the absorbed or emitted photon lacks or includes the energy of the phonon. Raman-scattering means that during an electronic transition a phonon is absorbed and a phonon with a different energy is emitted. The energy of the absorbed or emitted photon is reduced or increased by this energy difference.

Effects determining the electron-phonon coupling

Electron-phonon coupling results from the relative displacement of the ligands by lattice vibrations and from the hereby changing crystal field, which modulates the initial and/or final wavefunctions of the electron making the transition. This dynamic perturbation smears out the energetic positions of the electronic levels, so that the spectral linewidths contain a Lorentzian-shaped component [Lei98b]. Furthermore, lattice vibrations may combine with the electronic levels to sets of distinct vibronic levels. Transitions involving these are observed in the spectra or can resonantly interact with other transitions, splitting or deforming the lines.

The symmetries of the crystal host cause restrictions for the coupling of electrons and phonons. The electron-phonon coupling strengths vary with the host and in case of anisotropic crystals also with the polarization, resulting in different homogeneous line broadening and different vibronic features. The broadening increases with the variance of the ion masses in the crystal; it also depends on the crystal density, the sound velocities, and the Debye temperature of the crystal [Luo02].

---

1 "vibronic": expression for states where electronic levels and lattice phonons are coupled or for transitions between such states; linguistically, from "electronic" and "vibrational"

2 This size contraction arises because of poor shielding of the atomic nucleus by the highly directional *4f* electrons.

2.2.2. Overview of hosts: spectroscopic properties

Table 2.1. displays a selection of the most important Yb^{3+} laser materials with their spectroscopic properties, including the tungstate and sesquioxide crystals used in the experimental part in chapts. 5 and 6.[1] The materials are arranged according to their anions or anionic groups; most of these contain oxygen. The Yb^{3+} ion mostly substitutes for a trivalent cation (Y^{3+}, lanthanides: Gd^{3+}, Sc^{3+}); in some crystals it is doped into the site of a monovalent or divalent cation (Li^+ in $LiNbO_3$, Sr^{2+} in $Sr_5(PO_3)_4F$). $KYb(WO_4)_2$ is actually not a doped material, but a stoichiometric laser crystal (see chapt. 2.3.).

Tabulated data

With the exception of $Y_3Al_5O_{12}$ (YAG), Sc_2O_3 (scandia), and glass all listed materials are anisotropic. This means that the absorption and emission properties vary with the orientation of the crystal relative to an incident light beam and its polarization. Therefore, in the case of uniaxial crystals two sets of spectroscopic data are given, wherever these were available from literature: for light polarization perpendicular or parallel to the crystallographic $\boldsymbol{c}$-axis ($\boldsymbol{E}\perp\boldsymbol{c} = \sigma$ polarization; $\boldsymbol{E}||\boldsymbol{c} = \pi$ polarization; $\boldsymbol{E}$ stands for the electrical field vector). Biaxial crystals are described by three sets of data: An adequate description relates the cross sections to the crystallo-optic axes ($\boldsymbol{E}||\boldsymbol{N_m}$, $\boldsymbol{E}||\boldsymbol{N_p}$, and $\boldsymbol{E}||\boldsymbol{N_g}$). Alternatively, data can be related to crystallographic axes ($\boldsymbol{E}||\boldsymbol{a}$, $\boldsymbol{E}||\boldsymbol{b}$, and $\boldsymbol{E}||\boldsymbol{c}$).[2] However, often spectra or single values are published for one orientation only, which is not specified; we may assume that it is the most favorable one.

The lifetimes given are radiative ones and were determined mostly from lowly doped samples, unless otherwise stated. The absorption and emission wavelengths are those likely to give the best laser results, but this can depend very much on individual demands and conditions, especially concerning the emission. In this context, we do not include emission bandwidths in the table. These seem to be interesting to estimate laser wavelength tunability or the minimum pulse durations from mode-locked lasers, but actually, what counts is the gain bandwidth. For a quasi-three- or quasi-four-level laser material, this quantity depends strongly on the inversion parameter (see e.g. the effective gain coefficient of KYbW in Fig. 3.3.). Furthermore, in the emission spectra of most laser materials no well-defined bandwidth is observed in the sense of full width at half maximum.

Comparison of hosts

A rough categorization can be made considering the ground state Stark splitting and the upper state lifetime:

A small splitting corresponds to a strong “quasi”-three- or “quasi”-four-level character due to thermal population of the terminal laser level. This means that the influence of reabsorption on laser operation can be strong, with a high minimum pump intensity to achieve transparency and with a relatively high laser threshold. On the other hand, small laser and fluorescence quantum defects can be realized.

---

[1] Their thermo-mechanical and thermo-optical properties are given in Table 2.2.

[2] Care has to be taken to avoid confusion that can arise from different settings for the crystallographic axes.

Table 2.1. Spectroscopic properties of Yb^{3+} in 13 crystalline hosts and a laser glass. Absorption and emission can depend on polarization: π - $\boldsymbol{E} \| \boldsymbol{c}$, σ - $\boldsymbol{E} \perp \boldsymbol{c}$, a - $\boldsymbol{E} \| \boldsymbol{a}$, b - $\boldsymbol{E} \| \boldsymbol{b}$, c - $\boldsymbol{E} \| \boldsymbol{c}$, m - $\boldsymbol{E} \| \boldsymbol{N_m}$, p - $\boldsymbol{E} \| \boldsymbol{N_p}$, g - $\boldsymbol{E} \| \boldsymbol{N_g}$ (electrical field vector $\boldsymbol{E}$, crystallographic axes $\boldsymbol{a, b, c}$, crystallo-optic axes $\boldsymbol{N_m, N_p, N_g}$). unpol. - unpolarized, n.d. - no data.

	aluminate		**borates**						**fluoride**	**fluorophosphate**		**tungstates**			**silicate**		**sesquioxide**		**niobate**	**glass**
compound	**$Y_3Al_5O_{12}$**		**$YAl_3(BO_3)_4$**	**$Sr_3Y(BO_3)_3$**	**$Ca_4YO(BO_3)_3$**		**$Ca_4GdO(BO_3)_3$**		**$LiYF_4$**	**$Sr_5(PO_3)_4F$**		**$KGd(WO_4)_2$**	**$KY(WO_4)_2$**	**$KYb(WO_4)_2$**	**$SrY_4(SiO_4)_3O$**		**Sc_2O_3**		**$LiNbO_3$**	**QX phosphate**
acronym	YAG		YAB	BOYS	YCOB		GdCOB		YLF	S-FAP		KGW	KYW	KYbW	SYS				LNB	QX
optical class	isotropic		biaxial	uniaxial	biaxial		biaxial		uniaxial	uniaxial		biaxial	biaxial	biaxial	uniaxial		isotropic		uniaxial	isotropic
$^2F_{7/2}$ Stark splitting $\Delta E_{7/2}$ [cm^{-1}]	789		n.d.	859/734 (site1/2)	1005		1003		438	1190		535	568	555	810		1017		766	564
radiative lifetime τ_{rad} (or fluorescence lifetime τ_f) [µs]	1000 (5% Yb^{3+})		1110 (τ_f)	1200 (13.7% Yb^{3+})	2280 (τ_f, 18.3% Yb^{3+})		2600 (τ_f)		2000 (τ_f, 40.5% Yb^{3+})	1140		320 (τ_f)	300 (τ_f)	270	800		800		540	1300 (τ_f)
absorption wavelength λ_a [nm]	968	941	975	975	900	976	901	976	960	900		981	981	981	918	979	942	975	980	975
absorption cross section $\sigma_a(\lambda_a)$ [10^{-20}cm^2]	0.63	0.72	3.4 (π) 2.1 (σ)	0.73 (σ) 0.94 (π)	n.d.	1.0	(0.4 unpol.)	1.1 (0.87 unpol.)	1.2 (π) 0.5 (σ)	9 (π)		12 (a) 2 (b) 1.9 (c)	13.3 (a) 3.1 (b) 2.1 (c)	11.7 (m) 2.2 (p) 1.7 (g)	0.34 (σ) 0.40 (π)	1.22(σ) 0.87(π)	0.87	4.4	1.0	0.7
absorption bandwidth $\Delta\lambda_a$ [nm]	2.6	~18	~20	6.9 (σ) 5.8 (π)	n.d.	2.5	(~15 unpol.)	2.5 (2.6 unpol.)	12 (π)	~3		3.7 (a)	3.5 (a)	4 (m)	~30 (σ) ~30 (π)	4.3 (σ) 5.4 (π)	~25	~1.5	~20	~7
reemission cross section $\sigma_e(\lambda_a)$ [10^{-20}cm^2]	0.5	0.15	n.d.	n.d.	n.d.	0.96	n.d.	1.1	~0.15 (π) ~0.15 (σ)	0.08		14.6 (a)	16.2 (a) 3.7 (b) 2.6 (c)	12.5 (m) 2.4 (p) 1.7 (g)	0.03 (σ)	1.47(σ)	0.15	4.6	1.0	0.7
emission wavelength λ_e [nm]	1030	1050	1040	1066	1032	1084	1032		1018	985	1047	1023	1025	1025	1040		1041	1095	1060	1060
emission cross section $\sigma_e(\lambda_e)$ [10^{-20}cm^2]	1.9	0.3	0.8 (π) 0.65 (σ)	0.2	0.39	0.10	0.36		0.85 (π) 0.75 (σ)	10 (σ)	7.3 (π)	2.8 (a)	3 (a) 2.2 (b) 0.8 (c)	2.6 (m) 1.0 (p) 0.37 (g)	0.44		1.4	0.33	1.0	0.05
reabsorption cross section $\sigma_a(\lambda_e)$ [10^{-20}cm^2]	0.1	0.01	0.04	n.d.	0.03		0.03		~0.15 (π) ~0.05 (σ)	2.2	0.4	0.3 (a)	0.3 (a) 0.2 (b) 0.15 (c)	0.3 (m) 0.1 (p) 0.04 (g)	~0.02		0.07	<0.01	0.02	0.001
data taken from	[Bre01b, Hau02, Hoe99b, Pat01]		[Bre01b, Foe03, Wan99b]	[Che02, Hau02]	[Aro01, Bre01b, Wan99]		[Aro01, Bre01b, Che02, Druo02c, Hau02]		[Kaw02, Ueh96]	[Bay00, Bre01b, Sch03]		[Bre01, Bre01b, Kul97b, Mun01]	[Dem00, Kul97b]	[Puj02b]	[Dru02, Hau02]		[Pet00, Pet01]		[Bre01b, Mon01b]	[Hoe99b, Lei98]

As already explained in chapt. 2.1.2. when comparing Nd^{3+} and Yb^{3+}, the reabsorption handicap will play a decisive role, if only low signal intensities in the active medium can be achieved, due to low peak pump power or since the signal experiences only one to few effective passes through the medium. In comparative studies aiming at such applications (like [DeL93]), materials in which Yb^{3+} shows a large $^2F_{7/2}$ state splitting $\Delta E_{7/2}$ will excel: $Sr_5(PO_3)_4F$ (strontium-fluorapatite, S-FAP), Sc_2O_3 (scandia), $Ca_4YO(BO_3)_3$ (YCOB), and $Ca_4GdO(BO_3)_3$ (GdCOB), with $\Delta E_{7/2} > 1000$ cm^{-1}. $LiYF_4$ (YLF, $\Delta E_{7/2} = 438$ cm^{-1}) will hold the last position in our field; the isostructural double tungstates $KGd(WO_4)_2$ (KGW), $KY(WO_4)_2$ (KYW), and $KYb(WO_4)_2$ (KYbW) with splittings around 550 cm^{-1} will come out as unfavorable, too. Nevertheless, Yb:YLF has proved to be a highly efficient amplifier material (68% extraction efficiency), when used at liquid-nitrogen temperature in a diode-pumped chirped-pulse regenerative amplifier [Kaw03]. A small laser quantum defect is advantageous in terms of lower heat production and higher intrinsic efficiency.[1] The latter contributes to the fact that Yb^{3+}-doped tungstates can permit higher extraction efficiencies than Yb^{3+}-doped materials with a much larger Stark-splitting, even at room temperature, if reabsorption is minimized by an appropriate length of the laser medium and bleached by high signal intensities (see chapt. 3.3.3.). Making these assumptions, an evaluation of 13 available Yb^{3+}-doped laser crystals for longitudinal pumping saw Yb:KGW and Yb:KYW in the first positions (third rank: Yb:Sc_2O_3) with respect to slope efficiency and output yield [Bre01b].[2]

A long lifetime of the upper state permits to store more energy for a laser pulse. Therefore, three materials are especially interesting for pulsed applications with low repetition rates ($\leq\tau_{rad}$): $Ca_4YO(BO_3)_3$ (YCOB), $Ca_4GdO(BO_3)_3$ (GdCOB), and YLF exhibit lifetimes larger than 2 ms. Aside from this application, a longer radiative lifetime has to be regarded as a disadvantage, since it is inevitably connected with lower cross sections. These can cause inefficient pump light absorption or too low single-pass gain, if it is not possible to realize high Yb^{3+} concentrations or long crystals.[3]

The product of emission cross section and fluorescence lifetime, together with reabsorption, is crucial for the laser threshold (see eqs. 3.69.b and 3.28.). This product differs with the material. Therefore we have to take a closer look at the cross sections and the related quantities.

The absorption and emission cross sections depend not only on the radiative lifetime, but also on the bandwidth of the optical transition and on the anisotropy of the crystal (see Füchtbauer-Ladenburg equation, appendix, eqs. a.7. and a.8.).

There are reasons to desire a broad transition: Concerning absorption, a good spectral overlap with the pump radiation is required to pump efficiently by laser diodes; concerning emission, a broader gain bandwidth will enable shorter mode-locked pulses (see "gain dispersion" in chapt. 4.2.) and wider wavelength tunability. Some materials are specially designed for such demands, at the cost of lower cross sections (most noticable with the emission). In $Sr_3Y(BO_3)_3$ (BOYS), $SrY_4(SiO_4)_3O$ (SYS), YCOB, GdCOB, and glass,[4] broad lines are generated mainly by

---

[1] Here, "intrinsic" means considering only the transitions of an Yb^{3+} ion without the influence of a laser resonator.

[2] This is not contradicted by our cw experiments, presented in chapt. 5.1.1., where a slope efficiency of 68% and a maximum output yield of 49% are obtained from a 5% Yb^{3+}-doped KYW medium, although the crystal was longer than optimum. Using Yb:Sc_2O_3 in another cw laser, but pumped by the same source (Ti:Sapphire laser, ≈2W), we achieve 65% and 57%, respectively (chapt. 6.1.).

[3] Long crystals, however, are not optimal with bad-beam-quality pump sources, since high pump intensities are difficult to achieve.

[4] We have chosen an often used phosphate laser glass for this comparison. Although the spectroscopic properties can be influenced by the chemical composition, the listed data represent features typical for all glasses.

inhomogeneous broadening. On the opposite we find S-FAP, in which Yb^{3+} exhibits extraordinarily high cross sections in connection with narrow lines.

In the tungstates, Yb^{3+} shows very high cross sections, too, but these are due to the short radiative lifetimes and the anisotropy of the crystals: The strength of the transition is “concentrated” mainly in the cross sections for the $\boldsymbol{E}||\boldsymbol{N_m}$ orientation. Because of this, the emission and possible gain bandwidths of Yb:KYW, Yb:KGW and KYbW are fairly large, permitting also relatively short pulses.

Conclusion from spectroscopic properties

The comparison of spectroscopic properties leads to the following recommendations:

For the generation of mode-locked pulses with durations significantly shorter than 100 fs, BOYS, SYS, glass, YCOB, and GdCOB are good choices, if high single-pass gain is not required. With their long upper state lifetimes, the latter two[1] apply also for lowly repetitive laser systems with high pulse energies.

S-FAP and YLF get recommendations for such systems, too. The Yb^{3+}-doped fluorapatite is especially interesting for few-path amplifiers because of its high gain cross sections. With Yb:YLF, however, strong cooling of the crystal is necessary, to take profit from the long excited state lifetime and the slightly larger cross sections compared to YCOB and GdCOB.

The Yb tungstates are an excellent choice for cw or mode-locked lasers in which high pump and signal intensities are realized, so that reabsorption is suppressed. In such systems very high efficiencies can be achieved, and the low heat production is advantageous. The minimum duration of mode-locked pulses is similar to those of the materials recommended above (<100 fs).

The other laser crystals, $Y_3Al_5O_{12}$ (YAG), $YAl_3(BO_3)_4$ (YAB), Sc_2O_3, and $LiNbO_3$ (LNB) do not exhibit extraordinary spectroscopic properties, neither good nor bad. Among them, Sc_2O_3 shows the best combination of properties. Therefore and since the thermo-optical and thermo-mechanical behavior of this host is very favorable, which will become obvious in chapt. 2.2.4., we have chosen Yb^{3+}-activated scandia as well as tungstates for our laser experiments.

---

[1] The properties of these two materials are generally very similar. This is the case also for the three Yb^{3+}-activated tungstates. Therefore, from spectroscopy there is no preference for Y^{3+} or Gd^{3+}, and in the tungstates, the active ion Yb^{3+} itself does not seem to strongly modify the crystal field.

2.2.3. Thermo-mechanical and thermo-optical properties of the host

Refractive index

In the absence of gain, absorption, or nonlinearities, the refractive index of a material is given by $n = (\kappa_e \kappa_m)^{1/2}$, where $\kappa_e = 1+X^{(1)}$ is the dielectric constant ($X^{(1)}$, first-order electric susceptibility) and κ_m is the relative magnetic permeability. With the exception of ferromagnetic materials, the relative magnetic permeability is ≈1. The dielectric constant depends on the polarizability of the material, which increases with the ion radii of the cationic constituents, the proton number of the cations (within the same group of elements), and the difference of the electronegativities between cations and anions [Luo02].[1]

For anisotropic materials, the refractive index depends on the polarization and the unit wave vector of the light beam. Conventions for refractive indices of such materials are explained in the appendix, A.3.

Dependence of the refractive index on temperature

The change of the refractive index with temperature is important especially for high-power lasers, since it causes thermal lensing and birefringence (see appendix A.6., eqs. a.17.-a.23.). It can be described as the sum of a variation caused directly by temperature, $\Delta n_T \propto dn/dT$, and a stress-dependent variation, $\Delta n_\varepsilon \propto \alpha$ (α, thermal expansion coefficient) [Koe92, Web99].

For anisotropic materials, the thermo-optic coefficient dn/dT (just like the refractive index n) depends on the polarization of the transmitted light beam. Furthermore, in case of inhomogeneous heating, dn/dT will additionally depend on the orientation of the heat flow and on the orientation and shape of the heated zone, if the optical indicatrix does not have the same orientation as the thermal conductivity tensor. The thermo-optic coefficient can have positive or negative values. It is temperature-dependent; many lasers materials will profit from reduced thermal lensing, if they are operated at low temperatures.

Dispersion

The wavelength-dependence of the refractive index, can be expressed by a "Sellmeier equation" for $n(\lambda)$, which is a suitable polynomial equation containing the so-called Sellmeier equation parameters. These are tabulated in literature for many laser materials. The dispersion $dn(\lambda)/d\lambda$ (and higher orders $d^2n(\lambda)/d\lambda^2$, ...) can be obtained easily by differentiation of the equation (see also appendix A.4.). For the influence of dispersion on the pulse duration obtained from mode-locked lasers and ultrashort-pulse amplifiers see chapt. 4.

The intensity-dependent nonlinear refractive index n_2 is also treated in chapt. 4.

Thermal expansion

Thermal expansion is the result of anharmonic terms (higher than quadratic dependencies on the distance) in the potential energies of the bound ions [Kit91]. The expansion coefficient α can be expressed by [Via03]

---

[1] The Füchtbauer-Ladenburg equation a.7. shows that the emission cross section σ_e is proportional to n^{-2}; effects increasing n should therefore decrease σ_e.

$$\alpha = \frac{mT^{m-1}}{T^m + \frac{T_{mp}^m}{\varepsilon_{sr}^3 - 1}} , \qquad (2.2.)$$

where

m, adjustable parameter, $1.3 < m < 1.5$,
T_{mp}, melting point temperature,
ε_{sr}, relative strain of the interatomic distances going from room temperature to T_{mp}.

With increasingly ionic character of the bonds, ε_{sr} will increase and therefore α will also. Among materials with equally ionic bonds, those with stronger bonds and therefore higher melting points show weaker thermal expansion.

Thermal expansion contributes to thermal lensing by stress-induced variation of the refractive index, $\Delta n_\varepsilon \propto \alpha$, and by deformation of the end-faces of the laser medium (see appendix, eqs. a.19-a.21.). Furthermore, thermal expansion and the resulting stress can lead to fracture of a laser medium. Especially, anisotropic crystals that show large variations of the thermal expansion coefficients for different orientations tend to crack at rapid changes of temperature [Gau03]. Such changes can occur during crystal growth or if the heat load changes during laser operation. For laser rods made from isotropic materials, the maximum permitted (continuous) heat load P_{heat}, before surface tensions will lead to fracture at a given tensile strength, decreases with the expansion coefficient $P_{heat} \propto 1/\alpha$ (see [Koe92] and eqs. a.24. and a.25.). In practice, the fracture limit of a laser crystal very much depends on the individual quality of the medium, including surface quality after polishing.

Thermal conductivity

In isolating materials, thermal conductivity is the result of phonon diffusion. The thermal conductivity κ can be expressed by [Kit91]

$$\kappa = \tfrac{1}{3} C\, v\, l , \qquad (2.3.)$$

with

C, specific heat per volume,
v, velocity of sound,
l, mean free path length of phonons.

For anisotropic materials, there is an equation analog to eq. 2.3. for each orientation.

C depends on the density of phonon states (concerning frequency and volume) and their population; therefore C increases with temperature. v decreases with increasing mass density ρ and with decreasing elasticity modul (weak bonds, usually corresponding to a low melting point).

The mean free path length of phonons is limited mainly by two processes [Kle60][1]:

---

[1] Here we neglect the extensions of the medium, which become important for very small structures at temperatures close to 0 K.

1. Two phonons scatter at each other in such a way, that one phonon with a different momentum results, compared to the previous total momentum (so-called "umklapp-process"). Conservation of momentum is fulfilled, since the lattice contributes the difference to the momentum. This contribution is possible only for relatively high phonon energies.[1] The population of suitable phonon states increases with temperature, which reduces thermal conductivity.[2]

2. Irregularities of the lattice structure act as scattering centers. Such include defects, impurities, and dopant ions. The effect explains the relatively low thermal conductivities of disordered materials and the sometimes drastic decrease of thermal conductivity with increasing doping level [Pad97, Pat01, Via03].

A relationship for the influence of the doping level on thermal conductivity is given by [Pad97]

$$\kappa = \kappa_{in}\sqrt{\frac{\chi T}{C_{dop}(1-C_{dop})}}\arctan\sqrt{\frac{C_{dop}(1-C_{dop})}{\chi T}} \qquad (2.4.)$$,

where

χ,	constant, characteristic for the material,
T,	temperature,
C_{dop},	relative dopant ion concentration, $0 \le C_{dop} \le 1$,
$\kappa_{in} = C_{dop}\kappa_2 + (1-C_{dop})\kappa_1$	"interpolated " thermal conductivity, obtained from that of the pure host, κ_1, and that of the "100% doped" material, κ_2.

If dopant ions and replaced ions are very similar in terms of radii, mass, and effective charge, or more generally, if the degree of total disorder in the material experiences only a minor change by doping, χ will take on a small value. In this case there will be no significant deviation of κ from the interpolated conductivity κ_{in}. Furthermore, for similar properties of dopant and replaced ions, we can expect $\kappa_{in} \approx \kappa_1 \approx \kappa_2$.

Equation 2.4. shows that for high doping levels C_{dop} (i.e. >50%, usually) the thermal conductivity can increase with C_{dop}, since structural disorder is reduced. This was also observed experimentally [Pat01].
In case of Yb^{3+} replacing Y^{3+} or trivalent lanthanide ions, which all show very similar chemical behavior, mass variance is the main contribution to disorder. The consequence is that Gd^{3+} (atomic weight 157), whose mass is close to Yb^{3+} (at. weight 173), is the better host ion compared to Y^{3+} (at. weight 89) with respect to thermal conductivity at higher dopant levels [Che03, Via03].[3]

All negative effects connected with heating of a laser medium (thermal lensing and birefringence, danger of fracture) scale linearly with the thermal resistance $1/\kappa$. Formulas are given in appendix A.6.

---

[1] This means energies in the order of $(1/2)k\Theta_D$, with Θ_D, Debye temperature.

[2] At very low temperatures, the effect of C increasing with temperature T is dominant, so that κ becomes larger with T in this region.

[3] The equation given in [Via03] for the thermal conductivity cannot be recommended in general, however; see comments in the appendix, A.5.

2.2.4. Overview of hosts: Thermo-mechanical and thermo-optical properties

Table 2.2. gives the thermo-mechanical and thermo-optical properties of twelve important Yb^{3+} laser crystal hosts, including the tungstate and sesquioxide crystals used in the experimental part in chapts. 5 and 6, and of phosphate glass.[1] Good thermo-mechanical and thermo-optical properties are important for high-power oscillators or amplifiers, with respect to lensing, birefringence and fracture as a result of dissipated heat;[2] lower-power applications usually do not suffer from such effects. Generally, thermal properties play less a role for the laser performance of Yb^{3+}-based laser materials, if compared to Nd^{3+}-activated crystals or glasses that are used as four-level laser materials, since the amount of heat generated is much lower (for diode-pumping, during laser operation less than <50% of the Nd^{3+} heat load).

Tabulated data

The refractive indices n are given for a wavelength of ≈1050 nm; their temperature-dependent variations dn/dT refer to homogeneous heating.[3] All thermo-mechanical and thermo-optical data are values at room temperature. Temperature-dependent properties are usually measured with large uncertainties; published values often vary within ±20 to 30% (see e.g. YAG [Pol98]).

For anisotropic crystals (here: the listed crystals except YAG and Sc_2O_3), all quantities depend on the sample orientation, thermo-optical ones additionally on light polarization. In some cases, however, only a single value was found for a quantity, without further specification; we may assume an averaged value. More information on the thermal expansion and conductivity of the double tungstates can be found in chapt. 2.4.; the crystal axes [302], [010], and [106] define the orientation of the diagonal thermal expansion tensor. Only if expansion data of anisotropic crystals refer to the appropriate diagonal tensor, they provide maximum and minimum values of the expansion.

Thermal conductivity is tabulated for the undoped hosts. Unfortunately, only in a few cases data were measured also for the Yb^{3+}-doped crystals (YAG [Che03, Pat01], BOYS [Gau03], SYS [Dru02], scandia [Pet01]). Viana et al. presented calculations of the thermal conductivity of YAG, GdCOB, YLF, KGW, scandia and others [Via03]. We will include the results in the discussion below. The value given for the stoichiometric KYbW crystal in Table 2.2. is an average over different orientations and was obtained by assuming that all three tungstates have very similar thermal properties.

Comparison of hosts

While comparing Yb^{3+}-activated materials we must keep in mind that Yb^{3+} laser and fluorescence quantum defects and the resulting heat production can differ significantly with the host and the laser configuration, so that less favorable thermal properties may be compensated. Efficient cooling reduces thermal effects, too.

---

[1] Their spectroscopic properties are given in Table 2.1.

[2] Here, thermal birefringence may play a role only for the three isotropic hosts.

[3] Data for inhomogeneously heated KGW are given in chapt. 2.4. and show significant deviations from the homogeneous-heating case; this may become important for the thermal lensing in different laser designs (shape of medium, cooling).

Among the materials in Table 2.2., two hosts stand out with the best thermo-mechanical and thermo-optical properties: YAG and Sc_2O_3 (scandia). Although the expansion coeffients α and the index variation *dn/dT* (for YAG) are not better than average, only relatively weak thermal lensing can be expected due to excellent thermal conductivity, $\kappa > 10$ $WK^{-1}m^{-1}$ in case of lowly doped crystals. Both materials show a high resistivity against fracture. This results from high values of κ, tight ionic bonds, which are indicated by the high melting-point temperatures, and the isotropy of thermal expansion.

Because of their isotropic nature, YAG and scandia may require compensation for thermal birefringence. Another disadvantage is that the ion masses of Yb^{3+} and Y^{3+} or Sc^{3+} differ strongly, and therefore κ is much lower already at medium or low doping levels (6 $WK^{-1}m^{-1}$ for Yb(15%):YAG [Che03], 6.6 $WK^{-1}m^{-1}$ for Yb(2.8%):Sc_2O_3 [Pet01]).[1] Therefore, if high dopant concentrations are required, isostructural analogs of YAG and scandia (i.e. other garnets and sesquioxides) are interesting alternatives, which exhibit very similar properties, but where the masses of the ions to be replaced by Yb^{3+} are closer to the mass of Yb^{3+}, e.g. $Gd_3Ga_5O_{12}$, $Lu_3Al_5O_{12}$, or Lu_2O_3 (see [Che03, Via03] and chapt. 2.2.3.). However, even doped YAG and scandia show better conductivities than most of the other undoped hosts.

Two host materials look attractive because of their good thermal conductivity, $\kappa > 5$ $WK^{-1}m^{-1}$: YLF and LNB. For YLF, the small variation *dn/dT* of the refractive index, too, helps to reduce thermal lensing. A problem with YLF is the low resistivity against fracture [Koe92], indicated by the low melting point (weak bonds). Anisotropic thermal expansion also has a negative influence on fracture resistivity.

Concerning thermal conductivity, YAB and the three double tungstates take an average position, with $\kappa \approx 3$ $WK^{-1}m^{-1}$. From the thermal-conductivity point of view, KGW may be favorable to KYW for high Yb^{3+} dopant concentrations, due to the similar masses of Gd^{3+} and Yb^{3+}. In the stoichiometric material KYbW, the presence of the active ions does not harm its thermal conductivity.

The data for *dn/dT* of the tungstates are contradictory. Experiments with Nd^{3+}-doped materials pumped by 400 W average power from a flash lamp showed a three times stronger thermal lens in Nd:KGW than in Nd:YAG [Mus97]. On the other hand, an experimental comparison of Yb laser crystals [Che03b] at average pump powers up to 6W found about the same strength of thermal lensing for Yb:KGW and Yb:YAG. For this result the low laser quantum defect of Yb^{3+} in the tungstate crystal was essential (see also chapt. 5.2.1.4. and [Klo03]).

Thermal expansion is strongly anisotropic for YAB as well as for the tungstates and may cause cracking problems, if heating is strong and changes rapidly.

The other laser crystals tabulated here show only poor thermal conductivity, $\kappa \approx 2$ $WK^{-1}m^{-1}$. At least, for BOYS and SYS it is known, that κ does not decrease much with the Yb^{3+} doping level [Dru02, Gau03]. For S-FAP and σ-polarized light, *dn/dT* is 0; therefore in this case only weak thermal lensing can be expected. On the other hand S-FAP, when pumped at 900 nm and lasing at 1047 nm, exhibits the largest laser quantum defect of the tabulated materials and therefore the largest thermal load. For BOYS, the strong anisotropy of thermal expansion corresponds to the brittleness observed [Gau03].

Low thermal conductivity is typical for all laser glasses, since their structural disorder limits the free path length of the phonons. QX phosphate is one of the more favorable glasses concerning

---

[1] Please note, in scandia the dopant concentration is higher for a given doping level than in YAG, since 40% of the ions are replacable by dopant, while Y^{3+}/Yb^{3+} only make 15% of all ions in Yb:YAG. Furthermore, spectroscopic cross sections are larger in scandia.

thermal lensing, since the value of *dn/dT* is relatively low. However, this quantity varies strongly with the composition of the glass. Glasses are very sensitive to thermal fracture.

Additionally, some of the hosts in Table 2.2. have advantageous nonlinear optical properties: YAB, GdCOB, YCOB, and LNB permit self-frequency doubling of the Yb^{3+} emission; with KGW, KYW, and KYbW efficient self-Raman generation is possible.

Conclusion from thermo-mechanical and thermo-optical properties

The comparison of thermo-mechanical and thermo-optical properties leads to the following recommendations:

For high-average power laser sources, YAG and scandia hosts exhibit the most advantageous thermal properties, which make cooling easy and reduce the danger of fracture. Thermal birefringence may need compensation, however.

YLF, YAB, and the tungstates KGW, KYW, and KYbW are less favorable, but can be suitable for high-average power applications, if efficient cooling or a small thermal load per volume is realized [Bow02, Bru02]. The latter approaches can help also with the other materials in Table 2.2.; fiber lasers are a good example. Otherwise they can be recommended only for low- and moderate-average-power laser systems.

Table 2.2. Thermo-mechanical and thermo-optical properties of 13 Yb^{3+} doped laser crystals and a laser glass. The refractive index and its variation with temperature can depend on polarization: π - ***E***||***c***, σ- ***E***⊥***c***, m - ***E***||N_m , p - ***E***||N_p, g - ***E***||N_g (electrical field vector ***E***, crystallo-optic axes N_m, N_p, N_g), av. - averaged value. Thermal expansion and thermal conductivity can depend on sample orientation: a – along ***a,*** b – along ***b*** , c -along ***c*** (crystallographic axes ***a, b, c***) , [ijk] – along crystal-axis [ijk]. n.d. - no data.

	aluminate	**borates**				**fluoride**	**fluorophosphate**	**tungstates**			**silicate**	**sesquioxide**	**niobate**	**glass**
compound	**$Y_3Al_5O_{12}$**	**$YAl_3(BO_3)_4$**	**$Sr_3Y(BO_3)_3$**	**$Ca_4YO(BO_3)_3$**	**$Ca_4GdO(BO_3)_3$**	**$LiYF_4$**	**$Sr_5(PO_3)_4F$**	**$KGd(WO_4)_2$**	**$KY(WO_4)_2$**	**$KYb(WO_4)_2$**	**$SrY_4(SiO_4)_3O$**	**Sc_20_3**	**$LiNbO_3$**	**QX phosphate**
acronym	YAG	YAB	BOYS	YCOB	GdCOB	YLF	S-FAP	KGW	KYW	KYbW	SYS		LNB	QX
optical class	isotropic	biaxial	uniaxial	biaxial	biaxial	uniaxial	uniaxial	biaxial	biaxial	biaxial	uniaxial	isotropic	uniaxial	isotropic
refractive index n (at 1050 nm)	1.82	1.76 (π) 1.69 (σ)	1.74	1.67 (p) 1.70 (m) 1.71 (g)	1.68 (p) 1.70 (m) 1.71 (g)	1.47 (π) 1.45 (σ)	1.61 (π) 1.62 (σ)	2.06 (g) 2.01 (m) 1.98 (p)	2.05 (g) 2.01 (m) 1.97 (p)	2.08 (g) 2.04 (m) 2.00 (p)	1.77 (av.)	1.965	2.16 (π) 2.23 (σ)	1.535
temperature-dependent variation dn/dT [$10^{-6}K^{-1}$]	8.3	11	n. d.	n. d.	n. d.	-4.3 (π) -2.0 (σ)	-5 (π) 0 (σ)	~0.4	~0.4	31 (g) 31 (m) 73 (p)	n. d.	n. d.	38 (π) 5 (σ)	-1.0
melting point temperature T_{mp} [°C]	1970	n. d.	1400	1510	1480	825	1790	1075	~1080	1045	~2000	~2430	1255	(450 glass transition)
thermal expansion coefficient α [$10^{-6}K^{-1}$]	6.7	1.4 (a) 8.1 (c)	5 (a) 20 (c)	9.9 (a) 8.2 (b) 12.8 (c)	10.2 (a) 8.3 (b) 14.3 (c)	13 (a) 8 (c)	9.5 (⊥c) 8.4 (c)	4 [100] 3.6 [010] 8.5 [001]	~4.6	8.7 [302] 2.6 [010] 16.7 [106]	n. d.	9	15 (a) 4.1 (c)	8.3
thermal conductivity of the undoped host κ_0 [$Wm^{-1}K^{-1}$]	10.7	~3	1.8	1.8 (a) 1.7 (b) 2.2 (c)	2.1	7.2 (a) 5.8 (c)	2.0	2.8 [100] 2.5 [010] 3.5 [001]	~3	~3	1.6 (⊥c) 2.85(c)	>=16.5	5.6	0.85
data taken from	[Che03, Koe92 , Kru86, Pol98]	[Blo03, Bou02b, Li03, Luo02]	[Che02, Gau03]	[Luo01, Luo02]	[Dru02c, Luo02, Wan00b]	[Koe92, Pol98]	[Sch03]	[Kam02, Kle69, Puj99]	[Kam01, Kam02]	[Kle69, Puj02, Puj02b]	[Dru02, Hau01b, Hau02]	[Mix99, Pet01]	[Bor93, Imp04, Luo02]	[Hoe99b, Lei98]

2.2.5. Crystal quality and dopability

Yb^{3+}-doped Al_2O_3 would be an interesting laser material, with extraordinarily high thermal conductivity (42 $WK^{-1}m^{-1}$ at 300 K [Koe92]) and high robustness. Unfortunately, the ion radii of Al^{3+} and Yb^{3+} differ too much to grow high-quality Yb:Sapphire laser crystals. The problem with different ion radii exists to some degree also when Yb^{3+} replaces other cations. Of the materials included in Tables 2.1. and 2.2., those are concerned where Yb^{3+} is doped into Sc^{3+}, Gd^{3+}, Li^{+}, or Sr^{2+} sites. On the other hand, the ion radius of Y^{3+} is very close to that of Yb^{3+}.[1]

Different ion radii at a crystal site lead to strong tensions in the lattice, which may result in structural defects, stress-induced birefringence, and, in the worst case, fracture. The distribution coefficient, which is the ratio of the active-ion concentration in the crystal and the active-ion concentration in the melt or solution with respect to the ions constituting the crystal, is significantly lower than 100% and decreases with increasing concentrations. Furthermore, the coefficient varies for different positions in the crystal, i.e. the material is doped inhomogeneously [Mix99, Pet01]. In practice, these effects require a careful choice of the growing parameters and limit the achievable maximum dopant content in the laser material. For Y^{3+}-based hosts, this limitation does not exist and very high Yb^{3+} doping levels have been realized with good optical quality (see [Pat01] and chapt. 5.2.); problems, however, may occur from impurities, whose importance increases with the Yb^{3+} concentration.[2]

Additional difficulties for growth arise, if the ions to be replaced by Yb^{3+} are not trivalent, like in S-FAP. Then charge compensation is required, which promotes structural irregularities and defects [Sch03]. Furthermore, unfavorable thermal properties (high anisotropic thermal expansion, low thermal conductivity) increase the danger of cracking during growth [Gau03, Li03]. Generally, high growing temperatures make the crystal production more complicated (thermal isolation, diffusion of impurities from the environment).

At the moment, much experience exists with the growth of some host materials, especially YAG. At least for the other yttrium-containing hosts or if Yb^{3+} doping levels are kept low in the other materials, it should also be possible to obtain a reliably constant crystal quality, which is required for use in industrial laser products.

---

[1] This is valid also for Lu^{3+} as a direct neighbor of Yb^{3+} in the lanthanide series. Considering also the small mass difference and the fact that the Lu^{3+} energy levels do not interfere with the Yb^{3+} transitions, lutetium-based materials deserve more attention as hosts for Yb^{3+}.

[2] The sensitivity of a host to impurity-related losses depends also on the phonon spectrum of the material. Large effective phonon energies support transfer processes, which may otherwise be prevented by energy mismatch of the electronic levels involved. Here, fluoride hosts are less critical compared to oxide hosts with chemical groups as anions.

2.3. Stoichiometric materials

What is a stoichiometric laser crystal?

For a crystal, being stoichiometric means that each site in the lattice is occupied by only one kind of ion. Therefore, a stoichiometric laser crystal is a material, where the active ion is not a dopant, but instead a chemical component of the crystal itself [Chi82, Dan75, Kam82]. Another term used is “self-activated crystal”. One could also speak of a “100%-doped” material thinking of a host in which one kind of ions is completely replaced by the dopant.[1]

Advantages of stoichiometric laser materials

The main advantage of stoichiometric laser crystals is that very high densities of active ions can be realized, which leads to short absorption and gain lengths.[2] These enable the use of very thin platelets as laser media. Such are optimal for face-cooled laser concepts and miniaturized laser oscillators. Stoichiometric laser materials are also interesting playing the active part in waveguiding media.

A face-cooled concept, which is ideally suited for high power generation, is that of the thin-disk laser or amplifier, where the laser medium has a reflective coating on one side and serves as an active mirror [Ste00]. Since the aspect ratio (length of active zone divided by diameter) is very small, the thermal gradient is parallel to the propagation of the laser signal beam in the medium. Furthermore, heat removal is highly efficient, because the heat generated in the pumped zone does not travel far to the sink. Due to these reasons, thermal lensing effects and the danger of heat-related fracture are minimized.

Aside from their compactness, microchip lasers [Zay99] whose resonator lengths are limited by the thickness of the active medium display further favorable properties: It is possible to operate a laser at a single frequency, if the free spectral range between the resonator modes is larger than the gain bandwidth of the laser material. For a resonator length L of 100 µm and a mean refractive index $n = 2$, the free spectral range is $\delta\nu_{fr} = c/2nL = 750\ \text{GHz}$ or, for $\lambda = 1\ \mu\text{m}$, $\delta\lambda_{fr} = 2.5\ \text{nm}$. Single-frequency operation is desired especially in connection with frequency doubling, for low-noise pump sources and for lasers used in measurement devices. Mode-locked miniature lasers can reach high pulse repetition rates (for single-pulse operation, $\nu_{rep} = \delta\nu_{fr}$).

With longitudinal pumping, very short active media enable tight focusing of the pump with a good overlap of pump and resonator mode, even if pump sources with poor beam quality are used (like typical laser diodes). This is important to achieve a low lasing threshold and good efficiency, especially with quasi-three- or quasi-four-level laser ions and their reabsorption losses (see chapter 3). With transversal pumping of waveguiding media (crystal fibers, sandwich composits), too, the pump radiation can be deposited in a relatively small active volume, due to the large absorption coefficient.

The advantages already mentioned exist for all materials with short absorption and gain lengths, i.e. also for highly doped laser hosts with these properties. For stoichiometric materials,

---

[1] 100% replacement of Gd^{3+} in $KGd(WO_4)_2$ or Y^{3+} in $KY(WO_4)_2$ by Yb^{3+} would lead to the stoichiometric material KYbW.

[2] “Absorption length” and “gain length” are the distances at which the intensity of radiation travelling through a material has dropped to *1/e* or risen to *e* times its initial value, respectively.

however, the high concentration of active ions can be realized without affecting the optical quality, which would be the case for doped materials where different ion radii cause problems (defects, inhomogeneities; see previous chapter). Furthermore, in contrast to doped materials, the thermal conductivity does not suffer from the presence of the active ions.

Disadvantages of stoichiometric laser materials

The disadvantages are those that occur for all materials with a high active-ion content. The main issues are the high susceptibility to processes of loss in the material and the enormous heat generation per volume connected with these. A further handicap is relevant only for pulsed light sources intended to produce high pulse energies: For intensive pumping, a high density of active ions means a high density of excited ions, and therefore amplified stimulated emission will limit the possible maximum inversion and stored energy [Fan92].

Due to the closeness of the active ions, energy transfer processes from one to the other are very likely. Transfer occurs by multipole (mainly dipole-dipole) and exchange interactions [Dia98, Kam82, Lup01]. The coupling decreases rapidly with increasing spacing R between the ions (for dipole-dipole interaction with $1/R^6$).

High probabilities for energy transfer are especially harmful with active ions that tend to self-quenching like Nd^{3+} or Pr^{3+}. Therefore, useful stoichiometric neodymium materials[1] show at least one of two characteristics: The active ions exhibit relatively large spatial separations, which are defined by the crystal structure and which make transfer processes less effective. The energy of the $^4F_{3/2}$ excitation does not match by far the energy needed to provide excitations for two ions in the $^4I_{15/2}$ and $^4I_{13/2}$ multiplets, which are responsible for Nd^{3+} self-quenching. Lattice vibrations have to balance the difference; the process becomes less probable due to the necessity of this contribution [Kam82].

For Yb^{3+} there exist no problems of self-quenching;[2] the low laser quantum defect and the low or negative fluorescence quantum defect help to obtain little or no heat generation (see append. A.1.). The only problem is energy migration to impurities and defects, which act as energy sinks ("killer traps", [Ger01]). This is not a minor problem, since an exciton may not merely jump onto a nearest neighbor, but migrate via many active ions over a long distance, until it finally hits an energy sink (see Fig. 2.2.). According to Danielmeyer [Dan75], in NdP_5O_{14} the $^4F_{3/2}$ excitons travel across 2 µm within their fluorescence lifetime of 110 µs.

In this context, it is important that also the surface of a laser medium can provide energy sinks [Dan75], since such a distance is only one to two orders of magnitude below the typical thicknesses of stoichiometric laser crystals. As an extreme case, for KYbW with an absorption length of only ≈13 µm, the optimum would be a 10- to 20-µm-thin platelet; we do not know the speed of the energy migration in this material, however. So it is possible, that a considerable part of the pump energy is transported to the crystal surface, where it is converted into heat. Therefore, surface quality may become crucial for the damage threshold of highly doped and stoichiometric laser materials.

The transfer of an exciton from an active ion to an impurity or defect, just like with Nd^{3+} self-quenching, requires matching energies. Here, phonons may provide assistance [Mia70]. With a

---

[1] "Useful" does not mean quantum efficiencies close to unity; typical values for stoichiometric laser materials are below 40% [Kam82].

[2] The probability for cooperative luminescence (see appendix A.1.) from neighboring excited Yb^{3+} is several orders lower than that for the Nd^{3+} downconversion process.

high effective phonon energy in a crystal, a large energy gap can be spanned and many defects and impurities contribute to loss. Therefore, crystals with covalent groups as anions, which exhibit high-energy vibrational modes, are more sensitive to energy sinks than “more simple” crystal structures like sesquioxides or fluorides. For Yb^{3+}-activated stoichiometric crystals, in practice, the minimum distance between the Yb^{3+} ions seems to play a larger role for quantum efficiency.

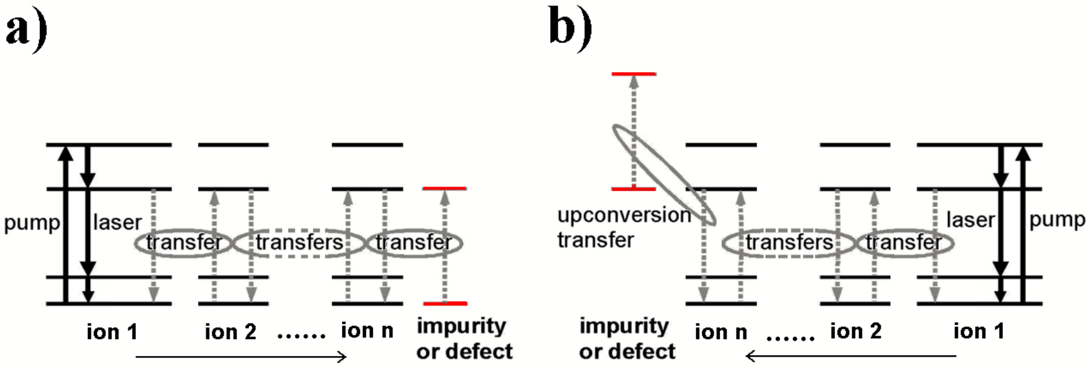

Fig. 2.2. Energy transfer to an impurity or defect. In laser materials with high concentrations of active ions, the spacings in between are small. Therefore, an exciton can migrate over many ions within its lifetime, before it hits an energy sink. An impurity or defect may absorb the exciton from a ground or excited state, a) or b) respectively.

Fast energy migration also has positive effects: For single-frequency operation of a laser, spatial hole-burning is harmful, since it promotes the oscillations of competing modes, which see gain in the regions of inversion not used up. The energy migration smooths out the holes. For an upconversion laser, the “active” ion of the stoichiometric crystal can act as a sensitizer ion, i.e. to collect the pump radiation and to transfer the energy to the actually laser-active ions. Due to fast energy migration, this will work efficiently. However, the sensitizer ions will not only transfer their energy to other ions, but also lose more or less energy by spontaneous decay. Therefore, the sensitizer ions must exhibit a relatively long lifetime with respect to spontaneous decay, compared to the effective lifetime (taking into account spontaneous decay and stimulated emission) of the laser-active ions. Otherwise, the lasing threshold may not be reached or the laser efficiency will be poor; then, lower sensitizer concentrations can be favorable.

Stoichiometric Yb^{3+}-containing crystals

In the wavelength region around 1 µm, Yb^{3+} is the better active ion compared to Nd^{3+}, especially in the case of stoichiometric laser materials, because of the low inherent losses and the weak heat production connected with these. On the other hand, reabsorption by thermal population of the lower laser state requires pump sources with high brightness; nowadays, such exist as laser diodes. If we compare the absorption lengths of Nd^{3+} self-activated crystals with those of the two stoichiometric Yb^{3+} laser materials (see Table 2.3.), we find that the Nd^{3+} materials do not profit from the typically large absorption cross sections of Nd^{3+} compared to Yb^{3+}, because the self-quenching tendency of trivalent Nd demands crystal structures with relatively low active ion concentrations.[1]

---

[1] e.g. $LiNdP_4O_{12}$: Nd^{3+} density 4.37 x 10^{21} cm^{-3}, absorption coefficient 115 cm^{-1} at 808 nm [Ots98].

Table 2.3. contains the two stoichiometric Yb^{3+}-activated crystals, for which laser operation has been demonstrated and two Yb^{3+}-self-activated materials having laser potential:

$KYb(WO_4)_2$ (KYbW) [Puj02b], which is isostructural to KYW and KGW; $Yb_3Al_5O_{12}$ (YbAG) [Pat01, Mue02], an analog of YAG; $YbAl_3(BO_3)_4$ (YbAB), which has the same structure as YAB; Yb_2O_3 (ytterbia), a cubic sesquioxide.

Table 2.3. Stoichiometric Yb^{3+}-activated crystals. Laser operation has been demonstrated for $KYb(WO_4)_2$ and $Yb_3Al_5O_{12}$. Please note that the fluorescence lifetime of $Yb_3Al_5O_{12}$ was measured for a thermally annealed sample.

compound	**$KYb(WO_4)_2$ (KYbW)**	**$Yb_3Al_5O_{12}$ (YbAG)**	**$YbAl_3(BO_3)_4$ (YbAB)**	**Yb_2O_3 (ytterbia)**
active ion concentration **N_{Yb3+} [10^{22} cm^{-3}]**	0.64	1.413	0.563	2.813
maximum absorption coefficient **α_{max} [cm^{-1}]**	750	≈90	118	>2000
wavelength of maximum absorption **$\lambda_{\alpha max}$ [nm]**	981	940	975	975
fluorescence lifetime **τ_f [µs]** (best value for stoichiometric)	200	980	140	67
fluorescence lifetime **$\tau_{f,Y/Yb}$ [µs]** (lowly doped Y^{3+}-based analog)	300	1000	1110	850
laser operation demonstrated	cw	pulsed	none	none
references	[Puj02b, Klo03]	[Pat01, Mue02]	[Xu03]	[Pet01]

For KYbW and YbAG, fluorescence lifetimes have been achieved that are close to those obtained for lowly Yb^{3+}-doped KYW and YAG, respectively. This means high quantum efficiencies, and therefore laser operation could be demonstrated. At present, the two other materials exhibit quantum efficiencies that are too low to enable lasing.[1] A better crystal quality seems to be realistic for YbAB in case of improved growth, appropriate annealing, and the avoiding of impurities. These matters had turned out to be crucial for YbAG [Mue02].

For Yb_2O_3, however, the sample used for lifetime measurement had been produced with great care; a crucible and its impurities where avoided by the growing method (laser heated pedestal growth) [Pet01]. Probably, ytterbia is extremly sensitive to all kinds of energy sinks, due to its very high Yb^{3+} concentration of 2.8 x 10^{22} cm^{-3}.

Aside from ytterbia, KYbW shows the highest absorption coefficient, ≈750 cm^{-1} at 981 nm (for polarization parallel to the N_m crystallo-optic axis). Compared to an YbAG medium with a given thickness, this value requires a crystal with only ≈1/8 of this thickness to achieve the same efficiency of pump absorption. An interesting feature of highly absorbing Yb^{3+} materials is that a considerable amount of fluorescence light is absorbed within the active zone of the laser medium, which has the effect of quasi increasing the excited state lifetime and decreasing the laser threshold. For laser applications with generation of harmonics, the anisotropy of KYbW is an additional advantage, because it automatically provides polarized laser emission.

---

[1] References for fluorescence lifetimes in lowly doped hosts, see Table 2.1.

2.4. Yb^{3+}-activated tungstates

In monoclinic double tungstates with the structure $KRE(WO_4)_2$, RE = Y, Gd, or Yb, the Yb^{3+} ion shows very favorable spectroscopic properties (see chapt. 2.2.2., Table 2.1.), especially for high-power and ultrashort-pulse lasers. Their thermal properties are decent (see chapt. 2.2.4., Table 2.2.); they permit the use in high-power applications. The tungstates described here are very similar; differences are due to the different RE and their masses and ion radii. Only thermal conductivity and dopability are concerned, however.

For unit cell parameters and crystal growth of monoclinic double tungstates, the reader may refer to the appendix, A.7. and A.8.

Crystal structure of monoclinic double tungstates

If grown from solutions, $KGd(WO_4)_2$ (KGW), $KY(WO_4)_2$ (KYW), and $KYb(WO_4)_2$ (KYbW) crystallize in the monoclinic space group C^6_{2h}, Z=4 (C2/c crystallographic setting), i.e. they are biaxial optical materials. Figure 2.3. shows the crystal structure (taken from [Mac00]). A detailed structural analysis can be found in [Kam01, Kam02, Puj02]. There exists only one crystal site for Yb^{3+}. The active ion experiences a strongly distorted crystal field, which explains the significant spectroscopic anisotropy of these materials.

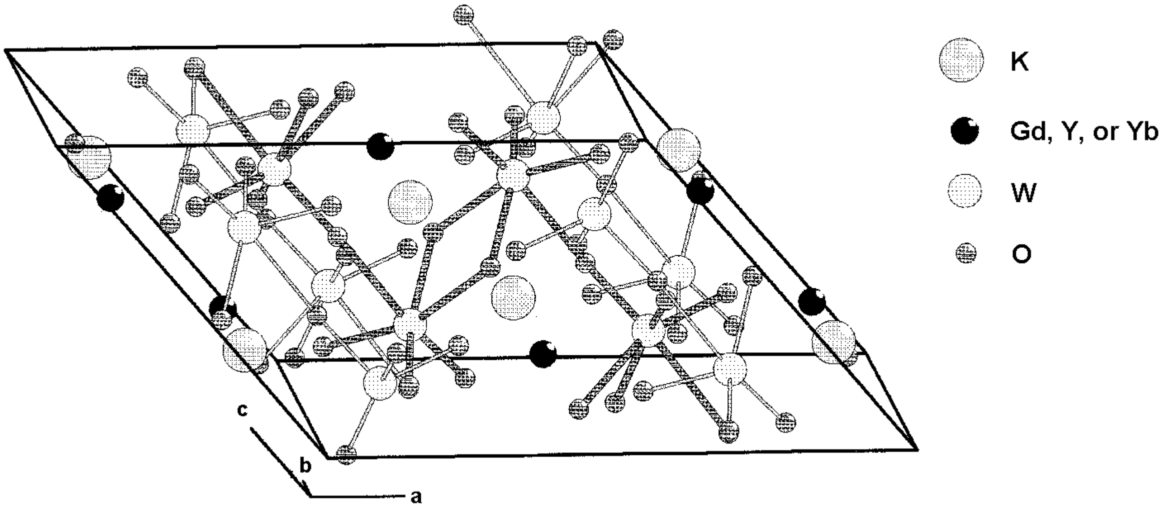

Fig. 2.3. Monoclinic crystal structure of $KRE(WO_4)_2$, RE = Y, Gd, or Yb. Taken from [Mac00].

The positions of the crystallographic axes ***a***, ***b***, and ***c*** are shown in Fig. 2.4.a, based on the C2/c crystallographic setting. Aside from slightly varying angles, the figure is valid for all monoclinic double tungstates. The ***c*** axis and the [101] axis are natural edges. In case of KYbW they define an angle of 85.92° [Puj02], for KGW the angle is 85.59° [Puj99]. The ***b*** axis is orthogonal to the natural (010) face; ***a*** and ***c*** are parallel to this face.

The projection of the optical indicatrix of KYbW on the ***a***-***c***-plane is shown in Fig. 2.4.b [Puj02b]. The crystallo-optic axes N_g and N_m lie in this plane, too. The N_p axis is parallel to the ***b*** axis, i.e. orthogonal to the ***a***-***c***-plane. The N_g axis is found by rotating clockwise from the ***c*** axis by 19° for KYbW, by 21.5° for KGW [Puj99], or by 18° for KYW [Kam02]. Conventions for crystallo-optic axes are explained in appendix A.3.

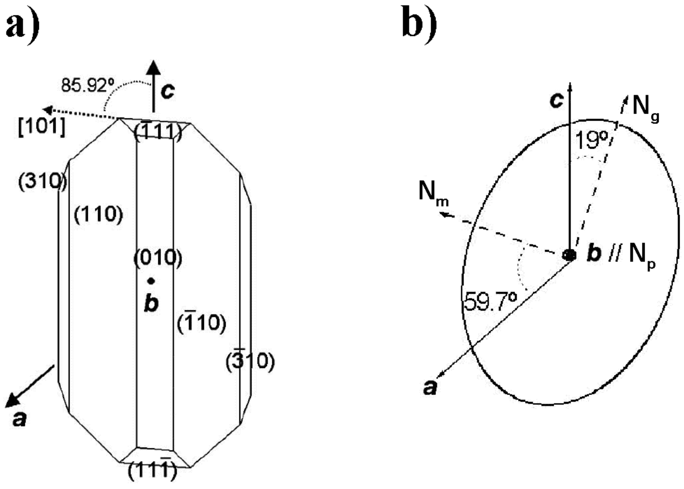

Fig. 2.4. Orientations of the crystallographic axes of KYbW, relative to the natural faces and edges (a); projection of the optical indicatrix on the *a*-*c*-plane (b). The *b* crystallographic axis is pointing towards the spectator.

The principal refractive indices of KGW, KYW, and KYbW can be calculated using the Sellmeier equations and coefficients listed in Table 2.4.

Table 2.4. Sellmeier equations for KGW [Puj99], KYW [Kam02], and KYbW [Puj02b].

material	Sellmeier equation	index	A	B	C [nm]	D [10^{-9} nm^{-1}]
KYbW	$n^2 = A + \frac{B}{1-(C/\lambda)^2} - D\lambda^2$	n_p	3.06172	0.88655	238.58	22.86
		n_m	3.17884	0.91624	250.87	4.85
		n_g	3.28412	0.9921	254.26	19.36
KGW	$n^2 = A + \frac{B}{1-(C/\lambda)^2} - D\lambda^2$	n_p	1.5344	0.4360	186.18	2.0999
		n_m	1.5437	0.4541	188.91	2.1567
		n_g	1.3867	0.6573	170.02	0.2913
KYW	$n^2 = 1 + \frac{B}{1-(C/\lambda)^2}$	n_p	-	2.81349	152.906	-
		n_m	-	2.95683	159.185	-
		n_g	-	3.12783	161.512	-

Spectroscopy of Yb^{3+}-activated tungstates

For the stoichiometric material KYbW, we have performed room temperature absorption measurements and determined the related spectroscopic properties. More data including low temperature absorption, fluorescence, and Raman spectra can be found in [Puj02b].

Several influences can lead to varying spectra (saturation effects, signal-to-noise ratio, different or unprecise sample orientation, crystal quality, not exactly known dopant concentration; see also appendix A.2.).[1] Obviously, such variations are more important than the small

---

[1] And never trust a distributor´s datasheet. Interestingly, the emission cross sections of Yb:KYW presented in [Mun01] look exactly like those of Yb:KGW in [Kul97b, Lag99], although the absorption cross sections slightly differ.

spectroscopic differences between isostructural Yb^{3+}-activated materials: Comparing the KYbW data to those published for Yb:KGW and Yb:KYW in [Kul97b, Lag99, Maj03], we find good agreement; enormous discrepancies (especially at the zero-line wavelength) exist with [Bre01, Dem00, Met99].[1]

It is a valid assumption that the absorption spectra presented here for KYbW show only minor errors, since much care was taken to avoid inaccuracies with the measurements, the results were reproducible with all samples, and a stoichiometric material can be more easily produced with good quality and without uncertainties concerning active-ion concentration. Therefore, in chapter 5 we will use the spectra obtained for KYbW also for the analogs, Yb:KYW and Yb:KGW. We will prefer them to those published specifically for these materials, also because the KYbW spectra refer to the crystallo-optic axes, which are relevant for laser operation, while the spectra in [Kul97b, Lag99] refer to the crystallographic axes. Furthermore, Demidovich et al. have found practically no variation of the absorption cross sections of Yb:KGW within a range of the doping level from 1% to 20% [Dem00].[2]

Transparency window

Figure 2.5. shows the transmission of a 200-µm-thin KYbW crystal at room temperature, for unpolarized light. The sample was cut parallel to the ***a*-*c*** plane. Please note the change of the abscissa scale above 9 µm. Aside from reflection at the surfaces, the KYbW platelet is fully transparent between approximately 350 nm and 5000 nm, with the exception of the region around 981 nm, where the $^2F_{5/2}$-to-$^2F_{7/2}$ transitions of Yb^{3+} are located.

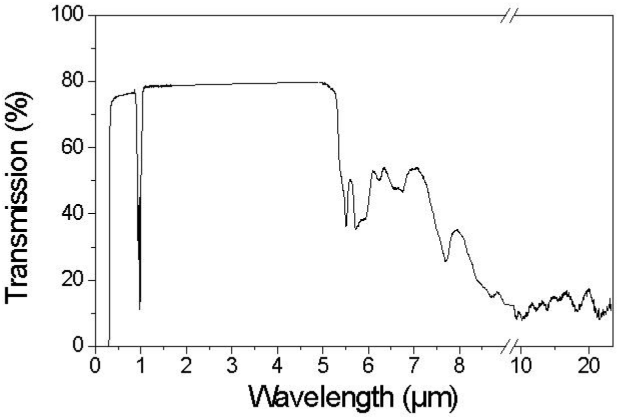

Fig. 2.5. Transparency window of a 200-µm-thin KYbW sample, for unpolarized light incident along the *b* axis.

Yb^{3+} transitions in monoclinic double tungstates

A level diagram of Yb^{3+} in KYW, KGW and KYbW is shown in Fig. 2.6.a). Bold arrows indicate the most pronounced $^2F_{5/2}$-to-$^2F_{7/2}$ transitions (absorption) and the $^2F_{7/2}$-to-$^2F_{5/2}$ transitions (emission) most suitable for lasing. The energetic positions of the Stark levels of the lower multiplet, (0), (1), (2), and (3) and of those of the upper multiplet, (0′), (1′), and (2′) are given in Table 2.5. The Stark splittings of the three tungstates are very similar.

---

[1] For Yb:KYW, a maximum polarized absorption cross section of 3.7×10^{-19} cm^2 is given in [Met99], which is too low by a factor of ≈3.

[2] The absorption peak at 981 nm is not resolved, however.

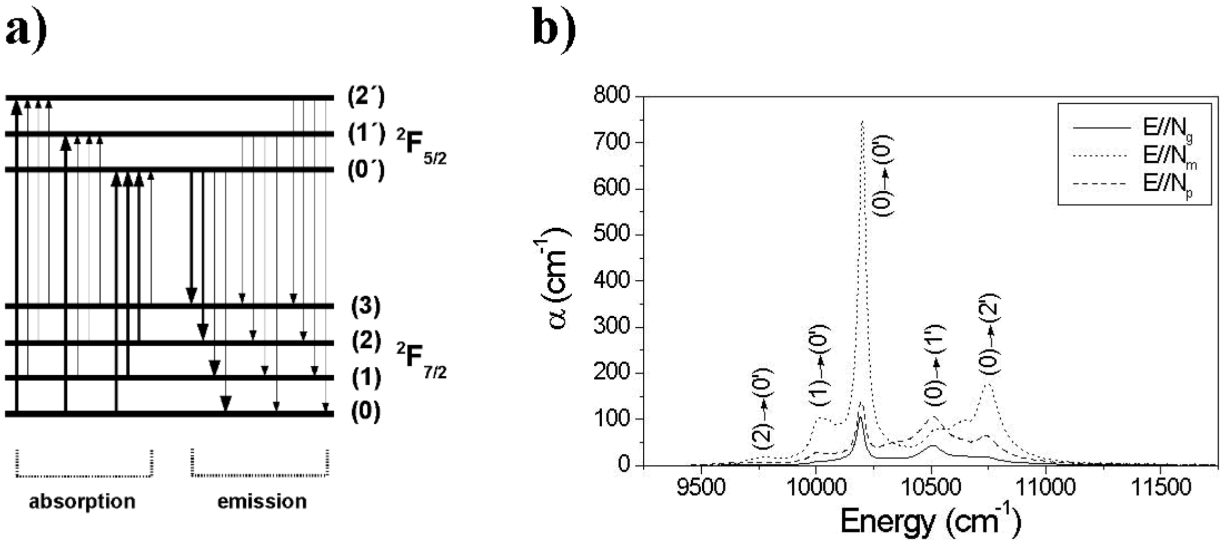

Fig. 2.6. Yb^{3+} level diagram for KYbW, Yb:KGW or Yb:KYW. Stark level energies are listed in Table 2.5. The most pronounced absorption transitions and the most suitable transitions for lasing are indicated by bold arrows (a). Absorption coefficient α of KYbW at room temperature, measured for light polarization parallel to the three crystallo-optic axes. For polarization $E||N_m$, α reaches an extremely high value of ≈750 cm^{-1} at the (0)-to-(0′) transition near 10195 cm^{-1} (≈981 nm) (b).

In the polarized room temperature absorption spectra of KYbW, Fig. 2.6.b), three main peaks are observed, centered at 10195 cm^{-1}, 10518 cm^{-1}, and 10742 cm^{-1}. They can be identified as the three transitions starting from the (0) level, where the largest part of the $^2F_{5/2}$ population is found (≈62% at room temperature). The less intensive peaks located near 10020 cm^{-1} and 9770 cm^{-1} are due to the (1)-to-(0′) and (2)-to-(0′) transitions.

Table 2.5. Stark level energies of Yb^{3+} in the monoclinic tungstates KYbW [Puj02b], KGW, and KYW [Kul97b]. Values from low temperature measurements.

material	**Stark level energy [cm^{-1}]**						
	(0)	**(1)**	**(2)**	**(3)**	**(0′)**	**(1′)**	**(2′)**
KYbW	0	168	438	555	10188	10500	10734
Yb:KGW	0	163	385	535	10188	10471	10682
Yb:KYW	0	169	407	568	10187	10476	10695

From Fig. 2.6.b) we see, that KYbW (as well as Yb:KYW and Yb:KGW) shows strong spectroscopic anisotropy. Absorption is strongest for light polarized parallel to the N_m crystallo-optic axis, with a maximum absorption coefficient of approximately 750 cm^{-1} at the zero-line near ≈981 nm, which is equivalent to an absorption length (1/*e* level) of only 13.3 µm. The latter value is the shortest absorption length of all Yb^{3+}-activated lasing materials and probably one of the shortest of all laser crystals.

The absorption coefficients presented in Fig. 2.6.b) are the result of measurements performed with different crystal samples: 0.2 mm and 3 mm thick for $E||N_p$, 0.2 mm and 3.3 mm thick for $E||N_g$, and 0.08 mm, 0.2 mm, and 3.3 mm thick for $E||N_m$. The different crystal thicknesses are necessary to achieve a sufficient signal-to-noise ratio for wavelength regions of low absorption as well as for those of high absorption; the respective curves have been merged. The spectral resolution is 1 nm.

For Yb:KYW and Yb:KGW crystals, the absorption coefficients are smaller than for KYbW, corresponding to their lower active-ion concentrations. The absorption and emission cross sections, however, can be assumed to be practically the same for the three materials, within the typical error bars for spectroscopic measurements. The cross sections are high compared to other Yb^{3+}-activated materials (see the comparison in chapt. 2.2.2.).

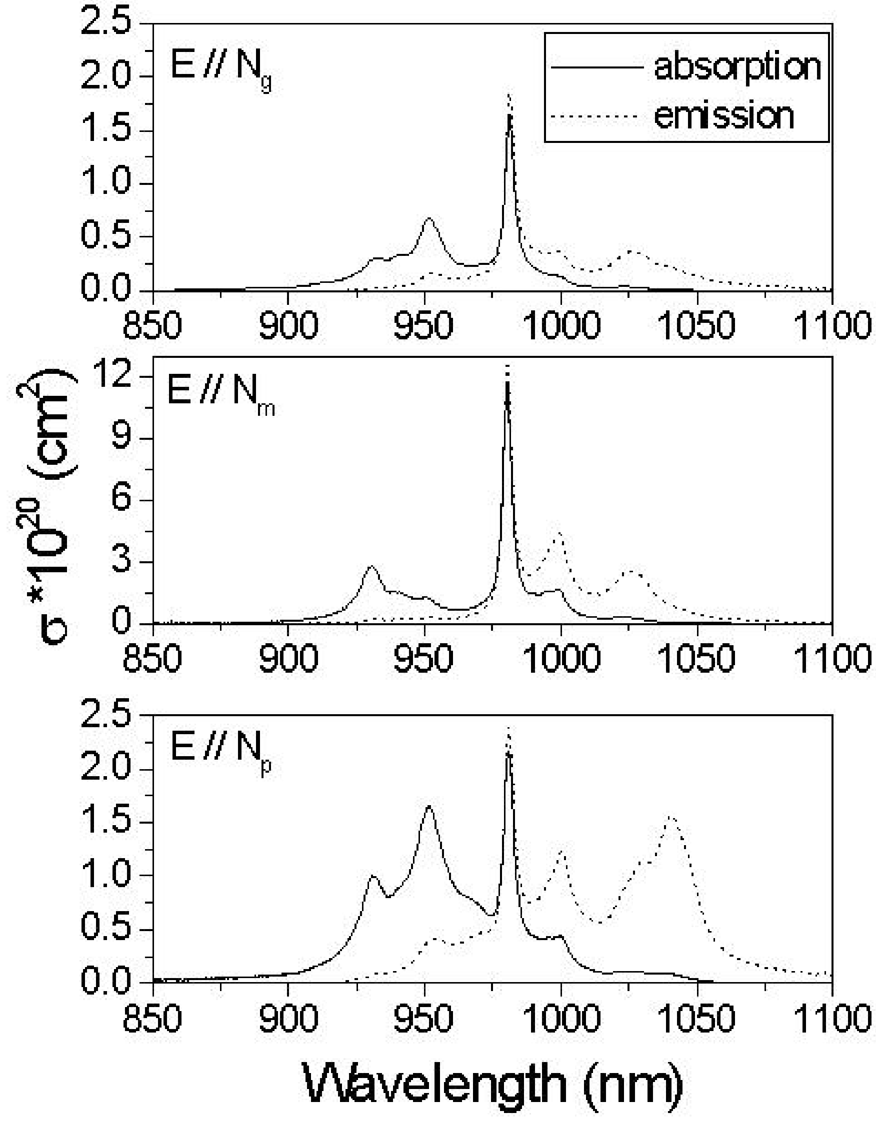

Fig. 2.7. Absorption and emission cross sections of KYbW at room temperature, for light polarization parallel to the three crystallo-optic axes. The largest values are obtained for polarization $E||N_m$. Please note the different ordinate scales.

Figure 2.7. shows the polarized absorption and emission cross sections of KYbW. The first have been calculated from the absorption data of Fig. 2.6.b), using eq. a.3. with an active-ion

concentration of $N = 6.4 \times 10^{21}$ cm^{-3}; the latter have been obtained by the reciprocity method, eq. a.5. We see from Fig. 2.7., that the largest absorption and emission cross sections are achieved for polarization parallel to the $\boldsymbol{N_m}$ crystallo-optic axis; for $\boldsymbol{E}||\boldsymbol{N}_g$ the smallest values are obtained.

Therefore, it is recommended to orient the pump and the crystal for $\boldsymbol{E}||\boldsymbol{N}_m$ or, if unpolarized pump radiation is used, to cut the tungstate crystal for propagation along the $\boldsymbol{N_g}$ axis. Laser oscillation will also experience the largest gain for $\boldsymbol{E}||\boldsymbol{N}_m$ and occur with this polarization, usually. However, to achieve a broader gain bandwidth for ultrashort-pulse generation or desiring a wider tunability, it can be interesting to cut and use KYbW, Yb:KYW or Yb:KGW media for $\boldsymbol{E}||\boldsymbol{N_p}$-polarized emission.

The maximum absorption cross sections of KYbW at the zero-line transition peak centered at ≈981 nm amount to 1.17×10^{-19} cm^2 for $\boldsymbol{E}||\boldsymbol{N_m}$, 1.66×10^{-20} cm^2 for $\boldsymbol{E}||\boldsymbol{N_g}$, and 2.17×10^{-20} cm^2 for $\boldsymbol{E}||\boldsymbol{N_p}$. The linewidths of this peak, 4 nm ($\boldsymbol{E}||\boldsymbol{N_m}$), 4.1 nm ($\boldsymbol{E}||\boldsymbol{N_g}$) ,and 5.1 nm ($\boldsymbol{E}||\boldsymbol{N_p}$), are sufficiently broad for laser diode pumping. Basically, the whole range between ≈910 nm and ≈1030 nm is suitable for pumping of Yb^{3+}-activated tungstate laser media. In connection with a high active ion concentration (KYbW or high Yb^{3+} doping level) or for multipassing pump geometries, pump light absorption will be sufficient even in the wings of the absorption band. Not to maximize the absorption, however, means to accept the higher reabsorption losses of longer crystals.

In several cases it makes sense not to pump at the zero-line: Choosing a pump wavelength around 940 nm or 990 nm relaxes the stability requirements concerning the pump wavelength, i.e. the amount of pump power absorbed will not decrease, while the laser diodes are aging. In case of the stoichiometric material or highly doped tungstates, it can be necessary to reduce the heat generation per pumped crystal volume (see chapt. 5.2.1.3.). Longer pump wavelengths mean smaller laser quantum defects; fluorescence cooling is achieved, if the pump wavelength is longer than the mean wavelength λ_{mf} of spontaneous emission (see appendix, eq. a.2. and [Mun01]). For KYbW, $\lambda_{mf} \approx 1009$ nm.[1]

The broad absorption band is a handicap of KYbW, Yb:KYW, and Yb:KGW, in so far as it overlaps with the emission band and causes reabsorption of the laser radiation generated here. At the pronounced peak near 1025 nm, the emission cross section of KYbW reaches a value of 2.6×10^{-20} cm^2 for $\boldsymbol{E}||\boldsymbol{N_m}$, 3.7×10^{-21} cm^2 for $\boldsymbol{E}||\boldsymbol{N_g}$, and 1.0×10^{-20} cm^2 for $\boldsymbol{E}||\boldsymbol{N_p}$. However, due to strong reabsorption present at 1025 nm (see Fig. 2.7.), the gain maximum and therefore laser operation will be found at this wavelength only in case of high inversion levels. This is the case for an inversion parameter $\beta \geq 10\%$. The inversion parameter is the ratio of the $^2F_{5/2}$ population to the total Yb^{3+} ion density. The spectral dependence of the net gain per unit length (effective gain coefficient) of KYbW for $\boldsymbol{E}||\boldsymbol{N_m}$-polarization is illustrated in Fig. 2.8., assuming different values of β. For the calculation we have used eq. 3.19.

---

[1] This value has been obtained as a weighted average of the mean fluorescence wavelengths for the three polarizations: 10.2% of the fluorescence occur with $\boldsymbol{E}||\boldsymbol{N_g}$ and $\lambda_{mf} \approx 1009.5$ nm, 58.5% with $\boldsymbol{E}||\boldsymbol{N_m}$ and $\lambda_{mf} \approx 998.6$ nm, and 31.3% with $\boldsymbol{E}||\boldsymbol{N_p}$ and $\lambda_{mf} \approx 1028.5$ nm. Here, $\lambda_{mf} = [\int \lambda \sigma_e d\lambda] / \int \sigma_e d\lambda$; σ_e, emission cross section. The resulting, averaged value of $\lambda_{mf} \approx 1009$ nm is slightly higher than that given in [Bow00, Mun01] for lowly doped Yb:KYW and Yb:KGW, which is 992-993 nm. Net cooling in this materials, however, was observed experimentally only for wavelengths equal to or longer than approximately 1010 nm. A fundamental problem with calculating λ_{mf} is that emission cross sections cannot be calculated exactly, neither with the reciprocity method nor with the Füchtbauer-Ladenburg equation (see chapter a.2.).

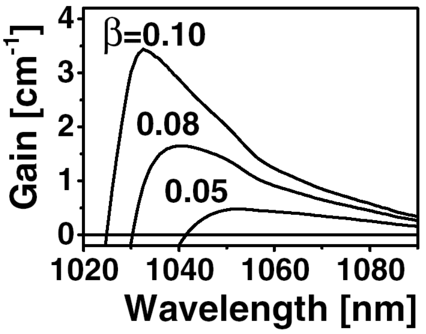

Fig. 2.8. Spectral dependence of the KYbW net gain for *E*||N_m-polarization, for three different values of the inversion parameter *β*.

Radiative Lifetime

From the emission cross sections as shown in Fig. 2.7., the radiative lifetime τ_{rad} of KYbW is estimated by the Füchtbauer-Ladenburg equation (eq. a.7.). The result, τ_{rad} = 270 µs, agrees well with the lifetime values from fluorescence measurements of lowly Yb^{3+}-doped crystals, 317 µs for KGW published in [Bre01] and 300 µs for KYW in [Dem00].[1] Kuleshov et. al. have found substantially longer lifetimes ≈0.6 ms for these materials [Kul97b]; most certainly, reabsorption of fluorescence light is responsible for these data [Heh97, Sum94]. Fluorescence lifetime measurements have also been performed with KYbW, using different concentrations of KYbW powder immersed in ethylene-glycol (for details: [Puj02b]), leading to a value of 200 µs. From this, we obtain a quantum efficiency of approximately 74% for the used KYbW material (top-seeded solution grown, no thermal annealing applied).

Stimulated Raman scattering

The strongest vibrational modes of tungstates are interesting for efficient frequency conversion by stimulated Raman scattering. Their energies are 763 cm^{-1} and 911 cm^{-1} for KYbW [Puj02b], 768 cm^{-1} and 901 cm^{-1} for KGW, and 767 cm^{-1} and 906 cm^{-1} for KYW [Bas99]. Yb:KGW and Yb:KYW lasers with self-frequency Raman conversion have been demonstrated in [Lag00] and [Gra02].

Thermal anisotropy

Monoclinic double tungstates show strong thermal anisotropy, including thermal conductivity κ, thermal expansion α and the variation of the refractive index *dn/dT*. Since KYW, KGW and KYbW are isostructural and their crystal parameters and the angles between crystallographic and crystallo-optic axes do not differ much (see Table a.2.), it is believed that their thermo-optical and thermo-mechanical properties are very similar.

Data for the anisotropic thermal conductivity of pure $KGd(WO_4)_2$ are given in [Kam02]. It has a value of $\kappa = 2.8$ $Wm^{-1}K^{-1}$ along the [100] crystal orientation, 2.5 $Wm^{-1}K^{-1}$ along [010] = ***b*** axis, and 3.5 $Wm^{-1}K^{-1}$ along [001]. This means an average conductivity of ≈3 $Wm^{-1}K^{-1}$, which we assume for undoped KGW and KYW as well as for KYbW.

---

[1] A similar value, 320 µs, is given for Yb:KYW in [Met99].

The variation of the refractive indices with temperature, dn_γ/dT, with $\gamma = p, m, g$, shows a different behavior for homogeneous and inhomogeneous heating. In the latter case, which is the typical situation in a pumped laser medium, dn_γ/dT will depend on the orientation of the heat flow. The values for homogeneous heating of KYbW [Puj02b] and inhomogeneous heating of KGW [Mus97] are compared in Table 2.6.

Table 2.6. Temperature dependent variation of the principal refractive indices of monoclinic double tungstates. Data for inhomogeneous heating along the crystallo-optic axes are given for KGW [Mus97], those for homogeneous heating refer to similarly behaving KYbW [Puj02b].

KGW	**orientation of the heating**	**variation of refractive indices**		
		dn_p/dT [10^{-6} K^{-1}]	**dn_m/dT [10^{-6} K^{-1}]**	**dn_g/dT [10^{-6} K^{-1}]**
	along N_p		43±9	17±4
	along N_m	-3±1		-19±4
	along N_g	-55±11	8±2	
KYbW	**homogeneous**	73	31	31

For a full description of the thermal expansion behavior, it must be related to the appropriate principal system, in which the thermal expansion tensor is diagonal. In case of monoclinic double tungstates the principal axes X_1' (along [302] direction) and X_3' (along [106] direction) do not coincide with crystallographic or crystallo-optic axes, only X_2' is parallel to the $b = N_p$ = [010] axis (see Fig. 2.9., taken from [Puj02]). In this system, the values of the thermal expansion coefficient of KYbW are $\alpha = 8.72 \times 10^{-6}$ K^{-1} (X_1' direction), 2.57×10^{-6} K^{-1} (X_2'), and 16.68×10^{-6} K^{-1} (X_3').

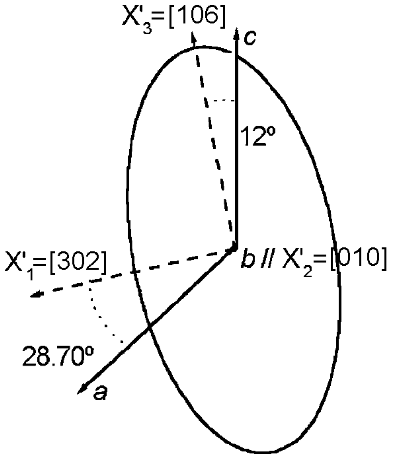

Fig. 2.9. Thermal expansion tensor of KYbW [Puj02]. Only in case of $X_2' = b$, one of the principal axes that are relevant for thermal expansion coincides with a crystallographic axis.

2.5. Yb^{3+}-activated cubic sesquioxides

Yb^{3+}-doped cubic sesquioxides are attractive laser materials especially for high-power lasers and for ultrashort-pulse oscillators and amplifiers in the 200-fs region. Their thermal properties are excellent; their spectroscopic properties support high efficiencies. In chapts. 2.2.2. and 2.2.4., we have already compared Sc_2O_3 scandia to a selection of important Yb^{3+}-activated laser hosts (Tables 2.1. and 2.2.). Concerning spectroscopic data, Yb^{3+}-doped Lu_2O_3 (lutetia) and Y_2O_3 (yttria) are almost as favorable as scandia. Differences exist with thermal conductivity and dopability, due to different masses and ion radii. Yb_2O_3 has been included in chapt. 2.3. in the comparison with other stoichiometric Yb^{3+}-activated crystals; at present it is not suited as a laser material, because its quantum efficiency is too low.

For lattice constants and crystal growth of cubic rare earth sesquioxides, the reader may refer to the appendix, A.10. and A.11.

Crystal structure

At room temperature, Sc_2O_3, Lu_2O_3, and Y_2O_3 are body-centered cubic ("C-type") sesquioxides and have the bixbyite structure, i.e. they belong to the space group Ia3 (T_h^7, Schönfließ notation).[1] In case of yttria, there exists a high-temperature modification (hexagonal, monoclinic structure, "B-Type"). The bixbyite structure is explained by Fig. 2.10.a) and b) [Moo68]. The Yb^{3+} ion can be incorporated at two cationic sites.

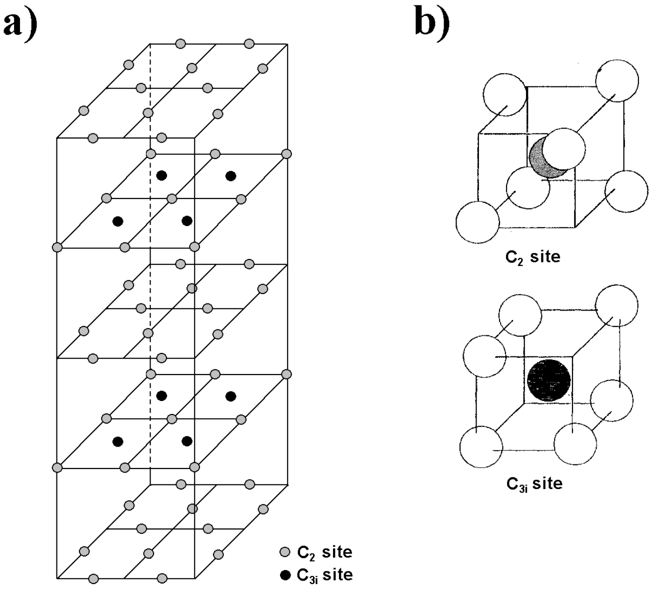

Fig. 2.10. (a) Bixbyite structure of "C-type" sesquioxides (Sc_2O_3, Lu_2O_3, Gd_2O_3, Y_2O_3, and others). The unit cell is cubic, but it has been expanded in the vertical direction for clarity. The oxygen anions between the rare earth layers are not shown. Black circles stand for C_{3i} cationic sites, grey ones symbolize C_2 sites. The latter are actually displaced from the positions shown by ≈1/30 of a cell edge.

(b) On the C_2 site, the rare earth ion is surrounded by six oxygens (open circles) that are located almost on the corners of a cube; two oxygens are missing along a face diagonal. For the C_{3i} site, two oxygens are missing at a space diagonal [Moo68]. At room temperature, Yb^{3+} absorption and emission are practically only due to the active ions at the C_2 positions.

---

[1] Compounds with the chemical formula X_2O_3 are called sesquioxides. Bixbyite is a mineral, formula $(Mn,Fe)_2O_3$.

At room temperature, absorption and emission can be observed only from the active ions on the sites with twofold rotational symmetry (C_2 sites, 75% of all cationic sites). Optical activity of the Yb^{3+} ions on the sites with threefold rotary inversion symmetry (C_{3i} sites, 25% of all cations) is very weak, since it is mainly due to magnetic-dipole transitions. C_{3i}-site fluorescence can be demonstrated by site-selective excitation at low temperatures; at increasing temperatures the intensities drop, because the excitation energy migrates to the C_2 sites [Mix99, Pet01, Pet02b].

Refractive indices of cubic sesquioxides

"C-type" sesquioxides are optically isotropic. The refractive index of scandia, lutetia and yttria can be expressed by the Sellmeier equations listed in Table 2.7. [Mix99].

Table 2.7. Sellmeier equations for cubic sesquioxides and refractive indices at 1050 nm. λ is given in µm.

sesquioxide	Sellmeier equation	refractive index at 1050 nm
Sc_2O_3	$n^2 = 3.83252 + 0.0492688/(\lambda^2 - 0.0237987) - 0.014094\lambda^2$	1.965
Lu_2O_3	$n^2 = 3.62004 + 0.0412526/(\lambda^2 - 0.0239454) - 0.0086344\lambda^2$	1.91
Y_2O_3	$n^2 = 3.5387 + 0.0421725/(\lambda^2 - 0.0243226) - 0.00914896\lambda^2$	1.89

Spectroscopy of Yb^{3+}-activated cubic sesquioxides

The transparency range of undoped yttria, lutetia, and scandia in the absence of color centers starts around 210-230 nm and, in case of the latter two materials, goes up to approximately 8 µm [Mix99, Pet01]. In the three hosts, Yb^{3+} exhibits similar absorption and emission spectra; the intensities of the relevant transitions are largest in scandia, however.

A level diagram of Yb^{3+} in Sc_2O_3 is shown in Fig. 2.11.a). Bold arrows indicate the most pronounced $^2F_{5/2}$-to-$^2F_{7/2}$ transitions (absorption) and the $^2F_{7/2}$-to-$^2F_{5/2}$ transitions (emission) most suitable for lasing. The energetic positions of the Stark levels of the lower multiplet (0), (1), (2), and (3) and of those of the upper multiplet (0′), (1′), and (2′) for the C_2 site ions are also included. C_{3i} ions do not play a role at room temperature. The values have been taken from [Pet01] and differ slightly from those published in [Bou02b, Lu03, Mix99], leading to small differences concerning the emission cross sections that are obtained by the reciprocity method (see eq. a.5.).

The absorption and emission spectra, as given by Peters [Pet01, Klo04], are presented in Fig. 2.11.b). The emission spectrum is based on a fluorescence measurement and was scaled by a fit to the emission spectrum calculated by the reciprocity method. The zero-line transition, (0)-to-(0′), can be identified clearly in both absorption and emission, as well as the (2)-to-(0′) transition in the absorption. The positions of the (0)-to-(1′), (0′)-to-(2), and (0′)-to-(3) transitions are also indicated. Here, a phononic influence (splitting or red-shift of the maxima) is observed.

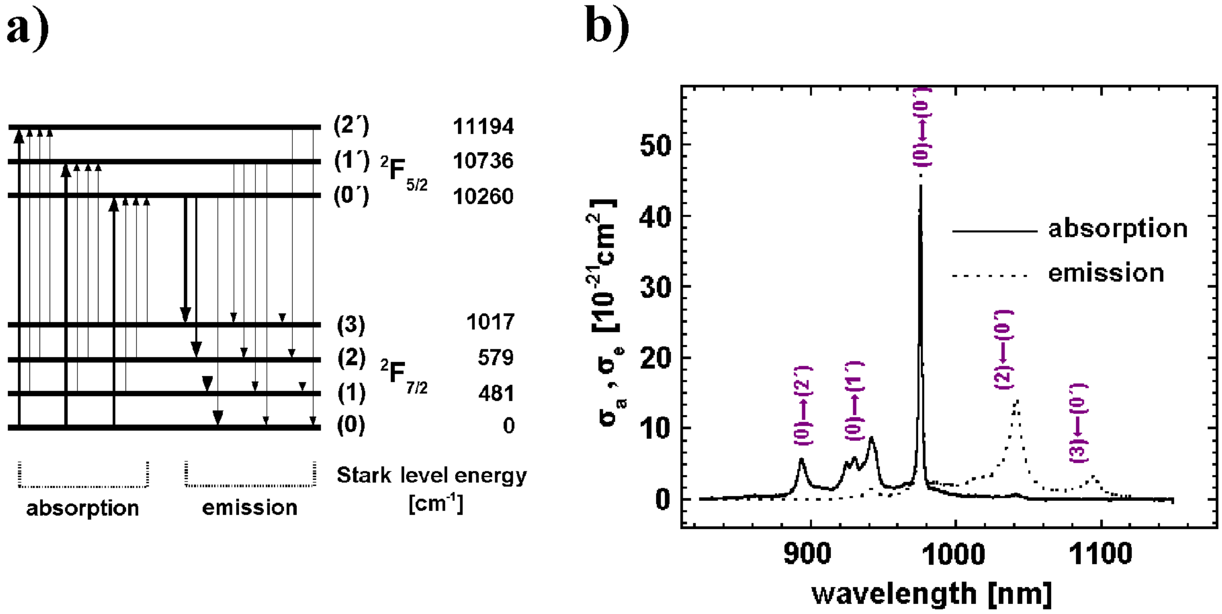

Fig. 2.11. (a) Yb^{3+} level diagram and Stark level energies for Sc_2O_3. The most pronounced absorption transitions and the most suitable transitions for lasing are indicated by bold arrows. (b) Absorption and emission cross sections at room temperature.

From Fig. 2.11.b) we see that the most suitable wavelengths for optical pumping are near the zero-line at ≈975 nm, where an absorption cross section σ_a of 4.4 x 10^{-20} cm^2 is measured, and in the region between ≈920-950 nm with $\sigma_a = 0.87 \times 10^{-20}$ cm^2 near 942 nm, which is comparable to Yb:YAG absorption (see overview in Table 2.1.). The zero-line absorption corresponds to an absorption length of approximately 0.68 mm for a 1%-doped crystal (i.e. for an Yb^{3+} concentration of $N = 3.36 \times 10^{20}$ cm^{-3}). The relatively small zero-linewidth of ≈1.5 nm (FWHM) can cause problems with laser diode pumping with respect to wavelength matching and stabilization. Therefore, the broader absorption region is favorable in many cases.

The emission cross sections at the peaks centered near 975 nm, 1041.5 nm, and 1095 nm amount to $\sigma_e = 4.6 \times 10^{-20}$ cm^2, 1.44 x 10^{-20} cm^2, and 0.33 x 10^{-20} cm^2, respectively. Laser emission can be observed at the position of the latter two lines. Due to the large ground-state Stark splitting, reabsorption is relatively low at the (0′)-to-(2)-transition ($\sigma_a = 0.07 \times 10^{-20}$ cm^2 at 1041.5 nm), which is much lower than for the same transition in tungstates (see chapt. 2.4.), for example. Nevertheless, reabsorption leads to lasing at the (0′)-to-(2)-transition near 1095 nm ($\sigma_a < 0.01 \times 10^{-20}$ cm^2), if the resonator losses (including output coupler transmission) and therefore the population-inversion in the laser medium are low. In this case the laser threshold, i.e. positive gain, is reached first at 1095 nm. The bandwidth of the 1041.5-nm-emission-line, 11.6 nm (FWHM), enables mode-locked pulses with a Fourier-limited duration of less than 200 fs.

The spectroscopic data presented in Fig. 2.11.b) agree fairly well with those of Lu et al. for Yb(2.5 at.%):Sc_2O_3 ceramics, with the exception of the zero-line [Lu03]. Here they measured ≈30% lower peak absorption and calculated an emission cross section of < 1x 10^{20} cm^2 at 975 nm using the Füchtbauer-Ladenburg approach (see eq. a.7.). Probably, these discrepancies are due to an insufficient signal-to-noise ratio and reabsorption of the fluorescence near 975 nm.[1]

The most relevant spectroscopic data of Yb^{3+}-doped yttria and lutetia are listed in Table 2.8., together with those of Yb:Sc_2O_3 [Mix99, Pet01]. Complete spectra can be found in [Pet01] and in the appendix (Figs. a.3. and a.4.). We see that the peak cross sections at the zero-line absorption and the (0′)-to-(2)-line emission are a little lower for Yb:Y_2O_3 and Yb:Lu_2O_3. Compared to the scandia material, the Yb^{3+} emission line positions are blue-shifted, as a result of smaller ground state Stark splittings.[2]

All three materials show strong electron-phonon coupling. Phonon energies are collected in [Lav01, Mix99, Pet01]. The maximum energies are given in Table 2.8.; the effective phonon energies are around 400 cm^{-1}.

Fluorescence lifetime

The fluorescence lifetime is similar for the three Yb^{3+}-doped sesquioxides (see Table 2.8.), about 800 µs at ≈3% doping level [Mix99]. For higher levels (≈10% and higher), in case of Yb:Y_2O_3 and Yb:Lu_2O_3 , strong concentration quenching was observed [Lav01, Lav02, Bou03, Mix99], possibly as a result of Ho^{3+} impurities. Pr^{3+}, Sm^{3+}, Dy^{3+}, Ho^{3+}, and Tm^{3+} have been identified as efficient quenchers for Yb:Sc_2O_3, and Nd^{3+}, Eu^{3+}, Tb^{3+}, and Er^{3+} have been shown to be less important [Pet01]; practically, however, dopability of scandia is limited by the different ion radii of Sc^{3+} and Yb^{3+}.

Thermal properties

The thermal properties of scandia, lutetia, and yttria are listed at the bottom of Table 2.8. [Mix99]. Their thermal expansion coefficients α are in the region of 8 to 9 x 10^{-6} K^{-1}. The biggest advantage of the sesquioxides are their high thermal conductivities, at least in case of undoped or lowly doped crystals. The values κ_0 measured at 30°K amount to 16.5 $Wm^{-1}K^{-1}$ (scandia), 12.5 $Wm^{-1}K^{-1}$ (lutetia), and 13.6 $Wm^{-1}K^{-1}$ (yttria); they are not exceeded by any other laser host for Yb^{3+} (see overview in Table 2.2.).

At 2.8% Yb^{3+}-doping level, the thermal conductivity of Sc_2O_3 decreases to 6.6 $Wm^{-1}K^{-1}$, which is an effect of the considerably different masses and ion radii of Sc^{3+} (atomic weight 45, ion radius 0.75 Å) and Yb^{3+} (at. weight 173, ion radius 0.87 Å), as explained in chapt. 2.2.3. Differences are smaller for Y^{3+} and Yb^{3+} (for radii, see Table a.5.), leading to a weaker decrease to 7.7 $Wm^{-1}K^{-1}$ for a 2.7% Yb^{3+}-doped yttria medium. Since Lu^{3+} and Yb^{3+} are direct neighbors in the lanthanides group, lutetia presents the optimum, i.e. only a slight decrease to 11 $Wm^{-1}K^{-1}$ for 2.7% Yb^{3+}-doping. Therefore, if the problems with concentration quenching are solved,

---

[1] Lu et al. used a sample with a thickness of about eight times the absorption length at 975 nm. Similar problems must be assumed also for the spectroscopic measurements of 5.6 at.% Yb^{3+}-doped scandia by Boulon et al. [Bou02b], which hardly resolved the smaller absorption peaks and gave a value of σ_a = 1.1 x 10^{-20} cm^2 for the zero-line absorption. Their emission cross sections (obtained by Füchtbauer-Ladenburg) are very close to those of Fig. 2.11.b), aside from the value at the zero-line, which is ten times too small. Analogly, for Yb:Lu_2O_3 and Yb:Y_2O_3, Laversenne et al. [Lav01] determined zero-line absorption cross sections that are about 50% smaller than those given in [Pet00, Pet01].

[2] On the other hand, just like with Yb:Sc_2O_3 (see Fig. 2.11.b)), the emission peak wavelengths are slightly longer than those corresponding to the energy differences between the respective Stark levels, as determined by Peters [Pet01].

Lu_2O_3 will be an excellent laser material for applications, where high dopant levels, fair spectroscopic properties, and good thermal conductivity are required.

Table 2.8. Spectroscopic and thermal properties of Yb^{3+}-doped cubic sesquioxides [Mix99, Pet01].

Yb^{3+}-doped sesquioxide	Sc_2O_3	Lu_2O_3	Y_2O_3
refractive index n (at 1050 nm)	1.965	1.91	1.89
cationic density [10^{22}cm^{-3}]	3.355	2.852	2.687
$^2F_{7/2}$ Stark splitting $\Delta E_{7/2}$ [cm^{-1}]	1017	903	874
fluorescence lifetime of 3% Yb^{3+}-doped host τ_f [ms]	0.8	0.82	0.85
largest phonon energy $E_{ph,max}$ [cm^{-1}]	672	618	597
absorption (0)-to-(0′) transition			
wavelength λ_a [nm]	975	976	977
cross section $\sigma_a(\lambda_a)$ [10^{-20}cm^2]	4.4	3.0	2.4
bandwidth $\Delta\lambda_a$ [nm]	~1.5	~2.2	~2.1
(0)-to-(1′) transition			
wavelength λ_a [nm]	942	949	950
cross section $\sigma_a(\lambda_a)$ [10^{-20}cm^2]	0.87	0.95	0.87
bandwidth $\Delta\lambda_a$ [nm]	~25	~20	~20
emission (0′)-to-(2) transition			
wavelength λ_e [nm]	1041	1032	1031
cross section $\sigma_e(\lambda_e)$ [10^{-20}cm^2]	1.44	1.28	1.06
reabsorption cross section $\sigma_a(\lambda_e)$ [10^{-20}cm^2]	0.07	0.07	0.08
emission bandwidth $\Delta\lambda_e$ [nm]	11.6	13	14.5
(0′)-to-(3) transition			
wavelength λ_e [nm]	1095	1079	1076
cross section $\sigma_e(\lambda_e)$ [10^{-20}cm^2]	0.33	0.43	0.42
reabsorption cross section $\sigma_a(\lambda_e)$ [10^{-20}cm^2]	<0.01	<0.01	<0.01
thermal expansion coefficient α [10^{-6} K^{-1}]	9	8	8.5
thermal conductivity of the undoped host (at 30°C) κ_0 [Wm^{-1}K^{-1}]	16.5	12.5	13.6
thermal conductivity of the x% Yb^{3+}-doped host (at 30°C) κ_x [Wm^{-1}K^{-1}]	6.6 (x=2.8%)	11 (x=2.7%)	7.7 (x=2.7%)

3. Quasi-three- and quasi-four-level lasers

At room temperature, all Yb^{3+}-activated glasses or crystals, including those used in chapts. 5 and 6, are operated as quasi-three- or quasi-four-level laser materials. Therefore, the laser physics of these materials are dealt with in this chapter.

3.1. Definitions

The common characteristic of "quasi-x-level lasers" ($x = 2$, 3, 4; there is no uniform terminology) is the existence of pump and laser levels that are energetically close to each other, usually being Stark levels of the same multiplet. Therefore, these levels are connected by a thermal distribution, i.e. at room temperature the fractional population of the respective higher-located level is not negligible. Non-zero population of the lower laser level leads to reabsorption of laser emission; non-zero population of the upper pump level results in stimulated reemission of the pump radiation. Spectroscopically, a strong "quasi-x-level" character of a laser material corresponds to a broad overlap of absorption and emission spectra.

Yb^{3+} is a typical "quasi-x-level" laser ion; a few others are Er^{3+} (at ≈1.5 µm), Tm^{3+} , Ho^{3+} (both at ≈2 µm), Nd^{3+} (Nd:YAG at 946 nm), or Mn^{2+} in MgF_2 (at ≈1.6 µm). The latter served as an example for McCumber´s "Theory of Phonon-Terminated Optical Masers" [McC64b], which describes the physics of "quasi-x-level lasers", without using such a term, however.

In our terminology, two levels in the same multiplet are considered "quasi separate", "quasi" expressing that their populations are not independent (for alternative definitions, see appendix A.13.). This enables to distinguish between the cases of three or four Stark levels involved in the laser operation scheme, which makes a difference for the strength of reemission and for the laser quantum defect to be expected. Hence, an Yb^{3+} medium can be a "quasi-four-level laser system" (term applied e.g. in [Pav01]) or a "quasi-three-level laser system", depending on the upper pump level being different from the laser level or not. This definition is illustrated in Fig. 3.1.(a) and (b).

Figure 3.1.(a) shows a quasi-four-level laser operation scheme of Yb^{3+}. Optical pumping has been chosen to start from the lowest Stark level of the ground-state multiplet and to lead to the highest Stark level of the excited-state multiplet. Alternatively, other levels may be used as lower and upper pump levels. If pumping occurs directly into the upper laser level, as illustrated in Fig. 3.1.(b), we speak of a quasi-three-level laser system. Laser emission starts from the lowest Stark level of the upper multiplet and, in our example, leads to the highest ground-state level (Fig. 3.1.(a) and (b)).

Contributions of laser emission from higher-located, lower-populated Stark levels have been neglected in this picture, as well as the possible existence of vibronic substructures which may be involved.[1] However, the formalism presented below is not limited to a specific choice of pump and laser levels, and it is generally valid without detailed knowledge about the populations of the Stark levels or about vibronic effects.

---

[1] At a given laser wavelength or, analogly, at a given pump wavelength, there may be contributions to emission or absorption from different transitions between Stark-levels or vibronic sublevels due to spectral overlap. Since the lowest Stark level of each multiplet exhibits the highest thermal population, transitions starting from this level will dominate emission or absorption, however.

3.2. Rate equations

The transition rates relevant for quasi-four-level laser operation, the multiplet populations, and the fractional populations of the Stark levels involved are indicated in Fig. 3.1.(a). The belonging eqs. 3.3.-3.17. are collected in Table 3.1. They can be applied for the quasi-three-level case as well. The formulas can be referred to any arbitrarily located point in a laser medium and do not depend on the existence of a laser resonator. Spatial dependencies and the influence of a resonator will be introduced in chapter 3.3.2.

Here, all transitions rates have to be understood as photons per time per volume. The effective pump rate R_p (net pump rate) is given by the absorption rate R_{abs} reduced by the reemission rate R_{reem} (eqs. 3.3.-3.8.); the stimulated emission rate R_{em} minus the reabsorption rate R_{reabs} provides the effective laser emission rate R_l (net stimulated emission rate, eqs. 3.9.-3.14.). Furthermore, spontaneous decay R_{spd} occurs. In case of a high-quality Yb^{3+} laser material, the decay rate R_{spd} is basically given by the fluorescence rate R_{rad}; additionally, there is a small contribution from non radiative decay, R_{nr}, due to defects and impurities (eqs. 3.15.-3.17.). For other active ions, additional loss processes play a role (see append. A.1.). In Fig. 3.1.(a) and (b), for the sake of simplicity, amplified spontaneous emission (ASE) and reabsorption of fluorescence have been left out. These effects can be significant for laser operation of media with high concentrations of active ions, but depend strongly on the individual medium geometry and coating.

Reemission of absorbed pump light is a result of the upper pump and laser levels being in the same Stark manifold; due to the lower pump and laser levels being in the same manifold, reabsorption of laser emission is observed. On all Stark levels, fast intraband thermalization produces non-zero fractional populations, which are denoted on the right-hand side of Fig. 3.1.(a) as products $f_{2p}N_2$ and $f_{2l}N_2$ for the upper pump and laser levels and as $f_{1p}N_1$ and $f_{1l}N_1$ for the lower pump and laser levels.[1] In case of a quasi-three-level system like in Fig. 3.1.(b), we find $f_{2p}N_2 = f_{2l}N_2$ (i.e. upper levels are identical). The fractions f_{2p}, f_{2l}, f_{1p}, and f_{1l} can be deduced from Boltzmann distributions within the multiplets, although this must be considered just an approximation (see [Ban88] and comment on eqs. a.5. and a.6.).

N_2 and N_1 are the respective total multiplet population densities, $N = N_1 + N_2$ is the total active ion density. Introducing the inversion parameter β, we can express N_1 and N_2 by

$$N_1 = (1-\beta)N \qquad \text{and} \qquad N_2 = \beta N \,. \qquad (3.1.), (3.2.)$$

The “one-way” (not including the respective reverse process) transition rates R_{abs}, R_{reem}, R_{em}, and R_{reabs} are proportional to the pump or laser signal photon fluences (photons per time per area), $I_p/h\nu_p$ or $I_l/h\nu_l$, and to the respective one-way absorption or gain coefficients $\alpha_0(\beta,\lambda_p)$, $g_0(\beta,\lambda_p)$, $\alpha_0(\beta,\lambda_l)$, and $g_0(\beta,\lambda_l)$; see eqs. 3.3.-3.6. and 3.9.-3.12. The effective pump and laser emission rates R_p and R_l can be expressed analogly by the pump or laser signal intensities and the effective coefficients $\alpha_{eff}(\beta,\lambda_p)$ or $g_{eff}(\beta,\lambda_l)$, respectively; see eqs. 3.7., 3.8., 3.13. and 3.14. Here, I_p and I_l are the pump and laser signal intensities, $h\nu_p$ and $h\nu_l$ the pump and laser phonon energies, and λ_p and λ_l the pump and laser wavelengths.

---

[1] Fast intraband relaxation means the phononic transitions occur much faster than electronic transitions, i.e. with phonon lifetimes in the order of 10^{-8} to 10^{-11} s [Koe92]. Furthermore, phonon saturation effects will not have an influence on the laser gain until extremely high (unrealistic) laser output intensities are assumed, which was estimated by McCumber for a phonon-terminated (terminated on vibronic levels) Mn^{2+}:MgF_2 laser [McC64b].

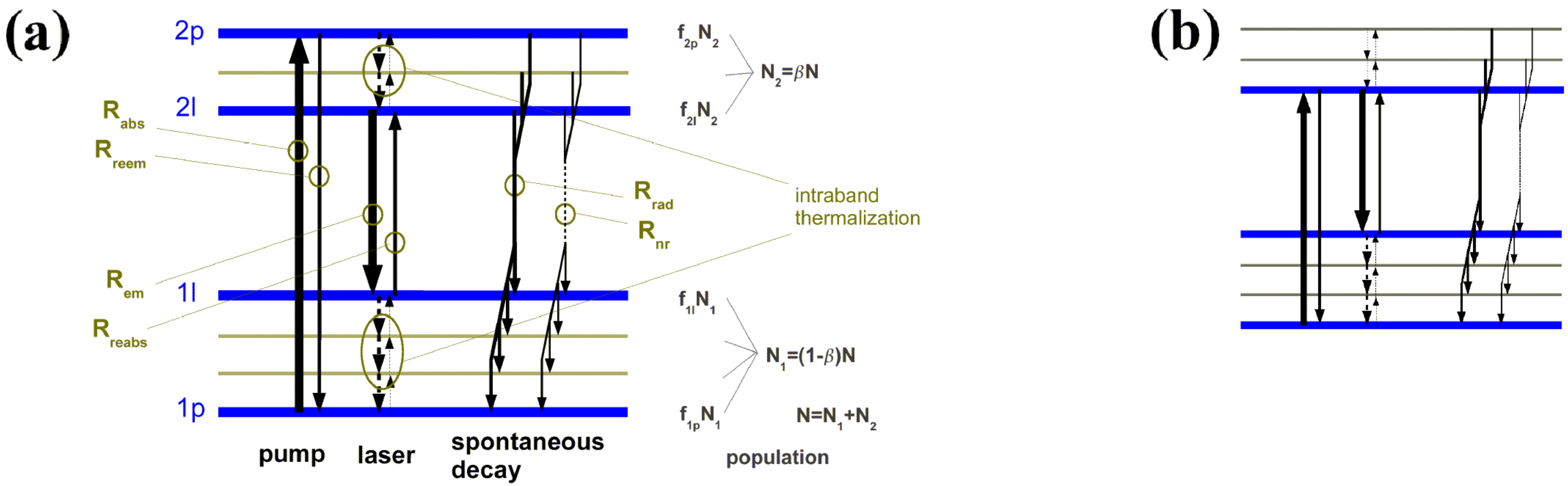

Fig. 3.1.(a) Quasi-four-level laser operation of Yb^{3+}. Transition rates R_{abs}, ..., multiplett populations N_1, N_2, and the fractional populations $f_{2p}N_2$, ... of the Stark levels are indicated. See also Table 3.1. and text. (b) Quasi-three-level laser operation. Pumping occurs directly into the upper laser level.

Table 3.1. Transition rates R_{abs}, ... for pumping, lasing and spontaneous decay as indicated in Fig. 3.1.(a); with intensities of pump and laser I_p, I_l, phonon energies $h\nu_p$, $h\nu_l$, wavelengths λ_p, λ_l, inversion parameter β, cross sections $\sigma_{1p,2p}$, ... for transitions between Stark levels (individual cross sections), experimentally obtainable absorption and emission cross sections $\sigma_a(\lambda)$ and $\sigma_e(\lambda)$. While $\alpha_0(\beta,\lambda)$ and $g_0(\beta,\lambda)$ are the absorption and gain coefficients of the one-way processes, $\alpha_{eff}(\beta,\lambda_p)$ and $g_{eff}(\beta,\lambda_l)$ are the effective coefficients taking into account both absorption and emission at the transition wavelengths.

***R**$_{abs}$* absorption	$R_{abs} = \alpha_0(\beta,\lambda_p)\frac{I_p}{h\nu_p}$ with	(3.3.)
	$\alpha_0(\beta,\lambda_p) = N_1 f_{1p}\sigma_{1p,2p} = (1-\beta)N\sigma_a(\lambda_p)$	(3.4.)
***R**$_{reem}$* reemission	$R_{reem} = g_0(\beta,\lambda_p)\frac{I_p}{h\nu_p}$ with	(3.5.)
	$g_0(\beta,\lambda_p) = N_2 f_{2p}\sigma_{2p,1p} = \beta N\sigma_e(\lambda_p)$	(3.6.)
$R_p = R_{abs} - R_{reem}$ effective pump	$R_p = \alpha_{eff}(\beta,\lambda_p)\frac{I_p}{h\nu_p}$ with	(3.7.)
	$\alpha_{eff}(\beta,\lambda_p) = -N\sigma_g(\beta,\lambda_p) = N\{(1-\beta)\sigma_a(\lambda_p) - \beta\sigma_e(\lambda_p)\}$	(3.8.)

***R**$_{em}$* stimulated emission	$R_{em} = g_0(\beta,\lambda_l)\frac{I_l}{h\nu_l}$ with	(3.9.)
	$g_0(\beta,\lambda_l) = N_2 f_{2l}\sigma_{2l,1l} = \beta N\sigma_e(\lambda_l)$	(3.10.)
***R**$_{reabs}$* reabsorption	$R_{reabs} = \alpha_0(\beta,\lambda_l)\frac{I_l}{h\nu_l}$ with	(3.11.)
	$\alpha_0(\beta,\lambda_l) = N_1 f_{1l}\sigma_{1l,2l} = (1-\beta)N\sigma_a(\lambda_l)$	(3.12.)
$R_l = R_{em} - R_{reabs}$ effective laser emission	$R_l = g_{eff}(\beta,\lambda_l)\frac{I_l}{h\nu_l}$ with	(3.13.)
	$g_{eff}(\beta,\lambda_l) = N\sigma_g(\beta,\lambda_l) = N\{\beta\sigma_e(\lambda_l) - (1-\beta)\sigma_a(\lambda_l)\}$	(3.14.)

***R**$_{rad}$* radiative decay	$R_{rad} = \frac{N_2}{\tau_{rad}} = \frac{\beta N}{\tau_{rad}}$	(3.15.)
***R**$_{nr}$* nonradiative decay	$R_{nr} = \frac{N_2}{\tau_{nr}} = \frac{\beta N}{\tau_{nr}}$	(3.16.)
$R_{spd} = R_{rad} + R_{nr}$ spontaneous decay	$R_{spd} = \frac{N_2}{\tau_f} = \frac{\beta N}{\tau_f}$	(3.17.)

The one-way absorption and gain coefficients can be described as the product of the respective transition cross section $\sigma_{1p,2p}$, $\sigma_{2p,1p}$, $\sigma_{2l,1l}$, or $\sigma_{1l,2l}$ for the two Stark levels involved (individual cross section) and of the fractional population of the starting level.[1] The individual cross sections are related to the absorption and emission cross sections $\sigma_a(\lambda)$ and $\sigma_e(\lambda)$, which can be obtained from spectroscopic measurements (see eqs. a.3.-a.8. and comments on the difficulties of determining these quantities), by the relationships

$$\begin{aligned} f_{1p}\sigma_{1p,2p} &= \sigma_a(\lambda_p) \\ f_{2p}\sigma_{2p,1p} &= \sigma_e(\lambda_p) \\ f_{2l}\sigma_{2l,1l} &= \sigma_e(\lambda_l) \\ f_{1l}\sigma_{1l,2l} &= \sigma_a(\lambda_l) \end{aligned} \quad . \tag{3.18.}$$

Using eqs. 3.1. and 3.2. leads to the right hand side of eqs. 3.4., 3.6., 3.10., 3.12., and 3.15.-3.17. Defining the effective gain cross section $\sigma_g(\beta,\lambda)$ as

$$\sigma_g(\beta,\lambda) = \beta\sigma_e(\lambda) - (1-\beta)\sigma_a(\lambda) \tag{3.19.}$$

and combining eqs. 3.3. and 3.5. as well as 3.9. and 3.11., the effective absorption and laser emission coefficients $\alpha_{eff}(\beta,\lambda_p)$ and $g_{eff}(\beta,\lambda_l)$ are obtained (eqs. 3.8., 3.14.). We find absorption is negative gain,

$$\alpha_{eff}(\beta,\lambda) = -g_{eff}(\beta,\lambda) = -N\sigma_g(\beta,\lambda) \quad . \tag{3.20.}$$

The spontaneous decay rate is given as the product of the total excited-ion density N_2 and the inverse fluorescence lifetime τ_f^{-1} (see eq. 3.17.). The difficulties with the experimental or calculational determination of τ_f are pointed out in appendix A.2. (see eqs. a.9.-a.12.). Furthermore, if a significant amount of fluorescence is reabsorbed within the laser-active zone, it should be taken into account by using a modified (longer) fluorescence lifetime.

In a general case, I_p and I_l can depend on time (due to pulsed pumping and/or extraction), leading to time-dependent level populations and transition rates:

$$\frac{dN_2(t)}{dt} = -\frac{dN_1(t)}{dt} = R_p(t) - R_l(t) - R_{spd}(t) \quad . \tag{3.21.}$$

---

[1] As the degeneracies of upper and lower levels are equal for Yb^{3+} (twofold Kramers degeneracy), we find $\sigma_{1p,2p} = \sigma_{2p,1p}$ and $\sigma_{2l,1l} = \sigma_{1l,2l}$.

3.3. Continuous-wave case

With respect to the experiments in chapts. 5 and 6 covering cw, quasi-cw and cw mode-locked lasing, it is sufficient to treat here only the cw case.[1] Formulas dealing with pulsed operation of Yb^{3+}-activated laser materials can be found e.g. in [Bay00, Fan92].

3.3.1. Inversion and saturation effects

In a cw laser oscillator or amplifier, at each point of the active medium,

$$\frac{dN_2(t)}{dt} = -\frac{dN_1(t)}{dt} = 0 \quad . \qquad (3.22.)$$

This means, the effective pump rate R_p is balanced by the effective laser emission rate R_l and the spontaneous decay rate R_{spd}. Therefore,

$$R_l = R_p - R_{spd} \quad . \qquad (3.23.)$$

Using eqs. 3.7., 3.13., 3.17., and 3.20. we obtain

$$R_l = N\sigma_g(\beta,\lambda_l)\frac{I_l}{h\nu_l} = -N\sigma_g(\beta,\lambda_p)\frac{I_p}{h\nu_p} - \frac{\beta N}{\tau_f} \quad . \qquad (3.24.)$$

Inversion parameter

Equation 3.24. relates the inversion parameter $\beta = \beta(I_p,I_l)$ to the pump and laser signal intensities I_p and I_l for the case of cw operation. We use the gain cross sections according to eq. 3.19., solve for $\beta(I_p,I_l)$, and obtain

$$\beta(I_p,I_l) = \frac{\frac{I_l}{h\nu_l}\sigma_a(\lambda_l) + \frac{I_p}{h\nu_p}\sigma_a(\lambda_p)}{\frac{I_l}{h\nu_l}\{\sigma_a(\lambda_l)+\sigma_e(\lambda_l)\} + \frac{I_p}{h\nu_p}\{\sigma_a(\lambda_p)+\sigma_e(\lambda_p)\} + \frac{1}{\tau_f}} \quad . \qquad (3.25.)$$

---

[1] In our experiments, quasi-cw means chopped pumping with an approximately flat-top temporal profile of the pump pulse and a pump pulse duration longer than the effective excited state lifetime in the presence of stimulated emission. For the laser-threshold estimation, it is tolerable to neglect the error caused by treating this case as cw, since thermal effects, including the – unknown – temperature-dependence of the absorption and emission cross-sections, obviously play a larger role. A further unknown influence is that of the quantum efficiences of the individual laser crystal samples used.
In case of cw mode locking of solid state lasers, in contrast to Q-switched mode locking or to mode locking of dye lasers, the fluctuations of the level populations are negligibly small compared to the size of these populations.

If a laser is operated below or at its lasing threshold, there is no laser signal:

$$\beta(I_p, I_l = 0) = \frac{\frac{I_p}{h\nu_p}\sigma_a(\lambda_p)}{\frac{I_p}{h\nu_p}\sigma_a(\lambda_p) + \frac{I_p}{h\nu_p}\sigma_e(\lambda_p) + \frac{1}{\tau_f}} \quad . \tag{3.26.}$$

If there is no pumping, e.g. in unpumped regions of a laser medium, the population of the excited state multiplet is only due to reabsorption of the laser signal:

$$\beta(I_p = 0, I_l) = \frac{\frac{I_l}{h\nu_l}\sigma_a(\lambda_l)}{\frac{I_l}{h\nu_l}\sigma_a(\lambda_l) + \frac{I_l}{h\nu_l}\sigma_e(\lambda_l) + \frac{1}{\tau_f}} \quad . \tag{3.27.}$$

An important value of the inversion parameter is β_{min}, the minimum value to achieve transparency of the active medium at the lasing wavelength, i.e. to overcome the reabsorption loss and achieve non-negative gain, $\sigma_g(\beta \geq \beta_{min}, \lambda_l) \geq 0$. In case of no pumping, β_{min} is achieved for $I_l \rightarrow \infty$. It is given by (see eq. 3.19. for the effective gain cross section)

$$\beta_{\mathrm{min}} = \frac{\sigma_a(\lambda_l)}{\sigma_a(\lambda_l) + \sigma_e(\lambda_l)} \quad . \tag{3.28.}$$

Saturation intensities

The pump saturation intensity (or pump saturation irradiance) $I_{p,sat} = I_{p,sat}(I_l)$ is defined as the intensity, such that for an infinitesimally thin sample the effective absorption coefficient $\alpha_{eff}(\beta(I_{p,sat}, I_l), \lambda_p)$ is reduced by 50% compared to the value $\alpha_{eff}(\beta(I_p = 0, I_l), \lambda_p)$ at small pump intensities:[1]

$$\alpha_{\mathrm{eff}}(\beta(I_{p,sat}, I_l), \lambda_p) = \tfrac{1}{2}\alpha_{\mathrm{eff}}(\beta(I_p = 0, I_l), \lambda_p) \tag{3.29.}$$

or, according to eq. 3.20., divided by $-N$,

$$\sigma_g(\beta(I_{p,sat}, I_l), \lambda_p) = \tfrac{1}{2}\sigma_g(\beta(I_p = 0, I_l), \lambda_p) \quad . \tag{3.30.}$$

The laser signal saturation intensity $I_{l,sat} = I_{l,sat}(I_p)$ is defined as the signal intensity, such that for an infinitesimally thin sample the effective gain coefficient $g_{eff}(\beta(I_p, I_{l,sat}), \lambda_l)$ is reduced by 50% compared to the small signal coefficient $g_{ss}(\beta(I_p), \lambda_l) = g_{eff}(\beta(I_p, I_l = 0), \lambda_l)$:

---

[1] Alternatively, we could write $I_p \rightarrow 0$ instead of $I_p = 0$ and $I_l \rightarrow 0$ instead of $I_l = 0$ (below); "small pump" and "small signal" describe the limit of no pump or signal, respectively.

$$g_{\mathrm{eff}}(\beta(I_p, I_{l,\mathrm{sat}}), \lambda_l) = \tfrac{1}{2} g_{\mathrm{eff}}(\beta(I_p, I_l = 0), \lambda_l) \tag{3.31.}$$

or, according to eq. 3.20., divided by N,

$$\sigma_g(\beta(I_p, I_{l,\mathrm{sat}}), \lambda_l) = \tfrac{1}{2} \sigma_g(\beta(I_p, I_l = 0), \lambda_l) \;. \tag{3.32.}$$

In eqs. 3.30. and 3.32., the effective gain cross sections are given by eq. 3.19. Here and in the following, the expressions for the pump saturation intensity and the laser signal saturation intensity are strictly analog; only the wavelengths at which saturation is considered are different. This can be understood easily, since absorption is negative gain.

Using the definitions eqs. 3.30. and 3.32. with the effective gain cross sections according to eq. 3.19. and introducing $\beta(I_p=0,I_l)$ and $\beta(I_p,I_l=0)$ according to eqs. 3.26. and 3.27., we obtain the inversion parameter at the pump and laser signal saturation intensities,

$$\beta(I_{p,\mathrm{sat}}, I_l) = \frac{\sigma_a(\lambda_p)}{2\{\sigma_a(\lambda_p) + \sigma_e(\lambda_p)\}} + \frac{\frac{I_l}{h\nu_l}\sigma_a(\lambda_l)}{2\{\frac{I_l}{h\nu_l}\sigma_a(\lambda_l) + \frac{I_l}{h\nu_l}\sigma_e(\lambda_l) + \frac{1}{\tau_f}\}} \tag{3.33.}$$

and

$$\beta(I_p, I_{l,\mathrm{sat}}) = \frac{\sigma_a(\lambda_l)}{2\{\sigma_a(\lambda_l) + \sigma_e(\lambda_l)\}} + \frac{\frac{I_p}{h\nu_p}\sigma_a(\lambda_p)}{2\{\frac{I_p}{h\nu_p}\sigma_a(\lambda_p) + \frac{I_p}{h\nu_p}\sigma_e(\lambda_p) + \frac{1}{\tau_f}\}} \;. \tag{3.34.}$$

Setting $I_p = I_{p,sat}(I_l)$ in eq. 3.25., setting equal the right-hand sides of eq. 3.25. and 3.33., and solving for $I_{p,sat}(I_l)$ provides the **pump saturation intensity**; setting $I_l = I_{l,sat}$ in eq. 3.25., setting equal the right-hand sides of eq. 3.25. and 3.34., and solving for $I_{l,sat}$ provides the **laser signal saturation intensity**:

$$I_{p,\mathrm{sat}}(I_l) = \frac{h\nu_p}{\tau_f\{\sigma_a(\lambda_p) + \sigma_e(\lambda_p)\}}\left(1 + \frac{I_l}{h\nu_l}\tau_f\{\sigma_a(\lambda_l) + \sigma_e(\lambda_l)\}\right) = I_{p,\mathrm{sat}}(I_l = 0)\left(1 + \frac{I_l}{I_{l,\mathrm{sat}}(I_p = 0)}\right) , \tag{3.35.}$$

$$I_{l,\mathrm{sat}}(I_p) = \frac{h\nu_l}{\tau_f\{\sigma_a(\lambda_l) + \sigma_e(\lambda_l)\}}\left(1 + \frac{I_p}{h\nu_p}\tau_f\{\sigma_a(\lambda_p) + \sigma_e(\lambda_p)\}\right) = I_{l,\mathrm{sat}}(I_p = 0)\left(1 + \frac{I_p}{I_{p,\mathrm{sat}}(I_l = 0)}\right) , \tag{3.36.}$$

where the saturation intensities without laser signal or without pumping, respectively, are given by

$$I_{p,sat}(I_l=0)=\frac{h\nu_p}{\tau_f\{\sigma_a(\lambda_p)+\sigma_e(\lambda_p)\}}, \tag{3.37.}$$

$$I_{l,sat}(I_p=0)=\frac{h\nu_l}{\tau_f\{\sigma_a(\lambda_l)+\sigma_e(\lambda_l)\}}. \tag{3.38.}$$

Using the saturation intensities (eqs. 3.35-3.38.), we can express (deducable from eqs. 3.19. with eqs. 3.25.-3.27.) the effective absorption and gain coefficients for arbitrary pump and laser signal intensities I_p and I_l and the respective effective gain cross sections as

$$\alpha_{eff}(\beta(I_p,I_l),\lambda_p)=\frac{\alpha_{eff}(\beta(I_p=0,I_l),\lambda_p)}{1+\dfrac{I_p}{I_{p,sat}(I_l)}}, \qquad \sigma_g(\beta(I_p,I_l),\lambda_p)=\frac{\sigma_g(\beta(I_p=0,I_l),\lambda_p)}{1+\dfrac{I_p}{I_{p,sat}(I_l)}} \tag{3.39.}$$

and

$$g_{eff}(\beta(I_p,I_l),\lambda_l)=\frac{g_{eff}(\beta(I_p,I_l=0),\lambda_l)}{1+\dfrac{I_l}{I_{l,sat}(I_p)}}, \qquad \sigma_g(\beta(I_p,I_l),\lambda_l)=\frac{\sigma_g(\beta(I_p,I_l=0),\lambda_l)}{1+\dfrac{I_l}{I_{l,sat}(I_p)}}. \tag{3.40.}$$

Saturation of reabsorption loss

Please note, $\sigma_g(\beta(I_p,I_l),\lambda_l)$ can have a negative value in regions of a laser medium, which are not sufficiently pumped to achieve the minimum inversion for transparency, β_{min}; this means net absorption at the laser signal wavelength. Then eq. 3.40. expresses the saturation of the reabsorption loss occuring to the laser signal.

Comparison to saturation intensities of four-level laser materials

If optical pumping does not lead directly into the manifold containing the upper laser level (i.e. for true four-level laser materials; for 808-nm pumped Nd^{3+}, independent from the laser line), there is practically no reemission. Then, $\sigma_e(\lambda_p)=0$ in all equations, including 3.35. and 3.36. For Yb^{3+}, on the other hand, reemission may not be neglected. Pumping is more difficult than without reemission, especially on the zero-line, where absorption and emission cross sections have similar values, $\sigma_e(\lambda_p)\approx\sigma_a(\lambda_p)$.[1] Four-level laser materials do not show reabsorption, either, i.e. $\sigma_a(\lambda_l)=0$ in eqs. 3.35. and 3.36.

Saturation intensities depend on both, pump and laser signal intensities

In literature, saturation intensities are usually defined as in eqs. 3.37. and 3.38., although these refer only to the special cases of $I_l=0$ (valid for a cw oscillator below the lasing threshold) and $I_p=0$ (not valid for a cw oscillator during operation). From eqs. 3.35. and 3.36., which are

---

[1] In in some papers on Yb^{3+} lasers, e.g. [DeL93] and [Fan92], reemission is neglected for the pump saturation intensity.

generally valid for cw systems (amplifiers and oscillators),[1] we see that the pump and laser signal saturation intensities usually depend also on the laser signal and pump intensities, respectively.

Laser signal increases the pump saturation intensity and therefore reduces the saturation of the pump absorption. Analogly, optical pumping decreases the gain saturation or reabsorption saturation for the laser signal. As an example, Figure 3.2. shows the pump saturation as a function of the laser signal intensity for Yb:Sc_2O_3 with pumping at 975 nm and laser emission at 1041 nm.

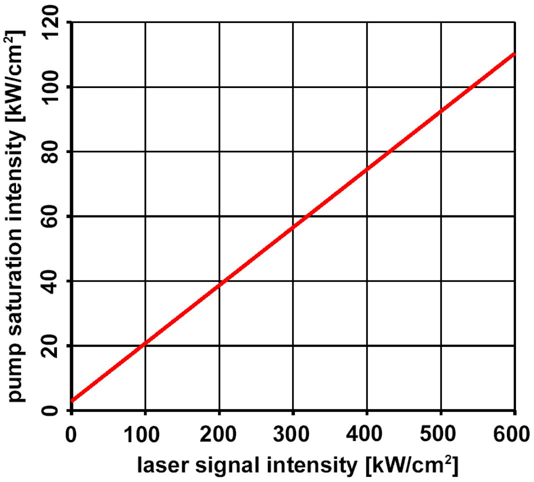

Fig. 3.2. Pump saturation intensity of Yb:Sc_2O_3 as a function of laser signal intensity. The material is pumped at 975 nm; laser signal occurs at 1041 nm. Without signal, the pump saturation intensity is ≈2.8 kW/cm². For typical signal intensities, this value is increased by two orders of magnitude, permitting efficient pumping.

Practical meaning of saturation intensities for cw laser oscillators

In case of cw laser oscillators with low round-trip losses, due to the relatively strong intracavity laser signal, only weak pump saturation is observed. Furthermore, if pump and laser mode show perfect overlap, pump saturation will not increase above its value at the lasing threshold.

In cw laser oscillators above the lasing threshold, the gain provided by the medium equals the resonator loss. Therefore, the inversion parameter averaged over the volume of the laser mode, $\beta_{avV(l)}$, is fixed to its value at the threshold (see [Ris88] and eqs. 3.62.-3.64.). If the pumped volume is identical with the laser mode volume, the effective (averaged over the pump beam) pump absorption coefficient will be reduced with increasing pump power, only until the lasing threshold will be reached;[2] above, it will be constant $\alpha_{eff}(\beta,\lambda_p) = \alpha_{eff}(\beta_{avV(l)},\lambda_p)$.

If the pump beam is smaller in radius than the laser signal beam in the medium, $w_p < w_l$, above the threshold a slight increase of the effective absorption $\alpha_{eff}(\beta,\lambda_p)$ can be observed, since the inversion parameter is reduced in the center of the laser mode. However, reduction starts from a

---

[1] For pulsed systems, the pump and gain saturation intensities as well as the absorption and gain coefficients depend on time, since pumping and extraction change the manifold populations; the above equations cannot be applied.

[2] This will be only a slight reduction, since $\beta_{avV(l)}$ is close to $\beta_{\min}$, for a low-loss resonator.

higher level of saturation; for very strong focusing of the pump beam, pump saturation will actually become significant. A decreasing pump absorption coefficient above the lasing threshold, if measurable, indicates bad overlap, $w_p > w_l$ or nonparallel beams, which is not desired with respect to the laser efficiency. Here, those regions of the medium are saturated where the stored pump energy is not extracted.

Spatial dependencies complicate estimations

In general, pump and laser intensities depend on the spatial coordinates. Consequently, all rates and level populations show spatial dependencies, too. If all these dependencies have to be taken into account, performance-related estimations become much more complicated for quasi-three- or quasi-four-level lasers than for four-level lasers. With many calculations, analytical treatment will not be possible and numerical methods must be applied, if other than plane waves are assumed.

Therefore, for the sake of simplification, several papers on lasers showing reabsorption at the signal wavelength use plane-wave approaches (no radial dependencies) [Bea95, Bou01, Lim02]. Since real-world pump and laser beams are usually not plane waves, the results of these approaches cannot describe important, experimentally observed effects. These include the meaning of the overlap of pump and laser mode for the laser threshold and efficiency and the saturation of reabsorption loss with increasing intracavity signal intensity. Plane waves are useful to treat fiber lasers [Pas95] or other long-waveguide lasers, where the pump and laser signal intensities are approximately radially constant.

Models based on Gaussian beams are presented in [Bre01c, Fan87, Ris88], of which Brenier´s work is the most general and the most suitable for Yb^{3+} laser materials, taking into account the reemission of pump radiation as well as the reabsorption of laser signal. Pump beams with a beam quality factor $M^2 > 1$ are treated in [Lin98]; [Tai97] deals with top-hat beam pumping and side-pumping.

Usually, laser efficiencies cannot be determined analytically. Estimating the pump power at the lasing threshold, however, is relatively simple due to the absence of a laser signal.

3.3.2. Laser threshold estimations

In the following, pumping occurs longitudinally along the *z*-direction with one pass of the pump through the laser medium. We have chosen $z = 0$ for the position of the crystal endface on which the pump beam is incident; the other endface is located at $z = L$. The transversal extensions of the laser medium are large, compared to the pump and laser signal beam diameters. We neglect possible spatial holeburning.

At first, we give equations for the evolution of the pump and signal beams while traveling along *z* in the laser medium (no approximations yet). The decrease of the pump intensity I_p along *z* is equal to the negative increase of the effectively absorbed pump intensity I_a and it is related to the effective pump rate R_p by

$$-\frac{dI_p(r,z)}{dz} = \frac{dI_a(r,z)}{dz} = R_p(r,z)\,h\nu_p = -N\sigma_g(\beta(I_p(r,z), I_l(r,z)), \lambda_p)\; I_p(r,z) \quad . \tag{3.41.}$$

For the laser signal intensity, both directions of the laser signal have to be taken into account (indices: "f" for forward, "b" for backward):

$$I_l = I_l(r,z) = I_{l,f}(r,z) + I_{l,b}(r,z)$$

The increase of the laser signal intensity $I_{l,f}$ along *z* is equal to the increase of the extracted intensity $I_{ex,f}$ and it is related to the effective laser emission rate $R_{l,f}$ (the formula for $I_{l,b}$ and $R_{l,b}$ is analog) by

$$\frac{dI_{l,f}(r,z)}{dz} = \frac{dI_{ex,f}(r,z)}{dz} = R_{l,f}(r,z)\,h\nu_l = N\sigma_g(\beta(I_p(r,z), I_l(r,z)), \lambda_l)\, I_{l,f}(r,z) \quad . \tag{3.42.}$$

The effective gain cross sections at the pump and laser wavelengths appearing in the above equations can be expressed by

$$\sigma_g(\beta(I_p(r,z), I_l(r,z)), \lambda_p) = \frac{\tau_f \dfrac{I_l(r,z)}{h\nu_l}\{\sigma_a(\lambda_l)\sigma_e(\lambda_p) - \sigma_e(\lambda_l)\sigma_a(\lambda_p)\} - \sigma_a(\lambda_p)}{1 + \tau_f \dfrac{I_l(r,z)}{h\nu_l}\{\sigma_a(\lambda_l) + \sigma_e(\lambda_l)\} + \tau_f \dfrac{I_p(r,z)}{h\nu_p}\{\sigma_a(\lambda_p) + \sigma_e(\lambda_p)\}} \tag{3.43.}$$

and

$$\sigma_g(\beta(I_p(r,z), I_l(r,z)), \lambda_l) = \frac{\tau_f \dfrac{I_p(r,z)}{h\nu_l}\{\sigma_a(\lambda_p)\sigma_e(\lambda_l) - \sigma_e(\lambda_p)\sigma_a(\lambda_l)\} - \sigma_a(\lambda_l)}{1 + \tau_f \dfrac{I_l(r,z)}{h\nu_l}\{\sigma_a(\lambda_l) + \sigma_e(\lambda_l)\} + \tau_f \dfrac{I_p(r,z)}{h\nu_p}\{\sigma_a(\lambda_p) + \sigma_e(\lambda_p)\}} \quad , \tag{3.44.}$$

where the inversion parameter from eq. 3.25. with spatially dependent intensities has been used.

We assume now, as an approximation, the pump and laser signal beams are circularly symmetric Gaussian with radii w_p and w_l and maintain their shape and radii within the laser medium. This assumption will be justified here, if the length *L* of the laser medium is much shorter than the Rayleigh lengths of the beams and if the distortion of the beam shapes by absorption and gain is small.

The latter condition is not fulfilled in case of strong pumping and/or high laser cavity losses, i.e. if the inversion parameter β reaches high values (more than just a few percent):

Due to pump saturation, the pump beam is less attenuated where the pump intensity is higher. Therefore, along the *z*-direction the pump beam fades less rapidly in the central regions than in the outer regions, at least as long as the laser being pumped is below or at its lasing threshold. If the laser signal comes into play, the situation gets more complicated, as the pump saturation effect is decreased by the laser signal intensity (see eq. 3.35. and Fig. 3.2.).
Furthermore, the signal intensity distribution within the laser medium may differ substantially from that of the fundamental Gaussian mode given by the laser cavity, if the gain per medium length is high, balancing high resonator losses (e.g. from strong output coupling). Then, the average laser signal photon will not experience many cavity round trips, and the spatial distribution of the signal intensity within the medium will contain a strong component of ”freshly generated” photons. This component will be shaped by the gain distribution within the active medium, and it will grow in the direction towards the output coupling.

Gaussian shape of the pump beam means, the pump intensity I_p depends on the radial coordinate r and is related to the power P_p, as follows:

$$I_p(r,z) = I_p(r=0,z)\exp\left(-\frac{2r^2}{w_p{}^2}\right), \tag{3.45.}$$

with

$$I_p(r=0,z) = \frac{2P_p(z)}{\pi w_p{}^2}. \tag{3.46.}$$

Therefore,

$$P_p(z) = \int_0^\infty r\,dr \int_0^{2\pi} d\varphi\, I_p(r,z).$$

For the laser signal beam:

$$I_l(r,z) = I_{l,f}(r,z) + I_{l,b}(r,z) = [I_{l,f}(r=0,z) + I_{l,b}(r=0,z)]\exp\left(-\frac{2r^2}{w_l{}^2}\right) \tag{3.47.}$$

with

$$I_{l,f}(r=0,z) = \frac{2P_{l,f}(z)}{\pi w_l{}^2}, \qquad I_{l,b}(r=0,z) = \frac{2P_{l,b}(z)}{\pi w_l{}^2}. \tag{3.48.}$$

The equations 3.41. and 3.42., describing the evolution of the pump and laser signal intensities, cannot be solved by Gaussian modes, since the inversion parameter β and the resulting effective coefficients show radial dependencies. Therefore, to maintain consistency, we move over to analog equations for the powers, where we use the radially averaged (index "*avr*") quantities $\beta_{avr(p)}(z)$ and $\beta_{avr(l)}(z)$. The averages are weighted with the respective Gaussian intensity profiles (indices "*(p)*" and "*(l)*" for pump and laser):

$$\beta_{avr(p)}(z) = \beta_{avr(p)}\left(P_p(z), P_l(z)\right) = \frac{4}{w_p^{\,2}} \int_0^\infty r\,dr \exp\left(-\frac{2r^2}{w_p^{\,2}}\right) \beta(I_p(r,z), I_l(r,z)) \quad , \tag{3.49.}$$

$$\beta_{avr(l)}(z) = \beta_{avr(l)}\left(P_p(z), P_l(z)\right) = \frac{4}{w_l^{\,2}} \int_0^\infty r\,dr \exp\left(-\frac{2r^2}{w_l^{\,2}}\right) \beta(I_p(r,z), I_l(r,z)) \quad . \tag{3.50.}$$

The evolution of the pump and laser signal powers is described now by

$$-\frac{dP_p(z)}{dz} = \frac{dP_a(z)}{dz} = -N\sigma_g(\beta_{avr(p)}(z), \lambda_p)P_p(z) \quad , \tag{3.51.}$$

$$\frac{dP_{l,f}(z)}{dz} = \frac{dP_{ex,f}(z)}{dz} = N\sigma_g(\beta_{avr(l)}(z), \lambda_p)P_{l,f}(z) \quad , \tag{3.52.}$$

$$-\frac{dP_{l,b}(z)}{dz} = -\frac{dP_{ex,b}(z)}{dz} = N\sigma_g(\beta_{avr(l)}(z), \lambda_p)P_{l,b}(z) \quad . \tag{3.53.}$$

By this ansatz, which is equivalent to Brenier´s [Bre01c], pump saturation is taken into account and a moderate longitudinal variation of the laser signal is permitted. For a strong variation of $P_{l,f}$ and $P_{l,b}$, however, the approach does not work due to the non-Gaussian distortion of the beam shapes. A rougher approximation would be to assume no ground state depletion and very low round-trip losses, leading to a spatially constant pump absorption coefficient and longitudinally constant laser signal intensities [Ris88].[1]

Necessary gain and inversion to reach the lasing threshold

Equations 3.52. and 3.53. can be fulfilled by

$$P_{l,f}(z) = P_{l,f}(z=0)\exp(G_f(z, \lambda_l)) \quad , \tag{3.54.}$$

$$P_{l,b}(z) = P_{l,b}(z=L)\exp(G_b(z, \lambda_l)) \quad , \tag{3.55.}$$

with forward- and backward beam gain

---

[1] Assuming no pump saturation can be legitimate for high-gain materials such as Nd^{3+}-based ones, since small values of β are required to achieve a desired gain. With Yb^{3+} laser materials and large resonator loss, pump saturation should be taken into account, as far as possible.

In case of our experiments in chapters 5 and 6, however, saturation does not play a significant role for the absorbed pump powers, since the laser crystals are much longer than the respective pump absorption lengths (i.e. much longer than optimum, actually).

$$G_f(z,\lambda_l)=\int_0^z d\tilde{z}\, N\sigma_g(\beta_{avr(l)}(\tilde{z}),\lambda_l)$$ for $0\le z\le L$. (3.56.)

$$G_b(z,\lambda_l)=-\int_L^z d\tilde{z}\, N\sigma_g(\beta_{avr(l)}(\tilde{z}),\lambda_l$$ for $0\le z\le L$. (3.57.)

The round-trip gain *G(λl)* is given by

$$G(\lambda_l)=G_f(L,\lambda_l)+G_b(0,\lambda_l)=2G_f(L,\lambda_l)=2\int_0^L dz\, N\sigma_g(\beta_{avr(l)}(z),\lambda_l) \qquad (3.58.)$$

Assuming a laser cavity, which employs an output coupling mirror with transmission T_{oc} on one side and exhibits extra loss Λ on the other side (extra loss may be due to parasitive mirror transmission, filter elements, etc.), we find

$$P_{l,f}(z=L)(1-T_{oc})=P_{l,b}(z=L)$$ and

$$P_{l,f}(z=0)=P_{l,b}(z=0)(1-\Lambda).$$

In case of a cw laser oscillator at or above lasing threshold, the round-trip gain $G(\lambda_l)$ balances the total attenuation $\delta(\lambda_l)$ by loss occuring on the round trip:

$$P_{l,f}(0)\exp(G_f(L,\lambda_l))(1-T_{oc})\exp(G_b(0,\lambda_l))(1-\Lambda)=P_{l,f}(0)$$ or shorter,

$$G(\lambda_l)=\delta(\lambda_l), \qquad (3.59.)$$

where the total attenuation $\delta(\lambda_l)$ is defined by

$$\delta(\lambda_l)=-\ln([1-T_{oc}(\lambda_l)][1-\Lambda(\lambda_l)]). \qquad (3.60.)$$ [1]

Using the round-trip gain $G(\lambda_l)$ from eq. 3.58. and the definition of the effective gain cross section, we obtain

$$G(\lambda_l)=2\int_0^L dz\, N\left[-\sigma_a(\lambda_l)+\beta_{avr(l)}(z)\{\sigma_a(\lambda_l)+\sigma_e(\lambda_l)\}\right]=\delta(\lambda_l). \qquad (3.61.)$$

Introducing the average (index "*av*") inversion parameter $\beta_{avV(l)}$ with respect to the effective volume of the laser mode (index "*V(l)*") as

$$\beta_{avV(l)}=\frac{1}{L}\int_0^L dz\,\beta_{avr(l)}(z)=\frac{4}{Lw_l^{\,2}}\int_0^L dz\int_0^\infty r\,dr\,\exp\left(-\frac{2r^2}{w_l^{\,2}}\right)\beta(I_p(r,z),I_l(r,z)), \qquad (3.62.)$$

equation 3.61. can be expressed as

$$\delta(\lambda_l)=2NL\{\sigma_a(\lambda_l)+\sigma_e(\lambda_l)\}\beta_{avV(l)}-2NL\sigma_a(\lambda_l)=2NL\sigma_g(\beta_{avV(l)},\lambda_l). \qquad (3.63.)$$

---

[1] We will usually call this "loss", since $\delta(\lambda_l)\approx T_{OC}+\Lambda$, if $T_{OC}<<1$ and $\Lambda<<1$.

From this, we obtain the average inversion parameter $\beta_{avV(l)}$ for the case of a cw low-loss laser oscillator at or above the lasing threshold

$$\beta_{avV(l)} = \beta_{min}\left(1 + \frac{\delta(\lambda_l)}{2NL\sigma_a(\lambda_l)}\right), \tag{3.64.}$$

with

$$\beta_{min} = \frac{\sigma_a(\lambda_l)}{\sigma_a(\lambda_l) + \sigma_e(\lambda_l)}.$$

The average inversion parameter $\beta_{avV(l)}$ consists of two parts: The first, β_{min}, is required to overcome reabsorption loss and to make the active material transparent; it vanishes for true four-level laser materials. The second, which depends on $\delta(\lambda_l)$, is necessary to provide enough positive gain to compensate for the round-trip loss of the resonator; the term becomes $\delta(\lambda_l)/\{2NL\sigma_e(\lambda_l)\}$ for laser materials without reabsorption loss.

Equation 3.64. shows, above the lasing threshold, $\beta_{avV(l)}$ will be clamped to its value at the threshold, if there exist no implicit dependencies on the pump and signal powers. Such possible dependencies are saturation effects concerning $\delta(\lambda_l)$ or changes of the cross sections $\sigma_a(\lambda_l)$ and $\sigma_e(\lambda_l)$ due to heat effects.

The pump power at the lasing threshold is found as the pump power needed to achieve $\beta_{avV(l)}$ in the absence of stimulated emission. If the losses of a resonator, $\delta(\lambda_l)$, are known (e.g. if $T_{oc} >> \Lambda$), $\beta_{avV(l)}$ can be determined using eq. 3.64. However, this may not be the case; then, $\beta_{avV(l)}$ has to be estimated as shown below. Afterwards, if desired, $\delta(\lambda_l)$ can be deduced from eq. 3.64.

Laser emission wavelength, determination of inversion and resonator loss

After start-up, a cw laser system will adjust its average inversion parameter $\beta_{avV(l)}$ to a value where the resulting gain balances the loss in the resonator. From eq. 3.64., however, we see that $\beta_{avV(l)}$ is a function of the stimulated-emission wavelength λ_l, since the spectroscopic cross sections and possibly also the resonator loss depend on λ_l. During the balancing process, the laser will tune λ_l to the value where the average inversion parameter $\beta_{avV(l)}$ is minimum,

$$\frac{d}{d\lambda}\beta_{avV(l)} = 0 \quad \text{at} \quad \lambda = \lambda_l. \tag{3.65.}$$

This means the energy stored in the laser medium will be minimized, the energy extraction from the medium (and therefore the efficiency of the laser) will be maximized.

If the spectra of the laser material and the wavelength-dependency of the loss are known and λ_l has been measured, eq. 3.65. enables us to calculate $\beta_{avV(l)}$ as well as $\delta(\lambda_l)$. The easiest case is $d\delta(\lambda)/d\lambda = 0$ (i.e. the resonator does not contain wavelength-selective elements). Then, minimum $\beta_{avV(l)}$ also requires that the laser emission wavelength λ_l must be located in the maximum of the gain cross section curve $\sigma_g(\beta_{avV(l)},\lambda)$, with $\beta_{avV(l)}$ treated as as a fixed value (assumed to be a minimum in agreement with eq. 3.65.),

$$\frac{\partial}{\partial\lambda}\sigma_g(\beta_{avV(l)},\lambda)=0 \qquad \text{at} \qquad \lambda=\lambda_l\,,^1 \qquad (3.66.)$$

and the average inversion parameter $\beta_{avV(l)}$ is found as

$$\beta_{avV(l)}=\frac{\frac{d}{d\lambda}\sigma_a(\lambda)}{\frac{d}{d\lambda}(\sigma_a(\lambda)+\sigma_e(\lambda))} \qquad \text{with} \qquad \lambda=\lambda_l\,. \qquad (3.67.)$$

Setting equal the RHS of eqs. 3.64. and 3.67. provides the resonator loss δ,

$$\delta=2NL\left(\frac{\frac{d}{d\lambda}\sigma_a(\lambda)}{(\sigma_a(\lambda)+\sigma_e(\lambda))\frac{d}{d\lambda}(\sigma_a(\lambda)+\sigma_e(\lambda))}-\sigma_a(\lambda)\right) \qquad \text{with} \qquad \lambda=\lambda_l\,. \qquad (3.68.)$$

Alternatively, the average inversion parameter $\beta_{avV(l)}$ and the effective gain cross section $\sigma_g(\beta_{avV(l)},\lambda)$ for the observed lasing wavelength λ_l can be obtained by comparison of the gain curves $\sigma_g(\beta_{avV(l)},\lambda)$ (effective gain cross section) or $N\sigma_g(\beta_{avV(l)},\lambda)$ (effective gain coefficient, net gain per unit length) obtained for different $\beta_{avV(l)}$ (see also [McC64b]). An example is given in Fig. 3.3. for KYbW. A regular observation with quasi-three- or quasi-four-level materials is that increasing the resonator loss $\delta(\lambda_l)$ will lead to a blue-shift of the lasing wavelength λ_l. The reason is that higher loss must be balanced by higher gain, which requires a larger inversion $\beta_{avV(l)}$. Due to a decreasing relative influence of reabsorption $\sigma_a(\lambda_l)$ (see eq. 3.19.), this results in a shift of the gain maximum towards shorter wavelengths. With true four-level-laser materials, no reabsorption and therefore no such shift exists; the laser would operate at the maximum of the fluorescence spectrum.

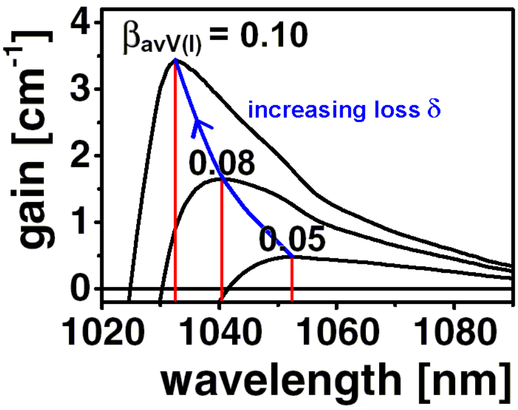

Fig. 3.3. Effective gain coefficient of KYbW for $E\|N_m$-polarization, for three different values of the inversion parameter $\beta_{avV(l)}$. Red vertical lines indicate the wavelength where laser emission will be observed for the respective $\beta_{avV(l)}$, if the resonator loss δ does not depend on wavelength. Using eq. 3.64. provides the respective value of δ. It increases with $\beta_{avV(l)}$ (blue arrow).

---

[1] Here, differentiation with respect to λ does not include the implicit dependency in $\beta_{avV(l)}$.

The following restrictions have to be paid attention to: If the gain curves $\sigma_g(\beta_{avV(l)},\lambda)$ exhibit strong peaks in the region of the observed λ_l, a small change of λ_l may correspond to a large change of the inversion. Then, wavelengths must have been determined with sufficiently high precision both in the laser experiment and in the spectroscopic measurements.[2] If the gain curves $\sigma_g(\beta_{avV(l)},\lambda)$ are rather flat, confusion may arise from noise peaks.

Absorbed pump power at the lasing threshold

If laser signal is absent, the effectively absorbed pump rate is equal to the spontaneous decay rate. This is valid also within the volume filled by the laser mode, for which we know the average inversion parameter $\beta_{avV(l)}$:

$$\frac{2}{\pi w_l^{\,2}}\int_0^L dz\int_0^{2\pi} d\varphi\int_0^\infty rdr\,R_p(r,z)\exp\left(\frac{-2r^2}{w_l^{\,2}}\right)=\frac{2}{\pi w_l^{\,2}}\int_0^L dz\int_0^{2\pi} d\varphi\int_0^\infty rdr\,R_{spd}(r,z)\exp\left(\frac{-2r^2}{w_l^{\,2}}\right).$$

Using eqs. 3.7. and 3.17. (rates) leads to

$$-\int_0^L dz\int_0^\infty rdr\frac{dI_p(r,z)}{h\nu_p dz}\exp\left(\frac{-2r^2}{w_l^{\,2}}\right)=\int_0^L dz\int_0^\infty rdr\frac{\beta_{avV(l)}N}{\tau_f}\exp\left(\frac{-2r^2}{w_l^{\,2}}\right),$$

and further,

$$\frac{P_p(0)-P_p(L)}{h\nu_p}\,\frac{2}{\pi w_p^{\,2}}\int_0^\infty rdr\exp\left(\frac{-2r^2}{w_p^{\,2}}+\frac{-2r^2}{w_l^{\,2}}\right)=\frac{\beta_{avV(l)}NL}{\tau_f}\int_0^\infty rdr\exp\left(\frac{-2r^2}{w_l^{\,2}}\right).$$

Finally, the pump power absorbed at the lasing threshold is obtained as

$$P_{a,thr}(L)=P_p(0)-P_p(L)=\frac{\beta_{avV(l)}NL\,h\nu_p}{\tau_f}\,\frac{\pi}{2}\left(w_p^{\,2}+w_l^{\,2}\right)\tag{3.69.a}$$

or,

using eq. 3.64.,

$$P_{a,thr}(L)=\beta_{min}\frac{NLh\nu_p}{\tau_f}\,\frac{\pi}{2}\left(w_p^{\,2}+w_l^{\,2}\right)\left(1+\frac{\delta(\lambda_l)}{2NL\sigma_a(\lambda_l)}\right).\tag{3.69.b}$$

The pump power absorbed in the whole medium at the lasing threshold, $P_{a,thr}(L)$, consists of a part to overcome reabsorption and a part, which depends on $\delta(\lambda_l)$, to compensate for resonator loss.

Minimization of the pump and laser signal beam radii minimizes $P_{a,thr}(L)$. A minimum value of $P_{a,thr}(L)$, however, does not necessarily mean maximum efficiency of the laser. If a laser is operated far above its lasing threshold, the slope efficiency will play a larger role than $P_{a,thr}(L)$.

---

[2] An example is Yb^{3+}-doped scandia, which we use in our experiments in chapter 6.

Incident pump power at the lasing threshold

To find a general relationship between the incident pump power $P_p(0)$ and the transmitted and absorbed pump powers, $P_p(z)$ and $P_a(z)$, we start with eq. 3.51.,

$$-\frac{dP_p(z)}{dz}=\frac{dP_a(z)}{dz}=-N\sigma_g(\beta_{avr(p)}(P_p(z),P_l(z)),\lambda_p)\ P_p(z)\ .$$

At or below the lasing threshold, there is no signal power, $P_l(z) = 0$. Using eqs. 3.49., 3.26., 3.35., 3.45., and 3.46., we find

$$\sigma_g(\beta_{avr(p)}(P_p(z),P_l(z)=0),\lambda_p)=\frac{4}{w_p^2}\int_0^\infty r\,dr\frac{-\sigma_a(\lambda_p)\exp\left(-\frac{2r^2}{w_p^2}\right)}{1+\frac{2}{\pi w_p^2}\frac{P_p(z)}{I_{p,sat}(I_l=0)}\exp\left(-\frac{2r^2}{w_p^2}\right)}\ .$$

The integral can be solved analytically [Bro91, integral no.455], obtaining

$$\sigma_g(P_p(z),P_l(z)=0,\lambda_p)=-\sigma_a(\lambda_p)\frac{\pi w_p^2}{2}\frac{I_{p,sat}(I_l=0)}{P_p(z)}\ln\left(1+\frac{2}{\pi w_p^2}\frac{P_p(z)}{I_{p,sat}(I_l=0)}\right)\ . \tag{3.70.}$$

The term to the right of $-\sigma_a(\lambda_p)$ is smaller than one; it is the effect of the pump saturation in case of a Gaussian pump beam and no signal beam. Please note that the pump saturation power ($P_{p,sat}$, so that $\sigma_g(P_{p,sat},0,\lambda_p) = -\sigma_a(\lambda_p)/2$) is given by

$$P_{p,sat}(I_l=0)\approx 2.5129\ \frac{\pi w_p^2}{2}I_{p,sat}(I_l=0)\ . \tag{3.71.}$$

The factor 2.5129 is specific for the Gaussian beam and can be calculated numerically. If the factor is left out, we obtain the power at which pump saturation occurs in the center of the pump beam.

Using eq. 3.70., the differential eq. 3.51. becomes

$$-\frac{dP_p(z)}{dz}=N\sigma_a(\lambda_p)\frac{\pi w_p^2}{2}I_{p,sat}(I_l=0)\ln\left[1+\frac{2}{\pi w_p^2}\frac{P_p(z)}{I_{p,sat}(I_l=0)}\right]\ . \tag{3.72.}$$

This differential equation is solvable by [Bro91, integral no.469]

$$\ln\ln\left[1+\frac{2}{\pi w_p^2}\frac{P_p(z)}{I_{p,sat}(I_l=0)}\right]+\sum_{n=1}^{\infty}\frac{\left(\ln\left[1+\frac{2}{\pi w_p^2}\frac{P_p(z)}{I_{p,sat}(I_l=0)}\right]\right)^n}{n!\,n}=-N\sigma_a(\lambda_p)z+C_1\ , \tag{3.73.}$$

where the constant C_1 can be determined by setting $z = 0$.

Equation 3.73. with $P_p(z) > 0$ can be solved numerically only. However, in case of **weak pump saturation,**

$$\frac{2}{\pi w_p{}^2}\frac{P_p(z)}{I_{p,sat}(I_l=0)} << 1 ,$$

the following **approximation** is permitted:

$$\sigma_g(P_p(z), P_l(z)=0, \lambda_p) \approx -\sigma_a(\lambda_p)\left[1-\frac{1}{\pi w_p{}^2}\frac{P_p(z)}{I_{p,sat}(I_l=0)}\right] .$$

Then the differential eq. 3.51. becomes

$$-\frac{dP_p(z)}{dz} \approx N\sigma_a(\lambda_p)\left[1-\frac{1}{\pi w_p{}^2}\frac{P_p(z)}{I_{p,sat}(I_l=0)}\right]P_p(z) ,$$

which is solvable by [Bro91, integral no.40]. We find for the case of weak pump saturation,

$$P_p(z) \approx \frac{P_p(0)\exp(-N\sigma_a(\lambda_p)z)}{1-\dfrac{P_p(0)\left[1-\exp(-N\sigma_a(\lambda_p)z)\right]}{\pi w_p{}^2 I_{p,sat}(I_l=0)}} \quad \text{and} \quad P_p(0) \approx \frac{P_p(z)\exp(N\sigma_a(\lambda_p)z)}{1-\dfrac{P_p(z)\left[1-\exp(N\sigma_a(\lambda_p)z)\right]}{\pi w_p{}^2 I_{p,sat}(I_l=0)}} . \tag{3.74.}$$

To estimate the incident pump power $P_{p,thr}(0)$ corresponding to $P_{a,thr}(L)$, in the weak-pump-saturation approximation, we set $z = L$ and use $P_{a,thr}(L) = P_p(0)-P_p(L)$. We obtain

$$P_{p,thr}(0) \approx \frac{\pi w_p{}^2 I_{p,sat}(I_l=0)+P_{a,thr}(L)}{2}\left(1-\sqrt{1-\frac{4}{1-\exp(-N\sigma_a(\lambda_p)L)}\frac{P_{a,thr}(L)\pi w_p{}^2 I_{p,sat}(I_l=0)}{\left(\pi w_p{}^2 I_{p,sat}(I_l=0)+P_a(L)\right)^2}}\right) . \tag{3.75.}$$

Incident pump power at the lasing threshold for equal beam radii, $w_p = w_l$

In the important case of perfect overlap of pump and laser signal beam, we can utilize the known value of the average inversion parameter $\beta_{avV(l)}$ to give an exact relationship between $P_p(0)$ and $P_a(L)$ at or above the lasing threshold (exact within the limits of the Gaussian-beam approach).

The differential equation 3.51. describing the evolution of the pump power while traveling through the crystal can be solved by an exponential function:

$$P_p(z) = P_p(z=0)\exp\left(-A(z,\lambda_p)\right) \tag{3.76.}$$

with

$$A(z,\lambda_p) = -\int_0^z d\tilde{z}\, N\sigma_g(\beta_{avr(p)}(\tilde{z}),\lambda_p) . \tag{3.77.}$$

This leads to

$$P_p(0)=\frac{P_a(L)}{1-\exp\left(-A(L,\lambda_p)\right)} \quad . \tag{3.78.}$$

Here, the attenuation $A(L,\lambda_p)$ experienced by the pump beam after traveling through the active medium of length L can be expressed as

$$A(L,\lambda_p)=-LN\sigma_g(\beta_{avV(p)},\lambda_p) \tag{3.79.}$$

with the inversion parameter averaged over the pumped volume

$$\beta_{avV(p)}=\frac{1}{L}\int_0^L dz\,\beta_{avr(p)}(z) \quad . \tag{3.80.}$$

Usually, $\beta_{avV(p)}$ would be a quantity whose value is unknown and changes with the pump and laser signal powers. However, for perfect overlap of the beams, $w_p = w_l$, the average inversion parameters being effective for pump and laser signal are constant and identical, $\beta_{avV(p)} = \beta_{avV(l)}$, where the value of $\beta_{avV(l)}$ is given by eq. 3.64. As a consequence, at or above the lasing threshold, the pump beam experiences a constant attenuation.

This is illustrated in Fig. 3.4. showing the typical behavior of the pump absorption efficiency $P_a(L)/P_p(0)$ (i.e. pump power absorbed by a crystal of length L versus incident pump power) as a function of the incident pump power in units of the threshold pump power, $P_p(0)/P_{p,thr}(0)$. Here, a 0.5-mm-thick Yb(1%):Sc_2O_3 crystal in a minimum-loss-resonator ($\delta = 0$, such that $\beta_{avV(l)} = \beta_{min}$) serves as an example. Below the laser threshold, of course, the inversion parameter is smaller than the value at the lasing threshold, i.e. $\beta_{avV(p)} < \beta_{avV(l)}$, and increases with the pump power. This part of the curve in Fig. 3.4. was simulated using eq. 3.74. (weak-pump-saturation case). In other lasers, stronger saturation may be experienced by the pump beam. Then, the decrease of the absorption efficiency will deviate from the approximately linear course shown here.

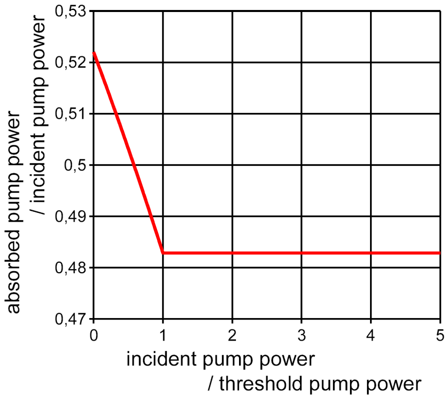

Fig. 3.4. Pump absorption efficiency as a function of incident pump power. The example shows the behavior of a 0.5-mm-thick 1%-Yb^{3+}-doped Yb:Sc_2O_3 crystal in a laser with perfect overlap of pump and resonator mode (no resonator loss assumed). The material is pumped at 975 nm; lasing occurs at 1041 nm. With increasing pump power, the absorption efficiency drops from the value for the unsaturated medium to a minimum value which is reached at the lasing threshold. Above threshold the value is constant, corresponding to a constant average inversion $\beta_{avV(l)}$.

Using eqs. 3.78., 3.79., and 3.69.a, we find for the incident pump power at the lasing threshold

$$P_{p,thr}(0) = \frac{P_{a,thr}(L)}{1-\exp\left(NL\sigma_g(\beta_{avV(l)},\lambda_p)\right)} = \frac{\beta_{avV(l)} NLh\nu_p \pi w_l^2}{\tau_f\left\{1-\exp\left(NL\sigma_g(\beta_{avV(l)},\lambda_p)\right)\right\}} \quad \text{for} \quad w_p = w_l . \qquad (3.81.)$$

Length of the active medium for minimum threshold pump power

There exists an optimum length L_{minthr} of the active medium so that the incident pump power at the lasing threshold is minimized.[1] This length is a compromise between avoiding reabsorption loss for the laser signal and avoiding transmission for the pump beam. The value of L_{minthr} is obtained from setting

$$\frac{d}{dL} P_{p,thr}(0) = 0$$

at L_{minthr}.

This leads to the length-for-minimum-threshold condition

$$1-\left[1-\sigma_g(\beta_{min},\lambda_p)\left(NL+\frac{\delta(\lambda_l)}{2\sigma_a(\lambda_l)}\right)\right]\exp\left\{NL\sigma_g(\beta_{avV(l)},\lambda_p)\right\}=0 \quad \text{for} \quad w_p = w_l . \qquad (3.82.)$$

This equation is similar to that given in [Ris88], but takes into account pump saturation, which increases the value of L_{minthr}.

---

[1] Here, as before, we assume one pass of the pump beam through the active medium.

3.3.3. Laser efficiency

For the estimation of the laser efficiency, no analytical solutions exist, if Gaussian beams with arbitrary radii are assumed for pump and laser signal. Therefore, we will discuss the mechanisms that determine the laser efficiencies and consider the results of Risk, who made numerical simulations [Ris88].

The extraction efficiency η_{ex} is defined as the ratio of power $P_{ex}(L)$, which is extracted from the laser medium, and absorbed pump power $P_a(L)$,

$$\eta_{ex} = \frac{P_{ex}(L)}{P_a(L)} . \tag{3.83.}$$

If loss and gain per round trip are small and therefore the laser signal power is approximately constant along z, the optical-to-optical conversion efficiency η_{opt} with respect to the absorbed pump power and that with respect to the incident pump power, η_{tot}, are given by

$$\eta_{opt} = \frac{P_{out}}{P_a(L)} \approx \frac{T_{OC}}{T_{OC}+\Lambda}\eta_{ex} \quad \text{and} \tag{3.84.}$$

$$\eta_{tot} = \frac{P_{out}}{P_p(0)} \approx \frac{P_a(L)}{P_p(0)}\frac{T_{OC}}{T_{OC}+\Lambda}\eta_{ex} , \tag{3.85.}$$

with P_{out},	output power of the laser;
T_{OC},	transmission of output coupling mirror;
Λ,	extra loss of the laser resonator.
$P_a(L)/P_p(0)$,	absorption efficiency described by eq. 3.78.

By volume integration of the rates in the cw case (see eqs. 3.7., 3.8., 3.17., 3.23., 3.24.) and multiplication with the respective quantum energies, the following relationship for the extraction efficiency is obtained from eqs. 3.83., 3.45., and 3.46.:

$$\eta_{ex} = \frac{\nu_l}{\nu_p}\left(1 - \frac{\nu_p}{\nu_{spd}}\frac{P_{spd}(L)}{P_a(L)}\right) , \tag{3.86.}$$

where the spontaneous decay power P_{spd} is given by

$$P_{spd} = \frac{h\nu_{spd}}{\tau_f}\int_0^L dz \int_0^{2\pi} d\varphi \int_0^\infty r dr\, N\beta(r,z) , \tag{3.87.}$$

with $h\nu_{spd}$, average quantum energy of a spontaneous decay.

Equation 3.86. shows, the larger the part of the absorbed pump power ending up in spontaneous decay (mainly fluorescence, usually), the lower the extraction efficiency. Below and at the lasing threshold, η_{ex} is 0, because there exists only spontaneous decay and no extracted laser signal, $P_{spd} = P_a$. The extraction efficiency is proportional to the quantum ratio ν_l/ν_p. This ratio is also the theoretical maximum value of η_{ex}, i.e. the value observed in the case where each absorbed pump photon results in the stimulated emission of a laser signal photon; and from eq. 3.84. we see it will be also the maximum of the optical-to-optical conversion efficiency η_{opt}, if the loss Λ is minimum.[1] Therefore, active materials with a laser quantum defect $(\nu_p-\nu_l)/\nu_p$ (usually given in percent, see eq. a.1.) as small as possible are desired for high-efficiency lasers. Equation 3.87. means, the power lost by spontaneous decay is proportional to the total number of excited ions in the active medium.

The differential extraction efficiency $dP_{ex}(L)/dP_a(L)$, too, is proportional to the quantum ratio ν_l/ν_p:

$$\frac{dP_{ex}(L)}{dP_a(L)} = \frac{\nu_l}{\nu_p}\left(1-\frac{\nu_p}{\nu_{spd}}\frac{dP_{spd}(L)}{dP_a(L)}\right), \tag{3.88.}$$

where the change of the spontaneous decay power with the change of the absorbed pump power is given by

$$\frac{dP_{spd}(L)}{dP_a(L)} = \frac{h\nu_{spd}}{\tau_f}\frac{d}{dP_a(L)}\int_0^L dz\int_0^{2\pi} d\varphi\int_0^{\infty} rdr\,N\beta(r,z). \tag{3.89.}$$

Assuming that loss and gain per round trip are small, the laser slope efficiency η_{sl}, i.e. the differential optical-to-optical conversion efficiency with respect to the absorbed pump power, is related to the differential extraction efficiency by

$$\eta_{sl} = \frac{dP_{out}}{dP_a(L)} \approx \frac{T_{OC}}{T_{OC}+\Lambda}\frac{dP_{ex}(L)}{dP_a(L)}. \tag{3.90.}$$

Equations 3.88.-3.90. mean, the differential extraction efficiency and the laser slope efficiency would be constant and maximum, ν_l/ν_p or $(\nu_l/\nu_p)\cdot T_{OC}/(T_{OC}+\Lambda)$, respectively, if the total number of excited ions in the active medium remained constant while the absorbed pump power was increased. Therefore, the spatial distribution of the inversion parameter $\beta(r,z)=\beta(I_p(r,z),I_l(r,z))$ and its variation with increasing pump and signal powers are the key to understanding laser efficiencies, especially in case of quasi-three- or quasi-four-level laser materials.

Variation of the inversion profile

From eq. 3.64. we have learnt that for any cw laser (quasi-three- or quasi-four-level or other) at or above the lasing threshold the weighted average of the inversion parameter over the laser mode volume, $\beta_{avV(l)}$, is constant (at least in the Gaussian beam approximation), providing the necessary gain to compensate for the round-trip losses of the resonator. This condition can be fulfilled by different distributions $\beta(r,z)$. Actually, with growing laser signal power, the distribution is distorted compared to its shape at the lasing threshold, which is approximately the shape of the pump beam profile (if pump saturation is small).

---

[1] In appendix A.1., we also use the term “laser quantum efficiency” for the number ratio of laser quants and pump quants, which is given by $T_{OC}/(T_{OC}+\Lambda)$ times the bracket in eq. 3.86.

The variation of $\beta(r,z)$ is illustrated in Fig. 3.5. The inversion is reduced in the central part of the inversion profile.[1] Here the laser signal intensity $I_l(r,z)$ is so strong, that the increase of the effective laser emission rate (extraction rate) is larger than that of the effective pump rate, $dR_l(r,z) > dR_p(r,z)$. This corresponds to a decrease of the spontaneous decay rate and therefore of the inversion, to keep eq. 3.23. At the same time, the inversion is increased in the outer regions of its profile, where $I_l(r,z)$ is weaker and $dR_l(r,z) < dR_p(r,z)$. This increase is larger than the reduction in the center, since, for $\beta_{avV(l)}$, the inversion in the outer regions does not weigh as much, i.e. it does not contribute as much to the gain as the central inversion. As a consequence, the total number of excited ions grows, and so does the spontaneous decay proportional to it; therefore, the differential extraction efficiency $dP_{ex}(L)/dP_a(L)$ is smaller than ν_l/ν_p (see eq. 3.88.).

With increasing pump power, $dP_{ex}(L)/dP_a(L)$ is improved, since increasing laser signal intensities lead to a more efficient extraction (increasing $dR_l(r,z)$) in the outer regions of the inversion profile, which counters the growth of $\beta(r,z)$.[2] Furthermore, the reduction of $\beta(r,z)$ in the center weakens, as $\beta(r,z)$ gets closer to 0; this is in agreement with $\beta_{avV(l)}$ remaining constant.

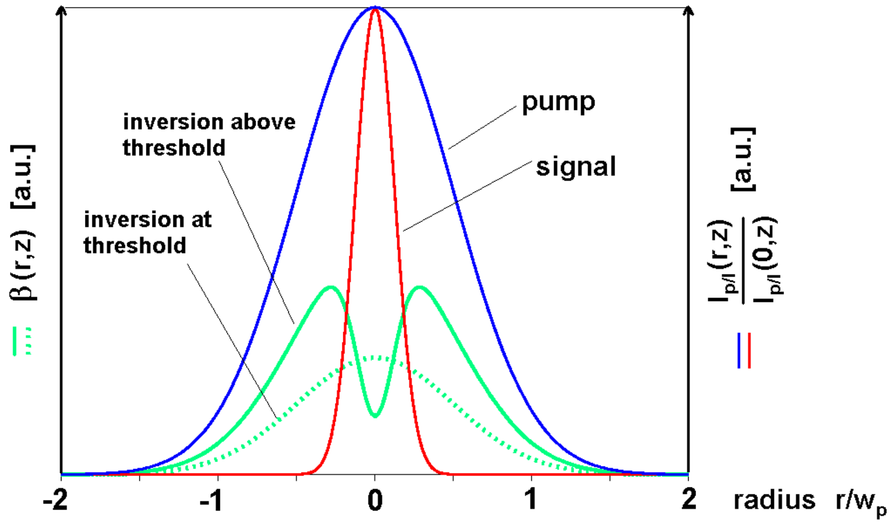

Fig. 3.5. Radial distribution of the inversion parameter $\beta(r,z)$ at the lasing threshold (green dotted curve) and above (green solid curve; example for one arbitrary value of the pump power). Pump and laser signal beam shapes are indicated in blue and red. If the pump beam radius is equal to or smaller than the signal beam radius, $\beta(r,z)$ above threshold will be higher in the wings and lower in the center, too, but there will be no dip.

Reabsorption and the role of the beam radii for the laser efficiency

In a laser material without reabsorption of the laser signal, the distortion of $\beta(r,z)$ is the stronger and the corresponding differential extraction efficiency is the lower, the larger the ratio of pump and laser signal beam radii, w_p/w_l, is. For a given diameter of the laser mode, the differential extraction efficiency (η_{ex} and η_{opt}, as well) can be optimized by minimizing w_p/w_l, i.e. by placing

---

[1] Here and throughout, the pump and laser signal beams are assumed to be concentric.

[2] The pump beam quality is assumed to be constant. For laser diodes this is not valid, usually, which may result in decreasing differential efficiencies with increasing pump power.

the pump power in the intensity maximum of the laser signal mode. This is because excited ions (non-zero $\beta(r,z)$) are only due to the part of the absorbed pump power that cannot be extracted by the laser field.
In case of a quasi-three- or quasi-four-level laser material, however, reabsorption has to be taken into account, as a mechanism which increases $\beta(r,z)$ in those regions where the pump intensity is too weak to provide positive gain. As a result of reabsorption, power that has been extracted in the central part of the laser signal beam is deposited in the outer regions where it cannot be extracted. This reduces the differential extraction efficiency $dP_{ex}(L)/dP_a(L)$.

With increasing pump power, $dP_{ex}(L)/dP_a(L)$ is improved, as $\beta(r,z)$ in the reabsorbing regions is increased, which reduces ("bleaches") reabsorption or even turns it into positive gain. If $\beta(r,z)$ is increased only by the reabsorbed laser signal power (no pump), it can reach maximally the minimum inversion parameter for transparency, $\beta(r,z) = \beta_{min}$. If the pump intensity is >0, higher values of the inversion parameter are possible, $\beta(r,z) > \beta_{min}$, and therefore positive gain can occur in regions that are lossy at lower powers.
For a laser material exhibiting strong reabsorption of the laser signal, i.e. $2NL\sigma_a(\lambda_l) \geq \delta(\lambda_l)$, at high pump and laser signal powers the highest differential extraction efficiency is achieved with perfect overlap of pump and laser signal beam, $w_p = w_l$ [Ris88].

Maximization of the optical-to-optical conversion efficiency η_{opt} has to take into account both, the differential extraction efficiency $dP_{ex}(L)/dP_a(L)$ and the absorbed pump power $P_{a,thr}(L)$ to reach the lasing threshold. Risk [Ris88] has shown by numerical simulations, that the advantage of a minimum value of $P_{a,thr}(L)$, which requires a minimum w_p for a given laser mode diameter w_l (see eq. 3.69.), cannot be made up for by a maximum differential extraction efficiency $dP_{ex}(L)/dP_a(L)$, which in case of large reabsorption losses would be the result of equal radii $w_p = w_l$.
Often, however, a lower limit exists rather for the pump beam radius than for the radius of the laser signal mode. The limit can be given by the increasing beam divergence with decreasing w_p (confocal parameter becomes smaller than L), by the possible geometry of the pump beam focusing optics (lack of space), or by the maximum acceptable heat load per volume. Losses that depend nonlinearly on the pump intensity $I_p(r,z)$ and/or the inversion $\beta(r,z)$ may also become a significant problem.[1]
For a fixed value of w_p the threshold will be lowest for a minimum waist w_l of the laser mode (see eq. 3.69.). Therefore optimization will lead to minimum w_l, if the available pump power is only sufficient to exceed the threshold pump power by just a small amount. At higher pump powers, $w_p > w_l$ becomes unfavorable due to low differential extraction efficiency; optimization will then lead to equal radii.[2]

For his calculations, Risk made simplifications, of which the neglect of pump saturation is an important one.[3] In practice, for an approximately optimum length of the active medium, a beneficial minimization of the ratio w_p/w_l is limited also by pump saturation, since the total optical-to-optical conversion efficiency η_{tot} depends on the absorption efficiency $P_a(L)/P_p(0)$ (see eq. 3.85.). In general, extensive computer simulations are required to determine the optimum length of the active medium with respect to η_{tot}. The length L_{minthr} that minimizes the threshold (see eq. 3.82. for the case $w_p = w_l$) will be favorable only, if little pump power is

---

[1] We describe such losses in append. A.1., but do not consider them in Fig. 3.1.; for a high-quality Yb^{3+} laser material such losses should be negligible.

[2] This is why equal beam radii have to be assumed for our laser experiments in chapter 3.

[3] Risk also assumed that round-trip loss and gain are small, corresponding to a longitudinally almost constant laser signal intensity $I_l(r)$.

available; at pump powers far above the threshold considerably longer active media are necessary, since the transmission of pump radiation must be decreased. A thorough numerical optimization of the optical-to-optical conversion efficiency η_{tot} should include the output coupler transmission T_{OC} as a further variable and must take into account the change of the lasing wavelength λ_l as a consequence of varying losses.

Countering reabsorption by improved pumping

The pump wavelength λ_p is often also an experimental degree of freedom. Generally, a minimum pump absorption length is desired, since this means the active medium can be chosen as short as possible to minimize reabsorption loss for higher efficiency. The strongest absorption is usually observed at the zero-line transition. Other pump wavelengths can be more attractive, however, e.g. because a broad-band pump source does not match a narrow absorption line or because pumping at longer wavelengths reduces the laser quantum defect, therefore improving laser efficiency (see eq. 3.86.) and reducing heat generation.

In such cases or with laser materials exhibiting generally weak pump absorption and/or strong signal reabsorption, one can realize short media and high optical-to-optical conversion efficiencies η_{tot}, if two or more pump passes through the active medium are enabled. Technical solutions for multiple passes exist for noncollinear and linear pumping schemes [Cut91, Erh99, Pav01].[1]

In chapters 5.2.1.4. and 5.2.2. we take profit from resonant pump enhancement like described in [Cut91], while a laser crystal is pumped longitudinally through a cavity mirror that is not fully transparent for the pump. What occurs as a side effect in our experiments, can be cultivated e.g. for microchip lasers. To maximize resonant enhancement, one has to choose the transmission of the incoupling mirror and the total loss of the laser cavity for good impedance matching, pump and oscillator must be mode-matched, and the length of the oscillator cavity must be stabilized.

---

[1] In [Erh99] a thin-disk laser was demonstrated, realizing up to 16 pump passes through a 240-µm-thin Yb:YAG plate by the use of a parabolic mirror and three roof prisms. A radially pumped microchip composite laser, which used a diffuse reflector to achieve almost complete pump absorption in the Yb:YAG core, was investigated theoretically and experimentally in [Das02, Pav01]. In [Cut91], due to resonant enhancement, a 300-µm-thin 1%-doped Nd:YAG crystal absorbed 95% of the 813-nm pump radiation incident on the laser cavity. The short crystal permitted laser operation at 946 nm with a very low lasing threshold.

4. Passive mode locking

In chapter 4.1., the mathematical principles of pulse shaping in passively mode-locked solid-state lasers are given. The differences between solitons, “solitonlike” and other pulses are explained as well as the differences that will result, if pulse shaping effects are weak, moderate or strong. In particular, this concerns the formulas describing pulse durations.

In chapter 4.2., we will have a closer look at the pulse shaping effects involved, especially at passive amplitude modulation as provided by saturable absorbers. Formulas will be deduced to describe saturable absorption in “real-world” lasers, since commonly used formulas cannot be applied in case of Gaussian beams and more than weak saturation of a saturable absorber.

In chapter 4.3., mode-locking stability will be treated.

4.1. Pulse shaping in passively mode-locked solid-state lasers

Mode locking of lasers can be realized by active or passive modulation of gain or loss, or using a combination of such techniques. The modulation must fulfil two conditions: It must be synchronized with the round-trip frequency in the laser cavity, and it must be strong and fast enough, to favor mode-locked laser operation over other kinds of operation (cw or Q-switched lasing).

Active mode locking by an acousto-optic or electro-optic modulator always requires an electronic feedback loop for stable synchronization. The same is necessary for synchronous pumping (using a mode-locked pump laser) and for methods using additional cavities (additive-pulse or coupled cavity mode locking [Hau91, Kel91, Mol84, Nel97, Spi91]), where the lengths of the involved resonators must be matched within less than 1 µm. No such efforts are needed with purely passive techniques, like mode locking by Kerr lens or saturable absorbers (dye or semiconductor absorbers). Here, the pulsed signals modulate themselves, usually by saturating a loss mechanism;[1] therefore modulation frequency and round-trip frequency are identical.

Pulse shaping effects – aspects of polarization

The mechanisms involved in the buildup and shaping of mode-locked pulses are similar for all passively mode-locked lasers: passive amplitude modulation (PAM) by gain and/or loss modulation, group delay dispersion (GDD), gain filtering (plus possible additional filtering), and self-phase modulation (SPM). PAM is always necessary to enable mode locking. GDD, filtering, and SPM become the more important, the shorter the pulses, the larger the spectral bandwidth and the higher the intensities are.

Aside from those effects that are due to spatial dispersion (e.g. GDD and filtering provided by prisms or gratings), all mechanisms mentioned above can be referred to the different aspects of the complex polarization vector $\mathcal{P}$ of materials. Pulse shaping in a mode-locked laser can be described by the wave equation for pulse propagation through a medium, which relates $\mathcal{P}$ to the electrical field strength $\mathcal{E}$,

---

[1] With soft-aperture Kerr lens mode locking, the gain is modulated.

$$\left(\nabla^2 - \frac{1}{c^2}\frac{\partial^2}{\partial t^2}\right)\mathcal{E}(\mathbf{r},t) = \mu_0 \frac{\partial^2}{\partial t^2}\mathcal{P}(\mathbf{r},t) \quad , \tag{4.1.}$$

with $\mu_0 \approx 1.257 \times 10^{-6}$ VsA^{-1}m^{-1}, vacuum permeability.

Equation 4.1. has to be applied successively for all elements of the laser resonator. Without simplifications, however, eq. 4.1. can hardly be solved, in general.

The frequency-dependent real part of $\mathcal{P}$, *Re*($\mathcal{P}$), is responsible for lossless GDD. The imaginary part *Im*($\mathcal{P}$) stands for loss or gain. Furthermore, if *Im*($\mathcal{P}$) depends on the frequency ω, it will cause GDD and filtering. PAM is related to a nonlinear dependency of $\mathcal{P}$ on the electrical field strength $\mathcal{E}$, in case of a saturable absorber to a nonlinearity of *Im*($\mathcal{P}$). SPM corresponds to a nonlinear *Re*($\mathcal{P}$). We may express the polarization with the help of first-order susceptibilities and functions containing higher-order susceptibilities,

$$\mathcal{P} = \varepsilon_0[\chi^{(1)} + j\breve{\chi}^{(1)} + f(\mathcal{E}) + j\breve{f}(\mathcal{E})]\,\mathcal{E} \quad , \tag{4.2.}$$

with $\varepsilon_0 \approx 8.854 \times 10^{-12}$ AsV^{-1}m^{-1}, vacuum permittivity.

In case of a slowly varying electrical field envelope, the polarization can be expressed as

$$\mathcal{P} = \varepsilon_0(n_c^{\,2} - 1)\,\mathcal{E} \quad , \tag{4.3.}$$

with n_c, complex refractive index.

If we assume $Re(n_c^2) >> Im(n_c^2)$ and $\chi^{(1)} >> f(\mathcal{E})$, the real part of n_c is given by

$$n = \mathrm{Re}(n_c) \approx \sqrt{1 + \chi^{(1)} + f(\mathcal{E})} \approx n_0 + \frac{f(\mathcal{E})}{2n_0} \quad , \tag{4.4.}$$

or, if $f(\mathcal{E}) \approx \chi^{(3)}|\mathcal{E}|^2$, by

$$n \approx n_0 + n_2|\mathcal{E}|^2 \quad , \tag{4.5.a}$$

with linear refractive index

$$n_0 \approx \sqrt{1 + \chi^{(1)}} \quad , \tag{4.5.b}$$

nonlinear refractive index

$$n_2 = \frac{\chi^{(3)}}{2n_0} \quad . \tag{4.5.c}$$

The imaginary part of n_c, which contains linear and nonlinear loss and gain, is given by

$$\mathrm{Im}(n_c) \approx \frac{\breve{\chi}^{(1)} + \breve{f}(\mathcal{E})}{2\sqrt{1 + \chi^{(1)} + f(\mathcal{E})}} \approx \frac{\breve{\chi}^{(1)} + \breve{f}(\mathcal{E})}{2n_0} \quad . \tag{4.6.}$$

The slowly varying envelope approximation (SVEA, see e.g. [Rud89]) for the electrical field strength is permitted, if the spectral bandwidth of the pulse is much smaller than its central frequency (or in the time domain: if the pulse duration is much longer than an oscillation period of the electrical field). Assuming a linearly polarized plane wave traveling in *z*-direction, the electrical field $\mathcal{E}(t,z)$ can then be described as the product of a complex slowly varying envelope

$\underline{\mathcal{E}}(t,z)$ and a phase term rapidly oscillating with the central frequency ω_0 (also called carrier frequency) and central wave number $k_0 = k(\omega_0) = \omega_0 n_c(\omega_0)/c$,

$$\mathcal{E}(t,z) = \tfrac{1}{2}\underline{\mathcal{E}}(t,z)\exp(j\{\omega_0 t - k_0 z\}) + \mathrm{c.c.} \quad . \tag{4.7.}$$

The envelope can be expressed as $\underline{\mathcal{E}}(t,z)=|\underline{\mathcal{E}}(t,z)|\ exp(j\phi(t,z))$, where $|\underline{\mathcal{E}}(t,z)|$ is the instantaneous amplitude and $\phi(t,z)$ is the instantaneous phase. The instantaneous frequency is defined as $\omega_i(t,z) = \omega_0+\partial\phi(t,z)/\partial t$ and will vary over the pulse, if the pulse is chirped. “Down-chirp” means $\partial\omega_i(t,z)/\partial t = \partial^2\phi(t,z)/\partial t^2 < 0$ near the pulse-maximum (“blue” frequencies go ahead of the “red”), “up-chirp” means $\partial\omega_i(t,z)/\partial t > 0$. The instantaneous light intensity $I(t,z)$ of the pulse is given by

$$I(t,z) = \tfrac{1}{2} n\varepsilon_0 c|\underline{\mathcal{E}}(t,z)|^2 \quad . \tag{4.8.}$$

Nonlinear Schrödinger equation (NLSE) and solitons

In SVEA, propagation in a homogeneous medium with moderate GVD and SPM action can be approximated by a nonlinear Schrödinger equation (NLSE), which can be deduced from eq. 4.1. (see e.g. [Sal91, Tar98]),

$$\left\{\frac{\partial}{\partial z} + \frac{j}{2}\left.\frac{d^2k(\omega)}{d\omega^2}\right|_{\omega=\omega_0}\frac{\partial^2}{\partial t_r{}^2} - j\gamma\,|\underline{\mathcal{E}}(t_r,z)|^2\right\}\underline{\mathcal{E}}(t_r,z) = 0 \quad , \tag{4.9.}$$

where $d^2k(\omega)/d\omega^2|_{\omega=\omega_0}$ is the GVD coefficient, γ is the SPM coefficient and $t_r = t-z/v_g(\omega_0)$ is the retarded time, i.e. the time in the reference frame moving with the pulse maximum with the group velocity $v_g(\omega_0)$. We will have a closer look at the pulse-shaping quantities later on (equations 4.23.-4.61.).

If a light pulse is launched into the medium, different things corresponding to different solutions of the NLSE may happen, depending on the intensity, prechirp, and shape of the original pulse, on the sign and the value of GVD, and on the strength of SPM in the medium.

In a regime of normal GVD (positive GVD coefficient $d^2k(\omega)/d\omega^2|_{\omega=\omega_0}$), on the long run, the pulse duration will steadily increase, because GVD and SPM both cause up-chirp. In case of an initial down-chirp, however, the pulse is shortened at first.

In a regime of anomalous GVD (negative GVD coefficient $d^2k(\omega)/d\omega^2|_{\omega=\omega_0}$), GVD will dominate and spread the pulse, if the pulse intensity is too low. For sufficiently intensive pulses, the effect of GVD (working towards down-chirp) and that of SPM may balance each other, such that the pulses do not change their properties while traveling, except for a change of phase. These solutions of the NLSE are called fundamental “solitons” or fundamental “solitary waves” (fundamental, i.e. soliton order $N = 1$). Furthermore, there exist higher-order soliton solutions ($N = integer > 1$). These are pulses that have N^2 times the energy of a fundamental soliton with the same pulse duration and that show periodically returning properties, i.e. they split and merge in a periodic evolution pattern. If the envelope of a launched pulse deviates from that of a soliton, it will adapt by shedding excess energy.

The electrical field envelope of a fundamental soliton is given by a hyberbolic secant [Sal91]

$$\mathcal{E}(t_r, z) = \mathcal{E}_0 \,\mathrm{sech}\left(\frac{t_r}{\tau}\right)\exp(j\phi) \quad (4.10.)$$,

with τ, pulse duration parameter for a *sech*-shaped pulse;
$\mathcal{E}_0$, peak value of the electrical field strength for the fundamental soliton;
$\phi = \phi_0 + \frac{1}{2}\{z/\tau^2\}\,\{d^2k(\omega)/d\omega^2|_{\omega=\omega_0}\}$, phase ($\phi_0$, value at $z = 0$).

The pulse duration parameter is related to the field amplitude by

$$\mathcal{E}_0\tau = \sqrt{\frac{1}{\gamma}\left|\frac{d^2}{d\omega^2}k(\omega)\right|_{\omega=\omega_0}} \quad (4.11.)$$.

Temporal and spatial integration shows that the pulse duration is inversely proportional to the pulse energy,

$$\tau = \varepsilon_0 c\, n \frac{\mathcal{A}_{eff}}{\gamma E_p}\left|\frac{d^2}{d\omega^2}k(\omega)\right|_{\omega=\omega_0} \quad (4.12.)$$,

with $E_p = \tau\varepsilon_0 c\, n\mathcal{A}_{eff}\mathcal{E}_0^2$, pulse energy;
$\mathcal{A}_{eff}$, effective beam area (for a plane wave: the actual beam area).

The FWHM pulse duration τ_p (with respect to intensity) is given by

$$\tau_p = 2\ln(1+\sqrt{2})\,\tau \approx 1.763\tau \quad (4.13.)$$.

The FWHM spectral bandwidth $\Delta\nu_p = \Delta\omega_p/(2\pi)$ (with respect to intensity) is given by

$$\Delta\nu_p = \frac{2}{\pi^2}\ln(1+\sqrt{2})\frac{1}{\tau} \approx \frac{1.122}{\tau} \quad (4.14.)$$.

Modifications of the NLSE, master equations

While the NLSE (eq. 4.9.) is the central equation for signal transmission in homogeneous loss- and gainless fibers, a mode-locked laser oscillator exhibits several differences compared to the case of the NLSE. These result in modifications of the NLSE and lead to master equations describing pulse shaping in ultrashort-pulse lasers:

I.) Gain and loss, including PAM and spectral filtering, must be taken into account. An according modification of the NLSE leads to a **complex Ginzburg-Landau equation** (CGLE; see e.g. [Tar98]).[1]

II.) Due to the **closed cycle in the resonator**, the system must evolve into a **steady or quasi-steady state**, where the pulse-shaping effects for a round trip balance each other and the signal is reproduced after each round trip. By this requirement, a master equation for the mode-locked laser can be obtained [Hau75, Hau91] (deduction from the CGLE, [Tar98]). Solutions of the master equation describe pulsed or cw operation, depending on the boundary conditions.

---

[1] The CGLE describes fiber amplifiers, too.

III.) In a bulk laser, there are **separate pulse-shaping elements** instead of one homogeneous medium.[1] In case of weak pulse shaping (WPS), calculations can be performed using the appropriate master equation with longitudinally averaged or integrated quantities describing the pulse-shaping effects occuring during a round trip.[2] Integration means e.g. that the GVD coefficient is replaced by the group delay dispersion $D = d^2\phi(\omega)/d\omega^2|_{\omega=\omega_0} = L_D\, d^2k(\omega)/d\omega^2|_{\omega=\omega_0}$, with L_D, effective length of dispersive element. The interdependence of the effects and therefore the temporal and spatial order of their action is neglected.

For ultrashort pulses in the 100-fs region, WPS is usually not a valid assumption. It makes a difference e.g. wether GVD effects the pulse before, after, or simultaneously to SPM. A chirped and therefore less intensive pulse will experience less SPM traversing a Kerr medium compared to a spectrally and energetically identical pulse without chirp.

An appropriate description is to use non-commuting operators O_i, each representing a pulse-shaping effect of an element in the resonator (for pulse-shaping effects, see eqs. 4.23.-4.61.). This results in a position-dependent transfer operator $O_{transfer}(z)$, which can be expressed by [Kra92]

$$O_{\text{transfer}}(z) = \exp\left\{ \sum_i O_i + \sum_{i,j} c_{ij}(z)\left[O_i, O_j\right] + \sum_{i,j,k} c_{ijk}(z)\left[O_i,\left[O_i, O_i\right]\right] + \ldots \right\}, \tag{4.15.}$$

and the master equation takes on the form

$$\underline{\mathcal{E}}_{n+1}(t_r, z) = O_{\text{transfer}}(z)\,\underline{\mathcal{E}}_n(t_r, z) = \underline{\mathcal{E}}_n(t_r, z)\exp(j\psi), \tag{4.16.}$$

with $\underline{\mathcal{E}}_n$ and $\underline{\mathcal{E}}_{n+1}$, electrical field envelope after n and $n+1$ round trips.
$\psi = \psi(T)$, phase shift, slowly varying on the time scale of the round-trip period T_R (T, slow time coordinate).

WPS approximation means, all commutators and double commutators in eq. 4.15. can be neglected and the exponential function can be approximated by 1 plus the exponent. Then, eq. 4.16. becomes equivalent to a master equation similar to that in [Hau91, Tar98].

As long as pulse shaping is still moderate, it is not necessary to explicitly consider the variation of pulse shaping within an element, i.e. one may still operate with $O_i = C\,L_i$ (L_i, length of element; C, constant or average). Simultaneous occurance of strong pulse-shaping effects requires a numerical approach, where pulse propagation is split into steps, such that within each step the changes to the pulse are small enough to treat the effects independently.[3]

---

[1] A similar situation in fiber communication is that of dispersion-managed systems [Tur03].

[2] WPS can be assumed, if during a round trip a pulse experiences only little changes with respect to its energy, spectrum, duration, and shape. As a rule of thumb, 20% modification upon one passage through any one of the components of the laser system are acceptable [Hau75].

[3] Fortunately, in most cases of ultrashort pulse lasers, not all elements produce strong pulse-shaping effects; this simplifies calculations. For example, PAM of a saturable absorber is weak and the belonging operator can be commuted with any other operator, usually. A more difficult situation is that of SPM and simultaneous spectral filtering, which is likely to occur, if broadband laser materials are exploited for shortest pulses.

Solitonlike and other pulses

In general, the deviations from the case of NLSE do not permit “true” soliton solutions in a mathematical sense. “True” solitons will scatter elastically, if they collide; this condition is not fulfilled any more. Furthermore, in contrast to the fundamental soliton as described by eq. 4.10., pulsed solutions may exhibit considerable chirp, and the pulse parameters (duration, chirp, spectrum, and possibly also energy) may vary substantially along the round-trip path; the pulse does not necessarily show a *sech*-shaped field envelope.

However, the term “soliton” is often applied less strictly or replaced by “solitary waves” or “soliton-like pulses”, if pulses are considered where group delay dispersion and SPM are the dominant pulse-shaping mechanisms and where these balance each other.[1]

In the following, the modifications of the NLSE and its physical consequences are inspected more closely:

I.) Consequences of gain and loss

The complex Ginzburg-Landau equation (CGLE), which includes spectral filtering (by the limited bandwidth of the gain medium, i.e. gain dispersion) and passive amplitude modulation (PAM), can be solved by

$$\underline{\mathcal{E}}(t_r, z) = \underline{\mathcal{E}}_0 \left[\mathrm{sech}\left(\frac{t_r}{\tau} \right) \right]^{1+j\mathscr{b}} \exp(j\theta) , \tag{4.17.}$$

with $\mathscr{b}$, chirp parameter;
$\theta = \theta(z)$, phase shift.

From eq. 4.17. we see, compared to the fundamental soliton of the NLSE (eq. 4.10.), the pulse shape is not modified (still *sech*), but a chirp is introduced. In general, the chirp parameter $\mathscr{b}$ and the pulse duration parameter $\tau \approx \tau_p/1.763$ depend on all pulse-shaping effects present in a laser resonator (GDD, gain and other filter dispersion, SPM, and PAM). Therefore, the functional dependencies of $\mathscr{b}$ and τ have to be determined individually for the laser considered, since gain dispersion is specific for the laser material, and the dynamical behavior of saturable absorbers differs. Furthermore, in case of a Gaussian beam profile and more than weak saturation, PAM will show a relatively complicated intensity-dependence (see eqs. 4.25.-4.39.). Finally, for a bulk laser, the master-equation approach based on the CGLE using averaged or integrated quantities is valid only as long as pulse shaping is weak.

For a laser system with weak pulse shaping, weakly saturated fast saturable absorber, and parabolic gain spectrum, the chirp and the pulse duration are as given in [Hau91] (p.2070) or [Tar98] (p.109). The product of duration τ_p and spectral bandwidth $\Delta\nu_p$ (FWHM with respect to intensity) of the pulse is related to the chirp parameter by

$$\tau_p \Delta\nu_p = \frac{4}{\pi^2} \left[\ln\left(1+\sqrt{2}\right) \right]^2 \sqrt{1+\mathscr{b}^2} \approx 0.315 \sqrt{1+\mathscr{b}^2} . \tag{4.18.}$$

---

[1] Definition of a “solitary system” as given in [Kra92] for systems with weak to moderate pulse shaping: negative round-trip GDD; PAM weak compared to SPM.

If GVD and SPM are the dominant pulse-shaping mechanisms, the chirp will be small and there is little difference of the CGLE from the NLSE. This is the situation in a regime of "solitonlike" or "solitary" pulses [Hau91, Kra92]. Therefore, for these pulses a time-bandwidth product close to 0.315 (Fourier limit) can be found and, in good approximation, the pulse duration is given by eqs. 4.12. and 4.13.

The spectral shape of an unchirped pulse with hyperbolic-secant-shaped electrical field envelope (i.e. *sech*^{2}-shaped intensity) is also *sech* or *sech*^{2} with respect to field envelope or intensity, respectively. Chirp may result in a strong deviation from such a spectrum, which is obvious e.g. for the Yb^{3+}:Sc_2O_3 laser presented in chapter 6.2.1. If this laser is operated in the regime of positive round-trip GDD D (i.e. "non-solitary" pulse shaping, found without dispersion-compensating prisms), the spectrum becomes almost rectangular, while the field envelope is still *sech*-shaped (see e.g. Fig. 6.5.). In the WPS case, with weakly saturated absorber (saturation behavior obeying eqs. 4.27.b or 4.39.b) and approximately parabolic gain spectrum as in [Hau91, Tar98], eq. 4.17. is valid for all mode-locked pulses, "solitonlike" or not.[1] A hyberbolic secant field envelope will be obtained, also if GDD and SPM can be neglected [Hau75, Hau91, see also Kae98, Sch00]; in this case, the pulses are not even chirped, since the CGLE is reduced to a NLSE, where gain dispersion and PAM take over the roles of GDD and SPM.

II.) Consequences of optical resonator

While a fiber communication system is permanently fed with pulses, a passively mode-locked laser resonator is not. Instead, ultrashort pulses evolve (or do not evolve) as a regular, persistent temporal pattern from chaotic noise in stimulated emission (i.e. self-starting mode locking) or are maintained after seeding the system with a pulse pattern (active initiation). Furthermore, the pulses exist only due to the spectral modes supported by the resonator and the gain medium.[2] If no mode-locked pulses emerge, this will be a consequence of the boundary conditions provided for the evolution of a signal; then, cw radiation will be obtained, or possibly Q-switched pulses, if slow gain or loss dynamics are involved.

The necessary condition for persistent pulsed operation is that it is favorable to cw or different pulsed operation, due to higher gain and/or lower loss. Self-starting of mode locking requires that this advantage exists already for a mode-beating fluctuation occuring in the early stage of pulse build-up. Issues of self-starting mode locking and/or active initiation of pulse formation are treated e.g. in [Kra91, Kra92, Spi91].

III.) Consequences of separation of pulse-shaping effects

Compared to propagation in a homogeneous medium, the lumped structure of a bulk-laser has a consequence whose importance increases with the strength of the pulse-shaping effects: In general, the properties of a pulse are not constant during a round trip; spectrum and duration are "breathing", the chirp is varying. The pulse being a "stationary" solution means that the pulse properties are restored after a round trip (aside from a phase shift).

---

[1] Actually, there is no sharp distinction between "solitary" and "not solitary"; all pulse properties are described by continuous functions (see Fig. 3 in [Hau91]).

If PAM is strong and the saturation behavior deviates substantially from eqs. 4.27.b or 4.39.b, respectively, or if gain dispersion is dominant and the gain spectrum has a nontrivial shape, we may excpect deviations from a secant hyperbolic field envelope.

[2] Dispersive effects detune the resonator modes, however.

For WPS, the electrical field envelope obeys eq. 4.17.; and in case of solitonlike pulses, the temporal shape becomes approximately that of a “true” soliton as described by eq. 4.10., with the pulse duration given by eqs. 4.12. and 4.13.[1] However, the stronger the pulse-shaping effects are, the more substantial are the differences observed between a solitonlike pulse and a true soliton. For non-solitary pulses, also, the pulse properties show increasing deviations from those obtained by the formulas given for WPS e.g. in [Hau91, Tar98].

If pulse-shaping effects are still moderate, distortion of the pulse shape is small (we still find a hyperbolic secant field envelope), but the pulse properties including the pulse duration are modified. Krausz et al. did numerical calculations for a linear cavity containing (as separate effects on the longitudinal axis) a dispersive delay line, an amplitude modulator (including the action of the gain medium), and a Kerr nonlinearity [Bra91, Bra92, Kra92]. They found, the duration τ_p of a solitary pulse (FWHM with respect to intensity) can be estimated by

$$\tau_p = 2\ln(1+\sqrt{2})\frac{2|D|}{\Gamma E_p} + a(z)\Gamma E_p \quad ,^{2} \qquad (4.19.)$$

with E_p, pulse energy,

D, round-trip GDD, given by (see also eqs. 4.40.-4.56.)

$$D = D_m + D_{comp} + jD_g + jD_f \quad , \qquad (4.20.)$$

where $Re(D)$ has a negative sign; D_m stands for material dispersion contributed by the elements in the resonator (usually normal dispersion, i.e. with positive sign, if our definitions are used), D_{comp} for dispersion by prisms, gratings, chirped mirrors, or other elements introduced to provide negative GDD for dispersion compensation, D_g for gain dispersion due to limited bandwidth of the gain material, D_f for possible filter dispersion; elements traversed twice in a round trip count twice;

Γ, round-trip nonlinear phase shift per power, which in case of a single nonlinear element is given by

$$\Gamma = \frac{2\gamma L_{SPM,tot}}{\varepsilon_0 c\, n_0 \mathcal{A}_{eff}} = \frac{\underline{n}_2 \omega_0 L_{SPM,tot}}{c\, \mathcal{A}_{eff}} \quad , \qquad (4.21.)$$

where $L_{SPM,tot}$ is twice the length of the nonlinear element, as the medium is traversed twice in a round trip; $\underline{n}_2$, ω_0, c, and $\mathcal{A}_{eff}$ are the nonlinear refractive index (referring to intensity), the carrier frequency, light velocity in vacuum, and effective beam area, respectively;

$a(z)$, coefficient, which depends on the position inside of the resonator ($a \approx 0.1$ at the “dispersive end” [Bra91, Bra92, Kra92].)

(More details about the pulse-shaping effects are given in the following passages.)

---

[1] For the description of the solitonlike laser system in WPS approximation, $\gamma/\mathcal{A}_{eff}$ and $d^2k(\omega)/d\omega^2|_{\omega=\omega_0}$ have to be replaced in eq. 4.12. by quantities obtained by averaging or integration over one round trip.

[2] Please note, we use the definition of the round-trip GDD D and its components as in [Bra91, Bra92, Kra92] (see eqs. 4.40.-4.56.). In some literature, D can also be found being defined with an additional factor ½.

The first term of eq. 4.19. is equivalent to the pulse duration of a soliton or a solitonlike pulse obtained for WPS (eqs. 4.12. and 4.13.). The second term is a correction due to stronger pulse shaping; it can be neglected, if ΓE_p is small (i.e. WPS). The minimum value of the coefficient, $a \approx 0.1$, is found at the dispersive end of the resonator and corresponds to the minimum pulse duration; $a \approx 0.25$ is obtained at the other end [Bra91, Bra92, Kra92].[1] Krausz et al. state that eq. 4.19. with the given values of a are a good approximation, if PAM is small compared to SPM (PAM depth per power < 0.2Γ), the contribution of gain dispersion to the total GDD is still moderate ($D_g < 0.35|D|$), and

$$\frac{1}{2\pi}\frac{(\Gamma E_p)^2}{|D|} < 10 \qquad (4.22.)$$

.[2]

In case of strong pulse shaping, not only the properties of mode-locked pulses are modified, but the pulse shape will also deviate from a hyperbolic secant. If compression and stretching experienced by the pulses during a round trip are increased, the envelope of a solitonlike pulse will approach a Gaussian shape and then become increasingly more flat topped [Che99].[3] Furthermore, it is possible to obtain solitonlike pulses in a regime of zero or slightly positive round-trip GDD, while usually the necessary balance of SPM and GDD can be achieved only in a regime of negative round-trip GDD.[4] The reason is that negative GDD may have a larger effect at one position than positive GDD at another (we remember the non-commuting operators in eq. 4.16.).

Shedding of radiation

Since the solitonlike pulse is not a true soliton, it sheds radiation, while it is passing through the elements in the resonator. (It tries to become a soliton in the respective medium.) The shedding is the stronger, the stronger the pulse shaping is and the more discrete the shaping effects are. However, it will be important in a laser oscillator, only if the contributions of this radiation from each round trip are in phase and if the shedded radiation experiences gain (e.g. in the aftermath of saturable absorber action), so that it may claim a large part of the pump power and even supersede mode locking.

4.2. Pulse-shaping effects in detail

If mode locking is described by models assuming plane waves, in many cases quantitive predictions will become inaccurate, since in a bulk laser the signal beam usually exhibits a Gaussian transversal intensity profile. For strong pulse shaping, transversal dependencies must be considered explicitly. In case of strong SPM, Kerr lensing must not be neglected; for a

---

[1] In case of our lasers, Figs. 5.3. and 6.1., the dispersive end is the output coupler position, where the resonator arm containing the compensation prisms terminates. The saturable absorber is placed at the end of the oscillator.

[2] For WPS, this ratio would be <<1.

[3] Chen et al. call this regime of mode locking “dispersion-managed”, borrowing a term from fiber communication technology, where alternating fiber sections are employed for compression and stretching of the solitonlike signal pulses, which reduces noise.

[4] “Positive” and “negative” refer to the definitions used in this chapter.

saturable absorber with large modulation depth or for a high-gain medium, guiding by loss or gain must be taken into account.

As long as pulse shaping is weak, however, it will often be sufficient to use transversally averaged quantities, e.g. for SPM or for PAM by a saturable absorber. The reason is that the beam profile is not affected to first order (see eqs. 133-137 in [Tar98]). Averaging must take into account the intensity profile. If the absorption of a more than weakly saturated saturable absorber is weighted with a Gaussian profile, the saturation behavior does not obey a simple law any more. The equations presented here should be used, whenever PAM is the dominant pulse-shaping mechanism or if questions of mode-locking stability are concerned.

We will deal with the different contributions to the round-trip GDD. For many mode-locked lasers, it is important to consider gain dispersion, also in case of solitonlike pulse shaping.

Passive amplitude modulation (PAM) by gain modulation

In case of laser media with a long upper-state lifetime τ_f, temporal variations of the pump and signal intensities occuring on a short time scale, i.e. on or below that of the cavity round-trip time $T_r << \tau_f$, usually lead to very small variations of the excited-state population density. Therefore, for most mode-locked solid state lasers, including Yb^{3+}-based ones,[1] short-term gain dynamics can be neglected due to small modulation depths; in particular, these dynamics are not able to maintain mode-locking. In steady state, “gain equals loss” is a good assumption, where loss includes linear, saturable, and filtering loss. With respect to gain, a stably mode-locked solid state laser is (aside from gain dispersion) equivalent to a cw laser (see chapt. 3.3. for laser equations) whose cw power is equal to the temporally averaged mode-locked power. Long-term gain dynamics will exist, however, if the laser is not in steady state, and they also describe the occurance of Q-switched pulses.

To estimate the depth of gain modulation during mode locking and thus validate the above statements, let us assume the case of a typical Yb^{3+}-activated laser with upper-state lifetime $\tau_f = 1$ ms, resonator length $L_R = cT_R/2 = 1.5$ m, for operation $x = 10$ times above the lasing threshold power.

Energy extraction by a single mode-locked pulse changes the inversion parameter $\beta_{avV(l)}$ (for definition see eq. 3.62.) by

$$\Delta\beta_{avV(l)} = x\,\Delta\beta_{avV(l),f} = x\,\frac{\beta_{avV(l)}T_R}{\tau_f}\,,^{2} \qquad (4.23.)$$

where $\Delta\beta_{avV(l),f}$ stands for the change of inversion equivalent to the energy that is pumped into the gain medium within the round-trip period T_R at the lasing threshold; this energy equals the energy lost by fluorescence within T_R.

In our example, $\Delta\beta_{avV(l)}/\beta_{avV(l)} \approx 1/10000$. The change of gain, ΔG, caused by $\Delta\beta_{avV(l)}$ is practically negligible, since

---

[1] Ti:sapphire with τ_f=3.2 µs is an exception.

[2] The index “avV(l)” denotes the averaging over the region of the gain medium filled by the laser mode, see chapter 3.2.2.

$$\Delta G \approx \frac{\Delta\beta_{avV(I)}}{\beta_{avV(I)}} G(\beta_{avV(I)}) << G(\beta_{avV(I)}) \quad (4.24.)$$

Thus it is obvious, that a single signal pulse does not extract enough energy to substantially affect the gain experienced by the pulse itself or by noise following close by. Therefore, gain modulation does not play a role for the onset of mode-locking instabilities; however, it may have some influence on the temporal spacing of multiple pulses, if such a regime of mode locking occurs. It is also clear, that for solid-state lasers, in contrast to dye lasers, synchronous pumping is not capable of significant pulseshortening or to maintain stable mode-locked operation. However, gain modulation may be used to initiate mode locking, if other mechanisms are present, which shape an initial fluctuation into a short pulse and stabilize it.

Passive amplitude modulation (PAM) by loss modulation

Amplitude modulation via loss, as provided by saturable absorbers, can be sufficiently strong to start and stabilize mode locking of solid-state lasers. As a necessary condition, the decrease q_0-q_p of saturable absorption by mode locking must be larger than the increase of filtering losses. Suitable absorbers (usually dyes or semiconductors) must exhibit relaxation times τ_a much shorter than the cavity round-trip time, $\tau_a << T_R$. If the relaxation time is much shorter than the mode-locked pulse duration, $\tau_a << \tau_p$, the absorber will be called a “fast” one; if $\tau_a >> \tau_p$, the absorber will be of the “slow” kind.[1]

For the following equations, we will use t as a fast time parameter, $(0 \le t < T_R)$,[2] and sometimes T as a slow time parameter, $(T > T_R)$, to describe short-term and long-term dynamics, respectively. Nonsaturable loss of the absorber is set to zero throughout; it may be included in the linear loss of the laser cavity.

Fast absorber – basic equations, calculations

The saturation of a fast absorber can be expressed by equations analog to those used for the absorption of pump radiation by a cw-laser medium (see chapter 3.3.2.), with the signal now playing the part of the “pump” (in the absence of “signal”). Equations 3.39. and 3.40. give a simple saturation law with respect to the “pump” intensity. In general, this intensity varies radially. Therefore, a saturation law containing the light power, which describes the absorption coefficient $q(P)$ experienced by the whole beam, will look different, unless plane waves are assumed. For arbitrary beam profiles, $q(P)$ will have to be calculated by numerical integration, as we have done for Fig. 4.1. for a Gaussian signal beam, whose power is given by $P = P(t,T)$ (we do not consider a longitudinal dependence).[3] Actually, for a Gaussian beam profile there exists an analytical solution (see eq. 3.70.); thus, we can obtain the same result by using

---

[1] Most often, saturable absorbers are just “quite fast” ($\tau_a < \tau_p$) or “quite slow” ($\tau_a > \tau_p$). Furthermore, there may be a bitemporal relaxation behavior. As another simplification, we will neglect a possible wavelength-dependence of absorption, which might limit the effect of PAM for very short pulses.

[2] Actually, t is a retarded time, i.e. time is considered in the system moving with the pulse.

[3] This assumption will not be justified for a large value of $q(P)\cdot L_a$, (with L_a, path length in the absorber,) if the absorption varies substantially over the radius of the beam due to varying saturation. In this case, an incoming Gaussian beam will not maintain its radial intensity profile while passing through the absorber.

$$q(T,t) = q_0 \frac{P_{a,sat}}{2.5129\,P(T,t)} \ln\left(1 + \frac{2.5129\,P(T,t)}{P_{a,sat}}\right) \qquad (4.25.)$$
,

with q_0, unsaturated (saturable) absorption coefficient of the absorber,
$P_{a,sat}$, (cw) saturation power of the absorber.[1]

The saturation power, which corresponds to the power reducing the absorption coefficient from q_0 to $q_0/2$, is given by

$$P_{a,sat} \approx 2.5129 \frac{\pi w_a^2}{2} I_{a,sat} \qquad (4.26.)$$
,

with w_a, beam radius of the Gaussian beam on the absorber,
$I_{a,sat}$, (cw) saturation intensity of the absorber.

Figure 4.1. illustrates, that in general, $q(P)$ cannot be described by a simple saturation formula. In the region of small to moderate signal powers P, however, the numerically calculated values of the absorption coefficient $q(t,T) = q(P(t,T))$ can be approximated by

$$q(T,t) \approx \frac{q_0}{1 + \frac{P(T,t)}{P_{a,sat}}} \qquad (4.27.a)$$
.

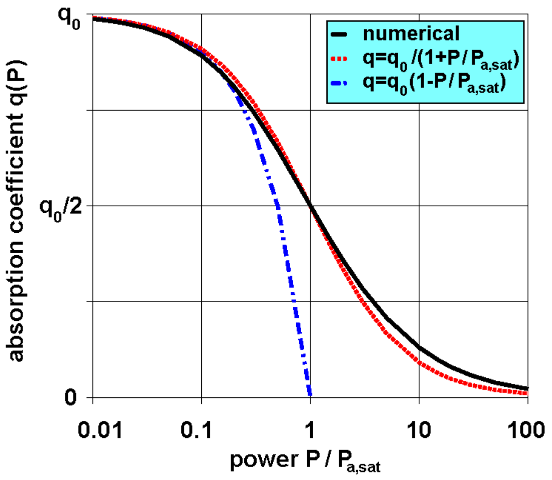

Fig. 4.1. Saturation of a fast absorber with increasing signal power *P* of a Gaussian beam. The absorption coefficient *q(P)* was calculated numerically (black solid line; eq. 4.25. leads to an identical result). The unsaturated absorption is given by q_0, unsaturable absorption was neglected. For low to moderate powers, *q(P)* can be approximated by a saturation law (red dotted line), which is similar to that describing the intensity-dependence of the absorption coefficient. The saturation power $P_{a,sat}$, such that $q(P_{a,sat}) = q_0/2$, is given by $P_{a,sat} \approx 2.51286(\pi/2)w_a^2 I_{a,sat}$, ($I_{a,sat}$, cw saturation intensity; w_a, beam radius). For low powers, one may also use a linear approximation (blue dash-dotted line).

---

[1] Please note, *P(T,t)* in eq. 4.25. has to be multiplied by a *factor* > 1, if forward and backward beams show temporal overlap in a saturable absorber that is used as an absorber mirror with highly reflective backside coating (*factor* ≈ 2, if the absorber thickness is much smaller than the longitudinal extension of the pulse).

If $P(T,t) << P_{a,sat}$, the absorption coefficient can also be approximated by the linear relationship

$$q(T,t) \approx \left(1 - \frac{P(T,t)}{P_{a,sat}}\right) q_0 \quad .^{1} \qquad (4.27.b)$$

For the fast absorber, the absorption coefficient $q(t,T) = q(P(t,T))$ deviates from its unsaturated value q_0 basically only while the signal pulse passes through, as shown in Figs. 4.2.a) and b), which present numerical results for the case of a $sech^2$-shaped pulse ($P(t) = P(0)\cdot sech^2(t/\tau)$).

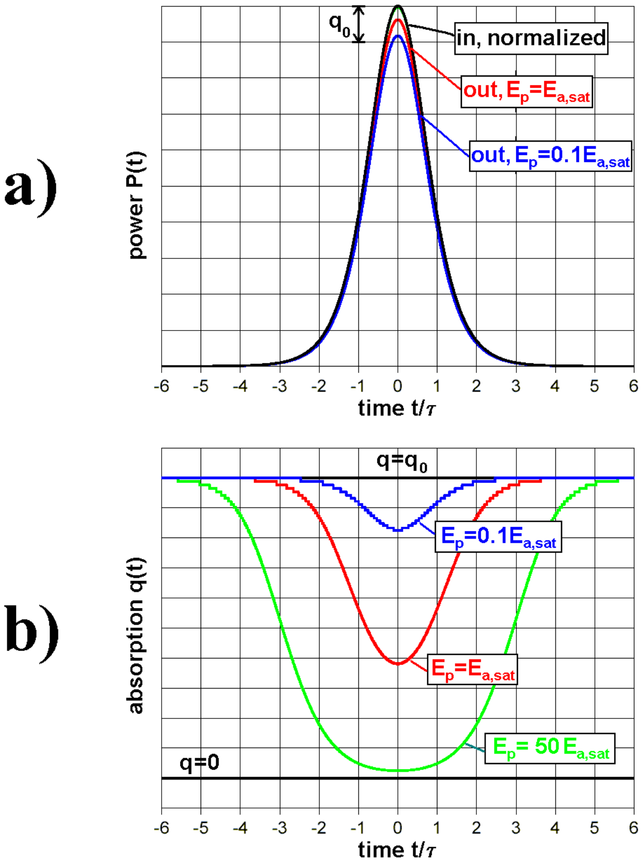

Fig. 4.2. a) Power *P(t)* of a signal pulse before and after passing through a fast saturable absorber. Black curve: incident pulse. Red: outgoing pulse, for energy equal to saturation energy, $E_p = E_{a,sat}$; blue: for $E_p = 0.1\ E_{a,sat}$. The temporal shape of the incoming signal is $sech^2(t/\tau)$ (FWHM $\tau_p \approx 1.763\ \tau$), the beam profile is Gaussian. The outgoing signal pulse is slightly shorter than the incoming, due to absorption being larger in the wings. The arrow indicates the difference at peak amplitude in the small-signal case ($q(t) = q_0$). The unsaturated loss has been chosen as $q_0\cdot L_a = 0.1$ (L_a, path length through absorber; unsaturable loss and the decrease of power within the absorber have been neglected).

b) Absorption coefficient as a function of time, while the pulse from a) passes through a fast saturable absorber, for different incident pulse energies: $E_p = 0.1\ E_{a,sat}$ (blue), $E_p = E_{a,sat}$ (red), and $E_p = 50\ E_{a,sat}$ (green).

---

[1] In mode-locking theory with fast absorbers, this relationship is usually assumed (see e.g. [Hau75, Hau91]). If working close to $P(T,t) = 0$, for more exact results one should use $\pi w_a^2 I_{a,sat} \approx P_{a,sat}/1.2564$ instead of $P_{a,sat}$ (analog case in eq. 4.39.b); then, however, deviations are larger in regimes of moderate absorption.

Since absorption is stronger in the wings of the pulse, the pulse duration is reduced, which is essential to start mode locking from a fluctuation (mode-beating spike) occuring during cw operation. Reduction becomes strongest for pulse energies in the vicinity of the saturation energy, where the contrast of $q(t)$ in the wings to $q(t)$ in the center is maximum (see Fig. 4.2.b)). Noise, which might destabilize mode locking, is suppressed by the almost fully unsaturated absorption q_0, unless it grows close to the signal pulse.

In case of a $sech^2$-shaped signal pulse and a Gaussian beam profile, the saturation pulse-energy $E_{a,sat}$, which reduces the temporally averaged absorption coefficient for the pulse from q_0 to $q_0/2$, is given by

$$E_{a,sat} = 2\tau_p P_{a,sat} \text{ ,}^{1} \tag{4.28.}$$

with $\tau_p \approx 1.763\ \tau$, pulse duration (FWHM),
$P_{a,sat}$, saturation power given by eq. 4.26.

Slow absorber – basic equations

The absorption coefficient $q(t)$ of a slow saturable absorber, experienced by a signal beam with an arbitrary radial intensity distribution $I(r,t)$, is related to the excited state population density $N_2(r,t)$ (and therefore to the absorbed energy at time t) by

$$q(t) = \frac{\int_0^\infty r dr \left[q_0 - N_2(r,t)(\sigma_a + \sigma_e)\right] I(r,t)}{\int_0^\infty r dr\, I(r,t)} \text{ ,} \tag{4.29.}$$

with σ_a, σ_e, absorption and emission cross sections of the saturable absorber at the signal wavelength (for some materials: $\sigma_e = 0$),
$q_0 = N\sigma_a$, unsaturated absorption coefficient,
N, total density of states involved.

The excited state population density $N_2(r,t)$ obeys to a rate equation analog to that for the excited states in a laser medium (eq. 3.21., with the signal now playing the part of the “pump” and $R_l(t) = 0$):

$$\frac{dN_2(r,t)}{dt} = q_0 \frac{I(r,t)}{h\nu} - N_2(r,t)\left\{(\sigma_a + \sigma_e)\frac{I(r,t)}{h\nu} + \frac{1}{\tau_a}\right\} . \tag{4.30.}$$

During a signal pulse with a duration $\tau_p >> \tau_a$, the relaxation term $1/\tau_a$ can be neglected.

Using a Gaussian beam and a non-trivial temporal shape of $I(r,t)$, calculation of $q(t)$ will require a numerical approach. However, we may assume a rectangular pulse shape, to calculate the temporally averaged absorption coefficient $q_p(E_p)$ and the minimum $q_{fin}(E_p)$ of the coefficient

---

1 Please note, a longitudinal dependence of the signal power and, if necessary, of the intensity distribution has to be considered, if the total absorption $q \cdot L_a$ is large.

("final absorption coefficient"), which is found just after the pulse has passed through the absorber (before relaxation must be considered). These quantities do not depend on the pulse shape, but only on the pulse energy E_p. The rectangular pulse is described by

$$I(r) = I(0)\exp\left(-\frac{2r^2}{w_a^{\ 2}}\right) \qquad \text{for } 0 < t < t_{\mathrm{fin}},$$

$$E_p = \frac{\pi w_a^{\ 2}}{2} I(0)\, t_{\mathrm{fin}} \ ,$$

where t_{fin} is the time marking the end of the pulse.

Then, the differential eq. 4.30. can be solved by

$$N_2(r,t) = \frac{q_0}{\sigma_a + \sigma_e}\left\{1 - \exp\left(-(\sigma_a + \sigma_e)\frac{I(r)}{h\nu}t\right)\right\} .$$

Using this in eq. 4.29. to determine the radially averaged absorption coefficient, we obtain

$$q(t) = q_0 \frac{h\nu}{(\sigma_a + \sigma_e)I(0)t}\left\{1 - \exp\left(-(\sigma_a + \sigma_e)\frac{I(0)}{h\nu}t\right)\right\} .$$

We can now express $q(t = t_{fin})$ using the pulse energy E_p and the saturation energy $E_{a,sat}$ (see eq. 4.28.) and obtain the "final" absorption coefficient $q_{fin}(E_p)$ (q just after the pulse; "final", unless relaxation is considered). The resulting relationship is valid for any mode-locked laser with a Gaussian beam profile, independently from the pulse shape, as long as the pulse duration is much shorter than the absorber relaxation time τ_a:

$$q_{\mathrm{fin}}(E_p) \approx q_0 \frac{E_{a,sat}}{3.8696\, E_p}\left\{1 - \exp\left(-\frac{3.8696\, E_p}{E_{a,sat}}\right)\right\} . \tag{4.31.}$$

In case of $E_p = E_{a,sat}$, the value of q_{fin} is given by

$$q_{\mathrm{fin}}(E_{a,sat}) \approx 0.2530\, q_0 . \tag{4.32.}$$

After a pulse ($t >> \tau_p$; $I(r,t) = 0$ in eq. 4.30.), the absorber recovers with the relaxation time τ_a, according to

$$q(t) = q_0 - \left(q_0 - q_{\mathrm{fin}}(E_p)\right)\exp\left(-\frac{t}{\tau_a}\right) . \tag{4.33.}$$

With the solution for $q(t)$ during a rectangular pulse and the help of [Bro91, integral no.451], the temporally averaged absorption coefficient q_p for such a pulse is obtained as

$$q_p = \frac{1}{t_{fin}} \int_0^{t_{fin}} dt\, q(t) = q_0 \sum_{i=1}^{\infty} \frac{1}{i \cdot i!} \left[-(\sigma_a + \sigma_e) \frac{I(0)}{h\nu} t_{fin} \right]^{i-1} .$$

Expressing this result in terms of E_p and $E_{a,sat}$, a relationship for $q_p(E_p)$ is found, which is valid independently from the pulse shape:

$$q_p(E_p) \approx q_0 \sum_{i=1}^{\infty} \frac{1}{i \cdot i!} \left(-\frac{3.8696\, E_p}{E_{a,sat}} \right)^{i-1} . \tag{4.34.}$$ [1]

The saturation energy $E_{a,sat}$ corresponds to the pulse energy necessary to saturate the absorption coefficient to 50% of its unsaturated value q_0 and is given by

$$E_{a,sat} \approx 3.8696 \frac{\pi}{2} w_a^2 \frac{h\nu}{\sigma_a + \sigma_e} = 3.8696 \frac{\pi}{2} w_a^2 I_{a,sat} \tau_a , \tag{4.35.}$$ [2]

with $I_{a,sat}$, (cw) saturation intensity of the absorber.

Equations 4.34. and 4.35. can also be expressed by the respective fluences instead of the energies. The saturation fluence $F_{a,sat}$, which is a parameter of the absorber device and does not depend on the beam area in the absorber, and the pulse fluence F_p are obtained by dividing the pulse energy and the saturation energy by the effective beam area $\mathbb{A}_{eff}$ on the saturable absorber:

$$F_p = \frac{E_p}{\mathbb{A}_{eff}} , \tag{4.36.}$$

$$F_{a,sat} = \frac{E_{a,sat}}{\mathbb{A}_{eff}} \approx 3.8696 \frac{h\nu}{\sigma_a + \sigma_e} , \tag{4.37.}$$

with $\mathbb{A}_{eff} = \frac{\pi}{2} w_a^2$, effective beam area. (Assuming a Gaussian beam with a central intensity $I_c = I(r=0)$, a beam with area $\mathbb{A}_{eff}$ and radially constant intensity $I(r) = I_c$ would contain the same power.)

Slow absorber – calculations

For a slow absorber, the absorption coefficient $q(t,T) = q(t,E_p(T))$ is being decreased throughout the pulse, the decrease $q(t,T)/dt$ getting weaker with increasing saturation. This is illustrated in Figs. 4.3.a) to c), which present numerical results using eqs. 4.29. and 4.30. for the case of a $sech^2$-shaped pulse, $P(t) = P(0) \cdot sech^2(t/\tau)$, with a Gaussian beam profile. Absorber relaxation has been neglected.

---

[1] Please note, for a standing-wave resonator, E_p in eq. 4.34. has to be multiplied by a *factor* > 1, if the absorber cannot fully recover after the pulse has passed through in forward direction, before it returns in backward direction. For a saturable absorber that is used as an absorber mirror with highly reflective backside coating, *factor* ≈ 2 is obtained.

[2] Alternatively, a saturation energy could be defined, which does not correspond to $q_p(E_{a,sat})=q_0/2$. In this case, the saturation law on which the estimation of a particular $E_{a,sat}$ is based must be given together with the value.

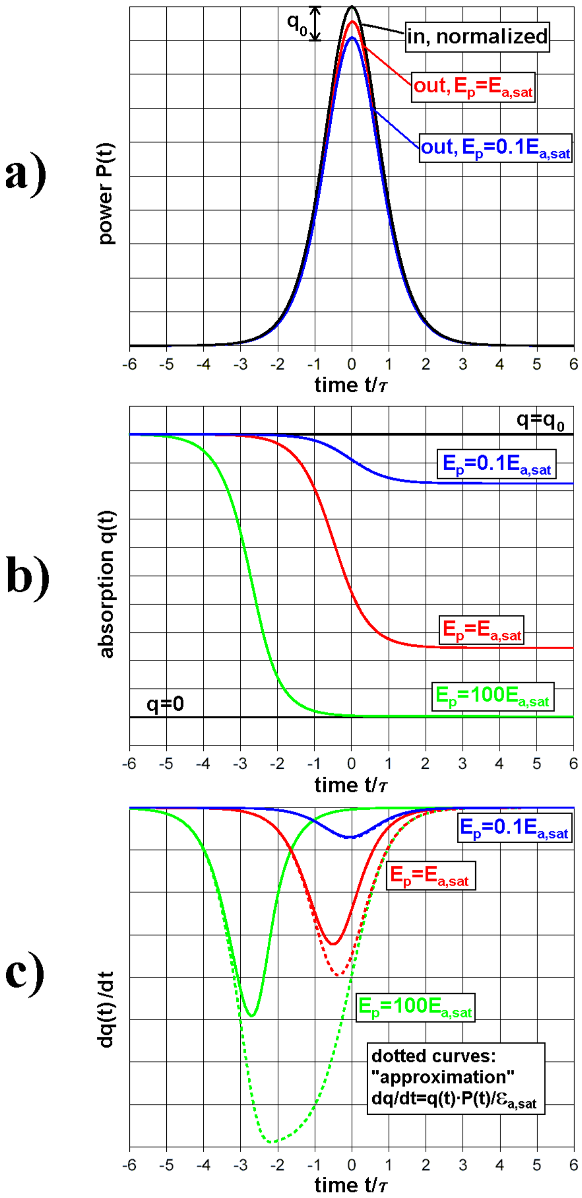

Fig. 4.3. a) Power of a signal pulse before and after passing through a slow saturable absorber. Black curve: incident pulse. Red: outgoing pulse, for incident pulse energy $E_p = E_{a,sat}$; blue: for $E_p = 0.1\ E_{a,sat}$. The temporal shape of the incoming signal is $sech^2(t/\tau)$ (FWHM $\tau_p \approx 1.763\ \tau$), the beam profile is Gaussian. The outgoing pulse is slightly shorter than the incoming and the pulse maximum is slightly delayed, since absorption is stronger for the leading edge of the pulse. The arrow indicates the difference at peak amplitude in the small-signal case ($q(t) = q_0$). The unsaturated loss has been chosen as $q_0 \cdot L_a = 0.1$ (L_a, path length through absorber; unsaturable loss and absorber relaxation during the pulse have been neglected.)

b) Absorption as a function of time, while the pulse from a) passes through a slow saturable absorber, for pulse energies $E_p = 0.1\ E_{a,sat}$ (blue), $E_p = E_{a,sat}$ (red), and $E_p = 100\ E_{a,sat}$ (green).

c) Change of the absorption as a function of time, while the pulse from a) passes through a slow saturable absorber, for incident pulse energies $E_p = 0.1\ E_{a,sat}$ (blue), $E_p = E_{a,sat}$ (red), and $E_p = 100\ E_{a,sat}$ (green). Solid curves display the results of numerical simulations taking into account the Gaussian beam profile; dotted curves are based on $dq/dt = -q(t) \cdot P(t)/\varepsilon_{a,sat}$ (eq. 4.38.a with relaxation neglected). Due to the large discrepancies, the latter is an approximation useful only for weak saturation of the absorber.

Since the effect of the stronger absorption experienced by the leading wing of the pulse exceeds that of the weaker absorption for the trailing wing, the pulse duration is reduced; the outgoing pulse is asymmetrical and its maximum is slightly delayed. Shortening and delay become maximum for pulse energies in the vicinity of the saturation energy.[1] The pulse shortening is required to start mode locking, the delay is essential to stabilize it.

After the pulse, absorption slowly recovers from $q_{fin}(E_p)$ towards the unsaturated value q_0 (recovery not shown in Fig. 4.3.). Therefore, after several round trips a pulse originally shaped like those in Fig. 4.3.a) will have developed a tail. Noise ("continuum") can grow in the tail region, claiming an increasing part of the power extractable from the gain medium and possibly destroying mode-locked operation. The problem is increased with decreasing $q_{fin}(E_p)$, i.e. with increasing pulse energies E_p. Fortunately, growth of noise will be limited, if a sufficient delay of the pulse maximum per round trip exists, i.e. if the pulse is pushed backwards into the noise fast enough to swallow it in time [Pas01].

In Fig. 4.3.c) we have also included an approximation, which can describe the absorber dynamics, $dq(t)/dt$, in case of pulse energies much lower than the saturation energy. For larger energies, discrepancies obviously become too large. This has consequences for mode-locking stability analysis. The relationship is given by [Hau76, Hoe99, Kae98, Sch00]

$$\frac{dq(t)}{dt} \approx -\frac{q(t)-q_0}{\tau_a} - q(t)\frac{P(t)}{\varepsilon_{a,sat}} , \qquad (4.38.a)$$

with

$$\varepsilon_{a,sat} = \pi w_a^{\;2} \frac{h\nu}{\sigma_a + \sigma_e} .^2 \qquad (4.38.b)$$

The first term on the RHS of eq. 4.38.a is due to the spontaneous decay of the upper state of the saturable absorber and can be verified easily by temporal differentiation of eq. 4.33. This relaxation term has been neglected in Fig. 4.3.c). The second term describes the change of upper-state population due to the instantaneously absorbed power. However, in general and as demonstrated in Fig. 4.3.c), it does not describe the change $dq(t)/dt$ of the absorption coefficient that is effective for the whole beam, since this quantity is not proportional to the total upper-state population in the absorber medium. Instead, $dq(t)/dt$ must be calculated from the changes of the local absorption coefficients, for which an equation similar to 4.38.a is always valid (with $q(t) = q(t,r)$; $P(t)$ replaced by $I(t,r)$; $\varepsilon_{a,sat}$ replaced by $I_{a,sat}\cdot\tau_a$), by spatial averaging with the local signal intensity as weight. Therefore, eq. 4.38.a applied to the whole beam would be exact only for a spatially constant intensity. For a Gaussian intensity distribution, it is not exact due to the same reason that does not permit a simple saturation law for $q(t)$: An amount P_a of absorbed power being absorbed in the outer regions of the beam means a smaller reduction of $q(t)$ (effective absorption for the whole beam) than an amount P_{abs} being absorbed in the beam center.

Figure 4.3. deals with the case of an absorber that is slow compared to the variation of the signal power ($\tau_a >> \tau_p$); for a faster absorber, $dq(t)/dt$ will not obey eq. 4.38.a, either. The curve will look different, because the curve of $q(t)$ looks different (see Fig. 4.2.b), but the tendency is

---

[1] Even if there were no pulse-stretching effects, pulse duration would asymptotically approach a lower limit, for pulse energies going towards infinity.

[2] $\varepsilon_{a,sat}$ is a saturation parameter, but not the energy reducing the absorption coefficient from q_0 to $q_0/2$.

the same, i.e. eq. 4.38.a will provide too large values for *dq(t)/dt*, if an absorber is more than weakly saturated. The temporal evolution of the laser gain is usually described by an equation analog to eq. 4.38.a [Hau76, Hoe99, Kae98, Sch00]. Therefore, an analog problem exists, whenever the gain medium experiences more than weak saturation, i.e. whenever laser operation cannot be considered close to the lasing threshold.

Figure 4.4. shows the absorption coefficient $q_p(E_p)$ as a function of the pulse energy E_p, where eq. 4.34. has been used to calculate values for pulse energies up to $E_p = 10\,E_{sat}$; for larger energies, $q_p(E_p)$ was calculated numerically on the base of eqs. 4.29. and 4.30.[1] For low to moderate pulse energies, it is possible to approximate the exact data by a simple saturation law

$$q_p(E_p) \approx \frac{q_0}{1+\dfrac{E_p}{E_{a,sat}}} \qquad (4.39.a)$$

.

If $E_p << E_{a,sat}$, the absorption coefficient can also be approximated by the linear relationship

$$q_p(E_p) \approx q_0\left(1-\frac{E_p}{E_{a,sat}}\right) \qquad (4.39.b)$$

.[2]

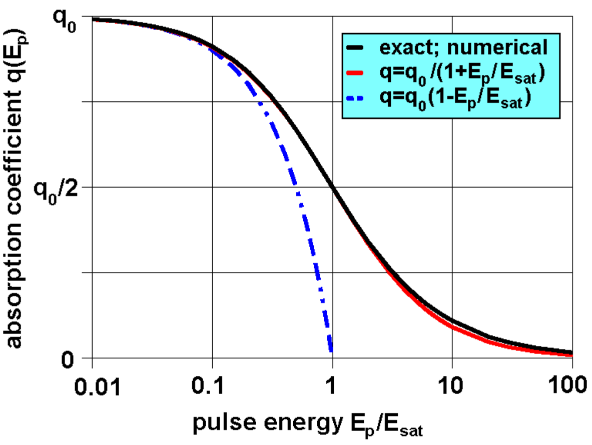

Fig. 4.4. Saturation of a slow absorber with increasing pulse energy E_p of a Gaussian signal beam. The absorption coefficient $q(E_p)$ was calculated mainly using the exact formula and partially numerically (black line). The unsaturated absorption is given by q_0, unsaturable absorption was neglected. For low to moderate energies, $q(E_p)$ can be approximated by a saturation law (red line), which is similar to that describing the intensity-dependence of the absorption coefficient. The saturation energy $E_{a,sat}$, such that $q(E_{a,sat}) = q_0/2$, is given by $E_{a,sat} \approx 3.8696\,(\pi/2)\,w_a^2 I_{a,sat}\tau_a$, ($I_{a,sat}$, cw saturation intensity; w_a, beam radius). For low powers one may also use a linear approximation (blue dash-dotted line).

---

[1] The formula given by eq. 4.34. together with eq. 4.35. is exact within the limits of the Gaussian-beam approximation; if necessary, a decrease of the pulse energy and a deformation of the intensity distribution while passing through the absorber must be considered. Unfortunately, $q_p(E_p)$ is hard to calculate for $E_p >> E_{a,sat}$, since many terms with large counters and large denominators have to be included.

[2] If working close to $E_p = 0$, for more exact results, one should use $\pi w_a^2 I_{a,sat}\tau_a \approx E_{a,sat}/1.9348$ instead of $E_{a,sat}$; then, however, deviations are larger in regimes of moderate absorption.

Group delay dispersion (GDD)

Lossless group delay dispersion (GDD) of materials, D_m, is related to a wavelength-dependent real part $Re(\mathcal{P})$ of the polarization $\mathcal{P} = \varepsilon_0(n_c^2-1)\mathcal{E}$ (with n_c, complex refractive index; see eqs. 4.4.-4.6., i.e. $d[Re(n_c^2)]/d\omega \neq 0$. Gain dispersion D_g and filter dispersion D_f can be expressed by a wavelength-dependent imaginary part $Im(\mathcal{P})$, i.e. $d[Im(n_c^2)]/d\omega \neq 0$. Furthermore, lossless GDD D_{comp} (and additional filter dispersion) can be achieved by utilizing spatial dispersion with prisms, gratings, chirped mirrors, or other elements. With normal D_m from the gain medium, D_{comp} is required to provide a regime for solitonlike pulse shaping, where the real part $Re(D)$ of the total round-trip GDD (i.e. the total lossless GDD) must be slightly negative, usually. In most cases of bulk solid-state lasers, pulse shaping is weak or moderate and the single contributions can be summed up to give the total GDD $D = d^2\phi(\omega)/d\omega^2|_{\omega=\omega_0}$ of the laser resonator:

$$D = D_m + D_{comp} + jD_g + jD_f \,. \tag{4.40.}$$

Material dispersion D_m.

The group delay dispersion D_m of a signal with center frequency ω_0 after passing over a distance L_D through a dispersive medium is defined as

$$D_m = \left.\frac{dt_g(\omega)}{d\omega}\right|_{\omega=\omega_0} = L_D \left.\frac{d^2k(\omega)}{d\omega^2}\right|_{\omega=\omega_0} , \tag{4.41.}$$

or, using eq. 4.46.b,

$$D_m = L_D \frac{\lambda^3}{2\pi c^2} \left.\frac{d^2n(\lambda)}{d\lambda^2}\right|_{\lambda=\lambda_0} , \tag{4.42.}$$

with	$t_g(\omega) = \dfrac{L_D}{v_g(\omega)} = L_D \dfrac{dk(\omega)}{d\omega}$	group delay; $t_g(\omega_0)$ is the transit time of the pulse maximum;
	$v_g(\omega)$,	group velocity; $v_g(\omega_0)$ is the velocity of the pulse maximum;
	$k(\omega) = \omega n(\omega)/c$,	(here, real part of complex) wave number;
	$n(\omega)$,	real part of complex refractive index (eq. 4.4.); for low to moderate light intensities, $n \approx n_0$;
	$\lambda = 2\pi c/\omega$,	wavelength in vacuum (λ_0, central wavelength).

Equation 4.41. is permitted, if the spectral bandwidth Ω_p (HWHM) of a pulse is small compared to the central frequency ω_0 (carrier frequency), which may be assumed for mode-locked lasers with pulse durations in the order of or longer than 100 fs. Then, the wave number $k(\omega)$ while travelling through the medium can be Taylor-expanded around ω_0,

$$k(\omega) = \sum_{i=0}^{\infty} \left.\frac{d^ik}{d\omega^i}\right|_{\omega=\omega_0} \frac{(\omega-\omega_0)^i}{i!} = \left.\frac{\omega}{v_{ph}(\omega)}\right|_{\omega=\omega_0} + \left.\frac{1}{v_g(\omega)}\right|_{\omega=\omega_0} (\omega-\omega_0) + \left.\frac{d}{d\omega}\left(\frac{1}{v_g(\omega)}\right)\right|_{\omega=\omega_0} \frac{(\omega-\omega_0)^2}{2} + \ldots , \tag{4.43.}$$

where higher-order terms can be neglected. The latter correspond to higher-order dispersion, which has to be taken into account for large spectral bandwidths.

The zeroth order term of eq. 4.43., $k(\omega_0)$, is the contribution of the phase velocity $v_{ph}(\omega)$,

$$v_{ph}(\omega) = \frac{\omega}{k(\omega)} = \frac{c}{n(\omega)}. \tag{4.44.}$$

The first order term, with coefficient $dk(\omega)/d\omega|_{\omega=\omega 0}$, is that of the group velocity $v_g(\omega)$,

$$v_g(\omega) = \frac{d\omega}{dk(\omega)} = \frac{c}{n(\omega) + \omega\frac{dn(\omega)}{d\omega}} = \frac{c}{n(\lambda) - \lambda\frac{dn(\lambda)}{d\lambda}}. \tag{4.45.}$$

The second order term, whose coefficient $d^2k(\omega)/d\omega^2|_{\omega=\omega 0}$ is called the group velocity dispersion coefficient (also called dispersion parameter), is the contribution of the group velocity dispersion $dv_g(\omega)/d\omega$,

$$\frac{d^2k(\omega)}{d\omega^2} = \frac{d}{d\omega}\left(\frac{1}{v_g(\omega)}\right) = -\frac{1}{v_g^{\,2}(\omega)}\frac{dv_g(\omega)}{d\omega}, \quad \text{or} \tag{4.46.a}$$

$$\frac{d^2k(\omega)}{d\omega^2} = \frac{2}{c}\frac{dn(\omega)}{d\omega} + \frac{\omega}{c}\frac{d^2n(\omega)}{d\omega^2} = \frac{\lambda^3}{2\pi c^2}\frac{d^2n(\lambda)}{d\lambda^2}. \tag{4.46.b}$$

Some hints, to avoid confusion:

1. The definitions of GDD D_m in eq. 4.41. and of D_g, D_f, and D_{comp} in eqs. 4.49., 4.50., and 4.55. are consistent with [Bra91, Bra92, Kra92]. In [Hau91, Kae98, Nel97], D_m is defined as half the quantity given here. This has to be taken into account, e.g. when comparing formulas for the pulse duration (eq. 4.19.).

2. When speaking of a "GVD coefficient", "GDD" or "GVD" with a positive or negative sign, the definitions used for these quantities should be given in the context. Referring to frequency will lead to the opposite sign compared to a wavelength-based definition (e.g. GVD: $v_g(\omega)/d\omega = -(2\pi c/\omega^2)dv_g(\lambda)/d\lambda$).

3. Sometimes, in literature the symbol "*D*" may stand for the material dispersion factor. This quantity may also be called dispersion parameter. However, it differs from the quantity given in eqs. 4.41. and 4.42. by a factor; we indicate this by "~". It is defined by

$$\tilde{D}(\omega) = -\frac{2\pi c}{\lambda^2}\frac{d^2k(\omega)}{d\omega^2} = -\frac{\lambda}{c}\frac{d^2n(\lambda)}{d\lambda^2}. \tag{4.47.}$$

In general, the chirp and change of pulse duration resulting from propagation through a dispersive material depend on the pulse shape and prechirp. For normal dispersion, higher-frequency components travel slower than the lower-frequency components, i.e. $dn(\omega)/d\omega > 0$ ($dn(\lambda)/d\lambda < 0$, respectively) and $dv_{ph}(\omega)/d\omega < 0$, and the GVD coefficient is positive, i.e. $d^2k(\omega)/d\omega^2 \sim d^2n/d\lambda^2 > 0$. If normal dispersion is the only pulse-shaping process, an initially unchirped pulse will become up-chirped (red-shift of instantaneous frequency on the leading edge, blue-shift on the trailing edge). Anomalous dispersion will result in down-chirp (“blue” at the front of the pulse, “red” at the rear).

In case of a Gaussian temporal pulse shape, the pulse duration obeys to a parabolic propagation law. Assuming no prechirp, we find $\tau_p^2(L_D) = \tau_p^2(0)+[\Delta\omega_p L_D\, d^2k(\omega)/d\omega^2)]^2$ (see e.g. [Rud89] for prechirped pulse), with $\Delta\omega_p = \Delta\lambda_p\omega_0^2/(2\pi c)$, FWHM-of-intensity spectral bandwidth. For small-distance propagation (“small” means “still WPS”), the broadening $\Delta\tau_p = \tau_p(L_D)-\tau_p(0)$ can be deduced as

$$\Delta\tau_p = \frac{\Delta\omega_p}{2} L_D \left.\frac{d^2k(\omega)}{d\omega^2}\right|_{\omega=\omega_0} = \frac{\Delta\lambda_p}{2} L_D \tilde{D}(\omega_0) \quad . \tag{4.48.}$$

In the appendix, helpful relationships for the derivatives of the refractive index with respect to ω and λ and the Sellmeier coefficients of a material are given.

Gain dispersion D_g and filter dispersion D_f

For the material dispersion D_m, only the real part of the complex refractive index n_c (see eqs. 4.4.-4.6.) was discussed, assuming the wave number $k(\omega)$ was real. Now we consider the imaginary part, which will not be equal to zero, if the medium shows gain or absorption, i.e. $\alpha(\omega)/2 = -g(\omega)/2 = Im[k(\omega)] = \omega\, Im[n_c(\omega)]/c$, with α and g, absorption and gain coefficients with respect to intensity.[1]

A Taylor expansion of α or g around the central frequency ω_0 in analogy to the expansion (eq. 4.43.) of the real-valued $k(\omega)$ is permitted, if the spectral bandwidth Ω_p (HWHM) of a pulse is small compared to ω_0 and small compared to the spectral bandwidth Ω_g or Ω_f (HWHM, with respect to intensity). The latter condition is not fulfilled in many cases, however.[2] The second-order term of the expansion contains the derivative $d^2g(\omega)/d\omega^2|_{\omega=\omega_0}$ or $d^2\alpha(\omega)/d\omega^2|_{\omega=\omega_0}$, which is two times the gain or filter dispersion coefficient, respectively (named analog to the GVD coefficient). Then, gain dispersion D_g and filter dispersion D_f can be defined as

$$D_g = \tfrac{1}{2} \left.\frac{d^2G(\omega)}{d\omega^2}\right|_{\omega=\omega_0} \tag{4.49.}$$

and

$$D_f = -\tfrac{1}{2} \left.\frac{d^2A(\omega)}{d\omega^2}\right|_{\omega=\omega_0} . \tag{4.50.}$$ [3]

where $G(\omega)$ and $A(\omega)$ are the total (longitudinally integrated and radially averaged) gain or absorption, respectively, experienced by the optical pulses when passing through a gain or absorber medium.

---

[1] The intensity-gain and intensity-loss coefficients are twice as large as the respective coefficients for the electrical field strength.

[2] See also the condition given by Krausz et al. for validity of the pulse duration formula eq. 4.19. (containing D_g), demanding the contribution of gain dispersion to the total GDD to be still moderate, i.e. $D_g < 0.35|D|$.

[3] Alternatively, using transmission 7 instead of A (thus also including other than absorption filters), filter dispersion can be defined as $D_f = ½\, d^2 7(\omega)/d\omega^2|_{\omega=\omega_0}$. Please also note, describing PAM by loss modulation, we have assumed that saturable absorption does not show a spectral dependence. In case of very large pulse bandwidth, however, the filter-dispersion D_f of the saturable absorber must be taken into account. This will require a more complicated treatment, since D_f will be intensity-dependent.

In case of a Lorentzian lineshape, D_g and D_f are given by

$$D_{g,Lorentz} = -\frac{G(\omega_0)}{\Omega_g^{\,2}} \tag{4.51.}$$

and

$$D_{f,Lorentz} = \frac{A(\omega_0)}{\Omega_f^{\,2}} \tag{4.52.}$$

.

For a parabolic lineshape, $D_{g,parabola} = \frac{1}{2}D_{g,Lorentz}$; for a Gaussian lineshape, $D_{g,Gauss} = ln(2)D_{g,Lorentz}$; analog equations are valid for filter dispersion. Unfortunately, most solid state laser media will not show trivial lineshapes of the gain. In such cases and especially also if Ω_p is not small compared to Ω_g, the above equations will provide only rough estimations of the gain dispersion.

However, for the pulse properties, gain dispersion often must be taken into account as a part of the total GDD D (eq. 4.40.) not only in regimes of non-solitonlike pulses, but also in solitonlike mode-locking regimes. In the latter, D_g increases the pulse duration (eq. 4.19.). Due to self-phase modulation (SPM), the pulse spectral bandwidth may exceed the gain bandwidth; in practice, however, in most bulk lasers the achievable maximum bandwidth is in the order of the fluorescence linewidth of the laser material. For the best-suited Yb^{3+}-doped materials (see Table 2.1.), the pulse duration τ_p is limited to minimum values in the order of 100 fs (record: 58 fs with Yb:glass [Hoe98]). A related term in this context is “gain narrowing”, which in case of a laser amplifier describes the effect of gain dispersion leading to a decreased bandwidth of the output compared to the input pulse.

Furthermore, gain dispersion decreases the gain experienced by the mode-locked pulses, from the value $G(\omega_0)$ at the center frequency (maximum value of the saturated gain spectrum) to an “effective value” G_p, which can be calculated as the average of the saturated gain spectrum $G(\omega)$ weighted with the pulse spectrum $I(\omega)$. In a regime of solitonlike mode locking, the effective gain is a function of the pulse energy, $G_p = G_p(E_p)$. The one-way gain-filtering loss with respect to pulse energy or averaged mode-locked power is given by

$$l_g(E_p) = G(\omega_0) - G_p(E_p) \tag{4.53.}$$

.

In general, while pulses become more energetic and shorter, the filtering loss increases strongly. In case of WPS, with gain dispersion given by eq. 4.51. (Lorentzian-shaped gain spectrum) and the pulse duration $\tau \sim 1/E_p$ (as for a true soliton), the loss l_g can be estimated by [Sch00][1]

$$l_g = -\frac{D_g}{3\tau^2} \tag{4.54.}$$

.

Compared to a cw laser (with identical setup, aside from the missing saturable absorber), a mode-locked laser will always be less efficient, due to l_g, especially in a regime of solitonlike mode locking with its shorter pulses. Filtering loss also affects the mode-locking stability and can be responsible for multiple pulsing or parasitive noise radiation.

---

[1] Please note the different definitions of quantities here compared to [Sch00]. We refer to power instead of field strength; here, GDD and its components are twice as large and of opposite sign.

GDD D_{comp} from spatial dispersion / Dispersion compensation

Lossless GDD D_{comp} as well as lossy GDD (filtering) can also be achieved via spatial dispersion that leads to a frequency-dependent optical path length. Such may be angular dispersion or also longitudinal dispersion, as delay loops are added in a resonant interferometer or as penetration depth into a reflecting multi-layer structure depends on frequency. Prisms [Rud89], gratings [Rud89], Gires-Tournois interferometers (GTIs) [Des70, Rud89, Szi00], and/or chirped mirrors [Szi00] are the most common devices to generate negative GDD D_{comp} in bulk-media lasers for solitonlike mode locking.

With prisms, the spectral components of a laser pulse experience angular dispersion (diffraction is stronger for shorter wavelengths) and therefore travel along paths of different lengths corresponding to different delays. There exist several possible arrangements, employing one [Gor84], two [Ram94], or four prisms [For84]. A design using two identical Brewster prisms is shown in Fig. 4.5.

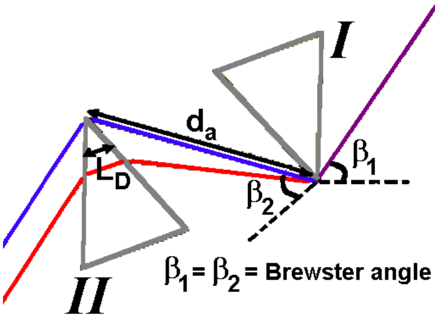

Fig. 4.5. Prism pair used for dispersion compensation. Angles β_1 and β_2 are Brewster angles; d_a, distance between apices; L_D, glass path for center frequency.

Prism ***I*** produces an angular-dispersive beam, while prism ***II*** does parallelization. For a single pass through this prism configuration, the resulting second-order GDD $D_{comp} = d^2 \phi(\omega)/d\omega^2 \big|_{prisms,\omega=\omega_0}$ can be approximated by

$$D_{comp} \approx \frac{\lambda^3}{2\pi c^2} \left\{ -4 d_a \left(\frac{dn(\lambda)}{d\lambda} \right)^2 + L_D \frac{d^2 n(\lambda)}{d\lambda^2} \right\} \Bigg|_{\lambda=\lambda_0} , \qquad (4.55.)$$

with d_a, distance between the apices;
λ_0, center wavelength of light pulse,
L_D, cumulative mean path through the prisms (mainly contributed by prism ***II***).

The first, negative term in the large brackets in eq. 4.55. is the second-order dispersion of the optical path due to angular dispersion, the second, normally positive term is due to prism-material dispersion (as described by eq. 4.42.). By inserting the prisms more or less into the beam, the latter term is changed. For derivatives $d^2n/d\lambda^2$ and $dn/d\lambda$ see appendix.

More general equations covering also non-Brewster prisms are given in [Bor85, Nak88, Yan01], of which the latter reference presents the most accurate method.[1]

---

[1] Non-Brewster prisms can be interesting for external pulse compression, where high dispersion-per-length is desired and losses are more acceptable. The 60° SF6 prisms used in our Yb:scandia experiments in chapt. 6 can be considered approximately Brewster-angled, the extra loss in the resonator is well below 1%.

The single-pass third-order dispersion $dD_{comp}/d\omega = d^2\phi(\omega)/d\omega^2|_{prisms,\omega=\omega_0}$ becomes important for very short pulses (usually for $\tau_p << 100$ fs, but depending on prism material). It can be approximated by

$$\frac{dD_{comp}}{d\omega} \approx \frac{\lambda^4}{4\pi^2 c^5}\left\{12d_a\left[\left(\frac{dn(\lambda)}{d\lambda}\right)^2\left(1-d_a\frac{dn(\lambda)}{d\lambda}(n^{-3}-2n)\right)+d_a\frac{dn(\lambda)}{d\lambda}\frac{d^2n(\lambda)}{d\lambda^2}\right]-L_D\left[3\frac{d^2n(\lambda)}{d\lambda^2}+d_a\frac{d^3n(\lambda)}{d\lambda^3}\right]\right\}\Bigg|_{\lambda=\lambda_0}. \tag{4.56.}$$

Self-phase modulation (SPM)

Self-phase modulation (SPM) exists due to a nonlinear dependency of the real part $Re(\mathcal{P})$ of the polarization $\mathcal{P} = \varepsilon_0(n_c^2-1)\mathcal{E}$ on the electrical field strength (with n_c, complex refractive index; see eqs. 4.4. to 4.6.), i.e. $d[Re(n_c^2)]/d\mathcal{E} \neq 0$. Analogly, passive amplitude modulation (PAM) is a consequence of $d[Im(n_c^2)]/d\mathcal{E} \neq 0$.

In our range of interest (pulse durations in the order of 100 fs or longer), the real part of the refractive index, $n = Re(n_c)$ can be expressed by

$$n \approx n_0 + n_2|\mathcal{E}|^2, \tag{4.57.}$$

where n_2 is the nonlinear refractive index given in units of [m^2/V^2] (MKS units) or [esu=cm^3/erg] (CGS units), or by

$$n = n_0 + \underline{n}_2 I, \tag{4.58.}$$

where $\underline{n}_2$ is the nonlinear refractive index (or "nonlinear refractive coefficient", "Kerr coefficient") with respect to the instantaneous light intensity I, usually given in units of [cm^2/W]. A useful relationship is the conversion $\underline{n}_2 = 8 \times 10^5\pi\ (n_2/cn_0)$ (cm^2/esuW).

The theory of the nonlinear refractive index is comprehensively explained in [Ada89], giving also an overview over several measurement techniques and tabulated data for various crystals (including sesquioxides). Theory permits to predict n_2 within a crystal family with fair accuracy, if values are known for some members. At present, n_2 has been measured for a lot of materials applying the so-called "z-scan" technique [She89, Yan03].

Since light intensity is a function of time and spatial coordinates, $I=I(t,r,z)$ for a radially symmetric beam, this is valid also for the refractive index. While consideration of the radial dependence explains Kerr lensing, in the context of SPM it is sufficient to take into account the spatial dependencies by using effective values for the intensity and the path length, $I(t) = P(t)/\mathcal{A}_{eff}$ (with $\mathcal{A}_{eff}$, effective area) and L_{SPM}, respectively, gained by weighted averaging over the nonlinear medium.

In SVEA, the self-phase modulation, i.e. the time-dependent phase shift $\Delta\phi(t)$ in the moving frame due to the refractive index nonlinearity after passing over a distance L_{SPM} through the nonlinear medium is given by

$$\Delta\phi(t) = \frac{\omega_0}{c} L_{SPM} \underline{n}_2 I(t) \quad . \tag{4.59.}$$

In the pulse-duration formula eq. 4.19., we have used the nonlinear phase shift per power, $\Gamma = \Delta\phi(t)/P(t)$, given by

$$\Gamma = \frac{\omega_0}{c \mathcal{A}_{eff}} L_{SPM} \underline{n}_2 \quad . \tag{4.60.}$$

In eq. 4.9. we have also introduced the SPM coefficient $\gamma = ½\, \omega_0 n_0 \varepsilon_0 \underline{n}_2$.

The nonlinear phase shift results in a time-dependent shift $\Delta\omega_i(t,L_{SPM})$ of the instantaneous frequency,

$$\Delta\omega_i(t, L_{SPM}) = \frac{\partial\Delta\phi(t, L_{SPM})}{\partial t} = \frac{\omega_0}{c} L_{SPM} \underline{n}_2 \frac{\partial I(t)}{\partial t} \quad . \tag{4.61.}$$

As a consequence, if no other effects are present, the instantaneous frequency will steadily increase at the leading part of the pulse and decrease at the trailing part, which means that the spectral bandwidth of the pulse is broadened. With SPM applied externally, the broadening can be strong; in a laser resonator, the spectrally broadening effect of SPM is countered by the limited gain bandwidth (and supported more or less by PAM).[1] However, the resulting FWHM pulse bandwidth may be considerably larger than the FWHM gain bandwidth, as demonstrated also by our mode-locked Yb:scandia lasers in chapter 6.

---

[1] In case of solitonlike pulse shaping, support by PAM is negligible.

4.3. Stability of passive mode locking

Practically, the performance of soliton-like and non-soliton-like mode-locked lasers experiences limitations due to competing modes of laser operation. These may destabilize the desired mode-locking regime, totally prevent it or result in an inacceptable amount of noise accompanying the mode-locked signal: cw operation, multiple-pulse mode locking, simple Q-switching, Q-switched mode locking, and/or a strong parasiting dispersive wave. If mode locking can be obtained, problems will occur preferrably when pulse duration is driven towards minimal values and pulse energy is maximized. As a consequence, the laser parameters connected with the pulse-shaping effects must be chosen carefully.

Mode-locking instabilities can always be referred to insufficient PAM, since it is the mechanism absolutely necessary for mode locking, which discriminates against other operation regimes. The saturable absorber may be bleached too weakly (resulting in cw radiation instead of mode locking), too easily (causing multiple pulsing), too rapidly (giving rise to Q-switching) or for too long (supporting a noise tail). In most cases, gain and/or filter dispersion is the opponent of PAM, preferring operation regimes with narrow spectra (cw radiation or longer pulses), because these experience less filtering losses. For Q-switching, gain and loss dynamics must be considered.

If pulse durations are in the range of a few ps or shorter, SPM and material GDD (as well as possible spatial GDD) must be included in stability considerations: They influence pulse intensity and spectrum and consequently PAM and filtering losses. Furthermore, the higher-order components of SPM and GDD and the discrete character of all pulse-shaping effects in a bulk laser lead to dispersive noise radiation. The speed of PAM action and the timing of signal and noise, which experience different SPM and GDD, play a role for noise suppression.

Table 4.1. lists the instabilities relevant for passively mode-locked Yb^{3+} based lasers, with possible causes and countermeasures.

In general, a laser system will tend towards minimum total loss $l_{tot,min}$, corresponding to maximally efficient extraction of power from the laser medium and maximum light power circulating in the laser cavity. This is where operation is ultimately stable. Any change from an operation regime (1) to a regime (2) is motivated by a reduction of total loss l_{tot}, resulting from altered spectra and intensities, such that[1]

$$l_{tot(1)} > l_{tot(2)} \geq l_{tot,min} , \tag{4.62.}$$

where $l_{tot(1)} = l_0 + l_{gf(1)} + l_{a(1)}$ and $l_{tot(2)} = l_0 + l_{gf(2)} + l_{a(2)}$, (4.63.)

with l_0, linear losses, independent from laser spectrum or intensity; they may include mirror transmission and also the unsaturable absorption part of a saturable absorber;

$l_{gf(1)}$, $l_{gf(2)}$, filtering losses; they may result from limited bandwidth of gain medium, mirrors, saturable absorber, and/or additional filters;[2]

$l_{a(1)}$, $l_{a(2)}$, saturable absorber loss; equivalent to $q \cdot L_a$ used in the description of PAM by loss (L_a, path length through absorber).

---

[1] In steady state, the total loss equals the laser gain. In chapter 3.3.2., $\delta = l_{tot}$.

[2] Filter loss by a saturable absorber may be neglected for systems, where the spectral bandwidth of the pulses is relatively small, like for the Yb^{3+} lasers mode-locked by a semiconductor saturable absorber (SESAM) in chapter 3. For very broadband pulses hitting a SESAM, however, the limited bandwidth of the basic reflector is a dominant source of filtering loss. This loss may be treated as intensity-independent.

So, $l_{tot} > l_{tot,min}$ is a necessary condition for laser instability. An operation regime with $l_{tot} > l_{tot,min}$ may exist due to three different reasons: 1.) Lasing has just been started, and the system is not running stably, yet. 2.) After start-up, the laser system has evolved into a regime, which is protected by a potential barrier against further reduction of loss. 3.) The conditions in the system have been changed compared to the start-up conditions (by variation of pump power, laser adjustment, or added group delay dispersion), in such a way that the present regime is not energetically favorable any more. There may be a potential barrier as well, preventing a change of the operation regime.[1]

If there exists a potential barrier, an appropriate perturbation (noise fluctuation) may overcome it and lead to a different regime with lower total loss and higher intracavity laser power. If there is no barrier and $l_{tot} > l_{tot,min}$, a change will occur instantly. A necessary condition for laser instability, referring to both cases, is

$$\frac{\Delta l_{tot(1)}}{\Delta P} < 0 \quad , \tag{4.64.}$$

with Δl_{tot}, change of total loss caused by a perturbation (barrier case: a fluctuation that is likely to occur within a reasonable period of time; no-barrier case: any perturbation, even if infinitesimaly small);

ΔP, change of intracavity laser power, related to the perturbation.[2]

The estimation of loss l_{tot} for an operation regime defined by a set of system parameters and of the change Δl_{tot} caused by a perturbation is nontrivial in real-world cases. Analytical approaches [Hau75, Hau76, Hoe99, Kra92, Kae98, Led99, Sch00, Sot99] will usually fail for bulk solid-state lasers, where the beam profile is Gaussian, a saturable absorber is more than weakly saturated and may show a bitemporal relaxation behavior, the gain medium cannot be described by a simple saturation law,[3] and/or pulse shaping may not be considered weak. Then, the stability limits (parameter ranges guaranteeing a desired operation regime) and the achievable laser performance (including minimum mode-locked pulse durations and maximum pulse energies) have to be calculated by numerical simulation. Improvement of the analysis can be achieved also by using the more exact equations developed in this work for PAM by loss modulation (see eqs. 4.25-4.39. and comments).

---

[1] If a parameter of the laser system is varied in both directions to change the operation regime forth and back, one will usually observe a hysteresis behavior, due to different relative barrier heights. For example, varying the negative GDD of a mode-locked laser, the transition from solitonlike single-pulse mode locking to multiple pulsing will occur for another value than the transition back.

[2] Relationship 4.64. will be also a sufficient condition for instability, if gain saturation can be neglected, i.e. for all regimes with the exception of Q-switched operation or Q-switch mode locking.

[3] The description of the saturation behavior of the gain can be a major problem, too. For a Gaussian profile of the laser signal beam, gain saturation is radially inhomogeneous in the gain medium.The gain provided by the whole medium can be described by a simple saturation law, only as far as the slope efficiency η_{sl} is constant and only if the small signal gain is proportional to the pump power. This may be assumed, if operation occurs significantly above the lasing threshold (in case of a quasi-three- or quasi-four-level material: far above the lasing threshold) and if the pump absorption in the active region of the gain medium is approximately constant for varying pump power. The latter will be the case, if saturation can be neglected for the pump radiation or if pump and laser signal beam show perfect overlap (see also chapter 3).

Table 4.1. Instabilities of passive mode-locking in Yb^{3+}-based lasers with weak or moderate pulse shaping. Problems and countermeasures.

problem	**possible cause**	**countermeasures**
cw replacing mode locking	absorber bleached too weakly, such that $l_{a(1)}$-$l_{a(2)}$ < $l_{gf(2)}$-$l_{gf(1)}$, where (1), cw; (2), mode-locked	increase bonus for mode-locked case from reduced saturable absorption loss, $l_{a(1)}$-$l_{a(2)}$, by - higher intensity in the saturable absorber, - choosing an absorber with larger modulation depth and/or lower saturation fluence (or saturation intensity in case of fast absorber); reduce malus for mode-locked case from increased filtering losses, $l_{gf(2)}$-$l_{gf(1)}$, by - operating with non-solitonlike pulse shaping (positive real part *Re(D)* of round-trip GDD *D*, where *D* is described by eqs. 4.40-4.56) or - optimization of dispersion compensation for stability rather than for minimum duration of solitonlike pulses (moderately small negative value of *Re(D)*), - optimization of SPM for stability rather than for maximum spectral bandwidth of pulses (lower value of the round-trip nonlinear phase-shift per power, Γ, e.g. by lower intensity in the laser medium; for Γ, see eq. 4.60), - in principle, increasing gain bandwidth or applying additional, inverse filtering will reduce $l_{gf(2)}$-$l_{gf(1)}$; but this cannot be considered isolated from other parameters
cw instead of mode locking, mode locking will not start	- as above; additionally: - spurious reflections, - insufficient initial fluctuations	- as above; additionally: - avoid spurious reflections, - actively provide sufficient initial fluctuations, - if dispersion-compensating elements involved: optimize compensation to support solitonlike pulses (moderately small negative value of *Re(D)*)
multiple pulsing	absorber bleached too easily, such that $l_{a(2)}$-$l_{a(1)}$ < $l_{gf(1)}$-$l_{gf(2)}$, where (1), single-pulse mode locking; (2), multiple pulsing; insufficient barrier against pulse break-up or growth of further pulse(s) from noise fluctuations	increase malus for multiple-pulsing case from higher saturable absorption loss, $l_{a(2)}$-$l_{a(1)}$, by - lower intensity in the saturable absorber, - choosing an absorber with larger modulation depth and/or higher saturation fluence (or saturation intensity); decrease bonus for multiple-pulsing case from reduced filtering losses, $l_{gf(1)}$-$l_{gf(2)}$, by - operating with non-solitonlike pulse shaping or - optimization of dispersion compensation for stability rather than for minimum duration of solitonlike pulses, - optimization of SPM for stability rather than for maximum spectral bandwidth of pulses, - in principle, increasing gain bandwidth or applying additional, inverse filtering will reduce $l_{gf(1)}$-$l_{gf(2)}$, but this cannot be considered isolated from other parameters;* increase barrier by measures against multiple pulsing mentioned above, additionally by - choosing a faster absorber
Q-switching, Q-switched mode locking	absorber bleached too rapidly compared to gain medium	decrease bleaching rate of saturable absorber (change of temporally averaged absorption q_p per round-trip, see eq. 4.34. for slow absorber) during Q-switch cycle by - lower intensity in the saturable absorber, - choosing an absorber with higher saturation fluence (or saturation intensity); increase bleaching rate of gain medium during Q-switch cycle by - higher intensity in the gain medium, - choosing a faster gain medium with lower saturation fluence; for solitonlike pulse shaping, filtering losses will additionally damp Q-switching, since the increase of pulse energy during a Q-switch cycle leads to a spectrally broader pulse
strong parasitic noise (may evolve into pure cw operation or into multiple pulsing)	absorber bleached for too long; net gain experienced by noise too high	suppress the noise tail (continuum), which follows the pulse in the temporal window opened by the bleached absorber, more efficiently by - larger relative delay of signal pulse per round-trip (making the signal swallow the noise), achievable by above measures against “cw replacing mode locking”, - choosing a faster absorber to shorten the window of bleached absorption (in this context, for solitonlike pulse shaping, the noise tail will be more dispersive, i.e. noise will drift out of the window of bleached absorption more quickly), - reduce net gain (gain minus losses) for noise described by above measures against “cw replacing mode locking”; reduce shedding of radiation from a solitonlike pulse by bringing it closer to a true fundamental soliton (reduce discrete character and strength of pulse shaping)

* If multiple pulsing occurs, the energetic advantage $l_{a(2)}$-$l_{a(1)}$+$l_{gf(1)}$-$l_{gf(2)}$ of this regime will be small. If multiple pulsing is suppressed, there is often just a small energetic barrier preventing this regime. From our experiments, the adjustment of the laser resonator plays a significant role in this context.

5. Yb^{3+}-activated tungstate laser experiments

Yb^{3+}-activated monoclinic double tungstates exhibit very good spectroscopic and decent thermo-mechanical properties (see chapts. 2.2. and 2.4.). They are an excellent choice for cw or mode-locked lasers and promise the highest efficiencies among all Yb^{3+}-activated hosts [Bre01b], if the pronounced quasi-three- or quasi-four-level character of their laser operation scheme is taken into account (for quasi-three- or quasi-four-level laser physics, see chapt. 3). The high Yb^{3+} concentrations that can be realized in tungstates are interesting especially for the thin-disk laser concept and for microchip lasers (see chapt. 2.3.).

In chapter 5.1., we examine the continuous-wave (cw) and mode-locked laser performance of lowly doped tungstates (≤20% replacement by Yb^{3+}). In chapter 5.2., quasi-cw and cw lasing of tungstates with high Yb^{3+}-concentration (≥20% replacement and stoichiometric crystals) is investigated.

Table 5.1. lists the crystal samples with the corresponding experiments and chapters. The crystals we use include Chochralski-grown Yb(5%):KGW and Yb(5%):KYW crystals, Kyropoulos-grown Yb(12%):KGW, Yb(20%):KYW, and KYbW, TSSG-grown Yb:KYW media with dopant concentrations of 41%, 60%, 80%, and TSSG-grown KYbW.

Table 5.1. Overview of ytterbium potassium tungstate laser experiments. *, identical crystal.

chapter	material	growing method	source	thickness [µm]	thermally annealed	laser operation	comment
5.1.1.	Yb(5%):KYW*	Chochralski	Eksma	3000	no	cw	
5.1.1.	Yb(12%):KGW	Kyropoulos	VCT	3000	yes	cw	
5.1.1.	Yb(20%):KYW	Kyropoulos	VCT	3000	yes	cw	
5.1.2.1.	Yb(5%):KYW*	Chochralski	Eksma	3000	no	ml	tapered diode laser pumped
5.1.2.2.	Yb(5%):KGW	Chochralski	Eksma	3000	no	ml	tapered diode laser pumped
5.1.2.3.	Yb_2O_3(5%): phosphate glass		Univ. Jena	3000	no	ml	tapered diode laser pumped, for comparison
5.2.1.1.	Yb(41%):KYW	TSSG	Univ. Tarragona	200	no	quasi-cw	1st lasing of a highly doped Yb tungstate
5.2.1.1.	Yb(60%):KYW	TSSG	Univ. Tarragona	510	no	quasi-cw	
5.2.1.2.	Yb(80%):KYW	TSSG	Univ. Tarragona	420	no	quasi-cw	
5.2.1.3.	KYbW	TSSG	Univ. Tarragona	500	no	quasi-cw	1st lasing of a stoichiometric Yb tungstate
5.2.1.4.	KYbW	Kyropoulos	VCT	125	yes	quasi-cw	smallest laser quantum defect
5.2.2.1.	Yb(20%):KYW	Kyropoulos	VCT	125	yes	cw	
5.2.2.2.	KYbW	Kyropoulos	VCT	125	yes	cw	1st cw lasing of a stoichiometric Yb material

5.1. Lowly Yb^{3+}-doped KYW and KGW experiments

5.1.1. Continuous-wave operation of lowly doped KYW and KGW

The experiments are performed in the laser setup shown in Fig. 5.1. with cw pumping by a Ti:Sapphire laser (Ti:Sa; details about this laser are given in chapt. 5.2.1.). The "V"-shaped cavity employs a flat output coupler M_1 with a transmission of $T_{OC} \approx 1\%$ or $T_{OC} \approx 3.5\%$ at 1060 nm, a folding mirror M_2 (radius of curvature $r = -100$ mm), through which the active medium is pumped, and an end mirror M_3 ($r = -100$ mm).

All tungstate laser media are used at the Brewster angle (≈64°) to avoid Fresnel loss at their uncoated surfaces. No special means of cooling are applied. The 20% Yb^{3+}-doped KYW and 12% Yb^{3+}-doped KGW crystals were grown by the Kyropoulos method and have a thickness of 3 mm and an aperture of 5 x 6 mm^2. The aperture is parallel to the natural (010) surface of the tungstate crystals; the crystals edges are cut in such a way that they are approximately parallel to the three crystallo-optic axes (see chapter 2.4.). The Yb(5%):KYW crystal was Chochralski-grown and it is also 3-mm-thick, with aperture of 3 x 5 mm^2. Its 5-mm-long edges point in the same direction as the crystallographic ***a***-axis, roughly. They are oriented with the $\boldsymbol{N_m}$ crystallo-optic axis lying in the plane of the pump beam polarization (horizontal), i.e. almost parallel to the pump beam polarization; the Yb:tungstate laser emission exhibits the same polarization. This orientation turns out to be favorable, delivering the highest output powers.

It is not known if the crystal qualities play a significant role for the performances observed here. However, the impurities in the materials are different, since the 5% doped KYW medium shows a parasitic turquoise-greenish fluorescence, when pumped, while the other two samples emit green radiation.

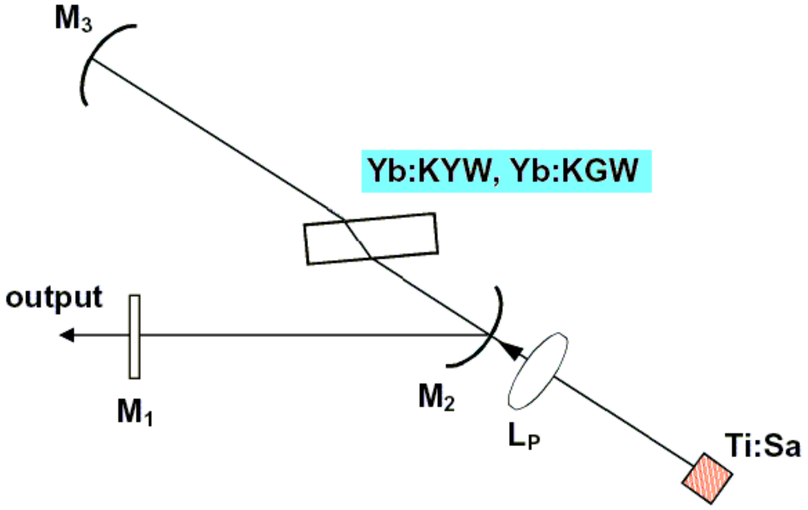

Fig. 5.1. Experimental setup for cw lasing of lowly Yb^{3+}-doped double tungstates.

The tungstate lasers are pumped at those wavelengths which yield the maximum output power for the individual laser crystal. Figure. 5.2. shows the absorption and emission spectra for light polarization parallel to the $\boldsymbol{N_m}$ crystallo-optic axis; triangles indicate the pump wavelengths used and the laser emission wavelengths observed. The spectra are assumed to be practically identical for all Yb^{3+}-activated monoclinic tungstates (see chapter 2.4.). In our experiments, a slight deviation from the cross sections shown in Fig. 5.2. occurs, since N_m axis and light polarization are not exactly parallel. For Yb(5%):KYW and Yb(12%):KGW, pumping close to the absorption maximum, at $\lambda_{pump} = 983$ nm, turns out to be favorable, because with the relatively low Yb^{3+} concentrations an efficient absorption pump light requires working in the region of large absorption coefficients. At the same time thermal effects remain small. For the 20% doped crystal, however, it is more appropriate not to pump at the zero-line transition, but at the secondary absorption maximum near $\lambda_{pump} = 999$ nm, which leads to a more even heat generation along the path in the crystal. With all three samples the pump radiation is almost completely absorbed.

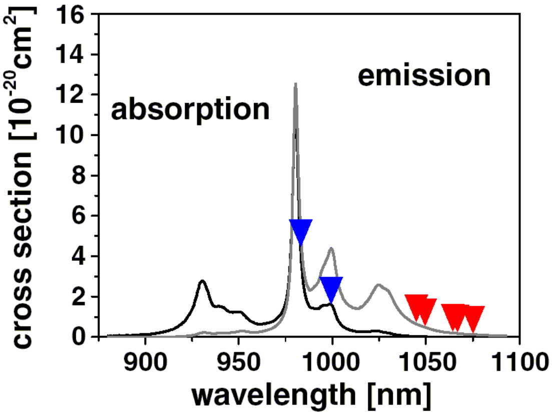

Fig. 5.2. Absorption and emission cross sections valid for both Yb:KYW and Yb:KGW with light polarization parallel to the N_m crystallo-optic axis. The pump wavelengths used and laser emission wavelengths observed are indicated by blue and red triangles, respectively.

Table 5.2. Performance of lowly Yb^{3+}-doped tungstate lasers. Results for two outcouplers with transmissions T_{OC} of ≈3.5% and ≈1%. λ_{pump} – pump wavelength (chosen for maximum output); λ_{laser} – laser wavelength; n.m. – not measured; $P_{a,thr}$ – absorbed pump power at lasing threshold; η_{sl} - slope efficiency; $P_{out,max}$ – maximum output power (at ≈2 W of absorbed pump power); η_{max} – laser efficiency at $P_{out,max}$.

T_{OC} [%]	laser material	λ_{pump} [nm]	λ_{laser} [nm]	$P_{a,thr}$ [mW]	η_{sl} [%]	$P_{out,max}$ [mW]	η_{max} [%]
3.5	Yb(5%):KYW	983	1046	≈450	68	930	49
3.5	Yb(12%):KGW	983	1049.5	≈750	56	640	34
3.6	Yb(20%):KYW	999	1064	≈1100	54	520	25
0.9	Yb(5%):KYW	983	n.m.	≈350	53	800	42
0.9	Yb(12%):KGW	983	1066	≈500	45	630	33
1.0	Yb(20%):KYW	999	1075	≈750	49	600	30

The experimental results are documented in Table 5.2. Comparing the laser performances of the tungstate materials with a ≈3.5%-outcoupler, we find that differences are correlated with the doping level: At 3 mm thickness of the active media 12% and 20% doping cause unnecessarily

high reabsorption losses, which are obvious from the relatively high lasing thresholds, approximately 750 mW of absorbed power for the Yb(12%):KGW crystal and ≈1100 mW for the Yb(20%):KYW sample, compared to ≈450 mW for Yb(5%):KYW. The lasing wavelength rising from 1049 nm to 1064 nm with increasing doping level is also a consequence of reabsorption, since reabsorption loss is reduced in the long-wavelength wing of the emission spectrum (Fig. 5.2.). By increasing the emission wavelength, the laser medium adjusts itself to the minimum value of inversion that still provides enough gain to balance the resonator loss (see also chapt. 3).
Because of the different threshold pump powers, the laser efficiency obtained at the maximum absorbed pump power (approximately 2 W) is highest for the lowest doping level, $\eta_{max} = 49\%$ for Yb(5%):KYW, while $\eta_{max} = 34\%$ and 25% are achieved for the 12% and 20% doped crystals, respectively. The Yb(5%):KYW laser exhibits also the highest slope efficiency, $\eta_{sl} = 68\%$, compared to 56% and 54%.

With a 1%-outcoupler the laser thresholds are decreased (Table 5.2.), but at the same time the slope efficiencies are lower than for the 3.5%-outcoupler. The ranking of the three materials with respect to the laser efficiencies does not change. Compared to the 3.5%-outcoupler, the lasing wavelengths are red-shifted (a typical behavior of quasi-three- or quasi-four-level lasers; for explanation, see Fig. 3.3.).

The cw laser results point out the importance of minimizing reabsorption for efficient use of Yb^{3+}-activated monoclinic tungstates; the investigated crystals are generally too thick. Taking this into account and considering the good slope efficiency of $\eta_{sl} = 68\%$ achieved with the most suitable crystal, the experiments actually indicate the potential of Yb:KYW and Yb:KGW with respect to high lasing efficiencies. For the mode-locked Yb^{3+} tungstate lasers in the next chapter we will use a doping level of 5%, which has here proven to be the most efficient.

5.1.2. Mode-locked operation of lowly doped KYW and KGW

The mode-locked laser experiments using Yb^{3+}-doped tungstate crystals are performed in the "Z"-folded cavity shown in Fig. 5.3. The folding mirrors M_2 and M_3 (r = -100 mm) provide a beam waist of $w_l \approx 30\ \mu m$ at the position of the laser medium. Another curved mirror, M_1, (r_{oc} = 100 mm or 150 mm) generates an additional focus on a semiconductor saturable absorber mirror (SESAM, [Jun97, Kel92, Tsu95]) with a saturable absorption of ≈2%, which terminates this arm of the resonator and serves as a passive mode-locker (see chapter 4.2.). The other arm contains an SF10-Brewster-prism pair P_1, P_2 with a tip-to-tip separation of ≈340 mm to compensate for dispersion and to enable mode-locked laser operation with solitonlike pulse shaping (see chapter 4.1.). The transmission of the outcoupler M_4 is varied from 1% to 5%.

In the ultrashort-pulse laser cavity of Fig. 5.3., three laser materials are used as active media: the 3-mm-thick 5% Yb^{3+}-doped KYW crystal presented in chapt. 5.1.1., a KGW crystal with the same thickness and doping level, and a 5 wt.% Yb_2O_3 doped phosphate laser glass (provided by Dr. Seeber, University of Jena). The thickness of the glass was chosen 6 mm, to compensate for the lower absorption coefficient. Yb:glass is a well-known active material for ultrashort-pulse lasers and amplifiers and therefore serves as a reference. All media are used at the respective Brewster angles. Again, for the tungstates, the orientation with the N_m crystallo-optic axis being almost parallel to the pump beam polarization is favorable, delivering the highest output powers and the most stable mode locking. Although the laser media are not actively cooled, they do not show thermal problems with the available pump powers.

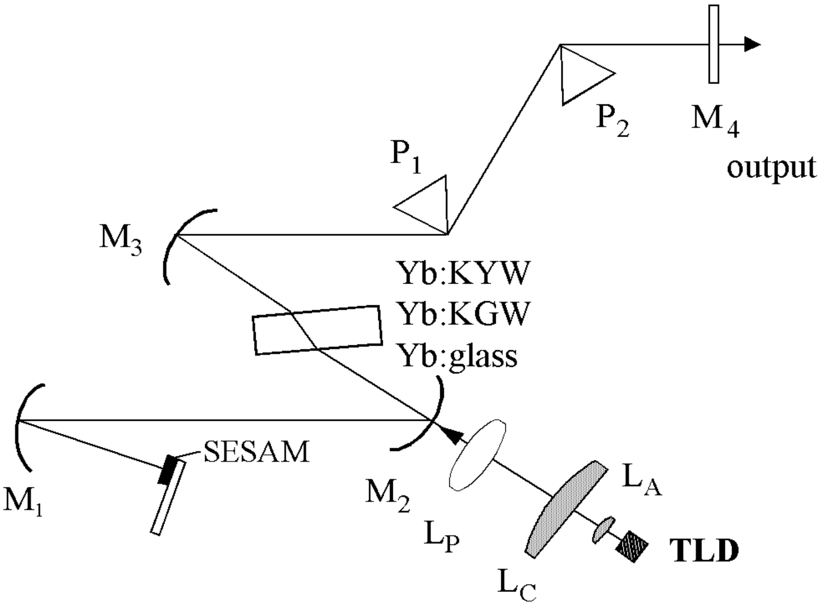

Fig. 5.3. Setup of the femtosecond Yb tungstate and glass lasers: SESAM – semiconductor saturable absorber mirror; M_1 – focusing mirror (r = -100 to -150 mm); M_2, M_3 – folding mirrors (r = -100 mm), P_1, P_2 – SF10 Brewster prisms; M_4 – output coupler (1 to 5% transmission); laser medium – 3-mm-thick, 5 at% Yb^{3+}-doped KYW or KGW crystal or 3-mm-thick, 5 wt% Yb_2O_3-doped phosphate glass; TDL – tapered diode laser; L_A – aspherical lens; L_C – cylindrical lens; L_P – focusing lens.

The pump light is provided by a tapered diode laser (TDL), whose beam is collimated by an aspherical lens L_A (f = 4.5 mm) and a cylindric lens L_C (f = 40 mm) and then focussed by the

$f = 62.8$-mm-lens L_p through the folding mirror M_2 onto the crystal or glass. Approximately 98% of the incident 1.1 W are absorbed. We have realized our femtosecond Yb tungstate laser also with a Ti:Sa pump source, but we do not further investigate this option in the present configuration, since the mode locking then shows strong multiple-pulsing instabilities.

Tapered diode laser (TDL) as pump source

The best way to provide the high pump intensities required for efficient operation of quasi-three-level materials is to use a diffraction limited pump beam from a high brightness source like the Ti:Sa laser used in the experiments in chapts. 5.1.1. and 5.2. In chapter 5.1.1. we have seen that reabsorption loss leads to a relatively high lasing threshold also with the 3-mm-thick Yb(5%):KYW crystal. Broad stripe laser diodes would not permit operation far above the laser threshold, due to their low brightness and large M^2 values. In contrast, narrow stripe diode lasers and tapered diode lasers (TDL) offer a high beam quality, so that the pump mode can easily be shaped and matched to the laser mode, even if its waist is relatively small at the crystal (30 µm in our case) at a low divergency. Besides, a small effective laser mode area in the active medium is favorable not only to avoid reabsorption loss and to achieve a low lasing threshold (see chapt. 3.3.); a higher intensity in the laser medium also increases the stability of the mode-locked regime against Q-switching (see chapt. 4.3., Table 4.1.).

Until recently, however, the available nearly diffraction-limited diode pump sources around 980 nm did not provide sufficient output power for pumping mode-locked lasers based on Yb^{3+}-doped materials. For the experiments reported here we use a novel TDL which was manufactured at Ferdinand-Braun-Institute (FBH, Berlin), delivering an output power up to 2 W at an $M^2 < 3$ for the slow axis emission ($1/e^2$-value).

The TDL (Fig. 5.4.) consists of a 1-mm-long ridge waveguide and a 3-mm-long tapered amplifier section. The highly reflecting ($R > 90\%$) facet is about 3 µm wide and the output aperture has a width of 300 µm. The diode laser is soldered epi-down on a CuW subcarrier with AuSn. The subcarrier is mounted on an open copper heat-sink (C-mount). A typical electrical-to-optical conversion efficiency of about 40% is measured for a fixed heat-sink temperature of 25°C corresponding to a diode current of 3.0 A (output power: 1.5 W).

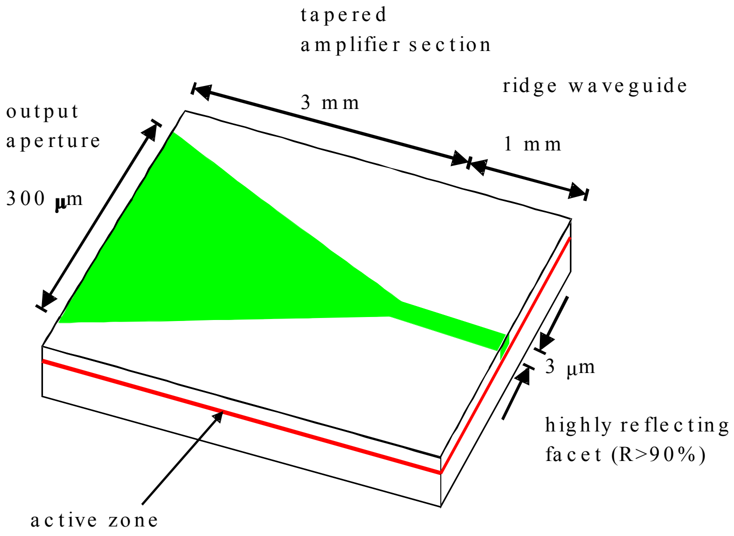

Fig. 5.4. Scheme of the tapered diode laser (TDL) used as the pump source in our experiments ($P_{max} = 2$ W, $M^2_{slowaxis} < 3$).

The maximum output power of 2 W is achieved near 978 nm with a spectral bandwidth of only 1 nm. An effective far field measurement of the slow axis emission shows that about 60% of the radiation emitted at 2 W belong to the fundamental mode (Fig. 5.5.). The measured fast axis divergence angle of the pump diode is below 30° due to a large optical cavity AlGaAs waveguide structure.

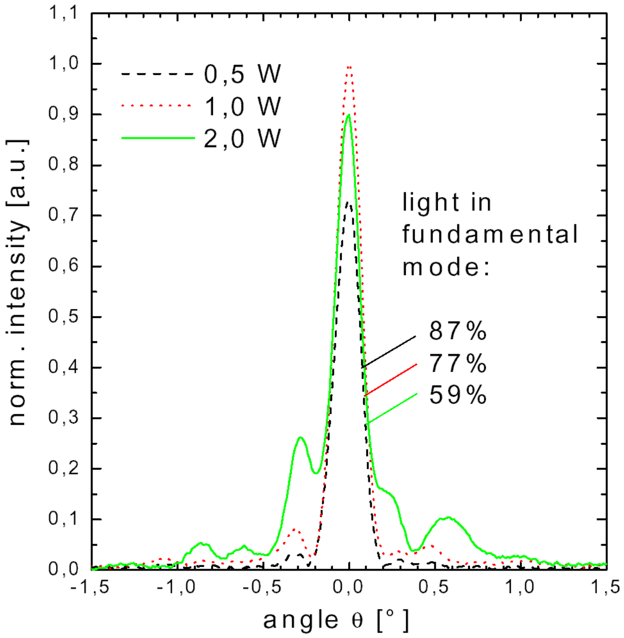

Fig. 5.5. Effective far field of the slow axis emission from the tapered diode laser (TDL) at different output powers.

5.1.2.1. Diode-pumped Yb(5%):KYW femtosecond laser

Using the setup of Fig. 5.3. with the Yb(5%):KYW medium, pulses as short as 101 fs (assuming a $sech^2$-shape) are generated at a center wavelength of 1046 nm with a 5% output coupler. An average output power of 100 mW is measured at a pulse repetition rate of 95 MHz. Figure 5.6. shows the Yb:KYW absorption and emission spectra and the wavelengths pumping and lasing occur at. The observed pulse spectrum and autocorrelation signal are shown in Fig. 5.7. The spectrum exhibits a FWHM of 12.5 nm, so that the pulses are almost Fourier-limited with a time-bandwith product of $\tau_p \cdot \Delta\nu_p = 0.34$.

The slight ripples seen in the spectrum in Fig. 5.7.a and also in the following mode-locked laser spectra in chapter 5 must not to be interpreted as a modulation of the laser output. Actually, they are an artifact caused by a window in front of the CCD array in our spectrum analyzer.

With a 3.5% output coupler a maximum mode-locked output power of 150 mW at 1045 nm is achieved, corresponding to an efficiency of 14% with respect to the absorbed pump power (≈1.1 W near 978 nm), while pulses with a duration τ_p of 134 fs are observed. Output powers of up to 180 mW are also possible, but the laser produces two or more pulses per round-trip time (10.5 ns).

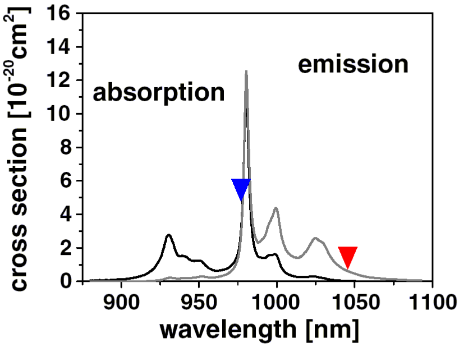

Fig. 5.6. Absorption and emission cross sections of Yb:KYW (light polarization parallel to the N_m crystallo-optic axis). Pump wavelength and central laser emission wavelength are indicated.

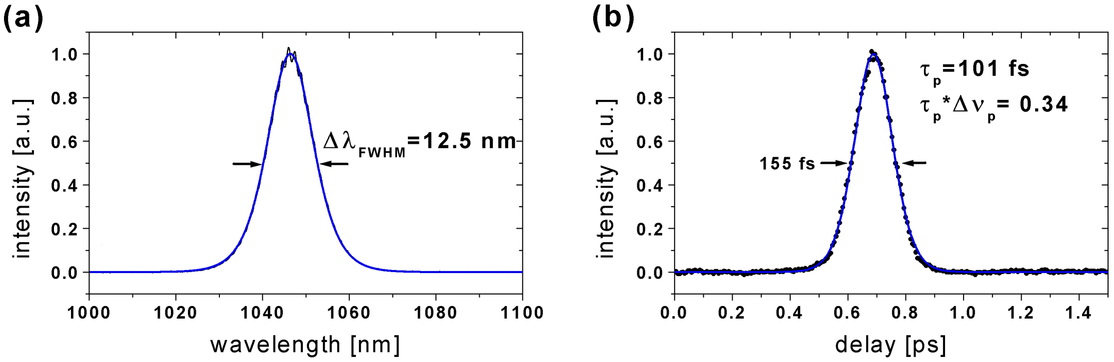

Fig. 5.7. Spectrum (a) and intensity autocorrelation (b) of the Yb:KYW laser at the minimum pulse duration, τ_p = 101 fs.

Self-starting mode-locked operation in a broader wavelength range between 1040 nm and 1070 nm is achieved with a maximum output power of 45 mW at 1053 nm, when an output coupler of 1% transmission is applied. The wavelength can be tuned by adjustment of the laser cavity. In this context, it is important that a change of the resonator loss results in a shift of the spectral position of the overall gain maximum (see chapt. 3.3.1.). Tuning with a knife edge inserted between prism P_2 and the outcoupler M_4 does not work, probably due to too high additional loss in this case. The observed tuning range indicates that a broad gain bandwidth can be exploited for ultrashort pulse generation, permitting pulse durations below 50 fs. For this purpose higher pump powers have to be applied, the gain spectrum must be equalized appropriately and single-pulse mode-locked operation has to be forced.

Mode-locking stability

In the present laser the range of usable pump and laser parameters is limited by Q-switching and multi-pulsing tendencies (see chapt. 4.3.). It can possibly be extended by the use of SESAMs suiting our laser better than those available here (higher saturation fluence). At lower intracavity powers the Yb:KYW laser tends to Q-switching operation, since the laser medium is not bleached fast enough during a Q-switch cycle compared to the saturable absorber. Therefore an absorbed pump power lower than 1 W or output couplers of transmission higher than 5% cannot be used for stable mode-locked operation.

The observed tendency towards double or multiple pulse operation, sometimes with irregular spacing between the pulses, is not unusual for solitary ultrashort-pulse laser systems, for SESAM-mode-locked as well as for Kerr-lens mode-locked lasers including the Yb:KYW laser in [Liu01]. Multiple pulsing behavior results from too strong saturation of the saturable absorber, as the intensity in the absorber is too high. Then, a splitting of the circulating pulse will increase the absorber loss only slightly, but the gain filtering loss will be significantly reduced. Due to the high intracavity power, multiple pulsing can hardly be avoided in our Yb:KYW laser for an output coupler transmission lower than 3.5%.

5.1.2.2. Diode-pumped Yb(5%):KGW femtosecond laser

The Yb(5%):KGW laser generates pulses with a minimum duration of 112 fs at an output power of ≈110 mW, if an outcoupler with a transmission of 3.5% is applied. Figure 5.8. shows the Yb:KGW absorption and emission spectra and the wavelengths pumping and lasing occur at; Fig.5.9. presents the pulse spectrum centered at 1045 nm and the autocorrelation signal. The spectral bandwidth (FWHM) of 11.7 nm corresponds to a time-bandwith product close to the Fourier limit, $\tau_p \cdot \Delta\nu_p = 0.36$. By a different adjustment a maximum output of 120 mW can be achieved, while the pulse duration is slightly increased to 131 fs. Using a 5% output coupler does not lead to stable mode locking. Aside from this, the stability of the pulse generation against Q-switching and multiple pulsing is similar to that of the Yb:KYW oscillator.

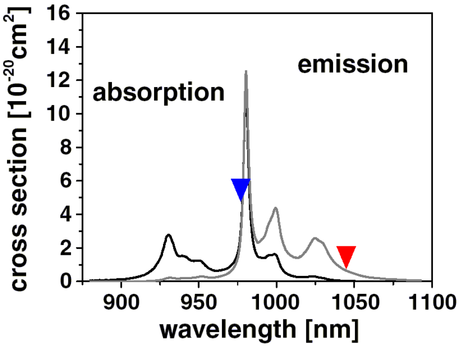

Fig. 5.8. Absorption and emission cross sections of Yb:KGW (light polarization parallel to the N_m crystallo-optic axis). Pump wavelength and central laser emission wavelength are indicated.

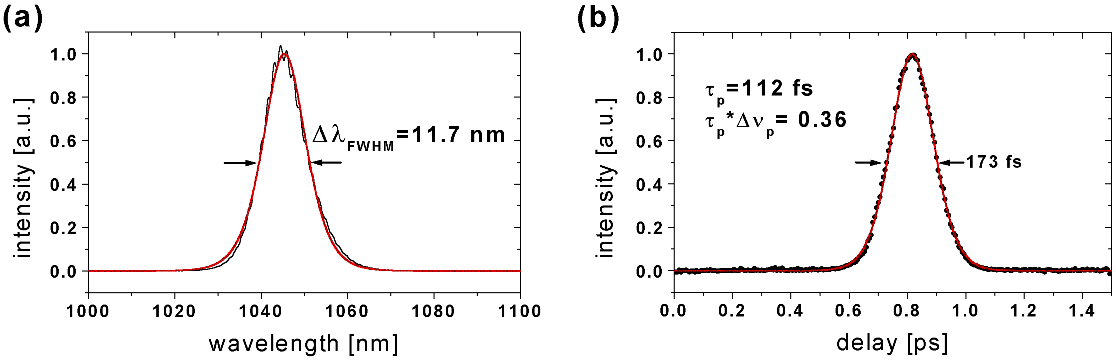

Fig. 5.9. Spectrum (a) and intensity autocorrelation (b) of the Yb:KGW laser at the minimum pulse duration, τ_p = 112 fs.

5.1.2.3. Diode-pumped Yb:glass femtosecond laser and comparison

To use the 6 mm-thick 5 wt.%-Yb_2O_3-doped phosphate glass medium in the laser configuration of Fig. 5.3., we operate the TDL at a wavelength near 975 nm, which is the absorption maximum of the Yb:glass (see Fig 5.10.). With a 3.5% output coupler, we obtain a maximum power of $\approx$150 mW from the mode-locked laser, observing a pulse duration of 181 fs. Stable mode locking is also possible with an output coupler transmission of 1%. In this case, we achieve pulses as short as 72 fs (autocorrelation trace in Fig. 5.11.a). The 17.1-nm-broad laser spectrum (FWHM, Fig. 5.11.b) corresponds to a time-bandwith product of $\tau_p \cdot \Delta\nu_p = 0.32$.

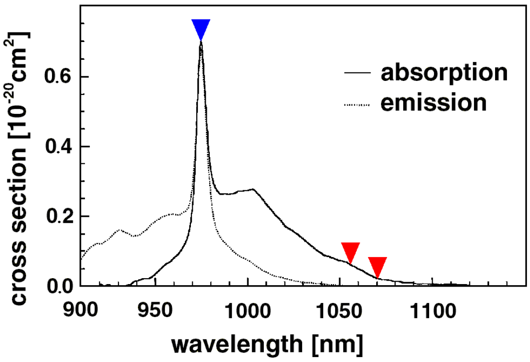

Fig. 5.10. Absorption and emission cross sections of Yb:phosphate glass (taken from [Hoe99b]. Pump wavelength and central laser emission wavelengths observed with 1% and 3.5% output couplers are indicated.

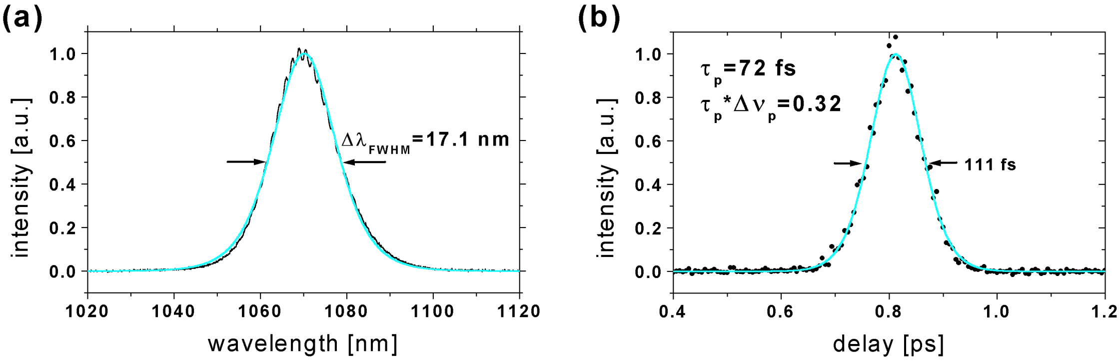

Fig. 5.11. Spectrum (a) and intensity autocorrelation (b) of the Yb:glass laser at the minimum pulse duration, τ_p = 72 fs.

Comparison of Yb^{3+} femtosecond laser performance in tungstate and glass hosts

The results obtained with the 3-mm-thick 5% Yb^{3+}-doped KYW and KGW crystals and the 6-mm-thick 5% Yb_2O_3 doped phosphate glass medium are listed in Table 3.5.

The upper three rows of Table 5.3. show that similar maximum output powers, around 150 mW, are achieved from all three laser materials. This is also valid, if we take into account that slightly higher output powers (180 mW with Yb:KYW) are possible in case of multiple-pulse mode-locked operation.

While a similar performance can be expected for the 5% Yb^{3+}-doped tungstate crystals due to their almost identical material characteristics, the fact that the output power of the Yb:glass is not exceeded reflects that the theoretical advantages of Yb:KYW and Yb:KGW do not play a significant role at the present thicknesses of the active media and at the available pump powers and wavelengths. Instead, the comparison indicates the stronger reabsorption at the obtained laser wavelengths in the tungstates at room temperature, which can also be deduced from the absorption spectrum (Fig. 5.8.). The differential conversion efficiencies of our mode-locked lasers cannot be determined and it is not possible to estimate the absorbed pump powers at the lasing threshold, since the wavelength of the laser diode is not stabilized and therefore the pump light absorption in the active media decreases rapidly with decreasing diode current (– we will solve that issue in the Yb:scandia experiments presented in the next chapter). We may, however, take the threshold pump power, approximately 450 mW, observed for the cw laser with the same Yb(5%):KYW crystal and the 3.5% output coupler (chapter 3.1.3.), as a lower limit here, noting that the cw oscillator does neither contain prisms nor a SESAM, which produce additional losses. Therefore it is evident that our mode-locked Yb:tungstate lasers operate relatively close to their lasing thresholds, i.e. the lasing threshold consumes a large part of the available pump power (1.1 W) and the reabsorption influence on the slope efficiency is not bleached (chapter 3.3.). Furthermore, reducing reabsorption is necessary to run Yb:KYW and Yb:KGW at shorter emission wavelengths; in combination with longer pump wavelengths a very low laser quantum defect and low heat production are achievable (see chapter 5.2.1.4.). This and the better thermal conductivity compared to the glass would become advantageous at higher pump powers.

Table 5.3. Performance of diode-pumped Yb:KYW, Yb:KGW, and Yb:phosphate glass femtosecond lasers. Bold: Maximum output powers, minimum pulse durations. The absorbed pump power is ≈1.1 W in all cases. T_{OC} – output coupler transmission, P_{out} – output power, λ_{laser} – central laser wavelength, $\Delta\lambda_{FWHM}$ – laser emission bandwidth, τ_p – pulse duration assuming a *sech*^{2}-shape, $\tau_p \cdot \Delta\nu_p$ – time-bandwidth product.

T_{OC} [%]	laser material	P_{out} [mW]	λ_{laser} [nm]	$\Delta\lambda_{FWHM}$ [nm]	τ_p [fs]	$\tau_p \cdot \Delta\nu_p$
highest output powers						
3.5	Yb:KYW	**150**	1045	9.5	135	0.35
3.5	Yb:KGW	**120**	1045	10.5	131	0.38
3.5	Yb:glass	**150**	1056	6.6	181	0.32
shortest pulses						
5.3	Yb:KYW	100	1046	12.5	**101**	0.34
3.5	Yb:KGW	110	1045	11.7	**112**	0.36
1.0	Yb:glass	25	1070	17.1	**72**	0.32

Concerning the minimum pulse durations, which are listed in three lower rows of Table 5.3., the use of the Yb:KYW and Yb:KGW crystals again leads to similar results, 101 fs and 112 fs. The pulses from the Yb:glass medium are somewhat shorter, $\tau_p = 72$ fs (almost as short as the 58-fs pulses from the Yb:glass bulk laser demonstrated in [Hoe98]).

We must note that the tendency of the mode-locked lasers towards multiple pulsing demands the choice of individual output coupler transmissions T_{OC} for the different active media in this context. Stable single pulses – one per round-trip time – are produced with $T_{OC} = 5.3\%$ for Yb:KYW, $T_{OC} = 3.5\%$ for Yb:KGW and $T_{OC} = 1\%$ for Yb:glass. For the tungstates, a transmission of 1% results in a split-up of the pulses and therefore in decreased pulse energies. In a solitary mode-locked laser system the pulse durations and emission bandwidths are related to the pulse energies, so that a split-up means longer pulses with a narrower spectrum (chapter 4.1.). We refer the better stability and therefore the shorter duration of the pulses obtained with the Yb:glass sample to the smoother net gain spectrum of the glass. The smaller gain bandwidth of the Yb tungstates produces higher loss by gain filtering and therefore favors longer pulses more strongly.

Further development of mode-locked Yb:tungstate lasers

Since the double tungstates Yb:KYW and Yb:KGW are relatively new laser materials, especially for mode-locked lasers, there are still only a few results by other research groups to compare our femtosecond laser data with. Ultrashort pulse lasers using Yb:KGW in similar cavity designs with passive mode locking by a saturable absorber mirror (SESAM) were demonstrated by Brunner et al. [Bru00] and Major et al. [Maj02]. Liu et al. [Liu01] showed the operation of a Kerr-lens mode-locked Yb:KYW laser. In all three cases the active media were pumped by broad stripe diodes. Here we present what is to our knowledge the first laser using Yb:KYW with a SESAM for a self-starting mode-locking process, and for the first time a novel tapered diode laser (TDL) is introduced as a high brightness source pumping Yb^{3+}-doped potassium gadolinium and yttrium tungstates.

The shortest pulse durations achieved by us, $\tau_p = 101$ fs (Yb:KYW) and 112 fs (Yb:KGW), are in the range of the minimum durations achieved in [Liu01], $\tau_p = 71$ fs (Yb:KYW), and in [Bru00], $\tau_p = 112$ fs (Yb:KGW). The pulses provided by the Yb:KGW laser in [Maj02] were somewhat longer with a duration of 169 fs.

Our maximum mode-locked output power (150 mW) does not exceed that in [Bru00] (1.1 W) and [Liu01] (190 mW), but our results are obtained using only 1.1 W of incident pump power ([Bru00]: 4 W, [Liu01]: 2.6 W) and by a simpler arrangement with pumping from one side only. Compared to the Yb:KYW laser in [Liu01], we increase the conversion efficiency by almost a factor of two. Pumping with a 100 µm-broadstripe diode laser and roughly 1 W of incident pump power, Major et al. [Maj02] achieved only 18 mW. This indicates the favorable beam quality of the TDL.

We have also performed an experiment with our Yb:KGW femtosecond laser using a 200 µm broadstripe diode laser with matched pump shaping optics replacing the TDL. The incident pump power amounts to 1.8 W and is absorbed effectively ($\lambda_{pump} \approx 980$ nm), but the beam quality factor of $M^2 \approx 30$ in the slow axis direction does not permit more than 100 mW of mode-locked output (at a pulse duration of 160 fs) instead of 120 mW with 1.1 W of TDL pump light.

From this we conclude that the further development of powerful high brightness diode pump sources like the TDL presented here is very important for an effective use of Yb:KYW and Yb:KGW, because high pump and laser intensities are advantageous to overcome the strong reabsorption loss in these materials. We have tried to double the available pump power in our experiments by the use of a second diode laser pumping the active medium from the opposite side, but we have found that TDLs are very sensitive to incident radiation. Non-absorbed pump power from the other diode or even feedback <0.1 mW strongly effects the spectral and spatial characteristics of the TDL, preventing stable Yb:tungstate laser operation, and damage of the diode is also possible. A Faraday isolator is required here.

The reabsorption influence in Yb:KYW and Yb:KGW could also be encountered by cooling of the laser crystals to reduce the population of the upper-lying ground state Stark sublevels, but at least for commercial laser systems cryogenic operation temperatures are not interesting. Another approach is to decrease the dopant concentration in the crystals as much as possible. Considering that about 98% of the incident pump power are absorbed in our laser media, 1-2% Yb^{3+} should be enough and more appropriate for 3-mm-long tungstate crystals. However, in this case a stabilization of the diode wavelength at the absorption maximum of the laser crystal is advisable to avoid fluctuations or shift of the absorbed pumped power. We will realize such a stabilization for the lowly doped Yb:scandia ultrashort-pulse laser in chapter 3.2. The opposite way might be even better, especially for high power lasers: to choose high doping levels while reducing the crystal thickness as far as possible, ending up with a thin-disk laser design. In this context our results with highly Yb^{3+}-doped tungstates including the cw lasing of stoichiometric KYbW are very promising (chapter 5.2.). The thin-disk laser concept offers excellent cooling, easy matching of pump and laser mode and large power scalability. The applicability of the concept to a passively mode-locked Yb:KYW laser has been demonstrated by Brunner et al. [Bru02], who achieved 22 W of output power at a pulse duration of 240 fs from a 160-µm-thin medium, which was pumped by 100 W from fiber-coupled diode bars using a 24-pass-pumping scheme.

5.2. Highly Yb^{3+}-doped KYW and stoichiometric KYbW experiments

In this chapter, quasi-cw and cw lasing of tungstates with high Yb^{3+} concentration is investigated. Important issues are if high Yb^{3+} concentrations in a tungstate host still permit a good optical crystal quality and if the heat produced in the relatively small active volumina of highly doped crystals can be handled.

For the first time, laser operation of tungstates with an Yb^{3+} doping level considerably higher than 20% and of the stoichiometric material KYbW is achieved, using a quasi-cw regime (chapters 5.2.1.1.-5.2.1.3.). While reducing thermal problems by pumping a KYbW laser crystal above the mean wavelength of fluorescence, we demonstrate the smallest laser quantum defect ever for a laser crystal, 1.6% (chapter 5.2.1.4., [Klo03]). Finally, with a face-cooled KYbW crystal platelet, the first cw lasing of a stoichiometric Yb laser material is demonstrated (chapter 5.2.2., [Klo03c, Klo03d]).

5.2.1. Quasi-cw operation of highly doped KYW and KYbW

Using highly doped or stoichiometric Yb tungstate crystals with no special meanings of cooling, strong heat-related effects occur. To avoid a damage of the crystals, we have to reduce the incident average pump power by chopping the pump beam. The thermal problems are documented in chapter 5.2.1.3. for the case of KYbW. The quasi-cw experiments take place in the setup shown in Fig. 5.12.

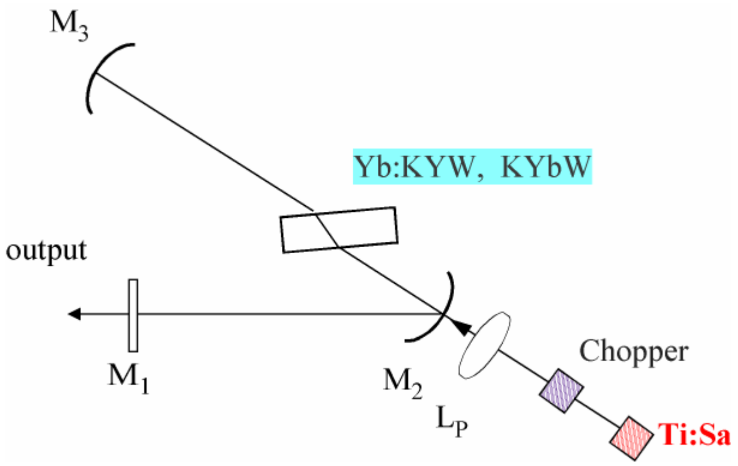

Fig. 5.12. Experimental setup for quasi-cw lasing of higly doped and stoichiometric Yb double tungstates.

The "V"-folded cavity in Fig. 5.12. employs a flat output coupler M_1 with a transmission of ≈1% at 1060nm, a folding mirror M_2 ($r = -100$ mm), through which the crystal is pumped, and an end mirror M_3 ($r = -100$ mm). The Yb:KYW and KYbW crystals are attached to a sheet of copper and used at the Brewster angle (about 64°) to avoid Fresnel loss at their uncoated surfaces. In case of the approximately 500-µm-thin crystal platelets, the folding angle is chosen to compensate for astigmatism from the Brewster configuration; for the 200-µm- and 125-µm-thin samples the angles cannot exactly be matched because of geometrical limitations, but the astigmatic error is supposed to be small.

Crystal orientation

All crystals have been cut and polished in the (010) plane, which is a natural surface (see chapt. 2.4., Fig. 2.4.), i.e. the $\boldsymbol{N_p}$ crystallo-optic axis (parallel to the [010] direction) is normal to the crystal faces. Pump light absorption is maximized by orienting the samples for the $\boldsymbol{N_m}$ crystallo-optic axis lying in the plane of the pump light polarization, so that the pump and KYbW laser electrical field vectors are roughly parallel to $\boldsymbol{N_m}$ and propagation occurs basically along $\boldsymbol{N_p}$.

Actually, the Brewster angle slightly modifies the absorption and emission cross sections, since the electrical field vectors are ≈26° tilted towards the $\boldsymbol{N_p}$ axis. This means, the effective cross sections $\sigma_a(Br)$ and $\sigma_e(Br)$ are given by $\sigma_{a/e}(Br) = cos^2(26.2°)\sigma_{a/e}(N_m)+sin^2(26.2°)\sigma_{a/e}(N_p)$ (for tabulated values of $\sigma_a(Br)$ and $\sigma_e(Br)$, see appendix a.9.). All gain calculations presented in this chapter take this into account; however, if we assumed purely $\boldsymbol{N_m}$-polarized beams – the case for normal incidence – this would lead to only small errors concerning lasing thresholds and population inversions. Another consequence of the use at Brewster angle is that the active path length is the crystal thickness times $1/cos(26.2°)$, i.e. for a 500-µm-thin sample the actual active length is about 557 µm.

Pump laser

Our pump source is a home-made cw Ti:Sapphire laser (Ti:Sa), which is pumped by up to 20 W (all lines) of an Ar ion laser. Depending on the choice of its outcoupler the Ti:Sa can be optimized for emission in the range from 915 to 990 nm delivering more than 2 W or from 960 to 1025 nm delivering more than 1.5 W of output power. The Ti:Sa emission is tuned and narrowed to a linewidth <1 nm by a 3-plate birefrigent filter. The pump laser beam from the Ti:Sa is chopped with a duty cycle of 4%, if not stated otherwise. A lens L_p ($f = 62.5$-mm) focusses the pump radiation onto the laser medium, at whose position a waist of ≈30 µm is measured.

5.2.1.1. Yb(60%):KYW quasi-cw laser

The first successful laser experiments with highly doped ytterbium tungstates are performed with a 200-µm-thin 41% Yb^{3+}-doped KYW crystal and already demonstrate the problems to cope with when using such materials. A relatively thin sample is necessary to make the reabsorption loss of the laser emission sufficiently small and reach the lasing threshold (chapter 3.3.2.). Due to heat up of the sample, cw pumping would not permit laser operation, and pumping at wavelengths close to the absorption maximum would neither, due to the strong and very uneven pump absorption in the crystal ("uneven": pump power is almost completely absorbed close to the entrance surface). Instead, such pumping conditions can harm the crystal. The 60% and 80% doped Yb:KYW and the KYbW samples in the following chapters show similar behavior.

Using the quasi-cw setup of Fig. 5.12. with pumping near 930 nm, we achieve laser operation of the Yb(41%):KYW platelet at an emission wavelength of 1054.5 nm. Unfortunately, the crystal fatally cracks, preventing a detailed investigation. A slightly thicker crystal seems to be more rigid, surviving a damage without breaking apart, so that all further TSSG grown crystals are polished to a thickness of approximately 500 µm.

A 510-µm-thin Yb(60%):KYW sample is investigated with different pump wavelengths λ_{pump} (see Fig. 5.13. for position in the absorption spectrum). The laser performance is shown in Fig. 5.14. The given absorbed pump and output powers are average values, obtained when the pump beam is chopped with a pulse frequency of approximately 110 Hz at a duty cycle of 4%.

The incident pump power at the crystal (pump beam waist: 30 µm) is in the order of the pump saturation power (see appendix, Table a.3.). However, since the absorption length is between 180 and 380 µm and since in a running laser the effect of the stimulated emission increases the pump saturation power, saturation plays a negligible role for the absorbed pump power P_{abs}. For the estimation of P_{abs} we take into account that part of the pump radiation which is not absorbed by a single pass through the crystal, but is then reflected by the end mirror M_3 (Fig. 5.12.), and experiences a second pass.

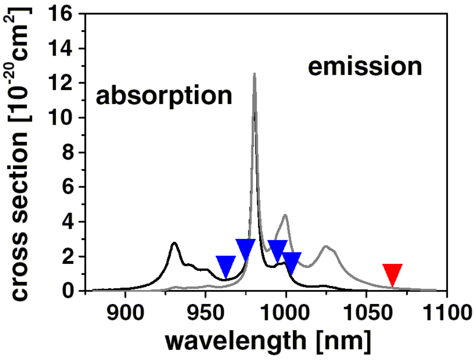

Fig. 5.13. Absorption and emission cross sections of Yb:KYW (light polarization parallel to the N_m crystallo-optic axis). Pump wavelengths and laser emission wavelength are indicated. Pumping near the absorption maximum at 981 nm would not permit lasing but damage the crystal instead.

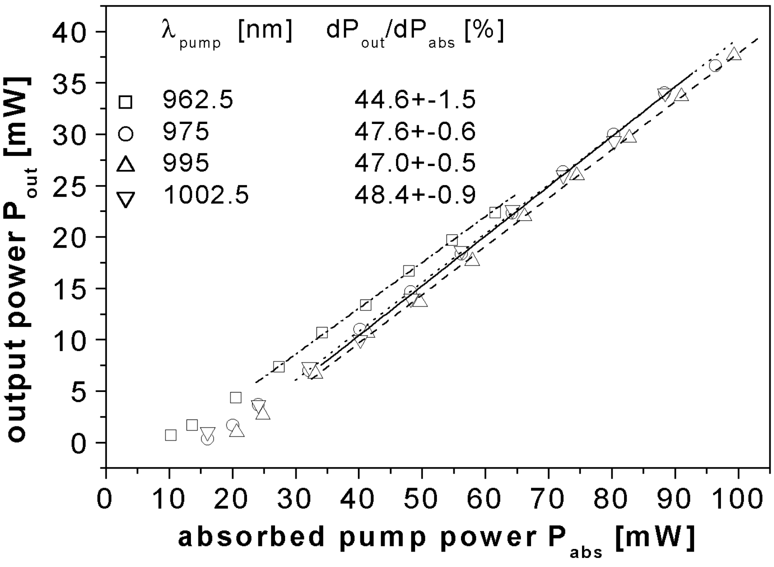

Fig. 5.14. Quasi-cw laser performance of Yb(60%):KYW. Average output power at 1067 nm versus absorbed pump power for four pump wavelengths between 962.5 nm and 1002.5 nm. The Ti:Sapphire pump laser is chopped with a duty cycle of 4%.

The slope efficiencies are very similar, between 45 and 48%, for all four pump wavelengths. The maximum Yb:KYW output power of 38 mW is achieved at an absorbed pump power of ≈100 mW. We observe a basically TEM_{00} output.

The laser emission occurs at a wavelength λ_{laser} = 1067 nm (see red mark in Fig. 5.13.) in case of the 1.1%-transmissive output coupler used here, which delivers the highest output powers. Higher output coupling loss shifts the emission to shorter wavelengths (1049 nm at 5.2% outcoupling), with lower loss the shift goes to longer wavelengths (1074 nm at 0.4%). This is a typical behavior for quasi-three-level materials (chapter 3.3.2.).

Estimated gain and threshold pump power

Assuming a free running laser excluding additional filtering mechanisms, we can refer the emission wavelength at 1067 nm to the gain maximum which exists, when $\beta_{avV(l)} = (3.2\pm0.1)\%$ of the total Yb^{3+} ion population averaged over the laser mode volume are in the upper manifold (see chapt. 3.3.2., Fig. 3.3.). From the inversion parameter $\beta_{avV(l)}$ we can estimate a gain cross section $\sigma_g = (0.0029\pm0.0002) \times 10^{-20}$ cm^2 and a round-trip gain of $G = 2\,N\,L\,\sigma_g = 0.013\pm0.001$. This value of G seems to be realistic. In connection with the outcoupling loss T of 1.1% it indicates additional loss Λ in the order of 0.2%.

Using eq. 3.69.a with $\tau_f = 0.2$ ms, $h\nu_p = 2 \text{ x } 10^{-19}$ J, and assuming equal waists of pump and laser $w_p = w_l = 30$ µm, we calculate an absorbed pump power of ≈200 mW at laser threshold. In case of our chopped pump this means an average power of ≈8 mW, which agrees with the value experimentally obtained at λ_{laser} = 962.5 nm (see Fig. 3.2.).

The higher threshold pump powers at the other pump wavelengths might be caused by thermal effects, since the absorption coefficients are higher than at 962.5 nm and make the intensity of the pump light drop fast along its path through the crystal. The estimated inversion parameter $\beta_{avV(l)}$ is an average value and this means that in case of strong absorption one side of the crystal will show a significantly higher inversion than the other. It is plain to see that the high-inversion side will experience a heavier heat load.

Influence of thermal effects

All calculations are based on room temperature spectra. Heat up of the crystal changes the Boltzmann distributions of the ground and excited states and therefore can be expected to increase the reabsorption, to decrease the population of the upper laser Stark level, and therefore to increase the laser threshold. However, this effect seems to be small (or it effects the gain non-selectively, not shifting the wavelength of the maximum gain), since the lasing wavelength remains basically constant (change <1 nm), when the pump power is varied between the threshold and 10 times above the threshold.

Other thermal effects are lensing and birefringence, which can worsen the performance. Actually, worsened performance should include the threshold, but also the slope efficiency. Another aspect of higher local inversion is that some loss processes related to impurities and defects depend nonlinearly on the upper state population (see appendix A.1.) and will therefore not be averaged out considering the whole active medium. Heat up and nonlinear loss processes might also help to understand the crystal damage which occurs when highly doped Yb:KYW or KYbW is pumped close to 981 nm.

Indepently from the pump wavelength, there are other uncertainties with the threshold calculation: Measurements of the exited state lifetime do not exist for highly doped Yb:KYW, $\tau_f = 0.2$ ms is the value measured for KYbW [Puj02b]. If the Yb^{3+} upper state lifetime of Yb(60%):KYW is longer (lowly Yb^{3+}-doped KYW: 0.3 ms), the threshold pump power should be accordingly lower. Crystal quality and purity can influence τ_f (worse – shorter).

Estimations concerning slope efficiency

An analysis of the achieved slope efficiencies based on the work of Risk [Ris88] (see also chapter 3.3.3.) does not yield results which are fully consistent, if we use the same assumptions as for the estimations related to the lasing threshold: For a ratio $a = w_p/w_l = 1$ of pump beam waist w_p and laser beam waist w_l, a ratio $B = \sigma_a(\lambda_l)/\sigma_g(\lambda_l) = 0.00321/0.0029 \approx 1.1$, an outcoupler transmission of 1.1%, and 0.2% additional cavity loss, we should expect considerably larger slope efficiencies (about 75%, while operating at pump powers >5 times above the lasing threshold). This discrepancy is observed similarly in the other experiments with highly doped and stoichiometric Yb tungstates which are performed with the same pump source and in the same laser resonator (chapters 5.2.1.2., 5.2.1.3.).

A reason for the discrepancy could be that the assumption of equal pump and laser waists $w_p = w_l = 30$ µm only roughly describes the actual experimental conditions. The pump beam waist diameter of 30 µm was measured using pinholes, which do not deliver information about a possible ellipticity of the pump beam. Our present setup does not permit to experimentally determine the laser beam waist. Actually, in case of non-optimum laser adjustment or to match an elliptical pump beam the resonator mode might be astigmatic.

The equality of pump and laser waists is assumed as a consequence of the numerical calculations presented in [Ris88] (see also chapt. 3.3.3.). These predict, that if the reabsorption loss is larger than the fixed cavity loss and if the pump power is many times above the lasing threshold, the slope efficiency will be maximized by exactly matching the pump and laser beams, $w_p = w_l$. Adjustment of the laser for maximum output would lead to this situation. Risk's calculations consider radially symmetric TEM_{00} beams only.

From Risk's curves one can deduce $w_p/w_l > 2$ for our (external) slope efficiency of ≈45%, i.e. the laser beam waist should be 15 µm or smaller. There are two arguments against this: The laser threshold absorbed pump power would be about 5 mW average, lower than observed. Assuming no astigmatism, $w_p/w_l > 2$ does not agree with an adjustment of the laser for optimum output power.

Another possible reason for the relatively low slope efficiencies is that the additional cavity loss might be larger than the value of 0.2% estimated above. A value of 1% would lead to the observed slope efficiencies, but require an accordingly higher gain and correspond to a shorter laser emission wavelength, if no filtering effects aside from the gain exist.

5.2.1.2. Yb(80%):KYW quasi-cw laser

Figure 5.16. shows the output power obtained with a 420-µm-thin Yb(80%):KYW sample with a 0.94%-transmissive outcoupler in the same laser cavity and with the same chopping of the pump as used for the 60%-doped crystal. The pumping wavelength is 962.5 nm, laser emission

occurs at 1068 nm (see Fig. 5.15.). A slope efficiency of about 35% is achieved, with a laser threshold of approximately 15 mW.

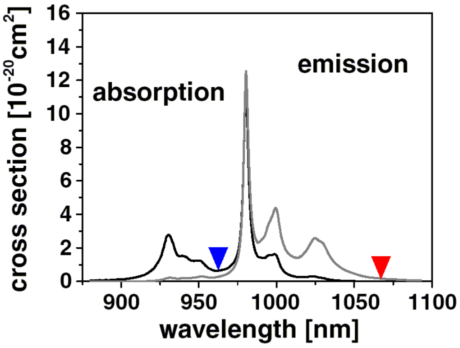

Fig. 5.15. Absorption and emission cross sections of Yb:KYW (light polarization parallel to the *N_m* crystallo-optic axis). Pump and laser emission wavelengths are indicated.

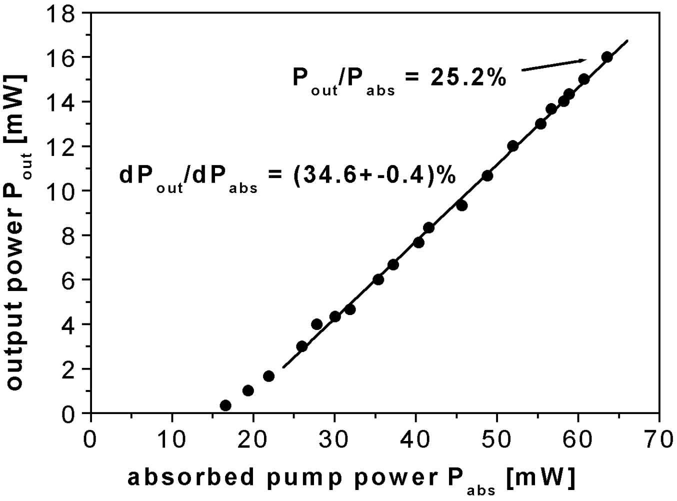

Fig. 5.16. Quasi-cw laser performance of Yb(80%):KYW. Average output power at 1068 nm versus absorbed pump power at 962.5 nm. The Ti:Sapphire pump laser is chopped with a duty cycle of 4%.

The emission wavelength corresponds to an inversion parameter $\beta_{avV(l)}$ of (3.1±0.1) %, a gain cross section σ_g of (0.0026±0.0002) x 10^{-20} cm^2, and a round-trip gain G of 0.0125±0.001. With the outcoupling loss $T_{OC} = 0.94\%$, this indicates additional loss Λ in the order of 0.3%. The average absorbed pump power (4% duty cycle) to reach the lasing threshold is estimated to be ≈9 mW, using the same assumptions as for the 60% doped Yb:KYW. For a detailed discussion on what might effect threshold and slope efficiency see chapt. 5.2.1.1.

While we had a relatively good agreement of estimated and experimentally observed threshold pump power at 962.5 nm with the 60% Yb^{3+}-doped crystal, the higher than estimated experimental value with the 80% doped sample could possibly be caused by lower crystal quality. Another explanation could be that heat effects by uneven pumping along the path in the crystal are significantly more important in the more highly doped material. The somewhat lower slope efficiency (35%) compared to those of the Yb(60%):KYW experiment (about

45-48%) can be referred partially to the slightly lower outcoupling T_{OC} (0.94% against 1.1%); higher intrinsic losses in the crystal may also contribute.

5.2.1.3. KYbW quasi-cw laser

After the successful laser experiments with 41% to 80% Yb^{3+}-doped KYW, now the question is can we achieve laser operation and similar performance with "100% Yb^{3+}-doped KYW" – the stoichiometric material KYbW. Top seeded solution grown (TSSG) and Kyropoulos grown KYbW samples will show if they provide the necessary crystal quality and if the extremely high Yb^{3+} ion concentration of 6.4×10^{21} cm^{-3} causes problems. Difficulties can arise from the concentrated heat generation in a very small crystal volume and from the fast migration of the excitation energy in the crystal (chapter 2.3.).

Starting with quasi-cw laser operation and aiming at cw lasing, we investigate methods to reduce the heat generated in the crystal: optical pumping above the mean wavelength of fluorescence and decreasing the crystal thickness, which reduces the reabsorption loss and therefore the pump power required to reach the lasing threshold.

Again the „V-shaped" laser cavity of Fig. 5.12. is used. The active medium is a 500-µm-thin TSSG KYbW crystal. By an appropriate choice of the Ti:Sa and KYbW laser mirrors, the setup is configurated for a pump wavelength λ_{pump} first in the region from 915 to 990 nm, then from 962 to 1025 nm. Using the first configuration laser operation can be achieved between $\lambda_{pump} = 915$ nm, the lower limit of the Ti:Sa tuning range, and $\lambda_{pump} = 974$ nm, with thermal effects not permitting lasing above this wavelength.

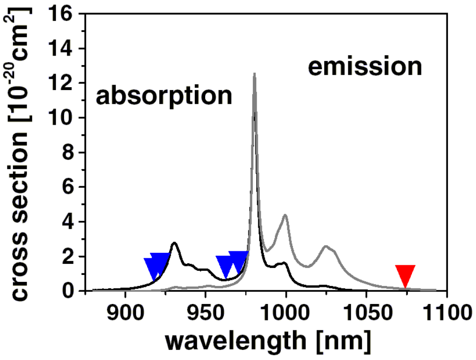

Fig. 5.17. Absorption and emission cross sections of KYbW (light polarization parallel to the N_m crystallo-optic axis). Pump and laser emission wavelengths are indicated.

The lasing efficiencies are determined with a 0.9%-transmissive outcoupler at two pump wavelengths, 922 nm and 962.5 nm (second and third blue mark in Fig. 5.17.), at a pump chopping frequency of 109 Hz and a pump duty cycle of 4%. The intensities of the pump pulses on the KYbW crystal (pump waist size: 30 µm), are in the order of the pump saturation intensities (see Table a.4., calculated for an excited state lifetime of 0.2 ms). However, since the absorption lengths, 195 µm at 922 nm and 230 µm at 962.5 nm, are considerably shorter than the active length in the KYbW crystal, 557 µm, and since stimulated emission decreases the lifetime of the upper laser state, pump saturation is negligible and 94% (922 nm) or 91% (962.5 nm) of the incident pump radiation are absorbed.

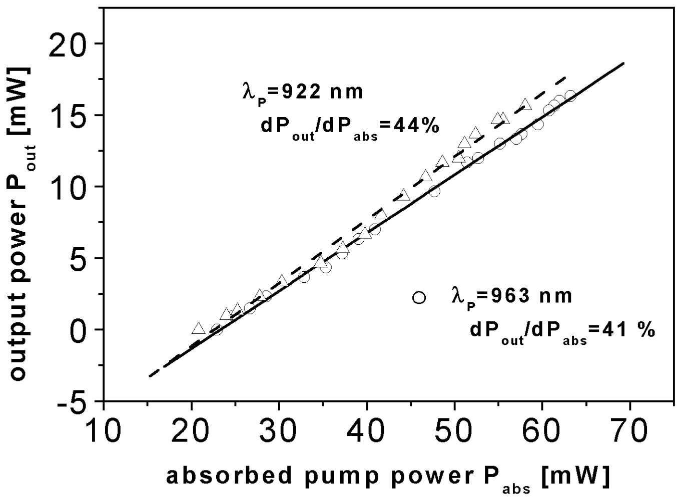

Fig. 5.18. Average output power of the quasi-cw KYbW laser versus average absorbed pump power for two pump wavelengths and a duty cycle of 4%.

Figure 3.4. displays laser slope efficiencies of 44% in case of 922-nm-pumping and 41% for 962.5-nm-pumping, both with respect to the absorbed pump power. The maximum optical-to-optical conversion efficiency amounts to 26-27% in both cases, corresponding to the maximum average output power of approximately 16 mW at ≈60 mW of average absorbed pump radiation. The laser threshold is reached at about 20 mW of absorbed power. KYbW lasing occurs at λ_{laser} = 1074 nm, i.e. very far in the red-wing of the emission spectrum (see Fig. 5.17.).

The 0.9% output coupling used is optimum for this laser. We observe that the output power drops to 60% of its maximum value when using an output coupler with less (0.6%) transmission and to 30% for an output coupler with higher (1.9%) transmission.

An estimation based on λ_{laser} as the free-running laser wavelength leads to a population of the upper laser multiplet of $\beta_{avV(l)}$ = 2.5% relative to the total number of Yb^{3+} ions, to a round-trip gain of 1.2% (±0.1%), and – taking into account the output coupler transmission T = 0.9% – to additional loss in the order of 0.3%. These values seem to be realistic.

The pump power required at the lasing threshold is estimated to be 265 mW, which means ≈11 mW of average pump power in our case of chopped pumping. The fact that the measured threshold pump power is about twice this value, can be referred again to thermal effects. Concerning the theoretically expected slope efficiencies the same is valid as for the other highly doped tungstates – they are higher than experimentally observed – and the same reasons as considered in chapter 5.2.1.1. could be responsible for this discrepancy. However, one should note that our KYbW slope efficiencies of approximately 40% are considerably higher than the slope efficiency of 27% presented in [Pat01] for a quasi-cw laser using YbAG, the other known stoichiometric laser material.

Comparison of 60%, 80% and “100%” Yb^{3+}-doped tungstates

Comparing the performance of the three differently doped tungstate crystals (Table 5.4.), one finds similar slope efficiencies, roughly about 40%. From that we may conclude on the one hand that in case of the investigated TSSG grown samples no observable problems (quenching) result from an increasing Yb^{3+} concentration. On the other hand the stoichiometric crystal does not seem to have the significantly advantageous crystal quality that one might have expected because of the uniformity of ions at the crystal sites which are inhabited only by Yb^{3+}.

Differences can be observed concerning the lasing threshold pump powers, if one compares the three crystals at a fixed pump wavelength λ_{pump} = 962.5 nm. The values increase with the Yb^{3+} concentration, about 10 mW, 15 mW, 20 mW. This behavior can be explained only partially by the increasing reabsorption of laser light by the ground state Boltzmann population, since the calculated thresholds, 8 mW, 9 mW, and 11 mW, do not differ so much; here we have to remember that the self-adjustment of the lasing wavelengths tends to minimize reabsorption loss, with λ_{laser} = 1067 nm, 1068 nm, and 1074 nm, respectively. We refer the increasing deviation of the experimental threshold pump powers from the theoretical values to the increasingly uneven absorption of the pump light, a consequence of the decreasing absorption length l_a. (Actually, the l_a of KYbW at λ_{pump} = 962.5 nm is approximately as short as the l_a of Yb(60%):KYbW at wavelengths at which the measured threshold pump powers are also twice the theoretical values.)

Table 5.4. Performance of TSSG grown Yb tungstate crystals. All crystals were used at the Brewster angle with an output coupler transmission of ≈1% and pumped at λ_{pump} = 962.5 nm with a duty cycle of 4%. $l_{a,Br}$ *(962.5 nm)*, pump absorption length at the Brewster angle.

crystal	**thickness**	**$l_{a,Br}$ (962.5 nm)**	**λ_{laser}**	**calculated threshold**	**experiment. threshold**	**slope efficiency**
Yb(60%):KYW	510 µm	380 µm	1067 nm	8 mW	≈10 mW	45%
Yb(80%):KYW	420 µm	290 µm	1068 nm	9 mW	≈15 mW	35%
KYbW	500 µm	230 µm	1074 nm	11 mW	≈20 mW	41%

Crystal quality

However, with these interpretations it has to be mentioned that all our TSSG grown tungstate crystals are not homogeneous, i.e. the values of output power and the laser threshold depend on the used part of the respective crystal. Furthermore, at the pumped crystal zone one can see a blue or bluish-green luminescence, whose intensity varies with the position and is weaker when laser operation starts. The reasons for the observed inhomogenities could be structural imperfections of the crystals – which have not been thermally annealed –, non-optimum polishing or inhomogeneously distributed impurities. The Yb_2O_3 used for crystal growth was specified to have a purity of 99.99%, with no data on the composition of the impurities given. While this might be sufficient for lowly doped crystals, for highly doped laser materials purer educts have to be considered and special care has to be taken to prevent contaminations from the crucibles (chapter 2.3.). In the present case, Er^{3+} (or Ho^{3+}) ions can be assumed to have caused green emission via an upconversion process, and/or Tm^{3+} ions could be responsible for a blue upconversion luminescence. Other ions acting as quenchers (Fe, Cr) do not give such clearly visible hints, but might also play a role. Another reason for blue emission could be cooperative luminescence (see overview of loss processes, appendix A.1.).

Heat effects – the curse of high absorption

The pump wavelengths for KYbW, 922 nm and 962.5 nm, have been chosen for maximum output powers in our given laser configuration. Having a look at the absorption spectrum for the used pump light polarization parallel to $\boldsymbol{N_m}$ (see Fig. 5.17.), at 922 nm we find ourselves in the short wavelength region of the absorption spectrum, where absorption is rising with the wavelength. At this position pump light absorption is effective, but not too uneven along the crystal. This is also valid for $\lambda_{pump} = 962.5$ nm, which is located in a dip of the absorption spectrum. The laser efficiency drops for larger absorption cross sections (or shorter absorption lengths) for the pump radiation. If λ_{pump} is approaching the absorption peak at 981 nm, KYbW laser operation will cease already at 974 nm – due to heat effects. This interpretation is supported by the fact that after switching on the pump laser beam there is KYbW laser operation in the beginning, but then lasing vanishes within less than a second.

With lowly doped laser materials, heat would lead to a degradation of laser performance at high pump powers only; with a stoichiometric laser crystal like KYbW or YbAG [Pat01] this problem has to be dealt with already at low pump intensities. We may consider this as the "curse of high absorption". The pump radiation is absorbed in a very small crystal volume and as a consequence, also the heat generation caused by laser and fluorescence quantum defects and by defect- and impurity-related loss processes is concentrated in a very small volume. The pumped zone can be heated up to several hundred degrees [Mue02],[1] resulting in thermal lensing and birefringence, and in quasi-three- or -four-level laser media increasing the reabsorption from ground state population. Furthermore, one could think of color centers as a result of the heat. The worst case is that tensions damage the crystal, and unfortunately this occurs a few times in our experiments when the pumping is chosen at wavelengths close to the absorption maximum.

One should note, in materials with high dopant concentrations excitation energy migrates rather fast within the crystal, and therefore impurities and defects of the crystal structure act as effective sinks for energy (chapter 2.3.). In case of non-perfect crystals, the matter becomes obvious as concentration quenching. With uneven absorption in a crystal which is significantly thicker than the absorption length, inversion too is variing along the pump path within the active medium. For example in the case of $\beta_{avV(l)} = 2.5\%$ in our KYbW experiment, this value stands for an average inversion parameter. On the pump entrance side of the medium the parameter can be much higher than the average, so that inversion-dependent loss processes (two-exciton-processes, upconversion) are enhanced.

To study the heat effects in KYbW, we investigate the dependence of output power and temporal shape of the laser pulse on the chopping parameters (pump pulse duration and duty cycle). After the previous discussion and the observation of a higher lasing threshold for highly absorbed pump wavelengths, it is not a surprise to find thermal effects being influenced by three parameters: average absorbed pump power, absorbed pump pulse energy, and in particular uneven absorption of pump light.

---

[1] For a very rough estimation of the temperature difference ΔT between the center and the boundary of the pumped zone, we assume a uniformly pumped long laser rod [Koe92]. Actually, our case is neither a long-rod laser (only radial heat flow, $\Delta T \sim P_{heat}/L$), nor a thin-disk laser (only axial heat flow, $\Delta T \sim P_{heat}/\mathcal{A}$; $\mathcal{A}$, area of pumped zone), but something in between. For a thermal conductivity $\kappa \approx 3\ \mathrm{Wm^{-1}K^{-1}}$ (average for KYbW) and a heat power $P_{heat} \approx 0.5$ W dissipated along a length $L \approx 20$ µm (near the entrance face of a KYbW medium, cw Ti:Sa-laser pumping close to 981 nm, KYbW quantum efficiency $\eta_q \approx 74\%$), we find $\Delta T = P_{heat}/(4\pi\kappa L) \approx 660$ K.

Thermal influence on KYbW laser pulses

Figure 5.19. shows four pairs of Ti:Sa pump pulses (dotted curves) and resulting KYbW laser pulses (solid curves). The pump wavelengths are 917.5 nm (upper row) and 962.5 nm (lower row), there is fast (left) and slow chopping of the pump beam (right), at a constant duty cycle of 4%. In case of fast chopping (left), which means a pump pulse duration of 350 µs, with both wavelengths an "ideal behavior" of the laser pulses is observed, i.e. thermal effects do not play an important role: About 150 µs after the start of the pump pulse, the KYbW laser reaches its lasing threshold. Relaxation oscillations follow and converge into cw operation. With the end of the pump pulse also the KYbW laser pulse fades away. In case of slow chopping (right, pump pulse duration is about 1.5 ms), the evolution of the laser pulse is similar at first, but the cw-part ends long before the pump pulse does. This is the result of heat effects, which have build up in the laser medium during the pump pulse.

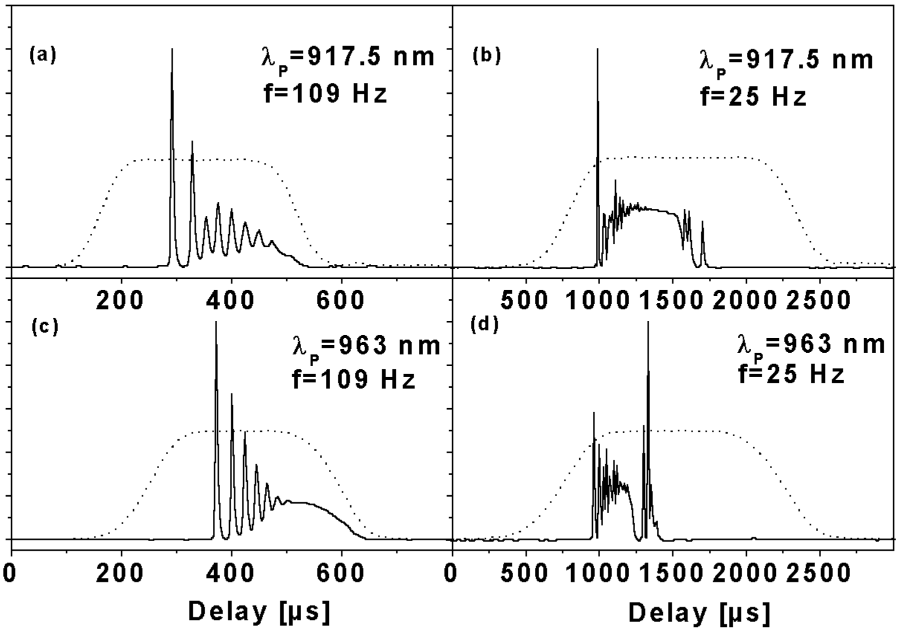

Fig. 5.19. Temporal profiles of the pump (dashed line) and laser (solid line) pulses for two pump wavelengths and for short (a,c) and long (b,d) pulse pumping at a constant duty cycle of 4%.

The situation for λ_{pump} = 962.5 nm (lower row) is worse than for λ_{pump} = 917.5 nm; KYbW laser intensity drops earlier and vanishes after a short second pulse. The difference is caused only partially by the higher absorbed pump energy at 962.5 nm (2.5 mJ, against 1.7 mJ at 917.5 nm), but mainly by the uneveness of the absorption along the crystal, since the absorption length is ≈230 µm at 962.5 nm and ≈330 µm at 917.5 nm. A pump wavelength of 971 nm at a pulse energy of 2.3 mJ would lead to a single pulse of only 200 µs duration, furthermore these operation conditions soon lead to a damage of the crystal.

Heat-related degradation of output power

The situations displayed in Fig. 5.19. correspond to the output powers when the pump pulse duration is varied at a constant duty cycle of 4% (Fig. 5.20.). Pump pulse durations shorter than the upper state lifetime of KYbW, 200 µs, cannot be realized experimentally, but from the

150-μs-delay of the KYbW laser pulse relative to the beginning of the pump pulse it is easy to understand that very short pump pulses would not provide enough energy to reach the lasing threshold. The minimum energy to achieve lasing still plays a little role at a pump pulse duration of 400 μs in case of pumping at 922 nm, 962.5 nm or 971 nm, and due to the lower pump power, in case of 917.5-nm-pumping at a duration between 350 and 800 μs, where the output power is slightly increasing with the pump pulse duration. At pump pulse durations above these values thermal effects become more and more important and lead to a drop of the output powers, which is the faster the stronger the absorption of pump radiation is (see the four pump wavelengths indicated in the KYbW absorption spectrum in Fig. 5.17.).

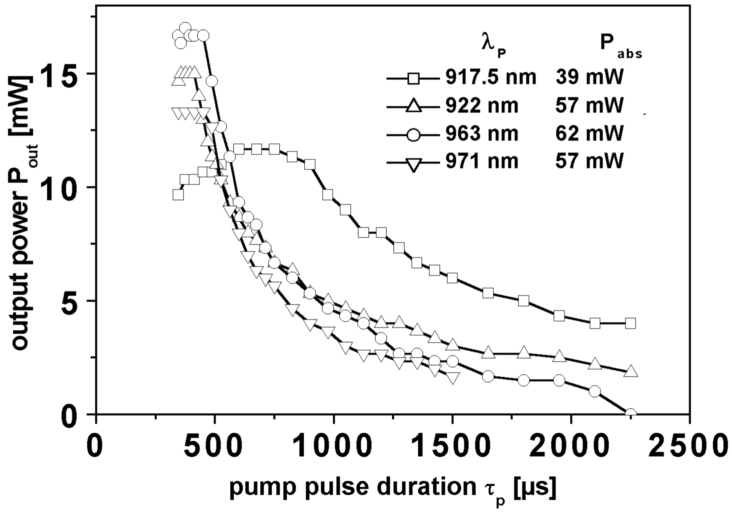

Fig. 5.20. Average output power of the quasi-cw KYbW laser versus pump pulse duration for four pump wavelengths and a duty cycle of 4%.

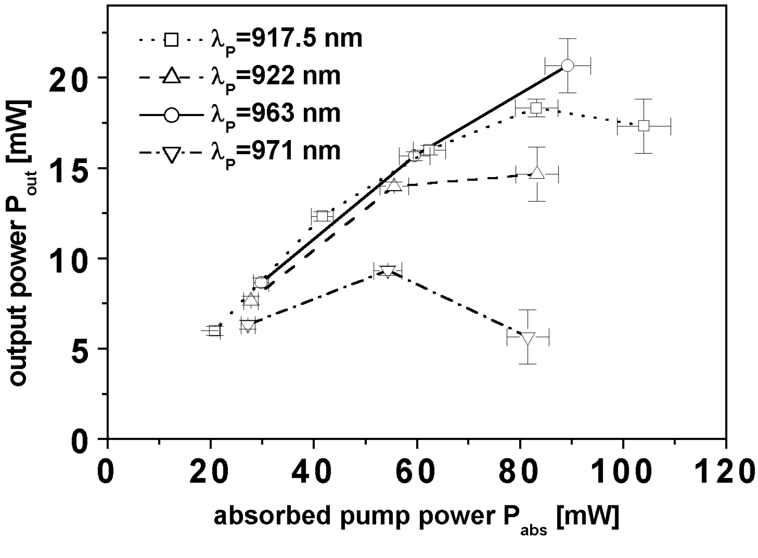

Fig. 5.21. Average output power of the quasi-cw KYbW laser versus average absorbed pump power for four pump wavelengths at a constant pump pulse duration of 350 μs.

From Fig. 5.20. we can deduce that in the given laser configuration cw lasing of the KYbW medium cannot be achieved. The same conclusion must be drawn from Fig. 5.21., which shows the output power of the laser at different duty cycles at a fixed pump pulse duration of 350 µs. The chopper enabled a variation using 2%-steps. At an average absorbed pump power of 20-30 mW the KYbW laser performance is approximately the same for all four pump wavelengths. Above this power, the curves begin to suffer from degradation one after the other, with the wavelengths of larger absorption coefficients first, i.e. 971 nm, then 922 nm, finally 962.5 nm and 917.5 nm. Because of the increasing heat effects, a plus of pump power then results in a minus of the KYbW laser output power. With each step in increasing the duty cycle, the KYbW laser had to be readjusted to maximize the output power by matching the resonator to the changed thermal lens. The curves end where thermal problems do not permit stable operation of the laser at larger duty cycles. In the best case, at $\lambda_{pump} = 917.5$ nm a duty cycle of 10% can be realized.

Towards cw lasing: Optical pumping in the long wavelength range

Our first approach to real cw operation of the KYbW laser is minimization of the heat generated in the crystal by pumping above the absorption maximum of KYbW, i.e. above 981 nm. For this purpose we have to change mirrors in both the Ti:Sa and KYbW lasers, while the principal setup (Fig. 5.12.) remains the same.

By increasing the pump wavelength we reduce the laser quantum defect (*lqd*, see eq. a.1.) as well as the fluorescence quantum defect (*fqd*, eq. a.2.). If we pump above the mean fluorescence wavelength λ_{mf}, there will be a negative *fqd*, which means a cooling contribution from that part of the excitation which decays by fluorescence [Bow00, Mun01]. For KYbW the value of λ_{mf} is 1009 nm, which is the weighted average of the three crystallo-optic orientations. If one succeeds in compensating the heat generated in the active medium as a result of *lqd* by the fluorescence cooling from the *fqd*, the outcome is a radiation-balanced laser, which can realize very high output powers without thermal problems [Bow02]. Only a few laser materials are suitable for this application. Conditions are a very small Stokes shift, focusing the search on quasi-three- or quasi-four-level laser glasses and crystals, a high quantum efficiency, requiring a very pure and perfect material with an only low rate of non-radiative decay, and an exact shaping and spatial matching of the thermally relevant processes. Until now, a net cooling effect could be demonstrated in Tm^{3+} and Yb^{3+}-doped passive media [Bow00, Mun01, Hoy00]. Yb^{3+}-doped tungstates were proposed as optimum active materials for radiation balancing [Bow00] and a laser prototype was presented with Yb:KYW [Bow02].

In our case, we are able to reduce the *lqd* from 10-15% in the previous KYbW laser experiment to 4-9% in the new configuration; the *fqd* is reduced from 5-10% previously to minus 1.5% to plus 5% now. Figure 5.23. displays the output power of the quasi-cw KYbW laser versus the absorbed pump power at a chopping frequency of ≈110 Hz with a duty cycle of 4% for four pump wavelengths. These wavelengths are indicated in the KYbW absorption spectrum shown in Fig. 5.22. $\lambda_{pump} = 962.5$ nm is at the lower end of the present Ti:Sa tuning range and is included because it was also used in the previous experiment (Fig. 5.19.). 994 nm is located above the KYbW absorption maximum, but connected with a relatively short absorption length ($l_a \approx 120$ µm) and an accordingly uneven absorption of the pump light. 1009 nm is the mean wavelength of KYbW fluorescence and here the absorption length of ≈490 µm corresponds to a relatively even pump absorption. 1024 nm is located at the upper end of the region useful for

KYbW pumping. Here we find an almost even pumping of the crystal ($l_a \approx 600$ µm); towards longer wavelengths the pump light absorption becomes inefficient rapidly.

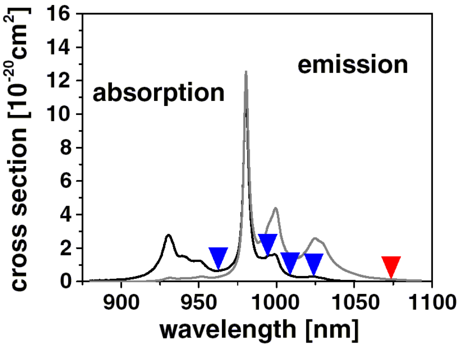

Fig. 5.22. Absorption and emission cross sections of KYbW (light polarization parallel to the *N_m* crystallo-optic axis). Pump and laser emission wavelengths are indicated.

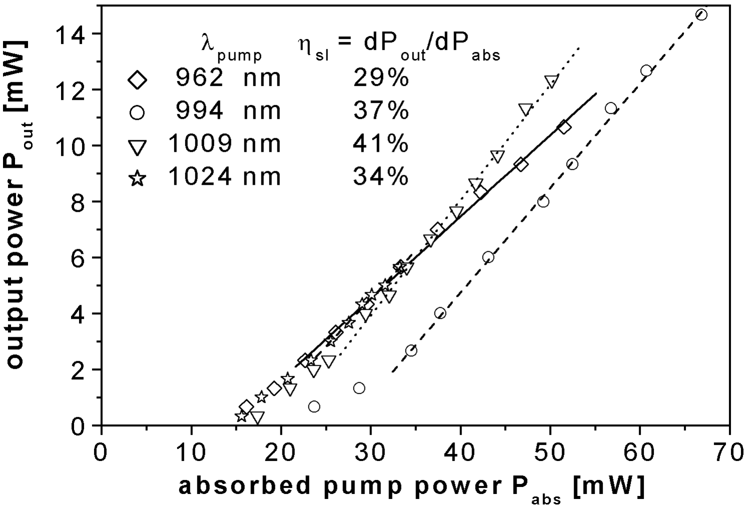

Fig. 5.23. Output power versus absorbed pump power (average values) of the quasi-cw KYbW laser (4% duty cycle) for different pump wavelengths from 962.5 to 1024 nm.

The curves in Fig. 5.23. are achieved with a 1.1%-transmissive outcoupler at $\lambda_{laser} = 1073$ nm, i.e. these optimum conditions are very similar to the previous ones. We see that the slope efficiencies are again roughly 40%, with slightly lower values at $\lambda_{pump} = 962.5$ nm, caused by the characteristics of the pump laser, and at $\lambda_{pump} = 1024$ nm, which can be referred to the pump laser and the lower absorption coefficient: At the lower end of its tuning range, the Ti:Sa pump laser does not operate purely in TEM$_{00}$ when its output power exceeds 1 W (40 mW after chopping). We refer the slight degradation of the performance at higher pump powers to this fact, and because of this the fit leads to a lower slope efficiency $\eta_{sl} = 29\%$. At 1024 nm the pump laser provides less power (maximum 1.75 W incident onto the crystal) and only about 50% of the incident pump radiation are absorbed, with pump saturation being partially responsible (see Table a.4.). Therefore the maximum absorbed pump radiation is twice the value at lasing threshold. Since in quasi-three- or quasi-four-level laser systems the slope efficiency close to the threshold is decreased by reabsorption loss in the medium (chapter 3.3.3.), here the fit results in η_{sl} = 34%. Below 40 mW of average absorbed pump power, the performance for 962.5, 1009 and 1024 nm is very similar. The curves are almost identical with an absorbed pump power of about 15 mW. With 994-nm-pumping the threshold is slightly higher, at ≈20 mW, which might again indicate stronger heat effects due to uneven absorption.

Actually, thermal effects become obvious at all four pump wavelengths, if the chopping rate of the pump beam is reduced: Efficiencies drop, cw-lasing cannot be realized. We assume that the still existing heat problems are caused by a quantum efficiency significantly lower than 100%. For the measurement of the KYbW upper state lifetime (chapter 2.4.) a similarly produced crystal sample was used, and a quantum efficiency of 74% was determined, so that this should play a larger role than *lqd* and *fqd*. As a positive result of the experiment we should note that relatively large KYbW laser efficiencies can be achieved also at long pump wavelengths.

Towards cw lasing: Reduction of reabsorption loss

The next step towards cw lasing is to use a thermally annealed, thinner KYbW crystal, while keeping the pump wavelengths long. From the annealing process an improvement of the quantum efficiency can be expected, since it heals the defects which are caused by lacking oxygen in the crystal structure. The sample thickness is now 125 µm, which leads to less mechanical stability, but aims at a significant reduction of the reabsorption loss in the medium, to get to a lower laser threshold and less heat generation. The present crystal exhibits perfect optical quality – like the TSSG samples – and was produced from a 50 g KYbW boule which was grown by the Kyropoulos method, actually mainly to prepare seeders for a subsequent Czochralski growth. The processing of our laser sample included the following steps: Cutting rods of ≈5 mm diameter oriented along [010] (i.e. along the crystallo-optic $\boldsymbol{N_p}$ axis, see Fig. 2.4.), slicing, thermal annealing in oxygen-enriched atmosphere, lapping and polishing down to the terminal thickness.

Due to reduced reabsorption we have to expect a lower lasing wavelength than before. We change the folding mirror of the V-resonator (Fig. 5.12.) against a mirror which is highly reflective above 1040 nm. In fact, we find λ_{laser} = 1054 nm. As a disadvantage, the folding mirror transmission at 1025 nm is only 6% and therefore limits the incident pump radiation in this wavelength region.

In the present configuration at a pump wavelength of 999 nm the pump power is not reduced by the mirror transmission and absorption is efficient ($l_a \approx$ 110 µm, see the KYbW absorption cross sections in Fig. 5.24.). With a 0.8%-transmissive output coupler this leads to the maximum output, which is about 23 mW at an absorbed pump power of 60 mW (see Fig. 5.25., average values at a duty cycle of 4% and a chopping rate of ≈116 Hz), corresponding to a maximum optical-to-optical conversion efficiency of approximately 38%. Here we take profit from the significantly reduced lasing threshold, which is now reached at 5 mW of average absorbed power. This power is corresponding to a peak power of about 125 mW and to a pump intensity of 8.8 kW/cm^2, approximately half the pump saturation intensity (data given in Table a.4.). We achieve a slope efficiency of ≈46%, which is about the same as for the 500-µm-thick crystal.

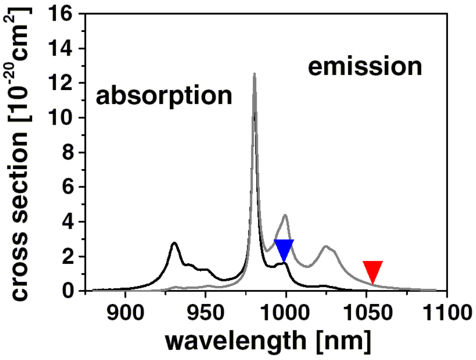

Fig. 5.24. Absorption and emission cross sections of KYbW (light polarization parallel to the N_m crystallo-optic axis). Pump and laser emission wavelengths are indicated.

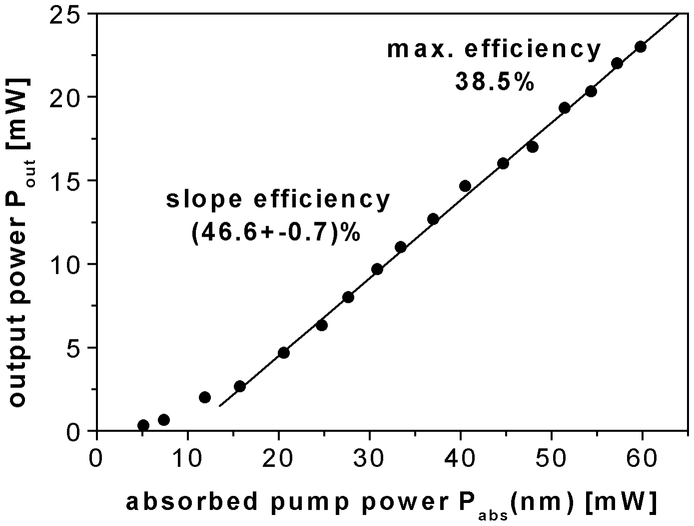

Fig. 5.25. Performance of the quasi-cw KYbW laser using a 125 µm-thin active medium (4% duty cycle).

Seeking the inversion parameter corresponding to the lasing wavelength observed (chapt. 3.3.2.), leads to a value of 4.7% for $\beta_{avV(l)}$. This results in round-trip gain of 1%, 0.2% additional resonator loss and a necessary threshold absorbed pump power and on-axis-intensity of 106 mW and 7.5 kW/cm^2, respectively, in good agreement with the experiment. Therefore we may deduce that thermal problems are less than for the previous experiments which showed a higher experimental threshold than estimated. For our calculations we have again used $\tau = 0.2$ ms as the lifetime of the excited state. However, if the quantum efficiency is higher than 74% (see chapter 2.4., [Puj02b]) thanks to the thermal annealing of the laser crystal, we must assume an appropriately increased lifetime and therefore a decreased threshold power.

Now that we have achieved a low threshold pump power with the 125-µm-thin crystal, as desired for cw lasing, we tune the pump laser towards longer wavelengths to reduce *lqd* and *fqd*. We find that the KYbW laser still shows thermal problems, even when we approach

λ_{pump} = 1025 nm. At least, with a pump duty cycle of 4% the laser does not show degradation of the performance, when the chopping frequency is decreased until pump pulse durations of a few ms are reached. This indicates less heat effects than previously observed (Fig. 5.20.). Nevertheless, pumping at 1025 nm without the chopper, an absorbed power of about 200 mW (peak on-axis intensity of I_{P0} = 14 kW/cm^2) immediately results in cracking of the crystal.

We do not consider a further investigation of the damage behavior, since the number of crystal samples is limited. Instead, before we change the present laser setup (Fig. 5.12.) to the design cw lasing will be achieved with (chapter 5.2.2.), we check out the minimum possible *lqd* with KYbW. Though heat reduction from a small *lqd* probably is still obscured by other heat-generating mechanisms in our present crystal, the *lqd* might become the most-contributing mechanism in future high power KYbW lasers, where crystal quality will be improved and lasing will occur many times above the threshold.

5.2.1.4. Smallest laser quantum defect

In this chapter the potential of KYbW for the realization of a laser with a very small laser quantum defect (*lqd*) is investigated. Recently, a lqd of 2.5% was demonstrated with Yb^{3+}:Y_2SiO_5, which was pumped at λ_{pump} = 978 nm and operated at λ_{laser} = 1003.4 nm [Jaq03]. The records reported previously were values of 4.1% and 4.3%, obtained from Yb^{3+}-doped KGW and KYW lasers, respectively. Both tungstate crystals were pumped by laser diodes at λ_{pump} = 981 nm, while lasing occurred at 1023 nm (Yb:KGW) and 1025 nm (Yb:KYW) [Kul97b]. These experiments have already indicated that Yb tungstates are very interesting active media for high power lasers with only small thermal effects, and they are even suitable for radiation balanced lasers [Bow02]. The smallest value ever for a fiber glass laser, 2.4%, can be deduced from experiments with a 90-m-long Yb^{3+}-doped germanosilicate fiber which was studied at 1090 nm with a pump wavelength of 1064 nm [Pas95]. The confinement of the pump and laser modes in the single mode core allowed pump intensities exceeding 10 MW/cm^2, which effectively suppressed reabsorption of the stimulated emission. For bulk materials, only pump intensities by two or three orders of magnitude lower can be realized.

The smallest *lqd* is achieved with basically the same resonator as before (Fig. 5.12.), when we use an output mirror M_1 transmitting 1.5% at the KYbW laser emission wavelength, which is now 1042 nm due to the increased output coupling. The pump beam is chopped with a duty cycle of 4% and a pulse duration of about 1 ms.

About 80% of the incident pump light are absorbed in the laser medium, with the help of the laser cavity which enables several passes, since the resonator mirrors show only low transmission at the pump wavelength of 1025 nm (end mirror M_3: $T \approx 0\%$, folding mirror M_2: $T \approx 6\%$, outcoupler M_1: $T \approx 1.8\%$). The transmission of the folding mirror would correspond to an incident average pump power of 5 mW, but this does not take into account a resonant enhancement of the pump [Cut91] that must be assumed in our experiments.

The smallest *lqd* for an optically pumped laser crystal, 1.6%, is documented by the spectrum in Fig. 5.27. It shows the KYbW laser line together with the pump line recorded from residual Ti:Sa pump radiation transmitted through the output coupler. The position of the lines within the KYbW absorption and emission spectra can be checked in Fig. 5.26.

Care is taken to clearly attribute the observed emission at 1042 nm to the KYbW laser medium alone. A feedback into the Ti:Sa pump laser at the KYbW lasing wavelength can be ruled out, since the folding mirror has a transmission of less than 0.2% at 1042 nm. The pump laser is running stable at a wavelength of 1025 nm (adjusted by a 3-plate birefringent filter) and there is no 1042 nm emission detected in leakage radiation from the Ti:Sa resonator.

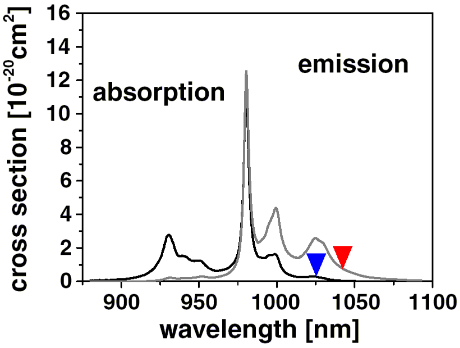

Fig. 5.26. Absorption and emission cross sections of KYbW (light polarization parallel to the N_m crystallo-optic axis). Pump and laser emission wavelengths are indicated.

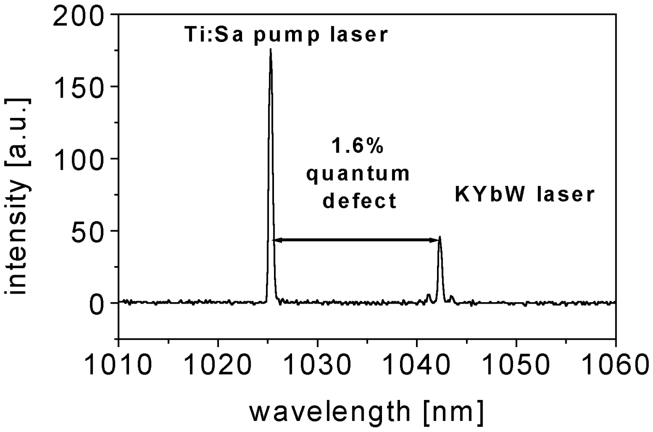

Fig. 5.27. Spectral record of the KYbW and pump lasers in the regime of minimum quantum defect.

The KYbW laser is operating close to its threshold, with an average output power at 1042 nm in the range of 100 µW. From the leaking pump radiation, which is about four times the KYbW laser output power, we estimate that a resonant pump enhancement up to a factor of 3 to 4 takes place. This corresponds to an absorbed peak pump power of ≈ 300 mW and agrees with the value of $P_{a,thr}$ = 190 mW for the threshold pump power calculated using eq. 3.69.a with lifetime τ_f = 0.2 ms and pump and oscillator mode waist sizes $w_p = w_l$ = 30 µm. The inversion parameter at λ_{laser} = 1042 nm is $\beta_{avV(l)} \approx 8\%$ (Fig. 3.3.).

From the inversion we can deduce a round-trip gain of 5.4%, indicating relatively high resonator losses of 3.9% additionally to the outcoupling loss of 1.5%. A possible reason is that the oscillator was adjusted as a configuration with collinear pumping and all resonator mirrors were relatively highly reflective for the pump. Here a maximization of the output means that multipassing and resonant enhancement of the pump were increased. This might not coincide with a minimization of loss for the KYbW emission.

The modest output power achieved in the present experiment is not expected to be a limitation for laser operation with a very small quantum defect, if higher peak and average pump powers can be applied. These will require laser designs, which provide better cooling of a thin KYbW crystal ([Ste00] or next chapter) and avoid the problems connected with the transmission characteristics of a resonator mirror through which the crystal is pumped. Using a laser design with a similar 125-µm-thin KYbW crystal and face-cooling similar to that in the next chapter, but still pumping through a cavity mirror, we apply a cw pump beam (no chopping) without crystal damage and obtain a laser quantum defect of 2.7%. Laser operation is still close to threshold, however, with an output power <1 mW. Cultivating resonant pump enhancement by stabilization and better mode and impedance matching of the oscillator cavity can considerably increase the pump power coupled in [Cut91]. This also has the advantage, that for a pump wavelength near 1025 nm yet thinner KYbW laser crystals could be used at still efficient absorption of the pump radiation, but at lower reabsorption of the stimulated emission. A more simple solution, which works with broadband pump sources and without stabilization, is to pump non-collinearly not involving transmissive resonator mirrors. The realization of such a pump scheme should be relatively easy because of the short KYbW absorption length.

To fully exploit the advantage of a small quantum defect, high quantum efficiency and therefore pure and perfect KYbW laser material is required. While the crystal used here was not intended to represent the state of the art, future crystals will be further improved in quality.

The record for the smallest laser quantum defect at room temperature, 1.6%, obtained with a 125-µm-thin crystal of KYbW, provides evidence that Yb^{3+}-doped monoclinic double tungstates can be operated as laser media with extremely low internal heat production, a property desirable for high power lasers. We do not attribute the very small laser Stokes shift observed here to the stoichiometric character of KYbW and predict that similar results should be achievable with the low-doped analogues $Yb:KY(WO_4)_2$ and $Yb:KGd(WO_4)_2$.

5.2.2. Continuous-wave face-cooled Yb:KYW and KYbW lasers

The heat removal from the active medium can be greatly improved by face-cooling. We test this principle with a Yb(20%):KYW laser. Finally, with KYbW, we achieve what is to our knowledge the first cw laser operation of a stoichiometric Yb-containing laser material. The experiments are performed in the laser setup shown in Fig. 5.28.

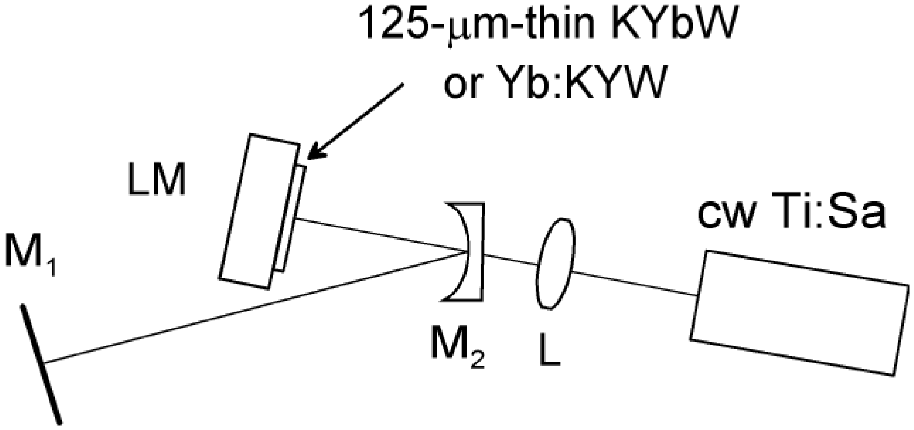

Fig. 5.28. Setup of the cw Yb:KYW and KYbW lasers. M_1 – outcoupling mirror, M_2 – folding mirror, L – focusing lens, LM – laser mount. The distance between M_1 and M_2 can be varied between 250 and 500 mm. 125-μm-thin KYbW crystals and also a Yb(20%):KYW sample are investigated.

In this configuration the laser crystal is used as an "active mirror" [Fan92]: It is coated high-reflective (HR) on one side both for the pump and the laser radiation (coating by Layertec GmbH). This side serves as an end mirror of the laser resonator, while the other side is coated broadband anti-reflective (AR). The crystal is positioned in the focus of the folding mirror M_2 and of the focusing lens L (Fig. 3.10.). We first use a Yb(20%):KYW sample to check the configuration. The radius of curvature of M_2 is $r = -100$ mm and the focal length of L is $f = 62.8$ mm. For the KYbW experiments we change M_2 and L to $r = -150$ mm and $f = 100$ mm.

Almost a "thin-disk laser"

Our face-cooled laser (Fig. 5.28.) is similar to a thin-disk laser described e.g. in [Ste00]: The thickness of the laser-active crystal platelets, $d = 125$ μm, is in the lower range of what is usual for thin-disk lasers until now. Therefore cooling is effective, because the heat generated in the pumped region does not travel far through the medium to get to the sink.

However, we would not use the term "thin-disk laser" here, since the pump spot size on the crystal is small, so that we cannot exploit the second big advantage of thin-disk lasers, the weakness of thermal lensing effects. To strongly reduce such effects, the thin-disk laser concept demands an aspect ratio A of the pumped zone (A = length d / beam waist w_p) much smaller than 1, resulting in a thermal gradient which is basically parallel to the propagation of the oscillator mode inside of the active medium. In our laser, we have $A = 4{:}1$ in case of the Yb(20%):KYW and $A = 2.5{:}1$ for the KYbW experiments. A real KYbW thin-disk laser would require a larger pump spot (and accordingly more pump power) and/or thinner disks.

KYbW laser crystals and mounting

The KYbW crystal samples were prepared from the same Kyropoulos-grown 50 g-boule and by the same method mentioned in chapter 5.2.1.3. and coated afterwards by a sputtering process. Likewise the 20% Yb^{3+}-doped KYW platelet was produced. The educts for the Kyropoulos-growth of the lowly doped crystal were the same as for the KYbW boule, aside from additional yttrium oxid. The KYbW material was checked for rare-earth impurities: The typical upconversion processes could not be found in the fluorescence spectra; instead relatively strong cooperative luminescence (see appendix A.1.) was observed, indicating high chemical purity [Kir02].

One of the difficulties with thin crystal platelets is how to manufacture and polish them without cracking, another is that the necessary HR coating on one crystal side causes tensions. While handling is not a problem for the 125 µm-thin samples yet, tensions already become obvious in deformations of the crystals. Deformations are individual for each platelet and can include aspherical contributions.

To achieve optimum cooling each crystal is glue-bonded to the gold-coated surface of a copper-made holder (see Fig. 5.29., “laminar laser mount” by VCT). A small channel in the mount directly applies a laminar water flow to the highly reflective crystal side near the laser-active spot. The cooling water is held at room temperature. Actually, the cooling capabilities of this mount are more than sufficient for our experiments.

To maximize the absorption of the pump radiation, in our lasers the crystals are oriented for parallelity of the $\boldsymbol{N_m}$ crystallo-optic axis and the pump light polarization.

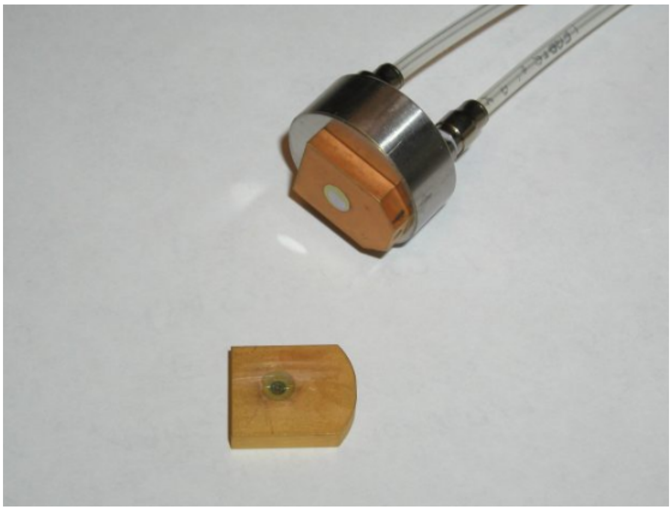

Fig. 5.29. “Laminar laser mount.” The KYbW crystal platelet is glue-bonded to the gold-coated copper plate. From the channel in the mount a laminar water flow directly contacts the backside of the crystal.

5.2.2.1. Yb(20%):KYW continuous-wave laser

At first we investigate the 125-µm-thin 20% Yb^{3+}-doped KYW platelet, using a 1.5%-transmissive output coupler M_1 (Fig. 5.28.). Operation of thin-disk lasers with 160-µm-thin Yb(5%):KYW and 120-µm-thin Yb(10%):KYW media, pumped at $\lambda_{pump} = 981$ nm, were reported in [Bru02] and [Erh01], respectively. With face-cooling, cw pumping was not a problem in case of these lowly doped tungstate crystal platelets, and we too succeed. The information about the damage behavior of the Yb(20%):KYW sample obtained in the configuration of Fig. 5.28. is helpful for the KYbW experiments.

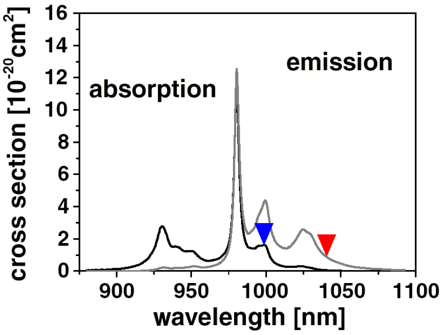

Fig. 5.30. Absorption and emission cross sections of Yb:KYW (light polarization parallel to the *N_m* crystallo-optic axis). Pump wavelength and central laser emission wavelength are indicated.

The cw laser emission of the face-cooled Yb(20%):KYW laser occurs centered near λ_{laser} = 1039.5 nm, exhibiting a spectrum with several peaks, which we will find similar with the KYbW cw laser (KYbW laser spectrum in Fig. 5.32.). The short lasing wavelength compared to our previous KYbW experiments is a result of the lower Yb concentration and therefore lower reabsorption of the stimulated emission. At a pump wavelength of 999 nm and an incident pump power of 2 W (neglecting feedback effects), an output power of approximately 600 mW is achieved. The pump wavelength used and the central lasing wavelength observed are indicated in the Yb:KYW absorption and emission spectra in Fig. 5.30. Actually, the pump light absorption at 999 nm for a double pass through the medium is below 40% due to the low dopant concentration, so that non-absorbed pump power is fed back into the Ti:Sa pump laser. Therefore it is not possible to determine the absorbed pump power, the slope efficiency of the Yb:KYW laser or its lasing threshold.

Studying crystal damage

When the laser crystal is cw pumped at λ_{pump} = 999 nm, it does not suffer damage during normal laser operation, but it does if lasing is interrupted by blocking the resonator with the pump load still being present. Furthermore, variation of the pump wavelength reveals that cw pumping near 981 nm leads to damage also, while a chopped pump beam (4% duty cycle) causes no such danger.

If the stimulated emission is stopped, the excitation in the crystal can only decay by fluorescence and by non-radiative processes. An estimation based on λ_{pump}, λ_{laser}, and the mean wavelength of fluorescence $\lambda_{mf} \approx$ 1009 nm (assuming a similar fluorescence spectrum as for KYbW), shows that this leads to an increased heat load, if the quantum efficiency η_q (according to eq. a.10.) is lower than 97%. However, a significant increase – able to damage the crystal – requires a much lower η_q. For example, assuming a (very optimistic) laser efficiency of 75% with respect to the absorbed power, doubled heat generation with blocked resonator would occur for η_q = 89% and correspond to a heat load of ≈0.5 MW cm^{-3} from ≈4.5 MW cm^{-3} of absorbed power. (With a lower laser efficiency, doubled heat in this situation would require an even lower quantum efficiency.)

From the pump powers and pump spot size given in [Erh01] one can calculate a (harmless) on-axis absorbed pump power density of ≈1.5 MW cm^{-3} near the uncooled face of the 120-µm-thin Yb(10%):KYW crystal. This means, that at $\lambda_{pump} = 999$ nm our pump intensity and probably also our heat load must be considered relatively high. For $\lambda_{pump} = 981$ nm, where the absorption length is about 70 µm, the heat load of our Yb(20%):KYW laser is even higher. Therefore it is not surprising, that cw pumping at 981 nm leads to crystal damage. For 2 W pump power incident from the Ti:Sa laser the absorbed power per volume is 21 MW cm^{-3} on axis near the uncooled face and 6.5 MW cm^{-3} near the cooled face.

At the high pump intensities used here it is also possible that initial damage occurs at the crystal surface. In this case damage and degradation effects depend on the surface quality.

Since the stoichiometric Yb tungstate will by its shorter absorption length and faster energy migration (see chapter 2.3.) enhance the damage problems, we will avoid to pump near the absorption maximum at 981 nm and increase the pump spot size on the crystal for our KYbW experiments.

5.2.2.2. KYbW continuous-wave laser

Changing the folding mirror M_2 and the pump focusing lens L (Fig. 5.28.), we increase the pump and laser beam waists at the crystal from previous $w_p = w_l = 30$ µm to estimated 50 µm. By this the heat load per volume is reduced and the heat flow is spread over a larger area, getting closer to the one-dimensional flow of a thin-disk laser. A pump spot with $w_p >> 50$ µm would not be useful in our laser, since the reabsorption loss and the laser threshold, which are much higher than in the 20% Yb^{3+}-doped tungstate, would not permit efficient lasing. To achieve lasing at the available pump powers it is also necessary to use a relatively low outcoupling, $T_{OC} = 0.3\%$ at 1068 nm.

At $\lambda_{pump} = 1025$ nm, the pump wavelength with which we achieve the first cw KYbW lasing, the transmission of the folding mirror M_2 is relatively low, about 16%. This limits the pump power incident on the crystal to a maximum of 220 mW at 1025 nm. Towards shorter wavelengths the mirror transmission increases and exceeds $T = 99\%$ near 1000 nm, so that approximately 2 W of pump radiation can be applied at this wavelength.

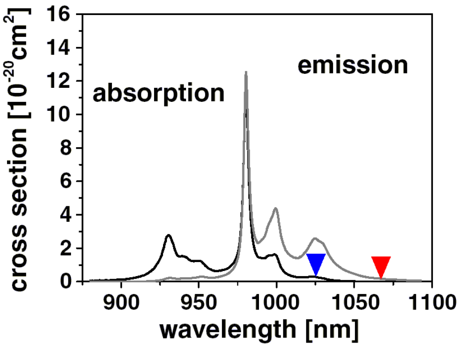

Fig. 5.31. Absorption and emission cross sections of KYbW (light polarization parallel to the N_m crystallo-optic axis). Pump wavelength and wavelength of cw laser emission are indicated.

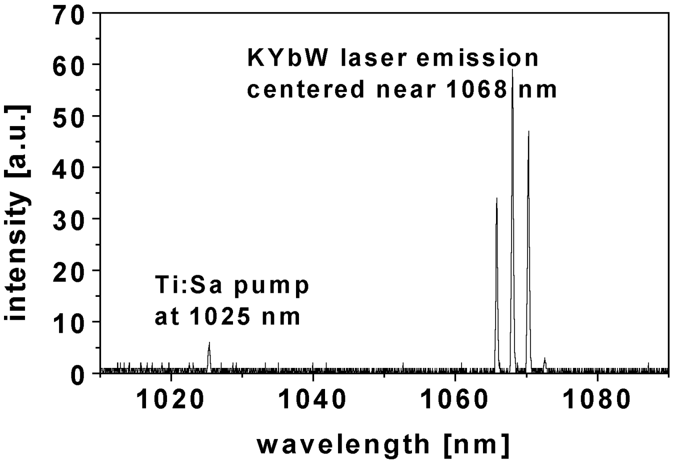

Fig. 5.32. Emission spectrum of the cw KYbW laser.

The spectrum of the cw laser is shown in Fig. 5.32. Residual nonabsorbed pump radiation at 1025 nm can also be seen. The KYbW spectrum is centered at 1068 nm and consists of several peaks with a separation of 2.2 nm, like with the Yb(20%):KYW platelet. This corresponds to the free spectral range of an etalon with the thickness of the crystal, $d = 125$ µm. Residual reflectivity of the antireflection-coated surface of the sample is responsible for this effect (although $R < 0.1\%$ is specified). In Fig. 5.31., wavelengths of pump and cw laser emission can be compared to the KYbW absorption and emission spectra.

The output power of the cw KYbW laser relative to absorbed pump power P_{abs} is presented in Fig. 5.33. The laser threshold is reached at $P_{abs} \approx$ 70 mW. The maximum output power amounts to ≈14 mW at $P_{abs} \approx$ 134 mW. The absorbed pump powers are calculated with multiple passes taken into account. (The single pass absorption is ≈20% at 1025 nm, but the resonator leaks only about 35% per round trip. Multiple passing gets obvious when the resonator is interrupted, since the blue fluorescence from the pumped crystal gets weaker then. With no multiple passing the absorbed pump power would remain constant and one would observe more intensive parasitive fluorescence during the absence of stimulated emission.)

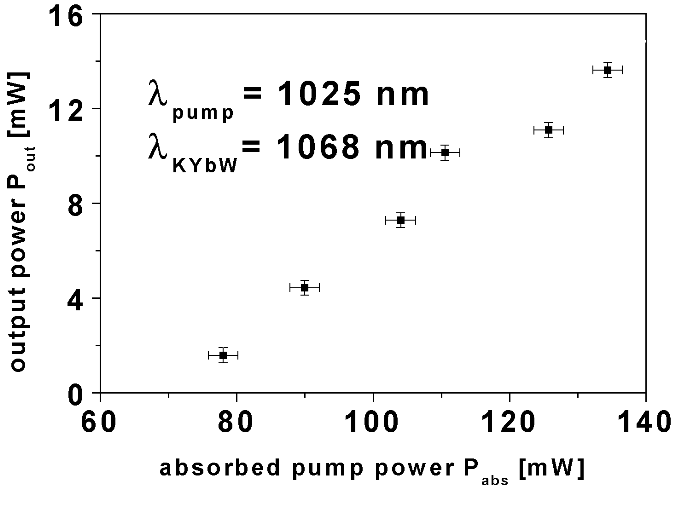

Fig. 5.33. Output power versus absorbed pump power at 1025 nm, obtained with the cw KYbW laser at room temperature.

The fluctuations of the laser intensity are less than 10% (standard deviation) on 200- and 2-ms time scales, verified by a photodiode. The KYbW laser output can be increased to 20 mW by a different adjustment regime with the pump beam being even more collinear to the propagation of the laser mode, at the cost of larger intensity fluctuations. The reason for these does not lie in the KYbW laser, since the observed transversal mode structure remains basically TEM_{00}, but in the Ti:Sa pump laser being disturbed by feedback of residual pump light.

In experiments with other 125-µm-thin crystal samples the KYbW laser performs similarly, i.e. the maximum output power is approximately the same. However, the crystal platelets require an individually optimized adjustment of the laser resonator, including varying optimum distances of folding mirror M_2 and outcoupler M_1, probably due to different crystal curvatures modifying the oscillator modes. We find that the polarization of the laser output is always determined by the crystal orientation which provides maximum active gain, i.e. parallel to crystallo-optic axis $\boldsymbol{N_m}$.

Resonant pump enhancement

The lasing wavelength at 1068 nm corresponds to a fractional excitation of $\beta_{avV(l)} \approx 3.1\%$ (Fig. 3.3.), a round-trip gain of 0.4%, and additional losses of 0.1%. Such an excitation level requires a threshold absorbed pump intensity of 4.8 kW/cm^2 on axis or a threshold absorbed pump power of approximately 200 mW, respectively, instead of 1.8 kW/cm^2 and 70 mW we have assumed until now. We consider resonant enhancement of the pump power a possible reason for this discrepancy from the experimental value, because we see a weak, but larger than expected, pump leakage through the output coupler. A factor of ≈2.5 for such an enhancement would result in a corresponding increase of the abscissa values in Fig. 5.33.

Thermal problems finally solved?

At $\lambda_{pump} \approx 1025$ nm the combined effects of low heat generation and improved cooling reduce thermal problems sufficiently that there is no danger of crystal damage under these conditions (absorbed pump power 3.4 kW cm^{-2} or 0.27 MW cm^{-3}, if no resonant pump enhancement is assumed; otherwise the values should be multiplied with ≈2.5). We observe no influence of heating on performance at the present laser parameters when the output power of the cw laser is compared with operation with a chopped pump beam: The chopped laser delivers exactly the output power of the cw laser times the duty cycle, not depending on the chopping frequency.

Pumping of the cw laser is possible also at shorter wavelengths (985 nm or even near 973 nm on the other side of the main absorption peak; see Fig. 5.31.), but pump attenuation is necessary then and operation close to threshold does not permit an estimation of the slope efficiencies versus λ_{pump}. If we approach $\lambda_{pump} = 1000$ nm from the long-wavelength side without pump attenuation, the output power of the laser drops despite of the increasing pump light transmission of the folding mirror and therefore increasing absorbed pump power. The KYbW crystal is partially damaged near $\lambda_{pump} = 1000$ nm at an absorbed intensity of ≈35 kW cm^{-2} on axis, corresponding to an absorbed power per volume of ≈2.8 MW cm^{-3}.

It is difficult to compare the resulting heat generation to that in the Yb(20%):KYW cw laser in chapter 5.2.2.1., since the quantum efficiencies of the laser crystals are unknown. The present incident pump intensity of up to ≈50 kW cm^{-2} is only about the third part of that applied to the Yb(20%):KYW crystal and this circumstance is only partially compensated by higher absorption in the stoichiometric material. We may assume that the quantum efficiency of the

KYbW material is worse than for the Yb:KYW sample, leading to comparable heat loads in the damage cases. For the stoichiometric medium, showing faster energy migration towards defects, also the influence of surface quality on the damage behavior is likely to be larger and should be object to further investigation.

Possible improvements

Future KYbW cw lasers may use crystal material exhibiting an improved quality and a quantum efficiency close to 100% and therefore not show the thermal problems observed here at pump wavelengths <1025 nm (see Fig. a.2.b showing a 1-kg-boule of Chochralski-grown KYbW which was not yet avaible for the experiments performed here). Diode pumping at the absorption maximum near 981 nm, which is in a standard spectral range of laser diodes, and scaling up to high output powers will be aimed at.

At any case, the use of even thinner KYbW media is desirable. These would enable better heat removal, that means lower temperatures or higher possible absorbed power in the pumped zone and a more one-dimensional heat flow, as demanded for a thin-disk laser concept eliminating thermal influences on the beam quality. While the present cw KYbW laser operates close to its lasing threshold, for efficient laser operation it is necessary to further reduce the reabsorption loss in KYbW lasers. Working at many times the lasing threshold and bleaching out the reabsorption loss by high intracavity laser intensity is not realistic for samples with a thickness in the order of 125 µm, since the applicable pump intensities are limited by the damage threshold of the KYbW material, maybe also by the damage threshold of the crystal surface, and by the brightness of the pump sources (for high-power lasers: fiber-coupled diode arrays). For many applications including harmonic generation and mode-locked lasers, the multiple-peak structure of the emission spectrum is very disadvantageous. It may be countered best by decreasing the medium thickness and therefore increasing the free spectral range of the Fabry-Perot resonator defined by the KYbW crystal surfaces, so that just one transmission maximum of this resonator lies within the spectral region of positive net gain. An anti-reflective coating is evitable then.

Depending on the pump source (wavelength, spectral bandwidth) and the pump optics, a KYbW medium thickness in the order of 10 µm might be optimum. A high-power very-low-quantum-defect laser as proposed in chapter 5.2.1.4. could be realized by combining a slightly thicker crystal with non-collinear multi-pass pumping at λ_{pump} = 1025 nm.

The problems of handling ultrathin KYbW platelets and coating them without deformations can be avoided by composite crystals, mating a thin layer of the active crystal to a thick stabilizing layer of inactive material. Diffusion bonding, sputtering, epitaxial or hydrothermal processes are possible ways to fabricate such composite structures in KYbW and KYW.

6. Yb^{3+}-doped scandia laser experiments

Yb^{3+}-doped Sc_2O_3 (scandia) exhibits good spectroscopic properties and is the Yb^{3+}-activated material that promises the highest achievable laser efficiencies, aside from the double tungstates investigated in the previous chapter [Bre01b]. The great advantage of scandia is its excellent thermo-mechanical properties, reducing cooling requirements and predetermining it as the ideal Yb^{3+} host for high-power laser applications (see chapts. 2.2. and 2.4.). If doping levels higher than 1% are desired, the analog sesquioxides $Yb:Y_2O_3$ and $Yb:Lu_2O_3$, though spectroscopically slightly inferior, may become more attractive due to higher thermal conductivities.

In chapter 6.1., we examine the cw laser performance of $Yb:Sc_2O_3$ with Ti:Sapphire-laser pumping. In chapter 6.2., mode-locked lasing is investigated in regimes of non-solitonlike and solitonlike pulse shaping. A Ti:Sapphire laser and a tapered laser diode are used as pump sources.

Our Yb:scandia experiments (chapts. 6.1. and 6.2.) are performed in the "Z"-folded astigmatically compensated resonator shown in Fig. 6.1. The setup is similar to that of the passively mode-locked Yb:tungstate ultrashort pulse lasers presented in chapter 5.1.2., but with the additional option of working without dispersion compensation (prisms P_1, P_2), so that mode-locked pulses can be generated in femtosecond and picosecond regimes.

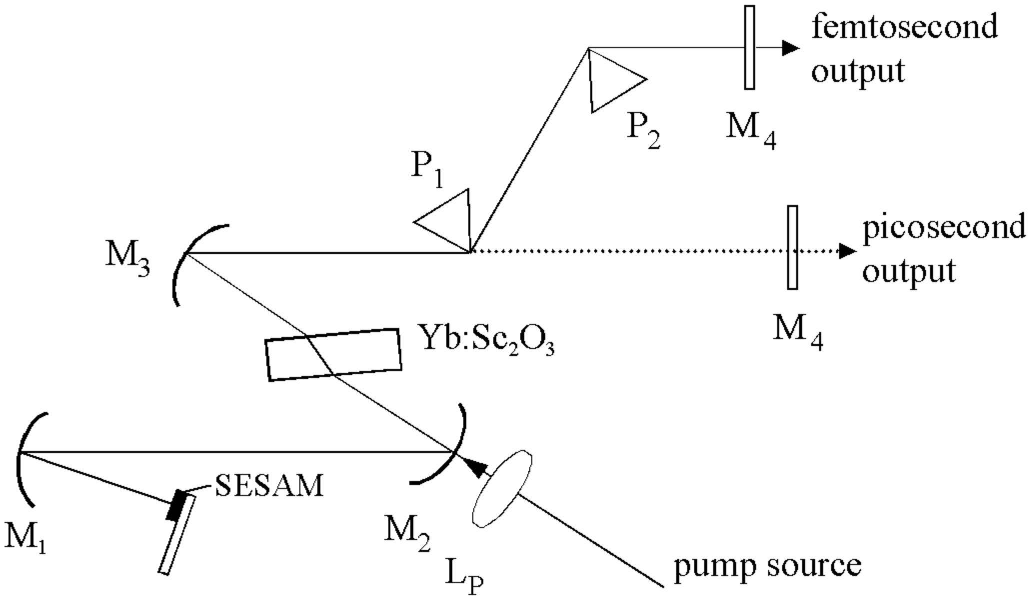

Fig. 6.1. Setup of the Yb:scandia laser: SESAM – semiconductor saturable absorber mirror (for cw lasing replaced by high-reflector); M_1 – focusing mirror (r = -100 to 150 mm); M_2, M_3 – folding mirrors (r = -100 mm), P_1, P_2 – SF6 60° prisms; M_4 – output coupler in cw and picosecond regimes; M_5 – output coupler in the femtosecond regime; laser medium – 2.75-mm-thick, 0.7 at%-Yb^{3+}-doped Sc_2O_3 crystal; L_P – focusing lens, pump source – Ti:sapphire or collimated tapered diode laser beam.

The active medium is placed in a beam waist of approximately 30 µm between curved mirrors M_2 and M_3 ($r = -100$ mm each). It is used at the Brewster angle without special means of cooling. Mirror M_1 with 100 mm or 150 mm radius of curvature provides an additional waist in the order of 100 µm or 150 µm, respectively, on the passive mode-locker, a semiconductor saturable absorber mirror (SESAM), which terminates this arm of the resonator. The SESAM is replaced by a high-reflective mirror in case of cw operation. For the other arm we can choose such with a plane output coupler M_4 (picosecond regime) or such including an SF6-prism pair P_1, P_2 with a tip-to-tip seperation of 640 mm and a plane output coupler M_5 (femtosecond regime).

Our laser crystal is a 2.75 mm-thick 0.7 at%-Yb^{3+}-doped Sc_2O_3 sample with an aperture of 4 x 5.8 mm^2. It was cut from a polycrystalline boule, which had been grown by V. Peters at the University of Hamburg in a ≈15% H_2 / ≈85% N_2 / ≈0.02% O_2 atmosphere, using the heat exchanger method. In the visible range, the crystal is colorless and completely transparent. Structural imperfections are indicated by measurements with polarized light, showing some stress-induced birefringence for one orientation of the crystal, while there is none if the crystal is rotated by 90°. However, we do not observe any influence on the laser performance. The pumped Yb:scandia crystal emits a slight green fluorescence, but since the laser sample was grown using educts with a purity of >99.999%, we may assume that rare earth impurities (traces of Er^{3+}) are negligible for the laser efficiency. In our case, with pumping at the zero-line transition located near 976 nm (see Fig. 6.2.), 97% of the pump radiation are absorbed by the $Yb:Sc_2O_3$ medium. This corresponds to an Yb^{3+} concentration of approximately 2.5×10^{20} cm^{-3}, which means that approximately 0.7% of the Sc^{+3} ions of the scandia host are replaced by Yb^{3+}. Actually, the dopant distribution is not completely homogeneous, with the doping level reaching ≈0.9% at some places of the crystal.

The pump beam is focused by lens L_p ($f = 62.8$ nm) to match the 30-µm-laser-waist in the crystal and introduced through mirror M_3, which is >99%-transmissive at 976 nm, but highly reflective at the Yb:scandia laser wavelengths. Since the zero-line-transition of $Yb:Sc_2O_3$ is spectrally narrow, potential pump sources must exactly hit the absorption line, i.e. they must exhibit a small spectral bandwidth and high spectral stability. Otherwise pump absorption is inefficient and Yb:scandia laser power may strongly fluctuate. We use a Ti:sapphire pump laser ($\Delta\lambda << 1$ nm, maximum output power $P_{max} \approx 2$ W at 976 nm) and in the femtosecond regime also a spectrally stabilized tapered diode laser ($\Delta\lambda \approx 1$ nm, $P_{max} \approx 1.4$ W at 976 nm with stabilization).

6.1. Continuous-wave operation of a Yb(0.7%):Sc_2O_3 laser

Continuous-wave lasing is studied in the Ti:sapphire-pumped picosecond configuration (Fig. 6.1., without prisms), with $r = -100$ mm chosen as the radius of curvature of mirror M_1 and with a plane highly-reflecting mirror instead of the SESAM. If an output coupler M_6 with a transmission T_{OC} lower than 5% is applied, the Yb:scandia laser will run near 1094 nm. This corresponds to the transition from the lowest level of the $^2F_{5/2}$ upper state to the highest level of the $^2F_{7/2}$ lower state (smaller maximum in the emission curve of $Yb:Sc_2O_3$, see Fig. 6.2.), which experiences the highest gain, when reabsorption loss caused by the ground state population dominates over cavity losses. For T_{OC} larger than 5%, $Yb:Sc_2O_3$ laser emission will occur near 1042 nm, leading from the lowest level of the $^2F_{5/2}$ upper state to the third level of the $^2F_{7/2}$ lower state.

Figure 6.3. shows the cw output power of the Yb^{3+}-doped scandia laser versus absorbed pump power in case of a 9.6%-output-coupler. The laser generates a maximum output power $P_{out,max}$ of 1.06 W with a conversion efficiency η_{max} of 57%, and the slope efficiency η_{sl} reaches 65%. Although the $Yb:Sc_2O_3$ crystal is not actively cooled, thermal problems do not occur, i.e. the slope does not show any tendency of worsened performance even at >1.8 W of absorbed pump power. Using a 6.2%-output-coupler, $P_{out,max} = 0.97W$, $\eta_{max} = 55\%$, and $\eta_{sl} = 63\%$ are achieved.

Our results confirm the high cw laser efficiencies demonstrated previously: A slope efficiency of up to 66% was obtained with a Ti:Sa-pumped Yb:scandia laser using a 1.3-mm-long 2.8%-doped crystal in a concentric cavity with output coupler transmissions of 7.5% and 16% [Mix99]. With InGaAs diode pumping, up to 58% slope efficiency could be achieved [Pet02b], and 124.5 W of cw output power were obtained from a $Yb:Sc_2O_3$ thin-disk laser pumped at 941 nm by 254 W from fiber-coupled laser diodes [Pet01].

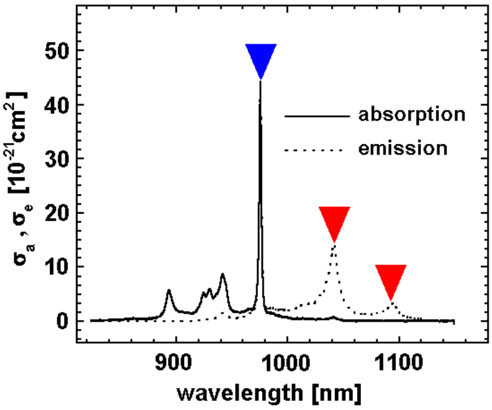

Fig. 6.2. Absorption and emission cross sections of $Yb:Sc_2O_3$. Pump and laser emission wavelengths are indicated.

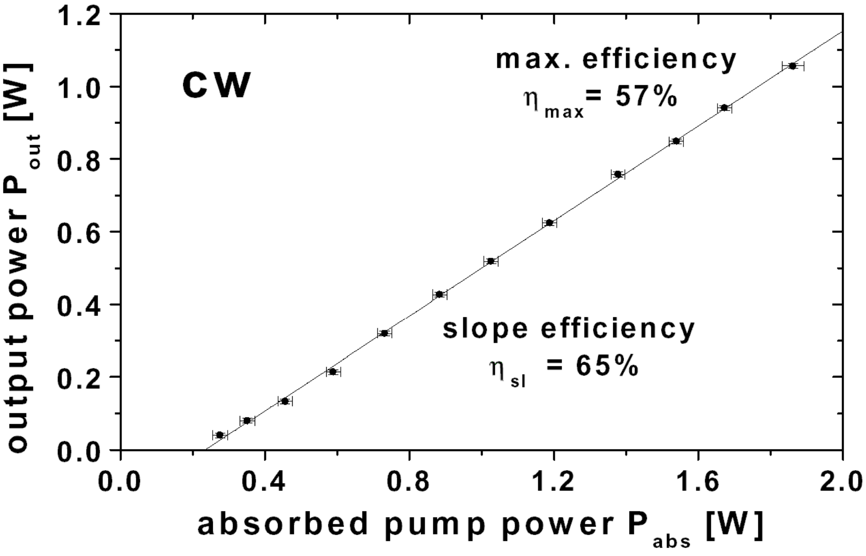

Fig. 6.3. Performance of the cw $Yb:Sc_2O_3$ laser with 9.6%-output-coupler.

6.2. Mode-locked operation of Yb:Sc_2O_3 lasers

Here we demonstrate for the first time to our knowledge mode-locked operation of a Yb:Sc_2O_3 laser, and more general, of an oscillator using a sesquioxide laser crystal.

The crucial element to start passive mode locking in both the picosecond and femtosecond regime and to stabilize the solitary pulses in the latter is the semiconductor saturable absorber mirror (SESAM [Jun97, Kel92, Tsu95], for a theoretical description of saturable absorber action see chapter 4.2.). The SESAM (Model 100352, WROE – Weimar, Germany) was designed for a central wavelength of ≈1045 nm, matching the gain maximum of the Yb:scandia medium near 1042 nm where we have observed cw lasing in the previous chapter. The reflection band of the device is from 995 to 1095 nm with 2% of saturable absorption and a saturation fluence of 70 $\mu J/cm^2$. The non-saturable loss is specified to be less than 0.3% and the relaxation constant to be equal to 20 ps. The saturated and non-saturated reflectivity curves are given in Fig. a.5. in the appendix. As the SESAM is mounted directly on a copper heat sink, we may expect no significant heating during operation.

Alternatively, in the femtosecond regime we have also tested three SESAMs with different center wavelengths λ_c and/or amounts of saturable absorption ΔR and with, aside from this, identical specifications as mentioned above: $\Delta R = 0.6\%$ at $\lambda_c = 1045$ nm, $\Delta R = 0.6\%$ at $\lambda_c = 1064$ nm, and $\Delta R = 1\%$ at $\lambda_c = 1064$ nm. With all these no stable mode locking can be achieved in our configuration. The observed temporal pulse structures are unstable and noisy, indicating incomplete mode locking. We refer this to the insufficient modulation depths of these SESAMs ($\Delta R \leq 1\%$).

To obtain stable mode locking with the $\Delta R = 2\%$-absorber, it is also necessary to optimize the intensity on the SESAM by the output coupler transmission and the spot size on the saturable absorber. In the picosecond regime (focusing mirror M_1 with $r = -100$ mm, 6.2%- or 9.6%-output coupler) mode-locked operation is achieved with an on-axis pulse fluence that is about four to ten times the specified saturation fluence; in the femtosecond regime (M_1 with $r = -150$ mm, 5.5%-output coupler in the Ti:Sa-pumped case; M_1 with $r_{oc} = 100$ mm, 1.5-3.5% output coupler transmission for diode-pumping) the on-axis pulse fluence is approximately two to five times the saturation fluence.

6.2.1. Ti:Sapphire-laser-pumped Yb(0.7%):Sc_2O_3 picosecond laser

Using the laser configuration without intracavity prisms but implementing the SESAM (Fig. 6.1.), the laser exhibits self-starting single-pulse mode locking in the picosecond regime with a cavity round-trip time of 9.2 ns, if output couplers with a transmission of 6.2% or 9.6% are applied. Best results are obtained with a 9.6%-output coupler. The cw laser threshold amounts to 250 mW of absorbed power (Fig. 6.4.). The small jump in the output power in the transition from cw to mode-locked operation is due to the saturated loss of the SESAM. For mode-locked operation we achieve a laser slope efficiency η_{sl} of 54% and a maximum output power $P_{out,max}$ of 820 mW, corresponding to a pulse energy of 7.4 nJ. The maximum optical to optical pump efficiency η_{max} reaches 47%. To the best of our knowledge this is the highest conversion efficiency with respect to the absorbed pump power for any mode-locked Yb^{3+} laser including those based on the thin-disk concept [Hoe99b, Inn03].

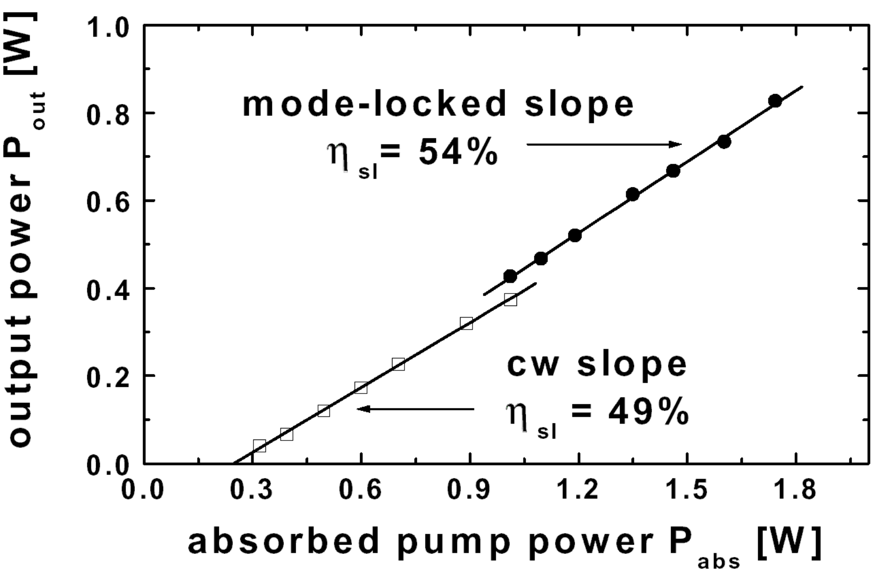

Fig. 6.4. Performance of the picosecond Yb:scandia laser with a 9.6%-output coupler. Output power versus absorbed power in the mode-locked regime and below the mode-locking threshold (cw).

Figure 6.5. shows the temporal/spectral characteristics of the Yb:scandia picosecond laser. The measured autocorrelation traces can be well fitted assuming *sech*^{2}-pulse shapes. The deconvolved FWHM of the pulse is 1.33 ps. The 4.6-nm-broad spectrum centered at 1041.5 nm could support about 250 fs long pulses which means that the experimentally obtained pulse duration lies about 5 times above the Fourier limit. At lower output powers (see Fig. 6.4.) the pulse duration remains unchanged but the pulse spectral width decreases about two times.

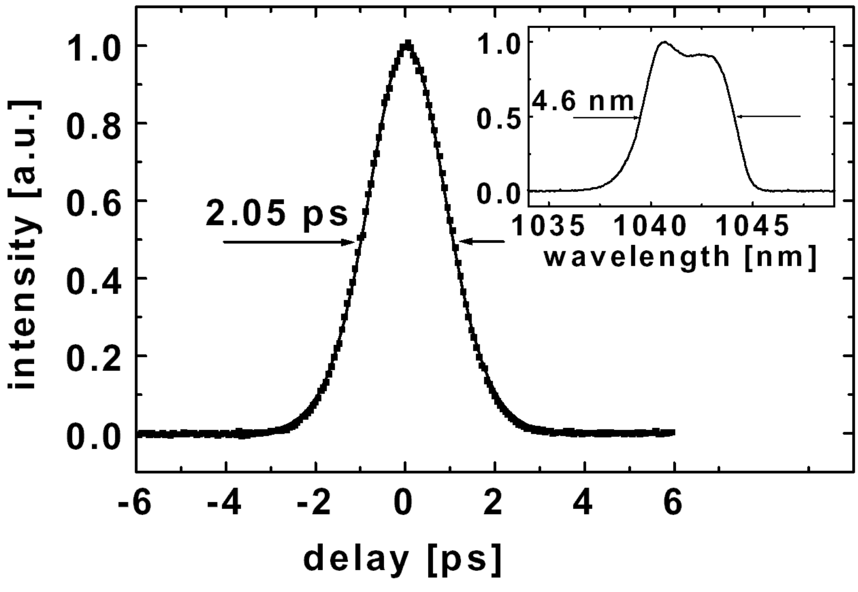

Fig. 6.5. Intensity autocorrelation and spectrum (inset) of the picosecond Yb:scandia laser. Squares: experimental autocorrelation data; line: *sech*^{2}-fit. The results are obtained at maximum output power (0.8 W).

With a 6.2%-output coupler we obtain a slightly lower maximum output power, $P_{out,max}$ = 760 mW, and lower efficiencies, as listed in Table 6.1. The pulse duration is the same as with an output coupler transmission of 9.6%, while the spectral width at $P_{out,max}$ is larger, approximately 6 nm, which corresponds to the higher intracavity-pulse energy. Table 3.6. also gives the experimental data obtained with output coupler transmissions T_{OC} of 21.2% and 41.8%. Only cw lasing is possible with these, since the energy density on the SESAM is too low to sufficiently bleach its absorption and start mode locking. However, the maximum output power of 930 mW with T_{OC} = 21.2% indicates that a somewhat better mode-locked performance compared to the 9.6%-output coupler could be achieved, if the intensity on the saturable absorber were increased appropriately. Outcoupling of 5% or less does not permit mode locking, because the laser emission wavelength changes to 1094 nm.

Table 6.1. Performance of the Ti:Sapphire-pumped Yb:Sc_2O_3 laser in the picosecond configuration with different output coupler transmissions T_{OC}. Mode locking is only achieved with 6.2%- and 9.6%-output couplers. $\eta_{sl}(cw)$ – slope efficiency for cw lasing or below mode-locking threshold, $\eta_{sl}(ml)$ – slope efficiency for mode-locked operation, $P_{abs,thr}(cw)$ – laser threshold (cw), $P_{out,max}$ – maximum output power (mode-locked or cw) at ≈1.7 W of absorbed pumped power, η_{max} – maximum optical-to-optical conversion efficiency (mode-locked or cw).

T_{OC} [%]	η_{sl}(cw) [%]	η_{sl}(ml) [%]	$P_{abs,thr}$(cw) [mW]	$P_{out,max}$ [mW]	η_{max} [%]
6.2	40	50	200	760 (ml)	44 (ml)
9.6	49	54	250	820 (ml)	47 (ml)
21.2	65	-	300	930 (cw)	54 (cw)
41.8	69	-	500	830 (cw)	48 (cw)

The observed transversal mode structure of the Ti:Sapphire-pumped Yb:Sc_2O_3 picosecond laser is basically TEM_{00}. The mode-locked operation does not show any tendencies towards passive Q-switching (see chapter 4.3.). We have also tried to operate the Yb:scandia picosecond laser using a wavelength-stabilized tapered diode laser (chapter 6.2.2.) as the pump source, but feedback of pump radiation that has not been absorbed by the active medium strongly disturbs the diode stabilization and possibly harms the diode.

6.2.2. Ti:Sapphire-laser-pumped Yb(0.7%):Sc_2O_3 femtosecond laser

For femtosecond pulse generation, we use two 60° SF6 prisms with a tip-to-tip separation of 64 cm in the arm containing a 5.5% output coupler M_5 (Fig. 6.1.) to compensate for dispersion and enable a solitary regime of mode locking (see chapter 4.1.). A r = -150 mm mirror M_1 is applied for focusing on the SESAM.

Figure 6.7. shows the output power of the femtosecond Yb:scandia laser versus absorbed pump power. The cw laser threshold is reached at ≈250 mW of absorbed power; mode locking is achieved for ≥800 mW of pump radiation. Continuous-wave lasing occurs near 1041.5 nm, whereas the mode-locked laser emission is centered near 1044 nm. Like with the picosecond laser, the transition to mode-locked operation is accompanied by an increase of efficiency, as the saturable loss of the SESAM is bleached. The slope efficiency η_{sl} of the mode-locked femtosecond laser amounts to 35%; the maximum output power of 540 mW corresponds to an

optical-to-optical conversion efficiency η_{max} of 30%. With the cavity round-trip time of 11.7 ns, this results in a maximum pulse energy of 6.3 nJ.

The efficiencies are somewhat lower than those of the picosecond laser ($\eta_{sl} = 54\%$ and $\eta_{max} = 47\%$). This can be referred to the lower output coupler transmission (T_{OC} = 5.5% instead of 9.6%), which is necessary to achieve stable mode locking in the experiment, and to the introduction of the prisms. The latter causes only small additional reflection loss (<1%), but to increase mode-locking stability and to achieve a large emission bandwidth and short pulses, we have to adjust the laser cavity in such a way that the center wavelength of the mode-locked laser emission is shifted from the emission maximum of Yb:scandia towards longer wavelengths (near 1044 nm, see Fig. 6.6.), which compromises the laser effiency. The idea behind this is to flatten the overall net gain spectrum for the pulses and to increase the loss for parasitive cw radiation at 1041.5 nm. Furthermore, the femtosecond regime exhibits a more asymmetric resonator compared to the picosecond Yb:Sc_2O_3 laser, slightly modifying the beam waist in the crystal and therefore the overlap of pump beam and resonator mode.

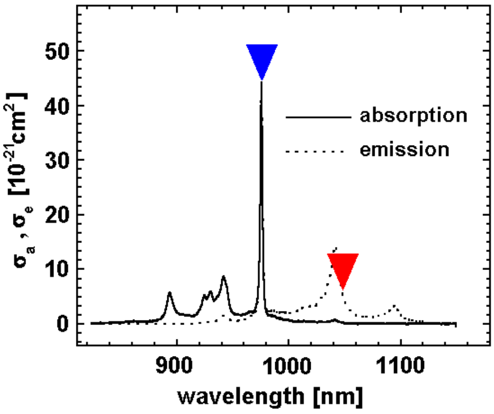

Fig. 6.6. Absorption and emission cross sections of Yb:Sc_2O_3. Pump and laser emission wavelengths are indicated.

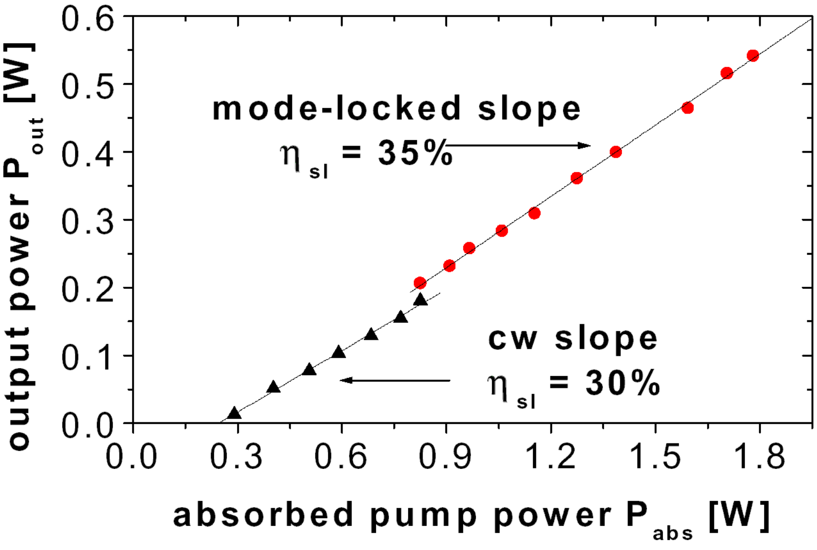

Fig. 6.7. Performance of the femtosecond Yb:scandia laser with a 5.5%-output coupler. Output power versus absorbed power in the mode-locked regime and below the mode-locking threshold (cw).

The intensity autocorrelation of the Yb:scandia femtosecond laser at maximum output power is shown in Fig. 6.8. Pulses as short as 230 fs (assuming a *sech²*-shape) are achieved, while we observe an emission spectrum with a FWHM of 5.3 nm centered at 1044.5 nm (inset of Fig. 6.8.). The time-bandwidth-product amounts to 0.33 which is close the Fourier limit (0.315). With decreasing intracavity power the pulse duration increases, as expected in a solitary regime (see chapt. 4.1.); at the mode-locking threshold we measure an output power of ≈200 mW and a pulse duration of 430 fs.

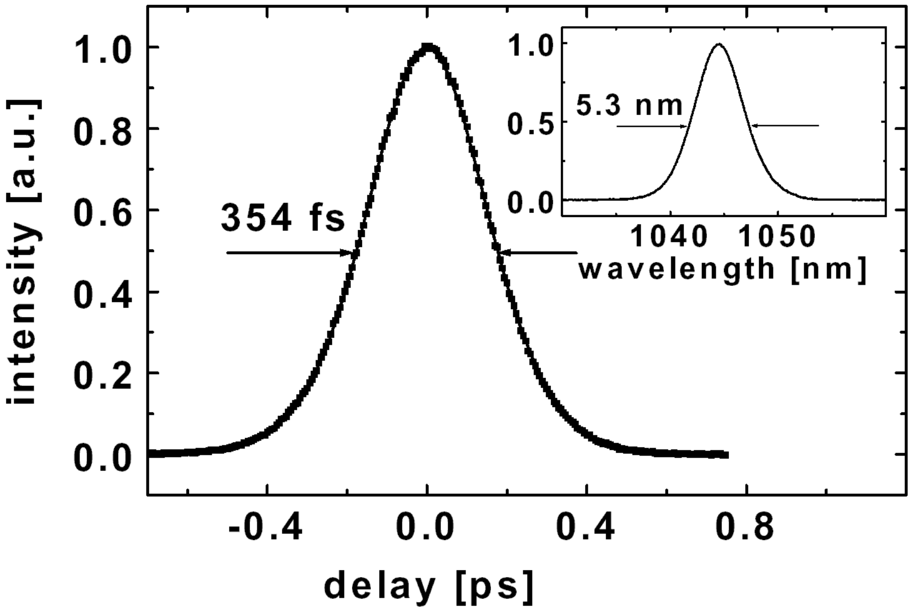

Fig. 6.8. Intensity autocorrelation and spectrum (inset) of the femtosecond Yb:scandia laser. Squares: experimental autocorrelation data; line: *sech²*-fit. The results are obtained at maximum output power (0.54 W).

The output of the femtosecond Yb:scandia laser exhibits a basically TEM_{00} mode structure. The laser shows some tendencies towards double-pulsing at higher powers and towards parasitive cw lasing, which may occur additionally to the pulses and eventually destroy mode locking (see chapter 4.3.); Q-switching is not observed. We are able to suppress the instabilities by the adjustment described above. Working with a 9.6%-output coupler, the higher loss does not permit enough freedom of adjustment to achieve a stable single-pulse mode-locked regime. However, we obtain double-pulse operation with a pulse duration of approximately 450 fs and an output power of 700 mW. We expect that better mode-locking stability and higher output powers will be possible, if a SESAM with a larger modulation depth ($\Delta R > 2\%$) is used.

The $Yb:Sc_2O_3$ femtosecond laser seems to require the relatively large amount of negative group velocity dispersion of ≈-3000 fs^2 provided by the SF6 prism pair (640 mm separation, less than 5 mm beam path inside of each prism). With SF10 prisms like used in the – aside from the prisms – similarly configurated, passively mode-locked Yb^{3+}-doped tungstate lasers (chapter 5.1.2.) or with considerably smaller prism separation than 640 mm, we do not achieve stable femtosecond operation.

6.2.3. Diode-pumped Yb(0.7%):Sc_2O_3 femtosecond laser

For the diode-pumped Yb:scandia femtosecond laser we use the same configuration as in the Ti:Sa pumped case, but with a stronger focusing upon the SESAM (M_1 with $r = -100$ mm, see Fig. 6.1.) to achieve saturation of the absorber and enable mode locking also at lower intracavity powers. Stable solitary mode locking is observed for output coupler transmissions between 1.5% and 3.5%. Instead of the Ti:Sa laser a wavelength-stabilized tapered diode laser (TDL) is applied for pumping.

Wavelength-stabilized diode pump laser

The pump diode is basically the same we have used in the Yb:KYW and Yb:KGW femtosecond experiments (chapter 5.1.2.), emitting up to 2 W of output power with a linewidth of <1 nm and a slow axis beam quality factor $M^2 < 3$. In the present case, the emission of the TDL is stabilized at 976 nm by feedback of a small amount of the radiation (<0.02%) using a reflection grating ($g = 750$ mm^{-1}). It is important to avoid additional feedback of similar or larger amount, for example from non-absorbed pump power reflected at the output coupler; in contrast to the picosecond laser with its shorter, prismless cavity, this condition can be fulfilled here.

Because of the excellent beam quality of the TDL, relatively simple beam shaping optics are sufficient. An asperical lens ($f = 4.5$ mm) and a cylindric lens ($f = 40$ mm) provide a collimated pump beam with a maximum power of ≈1.4 W, of which 73% are incident upon the crystal. Further improvement of the optics seems to be possible, since a considerable part of the pump power is lost at the aperture of mirror M_2 (see setup in Fig. 6.1.; 12.7 mm mirror diameter).

Without wavelength-stabilization the Yb:scandia laser would only generate strongly fluctuating cw output due to slight variations of the transversal mode structure and of the spectrum of the diode in combination with the sharpness of the Yb:scandia main absorption line. We also find that a change of the diode operation temperature by 1°C, which shifts the central emission wavelength of the diode by ≈0.3 nm, leads to a variation of Yb:Sc_2O_3 output power in the order of 30%. With wavelength-stabilization the diode-pumped Yb:scandia femtosecond oscillator exhibits better mode-locking stability than the Ti:Sa laser pumped one.

Diode-pumped femtosecond laser performance

The highest output is obtained with a 3.5% output coupler. Figure 6.9. shows that a maximum of 130 mW is obtained at ≈1 W of absorbed power, which corresponds to an optical-to-optical conversion efficiency η_{max} of 13% and results in an energy of 1.5 nJ per pulse. The threshold absorbed pump power for cw lasing amounts to about 200 mW; mode-locked operation occurs for more than 600 mW of absorbed pump light or at an output power of ≥75 mW, respectively. For mode-locked operation we measure a laser slope efficiency η_{sl} of approximately 14%, where we must consider that the TDL beam quality worsens slightly with higher pump powers (see effective far field measurement in Fig. 5.5.). At maximum output power of the Yb:scandia laser we observe a pulse duration of ≈350 fs.

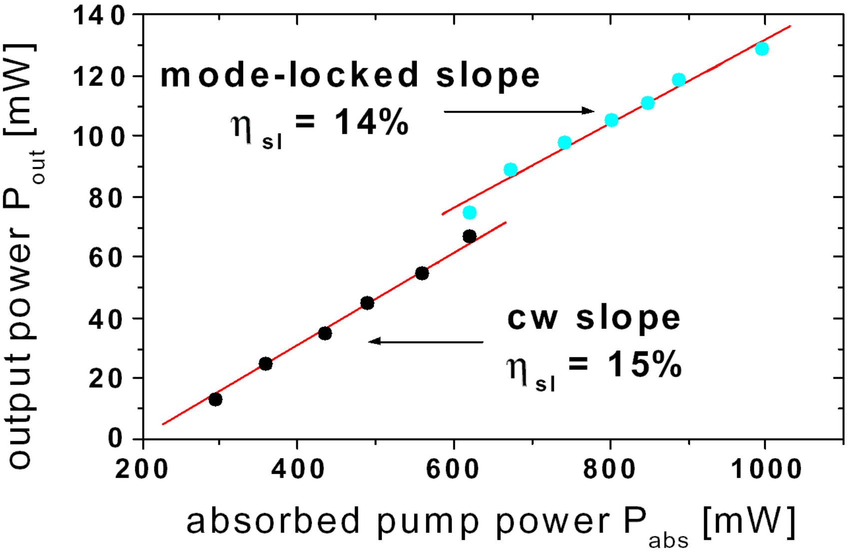

Fig. 6.9. Performance of the diode-pumped femtosecond Yb:scandia laser with a 3.5%-output coupler. Output power versus absorbed power in the mode-locked regime and below the mode-locking threshold (cw).

The shortest pulse duration, $\tau_p = 255$ fs, can be observed, if an output mirror with a transmission of 2.8% is used. This is documented in Fig. 6.10., which displays the intensity autocorrelation of the diode-pumped ultra-short pulse laser at an output power of 120 mW and the belonging *sech*^{2}-fit curve. Taking into account the measured emission spectrum (inset of Fig. 6.10.), which is centered at 1042.5 nm and exhibits a FWHM of 5.0 nm, we find that the pulses are almost bandwidth-limited with a time-bandwidth product $\tau_p \cdot \Delta\nu$ of 0.35. Towards lower powers the pulse duration increases up to 580 fs at the mode-locking threshold, at 40 mW of output power, while $\tau_p \cdot \Delta\nu$ remains approximately constant.

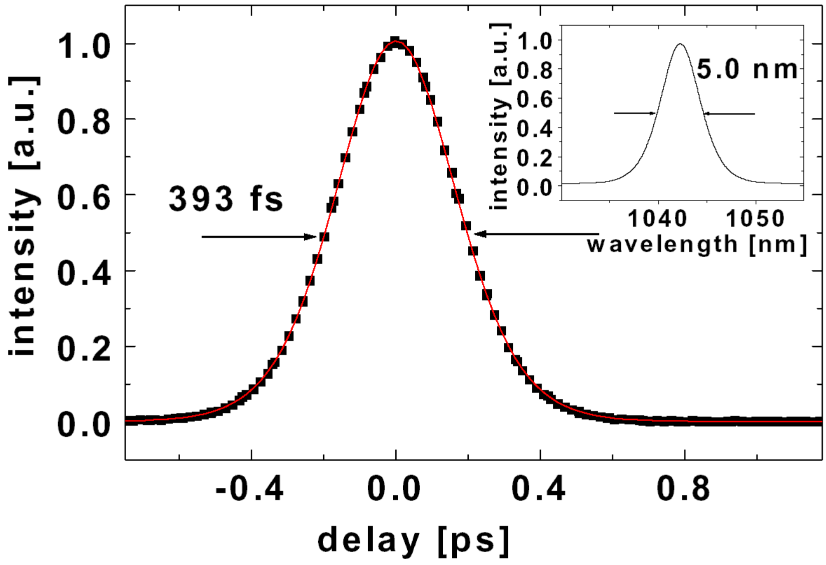

Fig. 6.10. Intensity autocorrelation and spectrum (inset) of the diode-pumped femtosecond Yb:Sc$_2$O$_3$ laser with a 2.8%-output coupler. Squares: experimental autocorrelation data; line: *sech*^{2}-fit. The results are obtained at an output power of 0.12 W.

With a 1.5%-transmissive output mirror we obtain only maximum 65 mW of mode-locked emission, i.e. the pulse energy is not higher than with the 2.8% outcoupler. Therefore no shorter pulses are observed. The mode locking results achieved for different output coupler transmissions T_{OC} are listed in Table 6.2.

The mode locking of the Yb:scandia laser in case of TDL pumping is stable for hours. Q-switching, parasitive cw emission, or multiple pulsing are not observed.

Table 6.2. Mode-locked performance of the diode-pumped Yb:Sc_2O_3 laser with different output coupler transmissions T_{OC}. $\eta_{sl}(ml)$ – slope efficiency for mode-locked operation, $P_{out,max}$ – maximum output power (output at ≈1 W of absorbed pumped power), η_{max} – maximum optical-to-optical conversion efficiency, $\tau_{p,min}$ – minimum pulse duration. Bold: best results.

T_{OC} [%]	η_{sl}(ml) [%]	$P_{out,max}$ [mW]	η_{max} [%]	$\tau_{p,min}$ [fs]
1.5	6	65	7	270
2.8	15	120	12	**255**
3.5	14	**130**	13	350

Comparison to previous results

The highest output power from the diode-pumped femtosecond Yb:Sc_2O_3 laser, 130 mW, is considerably lower than the maximum output demonstrated with the Ti:Sa pumped ultra-short pulse oscillator, 540 mW in case of single pulse mode locking; the same is valid for the highest efficiencies obtained (slope efficiencies: η_{sl} = 15% against 35%). The lower performance with the TDL is basically due to the lower power incident on the laser crystal, which is only ≈1 W instead of 1.8 W from the Ti:Sa laser, and due to less perfect matching of pump beam and resonator mode caused by the lower beam quality of the diode. Compared to the TDL-pumped Yb:tungstate femtosecond lasers in chapter 3.1.4. the output yield is similar; for 1.1 W of absorbed power 120 mW (Yb:KGW) and 150 mW (Yb:KYW) have been achieved.

The minimum pulse durations obtained with the Yb:scandia laser are similar for both pump options, 230 fs with the Ti:Sa laser and 255 fs with the TDL. They have an intermediate position between the Yb^{3+}-doped tungstate results, e.g. τ_p = 112 fs (Yb:KGW) and τ_p = 101 fs (Yb:KYW) in the experiments mentioned above, and the 340 fs limit reported with Yb:YAG [Hoe99b]. This can be attributed to the gain bandwidth of Yb:Sc_2O_3 being larger than that of Yb:YAG, but smaller than that of Yb:KYW or Yb:KGW.

Further development of mode-locked Yb:sesquioxide lasers

The results presented for the first mode-locked laser using an Yb^{3+}-doped sesquioxide are very promising; especially the extraordinarily high efficiencies in the picosecond configuration – to our knowledge the highest obtained from a mode-locked laser so far – indicate that Yb:Sc_2O_3 and its analogs may be optimum laser media for high-power oscillators and amplifiers emitting near 1 µm, if pulse durations in the range from 200 fs to a few ps are desired. Here (and in cw lasers as well) advantage can be taken also from the high thermal conductivity of scandia, which exceeds that of YAG by ≈50% and that of potassium yttrium or gadolinium tungstates by a factor of ≈5.

To exploit the possible very low laser quantum defect of approximately 6% with diode pumping, a wavelength stabilization of the diodes near 976 nm like demonstrated by us should be implemented or crystals with higher Yb^{3+} concentration or larger dimension longitudinal to the pump beam have to be used. Otherwise, pumping in the broader absorption band near 940 nm may be more appropriate to permit the use of diodes with broader or shifting emission spectra and to avoid fluctuations of the absorbed power, which decrease the mode-locking stability. With respect to higher Yb^{3+} doping levels Lu_2O_3 seems to be a favorable host to Sc_2O_3 because of the closeness of Yb^{3+} and Lu^{3+} ion radii; crystal quality is compromised for levels >1 at.% in scandia, at least if grown by the heat exchanger method. However, the growth of $Yb:Lu_2O_3$ is not as elaborated as $Yb:Sc_2O_3$ growth, yet. As an alternative approach, ceramic sintering may permit the production of large, highly doped sesquioxide media with good optical quality in the near future [Lu03].

7. Summary

Yb^{3+}-actived monoclinic double tungstates and cubic sesquioxides are the two most promising classes of laser materials with respect to achievable lasing efficiencies, and they permit the generation of mode-locked pulses in the subpicosecond region. The potential of these crystals was examined in the laser experiments of this work, using the structurally analog tungstates $Yb:KY(WO_4)_2$ (Yb:KYW), $Yb:KGd(WO_4)_2$ (Yb:KGW), and $KYb(WO_4)_2$ (KYbW) and the sesquioxide material with the most favorable properties, $Yb:Sc_2O_3$ (Yb:scandia).

With lowly Yb^{3+}-doped KYW and KGW, efficient continuous-wave (cw) and mode-locked laser operation was demonstrated. The best slope efficiency, 68%, was obtained with a 5%-doped $Yb:KY(WO_4)_2$ crystal in a Ti:Sa-laser pumped cw regime. With the same crystal, the first mode-locked oscillator employing an Yb^{3+}-doped tungstate medium in combination with a semiconductor saturable absorber mirror (SESAM) as passive mode-locker was realized. The pump source was a novel tapered diode laser (TDL), offering a slow-axis M^2 of ≈ 3 and providing 1.1 W of absorbed pump power. For single-pulse operation in a solitonlike regime, this yielded a maximum output power of 150 mW and a minimum pulse duration of 101 fs. The femtosecond laser performance was compared to that of a 5%-doped Yb:KGW and a 5wt%-Yb_2O_3-doped phosphate glass medium in the same resonator. The similar results achieved with Yb:KGW (120 mW maximum, 112 fs minimum) confirmed that the Yb^{3+} ion has very similar spectroscopic properties in the different monoclinic double tungsstates. A similar performance of the glass medium, however, pointed out that the tungstate crystals used here (3-mm-thick) should be thinner or exhibit a lower Yb^{3+} concentration, to reduce reabsorption loss and lasing threshold.

An optimum strategy to make efficient use of Yb^{3+}-actived monoclinic tungstates at room temperature would be to employ a very thin platelet of high Yb^{3+}-concentration material in a face-cooled laser design like the thin-disk concept, which enables multiple-pass pumping and excellent cooling. Therefore, 41% to 80% doped Yb:KYW and stoichiometric KYbW were investigated. Other applications like microchip lasers could also take profit from the very high absorption and gain coefficients of these crystals: From the spectroscopic measurements in this work, an amazing $1/e$-absorption length of ≈ 13 µm was determined for KYbW.

Important issues were if high Yb^{3+} concentrations in tungstate hosts permit a good optical crystal quality and if the heat produced in the relatively small active volumina of highly doped crystals can be handled. This was proofed in this work. For the first time, laser operation of tungstates with an Yb^{3+} concentration considerably higher than 20% and finally, with a 125-µm-thin KYbW crystal, the first cw lasing of a stoichiometric Yb laser material was achieved. Thermal problems were obvious, however, and cw lasing required a face-cooled laser design and pumping in the red-wing of the absorption spectrum, i.e. above the mean wavelength of fluorescence. While reducing thermal problems by long-wavelength-pumping a KYbW laser crystal, we demonstrated the smallest laser quantum defect (to the best of our knowledge) ever recorded for a laser crystal, 1.6%. Face-cooled concepts will be improved, if yet thinner media or composite media (Yb^{3+}-containing plus undoped material) are realized.

With Yb:scandia we achieved high output yield in all laser configurations investigated. A 0.7% Yb^{3+}-doped crystal was used in a cw regime pumped by a Ti:Sa laser. The slope efficiency amounted to 65%. With the same crystal, we demonstrated for the first time to our knowledge mode-locked operation of an Yb:Sc_2O_3 laser, and more general, of an oscillator using a sesquioxide laser crystal. In a Ti:Sa-laser-pumped picosecond regime, i.e. without solitonlike pulse shaping, an efficiency record was set for a mode-locked laser using a crystalline active medium, 47% output yield with 820 mW output power and 54% slope efficiency. Adding dispersion-compensating prisms led to solitonlike pulses with a duration of 230 fs at 540 mW output power (30% yield), with a slope efficiency of 35%. Using the dispersion-compensated cavity with the tapered laser diode that had been employed for the mode-locked tungstate experiments, similar output power compared to these experiments was achieved (130 mW output, at 1 W absorbed pump power). Minimum pulse durations were again slightly longer compared to Yb:KYW and Yb:KGW, 255 fs, which is a consequence of the narrower gain spectrum of Yb:scandia.

Despite of the fact that the laser media used here are not optimum (they are all too long with respect to reabsorption loss; high-Yb^{3+}-concentration crystals may additionally profit from a reduction of impurities), our results are very promising. One may predict that in the near future, Yb^{3+}-activated tungstate and sesquioxide crystals will be found operating in many commercial moderate- to high-power laser systems, preferably if mode locking is required. One should consider the following hints, however:

More than other Yb laser materials, Yb^{3+}-activated tungstates profit from high-brightness pump sources and should be combined with such; they will work best in face-cooled designs like the thin-disk laser. Due to the similar ion radii of Y^{3+} and Yb^{3+}, KYW is the better host compared to KGW, if higher Yb^{3+} doping levels are to be realized. The stoichiometric material KYbW will show the best crystal quality, however. Sc_2O_3 is an excellent host for low Yb^{3+} concentrations, i.e. up to ≈1% doping. Above this value the size mismatch of Sc^{3+} and Yb^{3+} increasingly worsens the crystal quality and the thermal conductivity is also significantly reduced. Then, if crystal growth of the analog sesquioxides Lu_2O_3 and Y_2O_3 can be improved, these materials, though spectroscopically slightly inferior, may be the better choice.

A. Appendix

A.1. Yb^{3+} – a low-loss laser ion / Overview of loss processes

Table a.1. lists the inherent loss processes that can occur with laser active ions, their relevance in general and for Yb^{3+}. Illustrations are given in Figs. a.1.a) to g). The schemes are examples referring to four-level or quasi-four-level lasers; in three-level or quasi-three-level lasers the ions are pumped directly into the upper laser level.

Table a.1. Inherent loss processes of laser active ions.

loss mechanism	Figure	relevance in general	relevance for Yb^{3+}	comment
laser quantum defect	a.1.a)	present for all laser ions	small or very small (1.6-14%)	depends on host and transitions
fluorescence	a.1.b)	present for all laser ions	main loss near laser threshold	counter: operation far above threshold
reabsorption	a.1.c)	only for quasi-3- or quasi-4-level-materials, where the lower laser level is populated	considerable, increases laser threshold	depends on host; counter: operation far above threshold
downconversion transfer (cross-relaxation)	a.1.d)	present, if suitable level between laser manifolds exists; e.g. with Nd^{3+}	absent	causes concentration quenching; counter: low dopant concentration, low inversion
upconversion transfer (cross-relaxation)	a.1.e)	present, if suitable level above laser manifolds exists	absent	same as for downconversion
excited state absorption	a.1.f)	present, if suitable level above laser manifolds exists	absent	counter: low inversion
cooperative luminescence	a.1.g)	higher order process, extremely low cross section	observable, but usually insignificant	could become significant at high dopant levels and high inversion

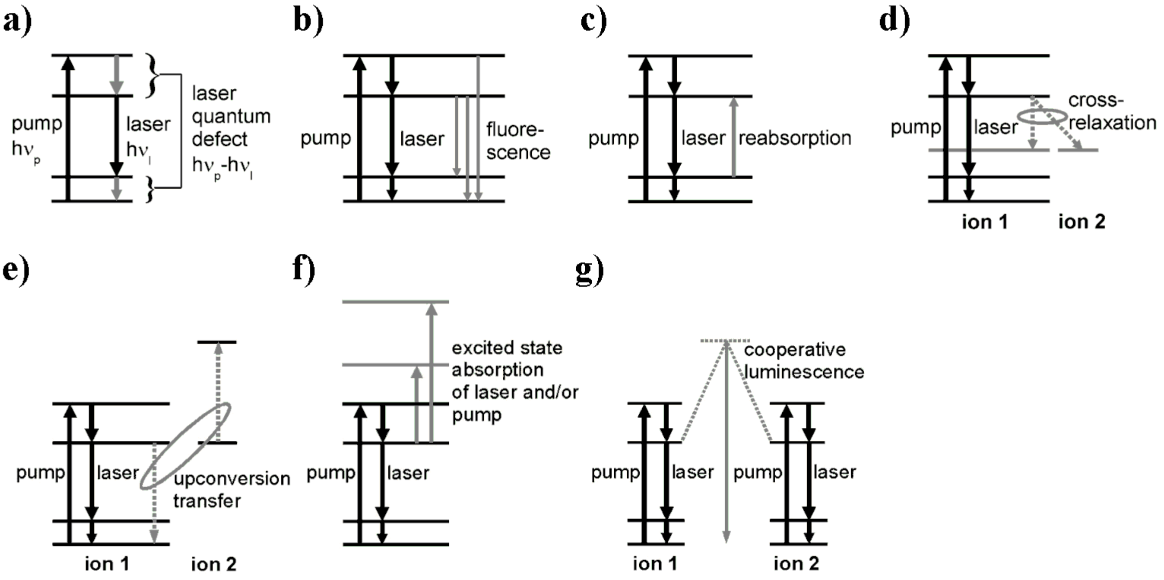

Fig. a.1. Inherent loss processes of laser active ions. See Table a.1. and text. a) Laser quantum defect. b) Fluorescence. c) Reabsorption of laser radiation by population of lower laser state. d) Down-conversion transfer. e) Upconversion transfer. f) Excited state absorption of pump and/or laser radiation. g) Cooperative luminescence.

When compared to its competitor in the 1-µm-range, the Nd^{3+} ion, Yb^{3+} must be considered a low loss laser ion, due to a smaller laser quantum defect and higher possible laser quantum efficiency. Historically, the potential of Yb laser materials could not be exploited because of their relatively high lasing thresholds, until suitable powerful, bright and reasonably priced pump sources became available [Lac91]. Today, laser diodes with good beam quality and high output powers enable laser operation far above the threshold, where the reabsorption influence from Yb^{3+} is small; therefore high efficiencies can be achieved from Yb^{3+} lasers.

The **laser quantum defect**, *lqd*, is the difference of pump and laser quantum energies, $h\nu_p$ and $h\nu_l$ (Fig. a.1.a). Values are usually given as percentage of the pump quantum energy,

$$\mathrm{lqd} = 100 \times \frac{h\nu_p - h\nu_l}{h\nu_p} \quad \text{(a.1.)}$$

Generally, in quasi-three- or quasi-four-level laser schemes the total *lqd* is relatively small, since the lower part of the *lqd* (Fig. a.1.a) is the energy difference of Stark levels within the ground-state manifold. Furthermore, in quasi-three-level laser schemes there is no upper part of the *lqd*, and therefore the total *lqd* is even smaller. For Yb^{3+} lasers, typically, *lqd* values between 4% and ≈10% are observed [Kul97b, Fan93]. The record is an *lqd* of only 1.6% with KYbW and demonstrated in this work (see chapt. 5.2.1.4. and [Klo03]).

While diode-pumped Nd^{3+} lasers are usually operated as four-level lasers with an *lqd* around 25%, a smaller *lqd* is also possible using quasi-three-level laser schemes (*lqd* ≈ 6.5% minimum with Nd:YAG) [Lup02b], but then – just like with Yb^{3+} – reabsorption loss occurs [Fan87] and the effective absorption and emission cross sections are smaller.

The *lqd* will be completely turned into heat, if, aside from the optical pump and laser transitions, the laser scheme contains only phononic transitions, which is the case for Yb^{3+}. The theoretical upper limit of the laser efficiency is given by 100% minus the *lqd.* For the actual laser efficiency this value has to be multiplied by the laser quantum efficiency, which stands for the number ratio of laser quanta and pump quanta (see chapt. 3.3.3.). The loss mechanisms described below reduce the laser quantum efficiency.

Fluorescence (Fig. a.1.b) is the most important loss process for Yb laser materials, if defect- or impurity-related loss can be neglected. All pump photons that are required to reach the laser threshold will be converted into fluorescence photons.

The mean fluorescence wavelength or quantum energy, λ_{mf} or $h\nu_{mf}$, and the pump wavelength or quantum energy, λ_p or $h\nu_p$, usually differ. The energy difference is balanced by the generation or annihilation of phonons from the host. Therefore, the contribution of spontaneous emission to heat generation in the medium depends on the fluorescence quantum defect *fqd*, defined by

$$\mathrm{fqd} = 100 \times \frac{h\nu_p - h\nu_{mf}}{h\nu_p} \quad \text{(a.2.)}$$

A positive *fqd* means heating, a negative *fqd* means cooling. Yb^{3+} is one of the few laser ions fluorescence cooling in a solid can be realized with (see [Bow00, Eps95], chapters 5.2.1.3. and 5.2.1.4.).[1]

---

[1] Fluorescence cooling was also demonstrated with Tm^{3+} [Hoy00].

Reabsorption of the laser radiation (Fig. a.1.c) is observed, if the lower laser level is thermally populated. Therefore it is a handicap of all quasi-three- or -four-level laser materials. The strength of reabsorption depends on the Boltzmann distribution of the ground state multiplet, and therefore on the Stark splitting and on the position of the lower laser level within the multiplet.

A part of the reabsorbed radiation is recycled by the generation of new laser photons, the other part goes into fluorescence or other channels of decay and affects the laser performance: The laser threshold is increased, the differential laser efficiency is decreased for operation near threshold [Fan87, Ris88] (see also chapter 3.3.). In case of an optical amplifier a minimum value of inversion is required to achieve positive gain in the medium; below this value, a signal is attenuated. Fortunately, with Yb materials, reabsorption does not necessarily heat the active medium, since fluorescence from reabsorbed radiation can provide a cooling effect due to a negative *fqd*.

Reabsorption can be countered by low temperature operation – reducing thermal population – or by intensive optical pumping. The latter means operation far above the lasing threshold, where the threshold plays a minor role for the total efficiency and where the influence of reabsorption on the slope efficiency is bleached by high radiation intensities inside of the laser cavity. For optical (single-pass) amplifiers with their usually lower signal intensities, however, active materials showing strong reabsorption at the extraction wavelength may not be suitable.

A **downconversion transfer** (Fig. a.1.d) is possible, if a quenching intermediate level exists. This is not the case for Yb^{3+} laser media, but a big problem with many Nd^{3+}-doped materials [Dan75, Kam82, Lup01, Lup03]. In YAG e.g., the $^4I_{15/2}$ manifold of Nd^{3+} is located approximately at the mean energy between the excited $^4F_{3/2}$ manifold and the ground state manifold $^4I_{9/2}$. This leads to a cross-relaxation, splitting an exciton onto two ions by dipole-dipole and superexchange interactions [Dia98, Kam82, Lup01]. The transfer rate grows with decreasing spatial separation of the active ions [Lup90, Dia98] and thus limits the useful dopant concentration to low values by concentration quenching in many hosts.

An **upconversion transfer** (Fig. a.1.e) can occur, if a suitable acceptor level above the laser level exists. The probability of an energy transfer from one single-excited ion to another increases with their closeness, too. Therefore, loss by this cross-relaxation process is the more important, the higher the dopant concentration and the higher the inversion. While Yb^{3+} has no acceptor level and consequently no problem with upconversion, this loss mechanism plays an important role for Nd:YAG [Lup01, Pol98] and other Nd^{3+}-doped materials [Lup02, Ost98].

Excited state absorption (Fig. a.1.f) is another upconversion process, which requires an energetically higher-located acceptor level, but it involves one ion only. A single-excited ion may absorb pump radiation or reabsorb the laser emission. With Yb^{3+} there is no such problem; in some hosts, Nd^{3+} shows weak excited state absorption on the main laser lines [For99b].

Cooperative luminescence (Fig. a.1.g) is a phenomenon, which has been reported only for Yb^{3+} so far [Gol97, Gol02, Nak70, Weg95]. It can be observed also with KYbW, a material used in this work [Kir02]. Two neighboring excited ions cooperatively emit a photon of about twice the energy of a single exciton (a phonon may also be involved). The probability of the process is very low, compared to relaxations of single-ion electronic states. However, cooperative luminescence may become important at very high Yb^{3+} concentrations and high inversion levels.

Loss processes connected with defects and impurities

Defects or impurities can provide considerable additional loss: The ground states of color centers and impurities may absorb pump or laser light or act as acceptors for non-radiative energy transfers. The same is possible for their excited states, causing excited state absorption similar to that shown in Fig. a.1.f) and giving rise to upconversion processes like in Fig. a.1.e), with the color center or impurity ion playing the part of the acceptor ion. Defects can also cause scattering losses ("milky-looking" laser media).

Countermeasures are optimized growing conditions, thermal annealing in a suitable atmosphere, and the use of pure basic materials.

With Yb^{3+}, problems can result from Yb^{2+} color centers, if the host structure lacks of electro-negative constituents (e.g. oxygen), or from cation impurities, including other rare earths [Mix99, Mue02, Bou03]. The transfer rates from Yb^{3+} to e.g. Er^{3+} or Tm^{3+} are large, especially at high active-ion concentrations, and can be exploited to create upconversion lasers with Yb^{3+} as a sensitizer collecting the pump light [Kul97, Bat02]. It is expensive to avoid traces of such elements in the Yb-containing basic material, since all rare earths show similar chemical behaviors.

Multiphonon relaxations

The interaction of an active ion with its crystalline or glass surroundings may also lead to a direct non-radiative decay by the generation of several phonons, which bridge the gap between the upper laser manifold and a lower manifold. However, the more phonons needed, the less likely this process. For Yb^{3+} it can be neglected, even in hosts with large maximum phonon energies; for Nd^{3+} it is relevant because of the smaller energy difference between the $^4F_{3/2}$ and the $I_{15/2}$ multiplets.

Secondary loss processes / thermal effects

Compared to other active materials, the low inherent losses of Yb^{3+} laser media and the low heat generation connected with these lead to lower danger of fracture and make thermal management easier. They mean less degradation of the beam quality and lower secondary losses by thermal effects, as increased temperatures cause tensions in the active medium and can change its optical properties considerably, resulting in thermal birefringence and lensing [Pol98, Web99]. The significance of these effects also depends on the host material, the cooling, and the resonator design.

A.2. How to determine spectroscopic properties

The formulas collected here are essential to determine the spectroscopic properties of a laser material from measured data. Often one finds different values for properties of a specific crystal in literature. This can be referred to measurement inaccuracies or varying crystal quality. Especially for novel materials, published data have to be considered preliminary. After all, laser experiments have to evaluate the potential of a material for laser applications.

For anisotropic materials the formulas are valid as well; in this case the arguments do not only contain the wavelength λ, but also the polarization and the unit wave vector of the light beam.

Absorption cross sections

The absorption cross section $\sigma_a(\lambda)$ at a wavelength λ is connected with the unsaturated absorption coefficient $\alpha(\lambda)$ by

$$\sigma_a(\lambda) = \alpha(\lambda)/N \quad , \qquad \text{(a.3.)}$$

with N, active ion concentration.

The absorption coefficient $\alpha(\lambda)$ is given by

$$\alpha(\lambda) = -\frac{1}{L}\ln\frac{I_t(\lambda)}{I_0(\lambda)\{1-R\}^2} \quad , \qquad \text{(a.4.)}$$

with L, length of light path through the crystal,
$I_t(\lambda)$, transmitted intensity,
$I_0(\lambda)$, incident intensity,
R, crystal reflectivity, for normal incidence: $R=[n(\lambda)-1]^2[n(\lambda)+1]^{-2}$; $n(\lambda)$, refractive index.

Uncertainties with the determination of $\sigma_a(\lambda)$ result from the difficulty to estimate the dopant concentration N (– errors in the order of 10% are usual –) and from an insufficient signal/noise ratio when measuring $I_t(\lambda)$. The latter is the case for very strong absorption, $\alpha(\lambda)L >> 1$, or for very weak absorption, $1/[\alpha(\lambda)L] >> 1$.[1] Therefore, at relatively high dopant concentrations the measurement of the absorption peaks requires a suitably short crystal sample. On the other hand, long samples are necessary to investigate the far wings of absorption spectra. Such an interest exists with Yb^{3+} laser materials, where knowledge about the long-wavelength region is important due to the worsening influence of reabsorption on laser operation. To measure the absorption of KYbW for polarization parallel to the $\boldsymbol{N_m}$ crystallo-optic axis (see chapt. 2.4.), three crystals with different thicknesses had to be used.

Of course, when trying to improve the signal/noise ratio, saturation of the absorption must be avoided. For anisotropic crystals whose cross sections vary strongly with the polarization of the incident light, one must also be careful to orient the optical axes exactly, relative to the polarization vector. Otherwise, in case of a very low transmission for the polarization to be

---

[1] That means for $I_t(\lambda)/[I_0(\lambda)\{1-R\}^2] << 1$ or $[I_0(\lambda)\{1-R\}^2-I_t(\lambda)]/[I_0(\lambda)\{1-R\}^2] << 1$, respectively.

investigated, even a small component having the wrong polarization can lead to a large fake signal. With an 80-µm-thin KYbW crystal whose absorption is measured for polarization parallel to the $\boldsymbol{N_m}$ crystallo-optic axis, a signal error of +20% (+130%) at the zero-line transition, (0) - (0′), would result from an orientation error of only 2° (5°) towards the $\boldsymbol{N_g}$ axis.

Furthermore, the crystal quality can have a large influence on the absorption. For Yb^{3+}-doped crystals, the distorting effects of impurities or defects on the crystal field can lead to significant changes of the spectrum (line broadening, additional lines), while their absorption is not observed within the absorption range of the active ion. In crystals, where the active ions can be doped into different sites, the occupation of the sites may depend on the growth technique and parameters, which will therefore lead to different spectra [Ito04, Sch03].

Emission cross sections

The emission cross section $\sigma_e(\lambda)$ can be obtained in two ways: The McCumber or "reciprocity" method [McC64, McC64b, DeL93, Pat01] uses the reciprocity of the individual absorption and emission cross sections for a single ion ($\sigma_{ij} = \sigma_{ji}$ for a transition from Stark level *i* to *j* and vice versa), to develop a relationship between the absorption and emission cross sections $\sigma_a(\lambda)$ and $\sigma_e(\lambda)$, which are effective for the average ion in the ground or excited state multiplet, respectively.[1] The energetic positions of the Stark levels are required to take into account the thermal population distribution within the multiplets. The second method is based on the Füchtbauer-Ladenburg equation and scales a measured fluorescence spectrum $I(\lambda)$ into a spectrum of $\sigma_e(\lambda)$. For this purpose the radiative lifetime of the excited state must be known.

Reciprocity method

The emission cross section $\sigma_e(\lambda)$ can be obtained using [DeL93, Pat01]

$$\sigma_e(\lambda) = \sigma_a(\lambda)\frac{Z_1}{Z_2}\exp\left\{\frac{hc}{kT}\left(\frac{1}{\lambda_{zl}} - \frac{1}{\lambda}\right)\right\}, \tag{a.5.}$$

with λ_{zl}, wavelength of zero-line transition, (0) - (0′),
Z_1, Z_2, partition functions of the lower and upper state multiplets, respectively,
k, Boltzmann constant.

The partition functions are given by

$$Z_1 = \sum_i d_i \exp(-\frac{E_i}{kT}) \quad \text{and} \quad Z_2 = \sum_j d_j \exp(-\frac{E_j}{kT}), \tag{a.6.}$$

with E_i, E_j, energetic position of Stark level *i* or *j*, relative to the lowest Stark level within the ground or excited state multiplet, respectively,
d_i, d_j, degeneracy of Stark level *i* or *j*; $d_i = d_j = 2$ in case of Yb^{3+} as the active ion, and the sums running over the $i = 0, 1, 2, 3$; $j = 0', 1', 2'$ for Yb^{3+}.

---

[1] $\sigma_a(\lambda)$ and $\sigma_e(\lambda)$ are the relevant quantities; the first is measurable in absorption experiments and the latter accounts for the observable laser gain.

Equations a.5. and a.6. are an approximation. They will serve fairly well, if the Füchtbauer-Ladenburg approach is not applicable, but the absorption can be measured with high precision. Actually, the equations lack accuracy to some degree, since they do not consider the influence of phonons and their distribution.

Band and Heller [Ban88] give basically the same relationship as eq. a.5., but keep it more general by not explicitly defining the partition functions. They point out that eq. a.5. is no longer strictly applicable, if the internal degrees of freedom of the electronic states do not obey Boltzmann statistics. This is a problem for phonons at temperatures lower than the phonon frequency. The partition functions of eq. a.6. do not include electron-phonon-interaction, which may considerably modify the simple Boltzmann distributions.[1] Furthermore, at room temperature (293 K), kT is given by 4.05 x 10^{-21} J or 204 cm^{-1}. For almost all laser hosts the maximum and also the effective phonon energies are larger than this value. As a consequence, one can expect that especially in the wings of the spectra (outside of the limits given by the energy splittings of ground and excited states), where phonons are responsible for nonvanishing cross sections, deviations of the calculated emission spectrum will occur from the shape of the fluorescence spectrum. Indeed, such deviations are observed [Hau02], but can to a large extent be referred to absorption measurement inaccuracies, however.

In some cases where different sites exist for the active ion in the crystal, the RHS of eq. a.5. can be substituted by averaged terms, if energy migration between the sites is fast (migration rate >> radiative relaxation rate) and the site occupations are known. Otherwise, the emission cross sections depend on the pump wavelength and – for pulsed excitation – on time. This will affect the usefulness of both the McCumber and Füchtbauer-Ladenburg methods.

Füchtbauer-Ladenburg equation

The relationship between the emission cross section $\sigma_{e,\gamma}(\lambda)$ and the measured fluorescence intensity $I_\gamma(\lambda)$, is given by [Mun01]

$$\sigma_{e,\gamma}(\lambda) = \frac{\lambda^4 g_\gamma(\lambda)}{8\pi n^2 c \tau_{rad}} , \qquad \text{(a.7.)}$$

with τ_{rad}, radiative lifetime of the upper state,
n, refractive index,[2]
$g_\gamma(\lambda)$, normalized lineshape function.

The latter is defined as

$$g_\gamma(\lambda) = \frac{\lambda I_\gamma(\lambda)}{\frac{1}{3}\sum\limits_\gamma \int d\tilde{\lambda}\,\tilde{\lambda}\, I_\gamma(\tilde{\lambda})} . \qquad \text{(a.8.)}$$

Here we account for anisotropic crystals by an index γ standing for the different polarizations. The summation over γ in eq. a.8. includes three orthogonal directions. In case of biaxial crystals these are, preferably, polarization vector parallel to the $\boldsymbol{N_m}$, $\boldsymbol{N_g}$, and $\boldsymbol{N_p}$ crystallo-optic axes. For

---

[1] Therefore it is questionable, if the accuracy of the calculation can be improved by trying to use the "exact positions" of the Stark levels, as they would be without vibronics.

[2] Actually, one should use $n_\gamma(\lambda)$, but the inaccuracy is negligible considering other effects.

uniaxial crystals, $I_\gamma(\lambda)$ is identical for two directions (σ polarization) and therefore counted twice; γ includes π and σ polarization. For isotropic laser materials, the averaging $^1/_3 \sum_\gamma$ is left out.[1]

The Füchtbauer-Ladenburg approach can provide more exact results than the reciprocity method in regions of low absorption where fluorescence measurements show a better signal/noise ratio.

On the other hand, close to the zero-line transition, especially, radiation trapping (reabsorption of fluorescence) can strongly distort the observed fluorescence spectra $I_\gamma(\lambda)$.[2] Therefore, the emission cross sections would be calculated too small in this region and too large in the long-wavelength wing. Ways to handle this problem are the use of thin, lowly doped samples, excitation close to the surface, and the avoiding of internal reflections which elongate the effective light path through the material. However, for highly doped crystals like KYbW (chapt. 2.4.), no reasonable results are achieved with the Füchtbauer-Ladenburg approach.

The radiative lifetime τ_{rad} is a crucial parameter in eq. a.7.; a large error will lead directly to a wrong scaling of the emission spectrum and consequently to a wrong estimation of the gain provided by the laser material. Unfortunately, the determination of τ_{rad} is a highly nontrivial task.

Radiative lifetime

There exist two ways to determine the radiative lifetime τ_{rad}: The fluorescence lifetime τ_f can be measured; if the material exhibits a high quantum efficiency, τ_f should be close to τ_{rad}. The radiative lifetime can be calculated from the integrated absorption spectrum, a quantity which is related to the oscillator strength of the transition between ground and excited states.

Radiative lifetime from measurement of fluorescence lifetime

The fluorescence lifetime τ_f is related to the radiative and nonradiative lifetimes, τ_{rad} and τ_{nr}, by

$$\frac{1}{\tau_f} = \frac{1}{\tau_{rad}} + \frac{1}{\tau_{nr}} \qquad \text{(a.9.)}$$

The quantum efficiency η_q is defined as

$$\eta_q = \frac{\tau_f}{\tau_{rad}} \qquad \text{(a.10.)}$$

The first problem is that the nonradiative lifetime τ_{nr} is not directly measurable. At least, loss processes which contribute to nonradiative decay of the excited state (defects and impurities as energy sinks, see chapt. 2.3. and appendix A.1.) may be recognized by additional heat production or by parasitive fluorescence, the absence of which may be taken as an indicator for

---

[1] Sometimes other definitions of the normalized lineshape function are used. Therefore eq. a.7. differs in literature:
$\sigma_e(\nu) = \lambda^2 g(\nu) / (8\pi n^2 \tau_{rad})$ in [Pat01] (isotropic case),
$\sigma_e(\theta,\psi,\lambda) = \lambda^5 [g_\pi(\lambda)\sin^2\psi \sin^2\theta + g_\sigma(\lambda)\{\cos^2\psi + \sin^2\psi \cos^2\theta\}] / [8\pi n^2 c \tau_{rad} \int d\lambda\, \lambda\, (2g_\sigma(\lambda)/3 + g_\pi(\lambda)/3)]$
in [Mou86] (uniaxial case, arbitrary incidence)

[2] In principle, it is also possible to produce distortions by stimulated amplified emission, if the sample is pumped too intensively, so that the concentration of active ions in the upper state becomes too high.

a high quantum efficiency. For novel materials usually the growth technique is not elaborated yet and they will often show a relatively low quantum efficiency. Under such circumstances, fluorescence lifetime measurements can yield only a lower limit for the radiative lifetime. It also has to be taken into account that many nonradiative losses increase with dopant concentration.

The second problem is that reabsorption and internal reflections lead to a seemingly longer fluorescence lifetime (the error can exceed +100%), especially for materials with high dopant concentrations and large refractive indices [Heh97, Pat01, Sum94]. This can be countered by the use of diluted samples (if concentration quenching does not have to be investigated), by very thin or small samples or by excitation close to the surface combined with an aperture, so that the detected fluorescence light has travelled only a short path through the material. Reflections can be suppressed by sandwiching the sample crystal between an index-matching, optically inactive solid or by preparing the material as a powder which is suspended in a liquid with such properties [Puj02b]. Finally, one can try to eliminate the reabsorption and reflection effects from the data by calculation [Pat01].

Calculation of radiative lifetime from absorption

Another way to obtain the radiative lifetime is to use the measured absorption or the emission data calculated from these. From McCumber´s theory [McC64b] we can deduce[1]

$$\frac{1}{\tau_{\mathrm{rad}}} = \frac{8\pi n^2}{c^2} \int d\nu\, \nu^2 \langle \sigma_e(\nu) \rangle \qquad \text{(a.11.)}$$

,

or in terms of the wavelength

$$\frac{1}{\tau_{\mathrm{rad}}} = 8\pi c n^2 \int d\lambda\, \frac{\langle \sigma_e(\lambda) \rangle}{\lambda^4} \qquad \text{(a.12.)}$$

,

with $\langle \sigma_e(\nu) \rangle = \frac{1}{3} \sum_\gamma \sigma_{e,\gamma}(\nu)$ or $\langle \sigma_e(\lambda) \rangle = \frac{1}{3} \sum_\gamma \sigma_{e,\gamma}(\lambda)$,

emission cross sections averaged over the polarizations
(see also comments on eq. a.8.).

Equation a.12. results also from the Füchtbauer-Ladenburg eq. a.7., we may write as

$$\frac{g_\gamma(\lambda)}{\tau_{\mathrm{rad}}} = \frac{8\pi c n^2 \sigma_{e,\gamma}(\lambda)}{\lambda^4}$$

,

by summation over γ and integration over λ of left and right hand side and using the definition of $g_\gamma(\lambda)$ given in eq. a.8.

---

[1] The equation follows from $\sigma_{e,\lambda}(\mathbf{k},\omega) = f_\lambda(\mathbf{k},\omega)\,(2\pi c)^2 / (\omega n_\lambda(\mathbf{k},\omega))^2$ and $1/\tau_{rad} = \sum_\lambda \int_{4\pi} d\Omega_{k\lambda} \int_0^\infty d\omega\, f_\lambda(\mathbf{k},\omega)/(2\pi)$, with the approximation $n_\lambda(\mathbf{k},\omega) = n$.

Here $f_\lambda(\mathbf{k},\omega)$ is the average intensity in photons/s per unit frequency interval, and λ and $\mathbf{k}$ stand for the polarization (the summation goes over two orthogonal polarizations) and the unit wave vector. The general result is $1/\tau_{rad} = (1/c^2) \int d\nu\, \nu^2 \sum_\lambda \int_{4\pi} d\Omega_{k\lambda}\, n_\lambda^2(\mathbf{k},\nu)\sigma_{e,\lambda}(\mathbf{k},\nu)$.

If we use the values for $\sigma_e(\lambda)$ we have calculated using eq. a.5., we will obtain a relatively exact result for the radiative lifetime. A possible error basically results from deviations of the assumed partition functions from the true ones, which are influenced by vibronics. Measurement inaccuracies in the wings of the absorption spectrum, however, will only contribute little to an error in τ_{rad}, i.e. correspondingly to the small absorption intensities.

Often, the following relationship is used to calculate τ_{rad} directly from the absorption spectrum [Web71, Jia00, Hau02]:

$$\frac{1}{\tau_{\mathrm{rad}}} = \frac{d_f}{d_i}\frac{8\pi n^2}{\lambda_0^2}\int d\nu\,\sigma_a(\nu) \quad \text{or} \quad \frac{1}{\tau_{\mathrm{rad}}} = \frac{d_f}{d_i}\frac{8\pi c n^2}{\lambda_0^4}\int d\lambda\,\sigma_a(\lambda) \qquad \text{(a.13.)}$$

,

with d_f, d_i, “degeneracies” of the ground and excited states, actually the number of Stark levels times Kramers degeneracy,

λ_0, center wavelength of transition.

This must be considered a very rough estimation, since the underlying assumption,

$$\int d\nu\,\nu^2\sigma_e(\nu) = \frac{d_f}{d_i}\int d\nu\,\nu^2\sigma_a(\nu)$$

,

will be valid, only if all Stark levels are equally populated or the strengths of all transitions between these do not differ [Min91]. For Yb^{3+} at room temperature these conditions are not fulfilled and this means a much stronger approximation than neglecting vibronics in the partition functions. An additional approximation is made by multiplying the integral with the averaged quantity $1/\lambda_0^2$ or $1/\lambda_0^4$ instead of using $1/\lambda^2$ or $1/\lambda^4$ as a weighting factor in the integral.

A.3. Conventions for refractive indices

In uniaxial crystals, the refractive index is the same for all polarizations orthogonal to the ***c***-crystallographic axis ($\boldsymbol{E} \perp \boldsymbol{c}$ = σ polarization), i.e. $n_o(\phi) = n_o$ for arbitrary angles ϕ around the axis. The basal plane of a light ray, which is given by the ***c*** axis (identical with the optical axis) and the wave vector, defines an "ordinary ray" component of the electrical field vector ***E***, which stands orthogonal to the basal plane, and an "extraordinary ray" component, lying in the plane. While the "ordinary ray" experiences the refractive index n_o, the index $n_e(\theta)$ of the extraordinary ray depends on the angle θ between the optical axis and the wave vector. It is given by $n_e^2(\theta) = \sin^2(\theta)\ n_e^2 + \cos^2(\theta)\ n_o^2$, where n_e is the maximum or minimum refractive index of the extraordinary ray,[1] which is obtained for $\theta = 90°$ ($\boldsymbol{E} \| \boldsymbol{c}$ = π polarization). Therefore, a revolution ellipsoid represents the refractive indices of the ordinary and extraordinary rays of a light beam with wave vector $\boldsymbol{k}(\phi,\theta)$. The semiaxes of the ellipsoid are n_o, n_o and n_e, and its ellipticity expresses the birefringence strength of the crystal.

Trigonal, tetragonal, and hexagonal crystals are uniaxial structures.

In biaxial crystals, there is no rotation symmetry; an orthogonal base is given by three principal crystallo-optic axes, with regard to which the refractive index shows mirror-symmetry. In the ellipsoid-representation, the values of the refractive index for polarization parallel to the principal axes are the three different semiaxes. A light ray is split into a "fast ray" and a "slow ray". Both can be considered extraordinary rays, since both show an angular dependence of the refractive index. The crystallo-optic axes are labeled, traditionally, $\boldsymbol{N_p}$, $\boldsymbol{N_m}$, and $\boldsymbol{N_g}$ or, alternatively, $\boldsymbol{x}$, $\boldsymbol{y}$, and $\boldsymbol{z}$, where the assignment is determined by the related refractive indices, such that $n_p < n_m < n_g$ or $n_x < n_y < n_z$, respectively [Puj02b].[2]

Orthorhombic, monoclinic and triclinic crystals are biaxial structures.

Note: Only in orthorhombic crystals, all principal axes coincide with the crystallographic axes.

---

[1] n_e is the maximum refractive index of the extraordinary ray in case of an optically "positive" crystal; if the optical sign is "negative", n_e is the minimum.

[2] However, Kaminskii [Kam02] sets $\boldsymbol{N_p} = \boldsymbol{y}$, $\boldsymbol{N_m} = \boldsymbol{x}$, $\boldsymbol{N_g} = \boldsymbol{z}$.

A.4. Sellmeier formula and derivatives

The dispersion characteristics of materials are often described by the following Sellmeier formula for the refractive index *n*, where *A*, B_i, and C_i are Sellmeier coefficients and the wavelength in vacuum *λ* has be to used in units of 1 µm:

$$n^2(\lambda) = A + \sum_i \frac{B_i\lambda^2}{\lambda^2 - C_i} \quad . \tag{a.14.}$$

Differentiation leads to

$$\frac{dn(\lambda)}{d\lambda} = -\frac{1}{n(\lambda)} \sum_i \frac{B_i C_i \lambda}{(\lambda^2 - C_i)^2} \quad , \tag{a.15.a}$$

$$\frac{d^2n(\lambda)}{d\lambda^2} = -\frac{1}{n(\lambda)} \left[\left(\frac{dn(\lambda)}{d\lambda} \right)^2 - \sum_i \frac{3B_i C_i \lambda^2 + B_i C_i{}^2}{(\lambda^2 - C_i)^3} \right] \quad , \tag{a.15.b}$$

$$\frac{d^3n(\lambda)}{d\lambda^3} = -\frac{3}{n(\lambda)} \left[\frac{dn(\lambda)}{d\lambda} \frac{d^2n(\lambda)}{d\lambda^2} - \sum_i \frac{4B_i C_i \lambda^3 + 4B_i C_i{}^2 \lambda}{(\lambda^2 - C_i)^4} \right] \quad . \tag{a.15.c}$$

A.5. Comments on thermal conductivity formula

In [Via03] an equation for the thermal conductivity is given, which takes into account only the mass variance caused by the dopant and can be deduced from [Kle60] by approximating the Debye-frequency (maximum phonon frequency) as $\omega_D \approx \pi v/a_0$:

$$\kappa = \frac{1}{\pi a_0}\sqrt{\frac{k_B 2v}{\delta}\kappa_0}\ \mathrm{arctan}\left(\pi a_0\sqrt{\frac{\delta}{k_B 2v}\kappa_0}\right)\,.\,. \tag{a.16.}$$

with

κ_0,	thermal conductivity of the undoped host,
a_0,	mean interatomic distance,
v,	mean velocity of sound,
δ,	mass variance when a dopant ion replaces a lattice ion.

A more exact relationship for the Debye-frequency for an isotropic host is $\omega_D = v(6\pi^2 N/V)^{1/3} = v(6\pi^2 N_A\rho/M_a)^{1/3}$, with N, number of of primitive elementary cells, V, volume of the sample, N_A, Avogadro number, ρ, mass density, M_a, atomic weight.

A problem is also to correctly define δ: Referring it to the average mass of all ions (replacable or not), will lead to an obviously false result, if the average mass is identical with the dopant ion mass, which may differ much from the mass of the ion to be replaced. Referring it to the average mass of dopant and replaced ions will not take into account the varying meaning of these ions for the whole crystal in different hosts ("100%-doped" does not mean the same concentration).

Equation a.16. cannot be used for highly-doped materials, since it does not consider the possibly different thermal conductivity of the "100%-doped" material.

A.6. Thermal effects – lensing, birefringence, fracture

For a cylindrical laser rod, made from an isotropic material, the following equations can be given for the case of a cw or mode-locked laser or amplifier [Koe92, Web99].[1]

Thermal lensing

Thermal lensing in laser media is mainly due to the variation of the refractive index Δn_T caused directly by increasing temperature; the stress-induced variation Δn_ε usually contributes somewhat less. The curvature of the end-faces of the hot laser medium gives only a small contribution [Koe92, Web99].

The refractive index of a pumped laser rod with radius r_0 and length L varies with the radial position r, according to

$$n_{r,\phi}(r) = n_0 + \Delta n(r)_T + \Delta n_{r,\phi}(r)_\varepsilon \quad , \tag{a.17.}$$

where

$$\Delta n(r)_T = -\frac{r^2 Q}{4\kappa}\frac{dn}{dT} \tag{a.18.}$$

is the temperature-dependent variation and

$$\Delta n_{r,\phi}(r)_\varepsilon = -n_0^3 \frac{Q}{2\kappa}\alpha C_{r,\phi} r^2 \tag{a.19.}$$

is the stress-dependent variation for radial or tangential polarization, with

n_0,	refractive index without heating,
$Q = P_{heat}/(\pi r_0^2 L)$,	dissipated heat power per volume,
$C_{r,\phi}$,	photoelastic coefficient for radial and tangential polarization,
κ,	thermal conductivity,
α,	thermal expansion coefficient.

From this we obtain

$$n_{r,\phi}(r) = n_0\left\{1 - \frac{Q}{2\kappa}\left(\frac{1}{2n_0}\frac{dn}{dT} + n_0^2\alpha C_{r,\phi}\right)r^2\right\} . \tag{a.20.}$$

The focal length $f_{r,\phi}$ of the thermal lens, including the effect of the refractive index variation as described above and also the end-face curvature caused by thermal expansion, if $L << f_{r,\phi}$, is given by

$$f_{r,\phi} = \frac{\kappa}{QL\left\{\frac{1}{2}\frac{dn}{dT} + \alpha C_{r,\phi} n_0^3 + \frac{\alpha r_0 (n_0 - 1)}{L}\right\}} . \tag{a.21.}$$

---

[1] In case of differently shaped and/or anisotropic media and for pulsed operation calculations become more complicated.

Thermal birefringence

The stress-dependent variation of the refractive index (eq. a.19.) is different for radially and tangentially polarized components of a light beam,

$$\Delta n_\phi(r)_\varepsilon - \Delta n_r(r)_\varepsilon = -n_0^3 \frac{Q}{2\kappa}\alpha r^2 (C_\phi - C_r) \quad \text{(a.22.)}$$

This thermal birefringence leads to a variation of the optical phase at different positions within the beam cross section; the phase difference is

$$\delta = \frac{2\pi L}{\lambda}\left\{\Delta n_\phi(r)_\varepsilon - \Delta n_r(r)_\varepsilon\right\} \quad \text{(a.23.)}$$

The depolarization caused by birefringence can be a significant source of loss for isotropic laser media operating in resonators including polarizing elements, if birefringence is not compensated (loss in the order of 25% in case of strong thermal birefringence [Koe92]). Furthermore, in such lasers the variation of the phase at different positions within the beam will worsen the beam quality, since the polarizer will distort the beam by removing intensity position-selectively. For anisotropic laser materials, however, the natural birefringence is usually two to three sizes of order larger and will determine the beam polarization; therefore thermal birefringence does not play a role.

Heat-related fracture

The thermal stress parameter *R* is a measure for the maximum heat load permitted, until the tension at the rod surface exceeds the tensile strength of the rod:

$$\frac{P_{heat}}{L} = 8\pi R\,, \quad \text{(a.24.)}$$

with L, rod length,
P_{heat}, total heat power dissipated by the rod.

It can be deduced from the material parameters [Koe92]

$$R = \frac{\kappa(1-\nu_{poi})\sigma_{str}}{\alpha E}\,, \quad \text{(a.25.)}$$

with κ, thermal conductivity,
ν_{poi}, Poisson´s ratio,
σ_{str}, maximum permitted surface stress (tensile strength),
α, thermal expansion coefficient,
E, Young´s modulus.

A.7. Unit cell parameters of monoclinic double tungstates

Table a.2. lists the unit cell parameters of KYbW, KGW, and KYW and relevant angles: β, which is defined by crystallographic axes $\boldsymbol{a}$ and $\boldsymbol{c}$; $\measuredangle(N_g,c)$, $\measuredangle(N_m,c)$, and $\measuredangle(N_m,a)$, defined by crystallographic and crystallo-optic axes. Data are included for the C2/c setting, which is the valid convention, and alternative settings I2/a and I2/c, which may be more appropriate for crystal processing [Puj99, Puj02, Kam02].[1] Crystallographic axes $\boldsymbol{a}$, $\boldsymbol{b}$, $\boldsymbol{c}$ in C2/c are transformed to alternative axes $\boldsymbol{a}'$, $\boldsymbol{b}'$, $\boldsymbol{c}'$ by

$a' = c,\ b' = b,\ c' = -(a+c)$ (to I2/a) [Puj99] or
$a' = a+c,\ b' = -b,\ c' = -c$ (to I2/c) [Kam02].

Table a.2. Unit cell parameters of KYbW, KGW and KYW and relevant angles. β, angle between axes a and c; $\measuredangle(N_g,c)$, $\measuredangle(N_m,c)$, and $\measuredangle(N_m,a)$, angles between crystallo-optic and crystallographic axes. Parameters and angles are very similar especially for KYbW and KYW, due to the similar Y^{3+} and Yb^{3+} ion radii.

material	space group	a [Å]	b [Å]	c [Å]	β [°]	$\measuredangle(N_g,c)$ [°]	$\measuredangle(N_m,c)$ [°]	$\measuredangle(N_m,a)$ [°]	reference
KYbW	C2/c	10.590(4)	10.290(6)	7.478(2)	130.70(2)	19	71	59.7	[Puj02]
KYbW	I2/a	7.478	10.290	8.049	94.08	75.08	14.92	71	
KYbW	I2/c	8.049	10.290	7.478	94.08	19	71	23.08	
KGW	C2/c	10.652(4)	10.374(6)	7.582(2)	130.80(2)	21.5±1	68.5±1	62.3±1	[Puj99]
KGW	I2/a	7.582	10.374	8.087	94.41	72.91±1	17.09±1	68.5±1	[Puj99]
KGW	I2/c	8.087	10.374	7.582	94.41	21.5±1	68.5±1	25.93±1	
KYW	C2/c	10.64	10.35	7.54	130.5	18	72	58.5	[Kam02]
KYW	I2/a	7.54	10.35	8.05	94	76	14	72	
KYW	I2/c	8.05	10.35	7.54	94	18	72	22	[Kam02]

---

[1] According to Fig.2 in [Puj99] the $\boldsymbol{c}$ axis of the I2/a setting coincides with the [101] natural edge. According to Fig.2b in [Kam02], however, the same axis (called $-\boldsymbol{a}$ in the I2/c setting) is parallel to the [100] direction; $\boldsymbol{b}$ and $\boldsymbol{c}$ are parallel to [010] and [001], respectively.

A.8. Crystal growth of monoclinic double tungstates

The monoclinic double tungstate crystals used in chapt. 5 (see also Table 5.1.) were grown with good optical quality by the top seeded solution growth (TSSG) slow cooling method [Puj99b, Puj02], the Kyropoulos method or a Czochralski technique.[1] It is also possible to obtain crystals by the top nucleated floating crystal method (no seed) [Met97, Met99, Bre01], the Bridgman-Stockbarger method [Gal00] or by a hydrothermal method (crystals used in [Der02, Kle69]). Furthermore, thin films of double tungstates can be prepared on a substrate by pulsed laser deposition [Ata00] or liquid phase epitaxy, which is especially interesting for the stoichiometric material.

For KGW, KYW, and KYbW, samples with optical quality suitable for lasing cannot be grown directly from the melt, but must be grown from high-temperature solutions, since these materials undergo a reversible polymorphic transition from orthorhombic (β) to monoclinic structure (α modification) close to their melting temperature [Kle69]. To improve the crystal quality by removing defects caused by lack of oxygen, the KYbW crystals used in chapts. 5.2.1.4. and 5.2.2. have additionally experienced a thermal annealing process in an oxygen atmosphere at a temperature slightly lower than 800° C.

Figure a.2.(a) shows a KYbW crystal produced at the University of Tarragona. Its size is typical for KYbW, KGW and KYW obtained by TSSG, with ≈1 cm for the largest dimension, i.e. in the ***c*** direction. Larger tungstate crystals can be produced by Czochralski growth, as demonstrated by the 1-kg single-crystal KYbW boule from Vision Crystal Technology AG, see Fig. a.2.(b). In both cases, the crystals were grown with ***b***-oriented seeds.

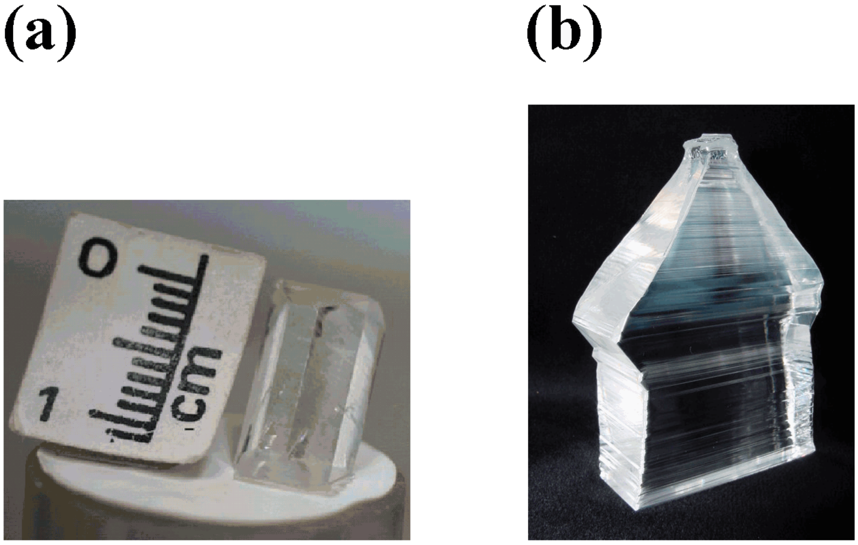

Fig. a.2. KYbW crystals, obtained by top seeded solution growth (a) and Czochralski growth (b).

---

[1] Demidovich et al. give details on modified Czochralski growth of Yb:KYW in [Dem00].

A.9. Effective cross sections of Yb^{3+} in KYW and KYbW crystals used at the Brewster angle

In chapter 5.2., for calculation of the absorbed pump power at the lasing threshold the data collected in Tables a.3. and a.4. were used.

Table a.3. Effective cross sections experienced by pump radiation in the Yb(60%):KYW laser experiments (chapt. 5.2.1.1.) and resulting quantities. $\sigma_a(N_m)$, $\sigma_e(N_m)$, $\sigma_a(N_p)$, $\sigma_e(N_p)$, absorption and emission cross sections for N_m- and N_p-polarized beams; $\sigma_a(Br)$, $\sigma_e(Br)$, effective cross sections in the crystal used at the Brewster angle; $\alpha(Br)$, effective absorption coefficient calculated for an active ion concentration of 0.6 x 6.4 x 10^{21} cm^{-3}; $I_{p,sat} = h\nu((\sigma_a(Br) + \sigma_e(Br))\ \tau_f)^{-1}$, pump saturation intensity for an upper state lifetime of τ_f = 0.2 ms. In case of a Gaussian pump beam, the pump saturation power (for the whole beam) is given by $P_{p,sat} \approx 2.51286\ (\pi/2)\ w_p^2\ I_{p,sat}$. The values are given for a waist size w_p of 30 µm. Please note that the on-axis pump saturation is achieved at a pump power of $(\pi/2)\ w_p^2\ I_{p,sat}$ already, i.e. when the on-axis intensity $I_p(0) = 2\ P_p/(\pi w_p^2)$ equals the saturation intensity.

λ [nm]	$\sigma_a(N_m)$ [10^{-20} cm^2]	$\sigma_e(N_m)$ [10^{-20} cm^2]	$\sigma_a(N_p)$ [10^{-20} cm^2]	$\sigma_e(N_p)$ [10^{-20} cm^2]	$\sigma_a(Br)$ [10^{-20} cm^2]	$\sigma_e(Br)$ [10^{-20} cm^2]	$\alpha(Br)$ [cm^{-1}]	hν [10^{-19} J]	$I_{p,sat}$ [kW cm^{-2}]	$P_{p,sat}$ (w_p=30µm) [W]	$P_{p,sat,on-axis}$ (w_p=30µm) [W]
962.5	0.636	0.275	0.857	0.371	0.679	0.294	26.07	2.0638	106.1	3.77	1.50
975.0	1.672	1.371	0.638	0.523	1.471	1.206	56.48	2.0373	38.1	1.35	0.54
995.0	1.566	3.452	0.421	0.929	1.342	2.960	51.55	1.9964	23.2	0.82	0.33
1002.5	0.930	2.943	0.327	1.036	0.813	2.571	31.20	1.9815	29.3	1.04	0.41

Table a.4. Effective cross sections experienced by pump radiation in the KYbW laser experiments (chapters 5.2.1.3, 5.2.1.4., 5.2.2.2.) and resulting quantities.

λ [nm]	$\sigma_a(N_m)$ [10^{-20} cm^2]	$\sigma_e(N_m)$ [10^{-20} cm^2]	$\sigma_a(N_p)$ [10^{-20} cm^2]	$\sigma_e(N_p)$ [10^{-20} cm^2]	$\sigma_a(Br)$ [10^{-20} cm^2]	$\sigma_e(Br)$ [10^{-20} cm^2]	$\alpha(Br)$ [cm^{-1}]	hν [10^{-19} J]	$I_{p,sat}$ [kW cm^{-2}]	$P_{p,sat}$ (w_p=30µm) [W]	$P_{p,sat,on-axis}$ (w_p=30µm) [W]
917.5	0.525	0.020	0.266	0.010	0.475	0.018	30.37	2.1651	219.9	7.81	3.11
922	0.898	0.043	0.400	0.019	0.801	0.039	51.26	2.1545	128.2	4.56	1.81
962.5	0.636	0.275	0.857	0.371	0.679	0.294	43.46	2.0638	106.1	3.77	1.50
971.0	0.985	0.659	0.705	0.472	0.930	0.622	59.52	2.0458	65.9	2.34	0.93
994.0	1.530	3.214	0.412	0.866	1.312	2.756	83.96	1.9985	24.6	0.87	0.35
999	1.624	4.344	0.436	1.166	1.392	3.725	89.11	1.9885	19.4	0.69	0.27
1009	0.359	1.548	0.147	0.632	0.318	1.370	20.35	1.9688	58.3	2.07	0.82
1024	0.297	2.564	0.106	0.916	0.259	2.243	16.60	1.9399	38.8	1.38	0.55

A.10. Lattice constants of rare earth sesquioxides

The lattice constants *a* and the cation radii *r* of scandia, yttria, lutetia and ytterbia (coordinated with six oxygens) are listed in Table a.5. [Mix99].[1] The value for Sc_2O_3, $a \approx 9.85$ Å, is a little smaller than the others, due to the small effective ion radius of Sc^{3+}, $r = 0.75$ Å. A smaller lattice constant means closer proximity of the O^{2-} ligands to the dopant ions and therefore a stronger crystal field; this is responsible for the larger crystal field splitting [For00, Bou02b] and contributes to the larger absorption and emission cross sections of $Yb{:}Sc_2O_3$, compared to the other Yb^{3+}-doped sesquioxides (see also chapt. 2.2.1.). Furthermore, the relatively large difference between the scandium and ytterbium ion radii ($r = 0.87$ Å for Yb^{3+}) may lead to a modification of the crystal lattice and thus influence the crystal field symmetry [Pet01].

Table a.5. Lattice parameters and cation radii of rare earth sesquioxides [Mix99]. The relatively small lattice constant of scandia corresponds to the high spectroscopic cross sections observed in this host. The radius of Sc^{3+} shows the largest difference to that of Yb^{3+}. This does not permit high dopant concentrations in scandia and contributes to the significant decrease of thermal conductivity with increasing Yb^{3+} concentration. On the positive side, the small Sc^{3+} radius helps to prevent impurities from other rare earths.

	Sc_2O_3	**Y_2O_3**	**Lu_2O_3**	**Yb_2O_3**
lattice constant a [Å]	9.85	10.60	10.39	10.44
cation radius r [Å]	0.75	0.90	0.86	0.87

---

[1] We have averaged the values from [Mix99]. Boulon et al. [Bou02b] give a value of 9.79 Å for the lattice constant of Sc_2O_3.

A.11. Crystal growth of rare earth sesquioxides

A severe problem with growing rare earth sesquioxide laser materials is their high melting point, at approximately 2400°C. It is difficult to control the growing conditions, especially the thermal gradient. The devices used for growth must be highly thermally stable. At such temperatures, impurities from the crucible are very mobile and can diffuse into the melt.

The crystal used in our experiments (chapt. 6) was cut from a polycrystalline boule, which had been grown by the heat-exchanger method (improved Bridgman) in a Rhenium crucible without seed crystal. With the heat-exchanger method, the crucible is insulated and cooled by a variable gas flow from the bottom side, applied at the central position where the crystallization is to be started [Pet01, Pet02]. Rare earth sesquioxide crystals have also been obtained using other growing techniques, including Czochralski [For99, For00, Mix99], Nacken-Kyropoulos [Mix99], top-seeded solution growth [Pet01], laser-heated pedestal growth [Bou03], and Bridgman [Mix99, Pet02b]. While most of these provide only small (millimeter dimensions) or low-quality crystals, large fair-quality crystals have been obtained by the Bridgman and heat-exchanger methods; this means polycrystalline boules of 25 cm^3 with single-crystalline areas of cm^3-dimensions.

For sesquioxides, too, differing cation radii (see Table a.5.) affect crystal growth and limit the maximum doping level. Petermann et al. measured the distribution coefficients for several optically active rare earth ions in Bridgman-grown sesquioxides. For Yb^{3+} they found a distribution coefficient of 0.56 in scandia, 0.88 in yttria, and 1.0 in lutetia [Pet02b]. In case of scandia, Yb^{3+} doping levels of ≈10% can be achieved, only if the melt is cooled down fast, at the cost of tensions and structural defects. A dopant level of up to ≈1% for $Yb:Sc_2O_3$, as with the sample used in our experiments (chapt. 6), provides sufficient crystal quality.[1]

Such limitations are not expected for yttria and lutetia. However, strong concentration quenching is found especially with $Yb:Lu_2O_3$ [Pet01]. In this context, the small ion radius of Sc^{3+} may be advantageous, since rare earth impurities show even smaller distribution coefficients in scandium oxide than Yb^{3+} [Pet02b].

In rare earth sesquioxides strong absorption due to color centers can be observed in crystals as grown. It can be removed by thermal annealing [Pet02b] or avoided by appropriate growth (very small oxygen amount in the atmosphere, low cooling rate) [Pet02].

An alternative approach is to manufacture rare earth sesquioxide laser media as ceramics, which has been demonstrated for Yb^{3+}-doped Y_2O_3 and Sc_2O_3 [Kon03, Shi03, Lu03] and avoids many of the problems described above: Large media can be produced. The sintering temperatures are around 1700 °C and therefore much easier to handle than the melting point temperatures. In case of scandia, large dopant concentrations can be incorporated more easily than in crystals. For yttria, the polymorphic transition from “B-Type” to “C-Type”, which harms the crystal quality, can be avoided [Kon03].

---

[1] With our sample, stress-induced birefringence is observable in transmission measurements using crossed polarizers and the doping level varies between 0.7% and 0.9% within a few millimeters. This does not prevent high laser efficiencies, however.

A.12. Absorption and emission spectra of Yb:Sc_2O_3, Yb:Lu_2O_3, Yb:Y_2O_3, and Yb_2O_3

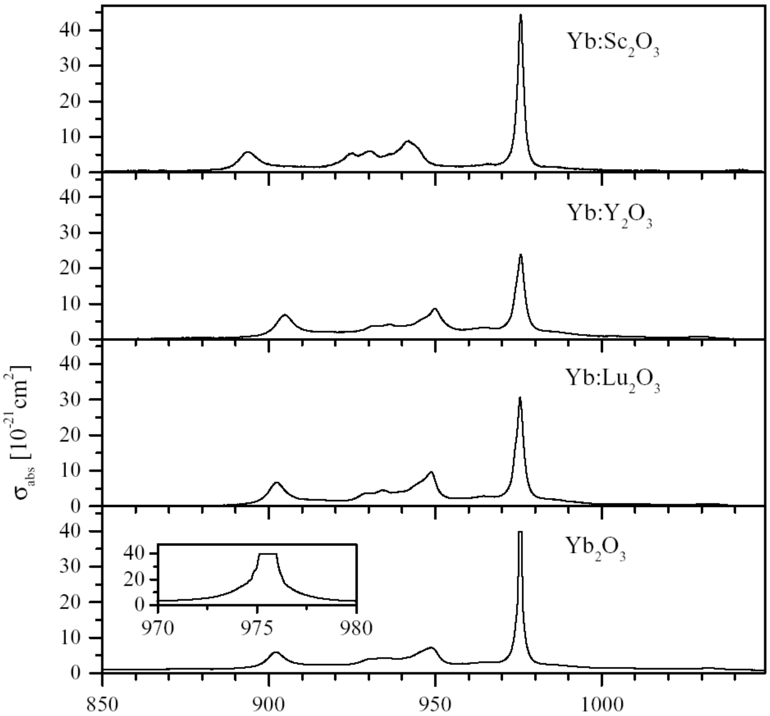

Fig. a.3. Absorption cross sections of Yb^{3+}-activated sesquioxides (taken from [Pet01]). The zero-line transition of Yb^{3+} in Yb_2O_3 was not resolved.

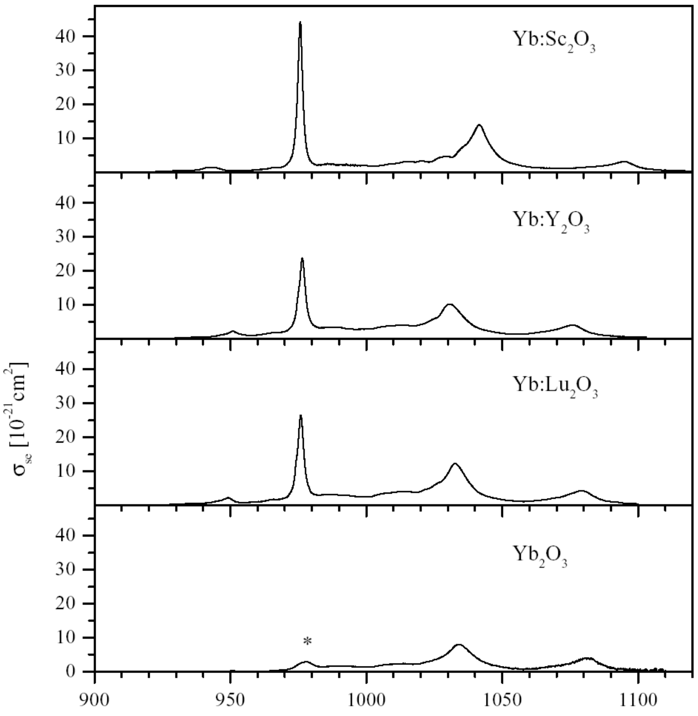

Fig. a.4. Emission cross sections of Yb^{3+}-activated sesquioxides (taken from [Pet01]). The zero-line transition of Yb^{3+} in Yb_2O_3 (*) was not resolved.

A.13. Quasi-two- and quasi-three-level lasers, alternative definitions

The terminology applied in this work is not dictated by a general convention. In contrast to our definitions of “quasi-three-level” and “quasi-four-level” lasers, where two Stark levels in the same multiplet are considered “quasi-separate”, there exist alternative definitions, which virtually melt two levels “quasi into one”:

Historically, the term “quasi-three-level-laser” appeared in the context of Nd:YAG lasers pumped at 808 nm and emitting on the 946-nm-line [Fan87, Ris87]. In this case, actually, four Stark levels are involved in the laser scheme, but the lower laser level lies in the ground-state multiplet, i.e. close to the lower pump level. Therefore, the laser behaves similarly to a three-level laser like ruby, where the lower pump and laser levels are identical. This means, reabsorption has to be overcome for lasing.

Different from ruby, Nd:YAG can be pumped, alternatively, directly into the upper laser level (885-nm line) or into a Stark level located in the same multiplet containing the upper laser level (869-nm line) [Lup02b]. The possible operation schemes for Yb^{3+}-activated laser media are analog to these cases of Nd:YAG laser operation. Most often, however, the authors stick to the term “quasi-three-level laser”, as a synonym for “laser exhibiting reabsorption” (e.g. [Fan92]). This is inconsequent, considering that there is actually one level less or “quasi” one level less involved, compared to the “quasi-three-level” operation scheme with 808-nm-pumping.

In some literature about Yb^{3+} materials and lasers (e.g. [Mun01]), a consequent terminology is used, speaking of a “quasi-two-level system”.[1] This underlines the additional difficulty for pumping caused by reemission, compared e.g. to a 808-nm-pumped Nd:YAG laser medium. Reemission can reduce the effective absorption coefficient by ≈50% in case of high inversion levels. On the positive side, “quasi-two-level system” indicates that very small laser quantum defects can be achieved.

---

[1] It seems that it has not yet been applied for analogly pumped 946-nm Nd:YAG lasers.

A.14. Reflectivity of the SESAM used in chapter 6.2.

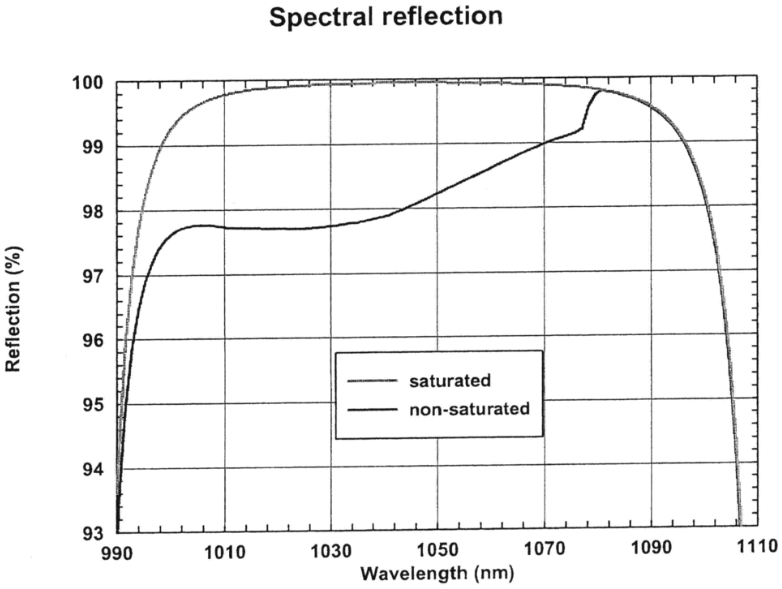

Fig. a.5. Reflectivity of SESAM Model 100352, WROE – Weimar, Germany.

List of references

[Ada89] R. Adair, L. L. Chase, and S. A. Payne, “Nonlinear refractive index of optical crystals,” Phys. Rev. B **39**, 3337-3350 (1989)

[Aro01] A. Aron, G. Aka, B. Viana, A. Kahn-Harari, D. Vivien, F. Druon, F. Balembois, P. Georges, A. Brun, N. Lenain, and M. Jacquet, “Spectroscopic properties and laser performances of Yb:YCOB and potential of the Yb:LaCOB material,” Optical Materials **16**, 181-188 (2001)

[Ata00] P. A. Atanasov, R. I. Tomov, J. Perriére, R. W. Eason, N. Vainos, A. Klini, A. Zherikhin, and E. Millon, “Growth of Nd:potassium gadolinium tungstate thin-film waveguides by pulsed laser deposition,” Appl. Phys. Lett. **76**, 2490-2492 (2000)

[Aus97] J. Aus der Au, D. Kopf, F. Morier-Genoud, M. Moser, and U. Keller, “60-fs pulses from a diode-pumped Nd:glass laser,” Opt. Lett. **22**, 307-309 (1997)

[Auz01] F. Auzel, “On the maximum splitting of the ($^2F_{7/2}$) ground state in Yb^{3+}-doped solid state laser materials,” J. Lumin. **93**, 129-135 (2001)

[Auz02] F. Auzel, “A relationship for crystalfield strength along the lanthanide series; application to the prediction of the ($^2F_{7/2}$) Yb^{3+} maximum splitting,” Optical Materials **19**, 89-94 (2002)

[Ban88] Y. B. Band and D. F. Heller, “Relationships between the absorption and emission of light in multilevel systems,” Phys. Rev. A **38**, 1885-1895 (1988)

[Bar90] N. P. Barnes, M. E. Storm, P. L. Cross, and M. W. Skolaut, “Efficiency of Nd Laser Materials with Laser Diode Pumping,” IEEE J. Quantum Electron. **26**, 558-569 (1990)

[Bas99] T. T. Basiev, A. A. Sobol, P. G. Zverev, L. I. Ivleva, V. V. Osiko, and R. C. Powell, “Raman spectroscopy of crystals for stimulated Raman scattering,” Optical Materials **11**, 307-314 (1999)

[Bat02] L. E. Batay, A. A. Demidovich, A. N. Kuzmin, A. N. Titov, M. Mond, and S. Kück, “Efficient tunable laser operation of diode-pumped Yb,Tm:$KY(WO_4)_2$ around 1.9 µm,” Appl. Phys. B **75**, 457-461 (2002)

[Bay00] A. J. Bayramian, C. Bibeau, R. J. Beach, C. D. Marshall, S. A. Payne, and W. F. Krupke, “Three-level Q-switched laser operation of ytterbium-doped $Sr_5(PO_4)_3F$ at 985 nm,” Opt. Lett. **25**, 622-624 (2000)

[Bea95] R. J. Beach, “CW Theory of quasi-three level end-pumped laser oscillators,” Opt. Commun. **123**, 385-393 (1995)

[Blo03] J. L. Blows, P. Dekker, P. Wang, J. M. Dawes, and T. Omatsu, “Thermal lensing measurements and thermal conductivity of Yb:YAB,” Appl. Phys. B **76**, 289-292 (2003)

[Bor85] Z. Bor and B. Rácz, “Group Velocity Dispersion in Prisms and its Application to Pulse Compression and Travelling-Wave Excitation,” Opt. Commun. **54**, 165-170 (1985)

[Bor93] P. F. Bordui and M. M. Fejer, “Inorganic crystals for nonlinear optical frequency conversion,” Annu. Rev. Mat. Sci. **23**, 321-379 (1993)

[Bou01] G. L. Bourdet, “New evaluation of ytterbium-doped materials for CW laser applications,” Opt. Commun. **198**, 411-417 (2001)

[Bou02b] G. Boulon, A. Brenier, L. Laversenne, Y. Guyot, C. Goutaudier, M.-T. Cohen-Adad, G. Metrat, and N. Muhlstein, “Search for optimized trivalent ytterbium doped inorganic crystals for laser applications,” J. Alloys and Compounds **341**, 2-7 (2002)

[Bou03] G. Boulon, L. Laversenne, C. Goutaudier, Y. Guyot, and M. T. Cohen-Adad, “Radiative and non-radiative energy transfers in Yb^{3+}-doped sesquioxide and garnet laser crystals from a combinatorial approach based on gradient concentration fibers,” J. Lumin. **102-103**, 417-425 (2003)

[Bow00] S. R. Bowman and C. E. Mungan, “New materials for optical cooling,” Appl. Phys. B **71**, 807-811 (2000)

[Bow02] S. R. Bowman, N. W. Jenkins, S. P. O´Connor, and B. J. Feldman, “Sensitivity and Stability of a Radiation-Balanced Laser System,” IEEE J. Quantum Electron. **38**, 1339-1348 (2002)

[Bra91] T. Brabec, C. Spielmann, and F. Krausz, “Mode locking in solitary lasers,” Opt. Lett. **16**, 1961-1963 (1991)

[Bra92] T. Brabec, C. Spielmann, and F. Krausz, “Limits of pulse shortening in solitary lasers,” Opt. Lett. **17**, 748-750 (1992)

[Bre01] A. Brenier, G. Métrat, N. Muhlstein, F. Bourgeois and G. Boulon, “Growth by the top nucleated floating crystal method and spectroscopic properties of Yb^{3+}-doped $KGd(WO_4)_2$,” Optical Materials **16**, 189-192 (2001)

[Bre01b] A. Brenier and G. Boulon, “Overview of the best Yb^{3+}-doped laser crystals,” J. Alloys and Compounds **323-324**, 210-213 (2001)

[Bre01c] A. Brenier, “A new evaluation of Yb^{3+}-doped crystals for laser applications,” J. Lumin. **92**, 199-204 (2001)

[Bro91] I. N. Bronstein and K. A. Semendjajew, “Taschenbuch der Mathematik,” B. G. Teubner Verlagsgesellschaft und Verlag Nauka, Stuttgart, Leipzig, Moskau, 25. Auflage (1991)

[Bru00] F. Brunner, G. J. Spühler, J. Aus der Au, L. Krainer, F. Morier-Genoud, R. Paschotta, N. Lichtenstein, S. Weiss, C. Harder, A. A. Lagatsky, A. Abdolvand, N. V. Kuleshov, and U. Keller, “Diode-pumped femtosecond $Yb:KGd(WO_4)_2$ laser with 1.1-W average power,” Opt. Lett. **25**, 1119-1121 (2000)

[Bru02] F. Brunner, T. Südmeyer, E. Innerhofer, F. Morier-Genoud, R. Paschotta, V. E. Kisel, V. G. Shcherbitsky, N. V. Kuleshov, J. Gao, K. Contag, A. Giesen, and U. Keller, “240-fs pulses with 22-W average power from a mode-locked thin-disk $Yb:KY(WO_4)_2$ laser,” Opt. Lett. **27**, 1162-1164 (2002)

[Che02] S. Chénais, F. Druon, F. Balembois, P. Georges, R. Gaumé, P. H. Haumesser, B. Viana, G. P. Aka, and D. Vivien, “Spectroscopy and efficient laser action from diode pumping of a new broadly tunable crystal: $Yb^{3+}:Sr_3Y(BO_3)_3$,” J. Opt. Soc. Am. B **19**, 1083-1091 (2002)

[Che03] S. Chénais, F. Druon, F. Balembois, P. Georges, A. Brenier, and G. Boulon, “Diode-pumped Yb:GGG laser: comparison with Yb:YAG,” Optical Materials **22**, 99-106 (2003)

[Che03b] S. Chénais, F. Druon, F. Balembois, G. Lucas-Leclin, Y. Fichot, P. Georges, R. Gaumé, B. Viana, G. P. Aka, D. Vivien, “Thermal lensing measurements in diode-pumped Yb-doped GdCOB, YCOB, YSO, YAG and KGW”, Optical Materials **22**, 129-137 (2003)

[Che99] Y. Chen, F. X. Kärtner, U. Morgner, S. H. Cho, H. A. Haus, E. P. Ippen, and J. G. Fujimoto, “Dispersion-managed mode locking,” J. Opt. Soc. Am. B **16**, 1999-2004 (1999)

[Chi82] S. R. Chinn, “2.1.2. Stoichiometric Lasers,” in CRC Handbook of Laser Science and Technology, “Volume 1, Lasers and Masers,” Editor Marvin J. Weber, CRC Press, Boca Raton, Florida, 147-169 (1982)

[Chi96] B.N. Chichkov, C. Momma, S. Nolte, F. von Alvensleben, and A. Tünnermann, “Femtosecond, picosecond and nanosecond laser ablation of solids,” Appl. Phys. A **63**, 109-115 (1996)

[Cut91] J. P. Cuthbertson and G. J. Dixon, “Pump-resonant excitation of the 946-nm Nd:YAG laser,” Opt. Lett. **16**, 396-398 (1991)

[Dan75] H. G. Danielmeyer, “Stoichiometric Laser Materials,” Festkörperprobleme XV, 253-277 (1975)

[Das02] T. Dascalu, T. Taira, and N. Pavel, “100-W quasi-continuous-wave diode radially pumped microchip composite Yb:YAG laser,” Opt. Lett. **27**, 1791-1793 (2002)

[DeL93] L. D. DeLoach, S. A. Payne, L. L. Chase, L. K. Smith, W. L. Kway, and W. F. Krupke, “Evaluation of absorption and emission properties of Yb^{3+} doped crystals for laser applications,” IEEE J. Quantum Electron. **29**, 1179-1191 (1993)

[Dem00] A. A. Demidovich, A. N. Kuzmin, G. I. Ryabtsev, M. B. Danailov, W. Strek, and A. N. Titov, “Influence of Yb concentration on Yb:KYW laser properties,” J. Alloys and Compounds **300-301**, 238-241 (2000)

[Der02] P. J. Deren, R. Mahiou, W. Strek, A. Bednarkiewicz, and G. Bertrand, “Up-conversion in $KYb(WO_4)_2:Pr^{3+}$ crystal,” Optical Materials **19**, 145-148 (2002)

[Des70] J. Desbois, F. Gires, and P. Tournois, “Mode-locked He-Ne laser pulse compression and expansion,” Opt. Commun. **2**, 370-372 (1970)

[Dia98] L. A. Díaz-Torres, O. Barbosa-García, J. M. Hernández, V. Pinto-Robledo, D. Sumida, “Evidence of energy transfer among Nd ions in Nd:YAG driven by a mixture of exchange and multipolar interactions,” Optical Materials **10**, 319-326 (1998)

[Dra03] A. Dragomir, D. N. Nikogosyan, K. A. Zagorulko, P. G. Kryukov, and E. M. Dianov, “Inscription of fiber Bragg gratings by ultraviolet femtosecond radiation,” Opt. Lett. **28**, 2171-2173 (2003)

[Dru02] F. Druon, S. Chénais, P. Raybaut, F. Balembois, P. Georges, R. Gaumé, P. H. Haumesser, B. Viana, D. Vivien, S. Dhellemmes, V. Ortiz, and C. Larat, “Apatite-structure crystal, $Yb^{3+}:SrY_4(SiO_4)_3O$, for the development of diode-pumped femtosecond lasers," Opt. Lett. **27**, 1914-1916 (2002)

[Dru02b] F. Druon, S. Chénais, P. Raybaut, F. Balembois, P. Georges, R. Gaumé, G. Aka, B. Viana, S. Mohr and D. Kopf, "Diode-pumped Yb:$Sr_3Y(BO_3)_3$ femtosecond laser," Opt. Lett. **27**, 197-199 (2002)

[Dru02c] F. Druon, S. Chénais, F. Balembois, P. Georges, A. Brun, A. Courjaud, C. Hönninger, F. Salin, M. Zavelani-Rossi, F. Augé, J. P. Chambaret, A. Aron, F. Mougel, G. Aka, and D. Vivien, "High-power diode-pumped Yb:GdCOB laser: from continuous-wave to femtosecond regime," Optical Materials **19**, 73-80 (2002)

[Ell97] A. Ellens, H. Andres, M. L. H. ter Heerdt, R. T. Wegh, A. Meijerink, and G. Blasse, "Spectral-line-broadening study of the trivalent lanthanide-ion series. II. The variation of the electron-phonon coupling strength through the series," Phys. Rev. B **55**, 180-186 (1997)

[Eps95] R. I. Epstein, M. I. Buchwald, B. C. Edwards, T. R. Gosnell, and C. E.Mungan, "Observation of laser-induced fluorescent cooling of a solid," Nature **377**, 500-503 (1995)

[Erh01] S. Erhard, J. Gao, A. Giesen, K. Contag, A. A. Lagatsky, A. Abdolvand, N. V. Kuleshov, J. Aus der Au, G. J. Spühler, F. Brunner, R. Paschotta, and U. Keller, "High power Yb:KGW and Yb:KYW thin disk laser operation," in OSA Trends in Optics and Photonics (TOPS) Vol. 56, Conference on Lasers and Electro-Optics, OSA Technical Digest, Postconference Edition (Optical Society of America, Washington, D.C., 2001), 333-334 (2001)

[Erh99] S. Erhard, A. Giesen, M. Karszewski, T. Rupp, C. Stewen, I. Johannsen, and K. Contag, "Novel Pump Design of Yb:YAG Thin Disc Laser for Operation at Room Temperature with Improved Efficiency," in OSA TOPS Vol. 26, Advanced Solid-State Lasers, 38-44 (1999)

[Fan87] T. Y. Fan and R. L. Byer, "Modeling and CW Operation of a Quasi-Three-Level 946 nm Nd:YAG Laser," IEEE J. Quantum Electron. **23**, 605-612 (1987)

[Fan92] T. Y. Fan, "Optimizing the Efficiency and Stored Energy in Quasi-Three-Level Lasers," IEEE J. Quantum Electron. **28**, 2692-2697 (1992)

[Fan93] T. Y. Fan, "Heat generation in Nd:YAG and Yb:YAG," IEEE J. Quantum Electron. **29**, 1457-1459 (1993)

[Foe03] I. Földvári, E. Beregi, A. Baraldi, R. Capelletti, W. Ryba-Romanowski, G. Dominiak-Dzik, A. Munoz, and R. Sosa, "Growth and spectroscopic properties of rare-earth doped $YAl_3(BO_3)_4$ single crystals," J. Lumin. **102-103**, 395-401 (2003)

[For00] L. Fornasiero, E. Mix, V. Peters, K. Petermann, and G. Huber, "Czochralski growth and laser parameters of RE^{3+}-doped Y_2O_3 and Sc_2O_3," Ceramics International **26**, 589-592 (2000)

[For84] R. L. Fork, O. E. Martinez, and J. P. Gordon, "Negative dispersion using pairs of prisms," Opt. Lett. **9**, 150-152 (1984)

[For99] L. Fornasiero, E. Mix, V. Peters, K. Petermann, and G. Huber, "New Oxide Crystals for Solid State Lasers," Cryst. Res. Technol. **34**, 255-260 (1999)

[For99b] L. Fornasiero, T. Kellner, S. Kück, J. P. Meyn, P. E. A. Möbert, and G. Huber, "Excited state absorption and stimulated emission of Nd^{3+} in crystals. Part III: $LaSc_3(BO_3)_4$, $CaWO_4$, and $YLiF_4$," Appl. Phys. B **68**, 67-72 (1999)

[Gal00] E. Gallucci, C. Goutaudier, G. Boulon, M. T. Cohen-Adad, and B. F. Mentzen, "Nonstoichiometric $KY(WO_4)_2$: crystal growth, chemical and physical characterization," J. Cryst. Growth **209**, 895-905 (2000)

[Gau02] R. Gaumé, P. H. Haumesser, E. Antic-Fidancev, P. Porcher, B. Viana, and D. Vivien, "Crystal field calculations of Yb^{3+}-doped double borate crystals for laser applications," J. Alloys and Compounds **341**, 160-164 (2002)

[Gau03] R. Gaumé, B. Viana, D. Vivien, J. P. Roger, D. Fournier, J. P. Souron, G. Wallez, S. Chénais, F. Balembois, and P. Georges, "Mechanical, thermal and laser properties of Yb:$(Sr_{1-x}Ca_x)_3Y(BO_3)_3$ (Yb:CaBOYS) for 1 µm laser applications," Optical Materials **24**, 385-392 (2003)

[Ger01] P. Gerner, O. S. Wenger, R.Valente, and H. U. Güdel, "Green and Red Light Emission by Upconversion from the near-IR in Yb^{3+} Doped CsMnBr3," Inorg. Chem. **40**, 4534-4542 (2001)

[Gol02] P. Goldner, B. Schaudel, and M. Prassas, "Dependence of cooperative luminescence intensity on Yb^{3+} spatial distribution in crystals and glasses," Phys. Rev. B **65**, 054103 - 1-10 (2002)

[Gol97] P. Goldner, F. Pellé, D. Meichenin, and F. Auzel, "Cooperative Luminescence in ytterbium-doped $CsCdBr_3$," J. Lumin. **71**, 137-150 (1997)

[Gra02] A. S. Grabtchikov, A. N. Kuzmin, V. A. Lisinetskii, V. A. Orlovich, A. A. Demidovich, M. B. Danailov, H. J. Eichler, A. Bednarkiewicz, W. Strek, and A. N. Titov, "Laser operation and Raman self-frequency conversion in Yb:KYW microchip laser," Appl. Phys. B **75**, 795-797 (2002)

[Hau01b] P. H. Haumesser, R. Gaumé, J. M. Benitez, B. Viana, B. Ferrand, G. Aka, and D. Vivien, "Czochralski growth of six Yb-doped double borate and silicate laser materials," J. Cryst. Growth **233**, 233-242 (2001)

[Hau02] P. H. Haumesser, R. Gaumé, B. Viana, and D. Vivien, "Determination of laser parameters of ytterbium-doped oxide crystalline materials," J. Opt. Soc. Am. B **19**, 2365-2375 (2002)

[Hau75] H. A. Haus, "Theory of mode locking with a fast saturable absorber," J. Appl. Phys. **46**, 3049-3058 (1975)

[Hau76] H. A. Haus, "Parameter Ranges for CW Passive Mode Locking," IEEE J. Quantum Electron. **12**, 169-176 (1976)

[Hau91] H. A. Haus, J. G. Fujimoto, and E. P. Ippen, "Structures for additive pulse mode locking," J. Opt. Soc. Am. B **8**, 2068-2076 (1991)

[Heh97] M. P. Hehlen, "Reabsorption artifacts in measured excited-state lifetimes of solids," J. Opt. Soc. Am. B **14**, 1312-1318 (1997)

[Hoe98] C. Hönninger, F. Morier-Genoud, M. Moser, U. Keller, L. R. Brovelli and C. Harder, "Efficient and tunable diode-pumped femtosecond Yb:glass lasers," Opt. Lett. **23**, 126-128 (1998)

[Hoe99] C. Hönninger, R. Paschotta, F. Morier-Genoud, M. Moser, and U. Keller, "Q-switching stability limits of continuous-wave passive mode locking," J. Opt. Soc. Am. B **16**, 46-56 (1999)

[Hoe99b] C. Hönninger, R. Paschotta, M. Graf, F. Morier-Genoud, G. Zhang, M. Moser, S. Biswal, J. Nees, A. Braun, G. A. Mourou, I. Johannsen, A. Giesen, W. Seeber, and U. Keller, "Ultrafast ytterbium-doped bulk lasers and laser amplifiers," Appl. Phys. B **69**, 3-17 (1999)

[Hoy00] C. W. Hoyt, M. Sheik-Bahae, R. I. Epstein, B. C. Edwards, and J. E. Anderson, "Observation of Anti-Stokes Fluorescence Cooling in Thulium-Doped Glass," Phys. Rev. Lett. **85**, 3600-3603 (2000)

[Imp04] Impex High-Tech GbR, D-48432 Rheine, http://www.impex-hightech.de, "Lithium Niobate ($LiNbO_3$)," datasheet (2004)

[Inn03] E. Innerhofer, T. Südmeyer, F. Brunner, R. Häring, A. Aschwanden, R. Paschotta, C. Hönninger, M. Kumkar, and U. Keller, "60-W average power in 810-fs pulses from a thin-disk Yb:YAG laser," Opt. Lett. **28**, 367-369 (2003)

[Ito04] M. Ito, C. Goutaudier, Y. Guyot, K. Lebbou, T. Fukuda, and G. Boulon, "Crystal growth, Yb^{3+} spectroscopy, concentration quenching analysis and potentiality of laser emission in $Ca_{1-X}Yb_XF_{2+X}$," J. Phys.: Condens. Matter **16**, 1501-1521 (2004)

[Jaq03] M. Jacquemet, F. Balembois, S. Chenais, F. Druon, P. Georges, R. Gaume, B. Viana, and D. Vivien, "CW Yb:YSO diode pumped laser emitting at 1003.4 nm for the realization of a stable frequency standard," in Advanced Solid-State Photonics, OSA Technical Digest, (Optical Society of America, Washington DC, 2003), 170-172 (2003)

[Jia00] C. Jiang, H. Liu, Q. Zeng, X. Tang, and F. Gan, "Yb:phosphate laser glass with high emission cross-section," Journal of Physics and Chemistry of Solids **61**, 1217-1223 (2001)

[Jud62] B. R. Judd, "Optical Absorption Intensities of Rare-Earth Ions," Phys. Rev. **127**, 750-761 (1962)

[Jun97] I. D. Jung, F. X. Kärtner,N. Matuschek, D. H. Sutter, F. Morier-Genoud, Z. Shi, V. Scheuer, M. Tilsch, T. Tschudi, and U. Keller, "Semiconductor saturable absorber mirrors supporting sub-10-fs pulses," Appl. Phys. B **65**, 137-150 (1997)

[Kae98] F. X. Kärtner, J. Aus der Au, and U. Keller, "Mode-Locking with Slow and Fast Saturable Absorbers - What´s the Difference?," IEEE J. of Selected Topics in Quantum Electron. **4**, 159-168 (1998)

[Kam01] A. A. Kaminskii, A. F. Konstantinova, V. P. Orekhova, A. V. Butashin, R. F. Kletsova, and A. A. Pavlyuk, "Optical and Nonlinear Laser Properties of the $\chi^{(3)}$-Active Monoclinic α-$KY(WO_4)_2$ Crystals," Crystallography Reports **46**, 665-672 (2001)

[Kam02] A. A. Kaminskii, J. B. Gruber, S. N. Bagaev, K. Ueda, U. Hömmerich, J. T. Seo, D. Temple, B. Zandi, A. A. Kornieko, E. B. Dunina, A. A. Pavlyuk, R. F. Klevtsova, and F. A. Kuznetsov, "Optical spectroscopy and visible stimulated emission of Dy^{3+} ions in monoclinic α-$KY(WO_4)_2$ and α-$KGd(WO_4)_2$ crystals," Phys. Rev. B **65**, 125108 1-29 (2002)

[Kam79] A. A. Kaminskii, A. A. Pavlyuk, T. I. Butaeva, L. I. Bobovich, and V. V. Lyubchenko, “Stimulated emission in the 2.8 μm band by a self-activated crystal of $KEr(WO_4)_2$,” Inorg. Mater. (USSR) **15**, 424 (1979)

[Kam82] A. A. Kaminskii, “Laser Crystals,” Springer-Verlag (1982)

[Kaw02] J. Kawanaka, K. Yamakawa, H. Nishioka, and K. Ueda, “Improved high-field laser characteristics of a diode-pumped Yb:LiYF4 crystal at low temperature,” Opt. Express **10**, 455-460 (2002), http://www.opticsexpress.org

[Kaw03] J. Kawanaka, K. Yamakawa, H. Nishioka, and K. Ueda, “30-mJ, diode-pumped, chirped-pulse Yb:YLF regenerative amplifier,” Opt. Lett. **28**, 2121-2123 (2003)

[Kel91] U. Keller, T. K. Woodward, D. L. Sivco, and A. Y. Cho, “Coupled-cavity resonant passive mode-locked Nd:yttrium lithium fluoride laser,” Opt. Lett. **16**, 390-392 (1991)

[Kel92] U. Keller, D. A. B. Miller, G. D. Boyd, T. H. Chiu, J. F. Ferguson, and M. T. Asom, “Solid-state low-loss intracavity saturable absorber for Nd:YLF lasers: an antiresonant semiconductor Fabry-Perot saturable absorber,” Opt. Lett. **17**, 505-507 (1992)

[Kir02] T. Kirilov, private communication (2002)

[Kit91] C. Kittel, “Einführung in die Festkörperphysik,” R. Oldenbourg Verlag (1991)

[Kle60] P. G. Klemens, “Thermal resistance due to point defects at high temperatures,” Phys. Rev. **119**, 507-509 (1960)

[Kle69] P. V. Klevtsov and L. P. Kozeeva, “Synthesis and x-ray and thermal studies of potassium rare-earth tungstates, $KLn(WO_4)_2$, Ln = Rare-earth element,” Soviet Physics Doklady **14**, 185-187 (1969)

[Klo02] P. Klopp, U. Griebner, V. Petrov, X. Mateos, M. A. Bursukova, M. C. Pujol, R. Solé, Jna. Gavaldà, M. Aguiló, F.Güell, J. Massons, T. Kirilov, and F. Diaz, “Laser operation of the new stoichiometric crystal $KYb(WO_4)_2$,” Appl. Phys. B **74**, 185-189 (2002)

[Klo02b] P. Klopp , V. Petrov, U. Griebner, and G. Erbert, “Passively mode-locked Yb:KYW laser pumped by a tapered diode laser,” Opt. Express **10**, 108-113 (2002), http://www.opticsexpress.org

[Klo03] P. Klopp, V. Petrov, and U. Griebner, “Potassium Ytterbium Tungstate Provides the Smallest Laser Quantum Defect,” Jpn. J. Appl. Phys. **42**, L 246-L 248 (2003)

[Klo03b] P. Klopp, U. Griebner, V. Petrov, K. Petermann, and V. Peters, “Highly-efficient mode-locking of the $Yb:Sc_2O_3$ laser,” in Advanced Solid State Photonics (ASSP 2003, San Antonio, USA), OSA Technical Digest, TuA7 (2003)

[Klo03c] P. Klopp , V. Petrov, U. Griebner, V. Nesterenko, V. Nikolov, M. Marinov, M. A. Bursukova, and M. Galan, “Continuous-wave lasing of a stoichiometric Yb laser material: $KYb(WO_4)_2$,” Opt. Lett. **28**, 322-324 (2003)

[Klo03d] P. Klopp , V. Petrov, U. Griebner, V. Nikolov, V. Nesterenko, and T. Kirilov, “Continuous wave lasing of Yb^{3+} in a stoichiometric double tungstate,” Photonics West 2003, San José, California, in Proceedings of the SPIE vol.4968, 46-53 (2003)

[Klo04] P. Klopp, V. Petrov, K. PetermannV. Peters, “Highly efficient mode-locked Yb:Sc_2O_3 laser,” Opt. Lett. **29**, 391-393 (2004)

[Koe92] W. Koechner, “Solid-state laser engineering,” Springer-Verlag, 3rd edition (1992)

[Kon03] J. Kong, J. Lu, K. Takaichi, K. Ueda, D. Y. Tang, D. Y. Shen, H. Yagi, T. Yanagitani, and A. A. Kaminskii, “Diode-pumped Yb:Y_2O_3 ceramic laser,” Appl. Phys. Lett. **82**, 2556-2558 (2003)

[Kra91] F. Krausz, T. Brabec, and C. Spielmann, “Self-starting passive mode locking,” Opt. Lett. **16**, 235-237 (1991)

[Kra92] F. Krausz, M. E. Fermann, T. Brabec, P. F. Curley, M. Hofer, M. H. Ober, C. Spielmann, E. Wintner, and A. J. Schmidt, “Femtosecond Solid-State Lasers,” IEEE J. Quantum Electron. **28**, 2097-2122 (1992)

[Kru86] W. F. Krupke, M. D. Shinn, J. E. Marion, J. A. Caird, and S. E. Stokowski, “Spectroscopic, optical, and thermomechanical properties of neodymium- and chromium-doped gadolinium scandium gallium garnet,” J. Opt. Soc. Am. B **3**, 102-113 (1986)

[Kul97] N. V. Kuleshov, A. A. Lagatsky, V. G. Shcherbitsky, V. P. Mikhailov, E. Heumann, T. Jensen, A. Diening, and G. Huber, “CW laser performance of Yb and Er,Yb doped tungstates,” Appl. Phys. B **64**, 409 (1997)

[Kul97b] N. V. Kuleshov, A. A. Lagatsky, A. V. Podlipensky, V. P. Mikhailov, and G. Huber, “Pulsed laser operation of Yb-doped $KY(WO_4)_2$ and $KGd(WO_4)_2$,” Opt. Lett. **22**, 1317-1319 (1997)

[Lac91] P. Lacovara, H. K. Choi, C. A. Wang, R. L. Aggarwal, and T. Y. Fan, “Room-temperature diode-pumped Yb:YAG laser,” Opt. Lett. **16**, 1089-1091 (1991)

[Lag00] A. A. Lagatsky, A. Abdolvand, and N. V. Kuleshov, “Passive Q switching and self-frequency Raman conversion in a diode-pumped Yb:$KGd(WO_4)_2$ laser,” Opt. Lett. **25**, 616-618 (2000)

[Lag99] A. A. Lagatsky, N. V. Kuleshov, and V. P. Mikhailov, “Diode-pumped cw lasing of Yb:KYW and Yb:KGW,” Opt. Commun. **165**, 71-75 (1999)

[Lav01] L. Laversenne, Y. Guyot, C. Goutaudier, M. T. Cohen-Adad, and G. Boulon, “Optimization of spectroscopic properties of Yb^{3+}-doped refractory sesquioxides: cubic Y_2O_3, Lu_2O_3 and monoclinic Gd_2O_3,” Optical Materials **16**, 475-483 (2001); Erratum in Optical Materials 17, 443 (2001)

[Lav02] L. Laversenne, C. Goutaudier, Y. Guyot, M.T. Cohen-Adad, and G. Boulon, “Growth of rare earth (RE) doped concentration gradient crystal fibers and analysis of dynamical processes of laser resonant transitions in RE-doped Y_2O_3 (RE=Yb^{3+}, Er^{3+}, Ho^{3+}),” J. Alloys and Compounds **341**, 214-219 (2002)

[Led99] M. J. Lederer, B. Luther-Davies, H. H. Tan, C. Jagadish, N. N. Akhmediev, and J. M. Soto-Crespo, “Multipulse operation of a Ti:sapphire laser mode locked by an ion-implanted semiconductor saturable-absorber mirror,” J. Opt. Soc. Am. B **16**, 895-904 (1999)

[Lei98] G. Lei, J. E. Anderson, M. I. Buchwald, B. C. Edwards, R. I. Epstein, M. T. Murtagh, and G. H. Sigel, “Spectroscopic Evaluation of Yb^{3+}-Doped Glasses for Optical

Refrigeration," IEEE J. Quantum Electron. **34**, 1839-1845 (1998)

[Lei98b] G. Lei, J. E. Anderson, M. I. Buchwald, B. C. Edwards, and R. I. Epstein, "Determination of spectral linewidths by Voigt profiles in Yb^{3+}-doped fluorozirconate glasses," Phys. Rev. B **57**, 7673-7678 (1998)

[Li03] J. Li, J. Wang, X. Cheng, X. Hu, P. A. Burns, and J. M. Dawes, "Thermal and laser properties of $Yb:YAl_3(BO_3)_4$ crystal," J. Cryst. Growth **250**, 458-462 (2003)

[Lim02] C. Lim and Y. Izawa, "Modeling of End-Pumped CW Quasi-Three-Level Lasers," IEEE J. Quantum Electron. **38**, 306-311 (2002)

[Lin98] I. D. Lindsay and M. Ebrahimzadeh, "Efficient continuous-wave and Q-switched operation of a 946-nm Nd:YAG laser pumped by an injection-locked broad-area diode laser," Appl. Opt. **37**, 3961-3970 (1998)

[Liu01] H. Liu, J. Nees, and G. Mourou, "Diode-pumped Kerr-lens mode-locked Yb:KYW laser," in OSA TOPS Vol.56, Conference on Lasers and Electro-Optics (CLEO 2001), OSA Technical Digest, 30-31 (2001)

[Lu03] J. Lu, J. F. Bisson, K. Takaichi, T. Uematsu, A. Shirakawa, M. Musha, K. Ueda, H. Yagi, T. Yanagitani, and A. A. Kaminskii, "$Yb^{3+}:Sc_2O_3$ ceramic laser," Appl. Phys. Lett. **83**, 1101-1103 (2003)

[Luo01] J. Luo, S. J. Fan, H. Q. Xie, K. C. Xiao, S. X. Qian, Z. W. Zhong, G. X. Qian, R. Y. Sun, and J. Y. Xu, "Thermal and Nonlinear Optical Properties of $Ca_4YO(BO_3)_3$," Cryst. Res. Techn. **36**, 1215-1221 (2001)

[Luo02] Z. Luo and Y. Huang, "An empirical relationship between laser threshold and chemical composition of laser crystals," Opt. Commun. **206**, 159-164 (2002)

[Lup01] V. Lupei, "Self-quenching of Nd^{3+} emission in laser garnet crystals," Optical Materials **16**, 137-152 (2001)

[Lup02] V. Lupei, N. Pavel, and T. Taira, "Efficient Laser Emission in Concentrated Nd Laser Materials Under Pumping Into the Emitting Level," IEEE J. Quantum Electron. **38**, 240-245 (2002)

[Lup02b] V. Lupei, G. Aka, and D. Vivien, "Quasi-three-level 946 nm CW laser emission of Nd:YAG under direct pumping at 885 nm into the emitting level," Opt. Commun. **204**, 399-405 (2002)

[Lup03] A. Lupei, V. Lupei, T. Taira, Y. Sato, A. Ikesue, and C. Gheorghe, "Energy transfer processes of Nd^{3+} in Y_2O_3 ceramic," J. Lumin. **102-103**, 72-76 (2003)

[Lup90] V. Lupei, A. Lupei, S. Georgescu, and I. Ursu, "Effects of nearest-neighbor pairs on the energy transfer in Nd:YAG," Appl. Phys. Lett. **59**, 905-907 (1990)

[Mac00] L. Macalik, J. Hanuza, and A. A. Kaminskii, "Polarized Raman spectra of the oriented $NaY(WO_4)_2$ and $KY(WO_4)_2$ single crystals," Journal of Molecular Structure **555**, 289-297 (2000)

[Maj02] A. Major, L. Giniunas, N. Langford, A. I. Ferguson, D. Burns, E. Bente, and R. Danielius, "Saturable Bragg reflector-based continuous-wave mode locking of $Yb:KGd(WO_4)_2$ laser," J. Mod. Opt. **49**, 787-793 (2002)

[Maj03] A. Major, I. Nikolakakos, J. S. Aitchison, A. I. Ferguson, N. Langford, and P. W. Smith, “Characterization of the nonlinear refractive index of the laser crystal Yb:KGd$(WO_4)_2$,” Appl. Phys. B **77**, 433-436 (2003)

[McC64] D. E. McCumber, “Einstein Relations Connecting Broadband Emission and Absorption Spectra,” Phys. Rev. **136**, A954-A957 (1964)

[McC64b] D. E. McCumber, “Theory of Phonon-Terminated Optical Masers,” Phys. Rev. **134**, A299-A306 (1964)

[Met97] G. Métrat, N. Muhlstein, A. Brenier, and G. Boulon, “Growth by the induced nucleated floating crystal (INFC) method and spectroscopic properties of $KY_{1-x}Nd_x$ $(WO_4)_2$ laser materials,” Optical Materials **8**, 75-82 (1997)

[Met99] G. Métrat, M. Boudeulle, N. Muhlstein, A. Brenier, and G. Boulon, “Nucleation, morphology and spectroscopic properties of Yb^{3+}-doped $KY(WO_4)_2$ crystals grown by the top nucleated floating crystal method,” J. Cryst. Growth **197**, 883-888 (1999)

[Mia70] T. Miyakawa and D. L. Dexter, “Phonon Sidebands, Multiphonon Relaxation of Excited States, and Phonon-Assisted Energy Transfer between Ions in Solids,” Phys. Rev. B **1**, 2961-2969 (1970)

[Min91] W. J. Miniscalco and R. S. Quimby, “General procedure for the analysis of Er^{3+} cross sections,” Opt. Lett. **16**, 258-260 (1991)

[Min01] K. Minoshima, A. M. Kowalevicz, I. Hartl, E. P. Ippen, and J. G. Fujimoto, “Photonic device fabrication in glass by use of nonlinear materials processing with a femtosecond laser oscillator,” Opt. Lett. **26**, 1516-1518 (2001)

[Mix99] E. Mix, “Kristallzüchtung, Spektroskopie und Lasereigenschaften Yb-dotierter Sesquioxide,” Shaker Verlag, Aachen, Germany (1999)

[Mol84] L. F. Mollenauer and R. H. Stolen, “The soliton laser,” Opt. Lett. **9**, 13-15 (1984)

[Mon01] E. Montoya, F. Agulló-Rueda, S. Manotas, J. García Solé, and L. E. Bausá, “Electron-phonon coupling in $Yb^{3+}:LiNbO_3$ laser crystal,” J. Lumin. **94-95**, 701-705 (2001)

[Moo68] R. M. Moon, W. C. Koehler, H. R. Child, and L. J. Raubenheimer, “Magnetic Structures of Er_2O_3 and Yb_2O_3,” Phys. Rev. **176**, 722-731 (1968)

[Mou86] P. F. Moulton, “Spectroscopic and laser characteristics of $Ti:Al_2O_3$,” J. Opt. Soc. Am. B **3**, 125-132 (1986)

[Mue02] V. Müller, V. Peters, E. Heumann, M. Henke, K. Petermann, and G. Huber, “Growth, characterization, and laser operation of Yb3Al5O12 with nearly intrinsic Yb^{3+}-fluorescence lifetime,” in OSA TOPS Vol.68, Advanced Solid State Lasers (ASSL, Quebec City, Canada), Technical Digest, MD4 (2002)

[Mun01] C.E. Mungan, S.R. Bowman, and T.R. Gosnell, “Solid-state laser cooling of ytterbium-doped tungstate crystals,” in Proceedings of the International Conference on Lasers 2000, edited by V. J. Corcoran and T. A. Corcoran (STS Press, McLean VA, 2001), 819-826 (2001)

[Mus97] O. Musset and J. P. Boquillon, “Flashlamp-pumped Nd:KGW laser at repetition rates up to 50 Hz,” Appl. Phys. B **65**, 13-18 (1997)

[Nak70] E. Nakazawa and S. Shionoya, “Cooperative Luminescence in $YbPO_4$,” Phys. Rev. Lett. **25**, 1710-1712 (1970)

[Nak88] M. Nakazawa, T. Nakashima, H. Kubota, and S. Seikai, “Efficient optical pulse compression using a pair of Brewster-angled TeO_2 crystal prisms,” J. Opt. Soc. Am. B **5**, 215-221 (1988)

[Nel97] L. E. Nelson, D. J. Jones, K. Tamura, H. A. Haus, and E. P. Ippen, “Ultrashort-pulse fiber ring lasers,” Appl. Phys. B **65**, 277-294 (1997)

[Obe92] M. H. Ober, E. Sorokin, I. Sorokina, F. Krausz, E. Wintner, and I. A. Shcherbakov, “Subpicosecond mode locking of a Nd^{3+}-doped garnet laser,” Opt. Lett. **17**, 1364-1366 (1992)

[Ofe62] G. S. Ofelt, “Intensities of Crystal Spectra of Rare-Earth Ions,” J. Chem. Phys. **37**, 511 (1962)

[Ost98] V. Ostroumov, T. Jensen, J.-P. Meyn, G. Huber, and M. A. Noginov, “Study of luminescence concentration quenching and energy transfer upconversion in Nd-doped $LaSc_3(BO_3)_4$ and $GdVO_4$ laser crystals,” J. Opt. Soc. Am. B **15**, 1052-1060 (1998)

[Ots98] K. Otsuka, R. Kawai, Y. Asakawa, P. Mandel, and E. A. Viktorov, “Simultaneous single-frequency oscillations on different transitions in a laser-diode-pumped $LiNdP_4O_{12}$ laser,” Opt. Lett. **23**, 201-203 (1998)

[Pad97] N. P. Padture and P. G. Klemens, “Low thermal conductivity in garnets,” J. Am. Ceram. Soc. **80**, 1018-1020 (1997)

[Pas01] R. Paschotta and U. Keller, “Passive modelocking with slow saturable absorbers,” Appl. Phys. B **73**, 653-662 (2001)

[Pas95] H. M. Pask, R. J. Carman, D. C. Hanna, A. C. Tropper, C. J. Mackechnie, P. R. Barber, and J. M. Dawes, “Ytterbium-doped silica fiber lasers: versatile sources for the 1-1.2 μm region,” IEEE J. Selected Topics in Quantum Electr. **1**, 2-13 (1995)

[Pat01] F. D. Patel, E. C. Honea, J. Speth, S. A. Payne, R. Hutcheson, and R. Equall, “Laser demonstration of $Yb_3Al_5O_{12}$ (YbAG) and Materials Properties of Highly Doped Yb:YAG,” IEEE J. Quantum Electron. **37**, 135-144 (2001)

[Pav01] N. Pavel, J. Saikawa, and T. Taira, “Radial-Pumped Microchip High-Power Composite Yb:YAG Laser: Design and Power Characteristics,” Jpn. J. Appl. Phys. **40**, 146-152 (2001)

[Pet00] K. Petermann, G. Huber, L. Fornasiero, S. Kuch, E. Mix, V. Peters, and S. A. Basun, “Rare-earth-doped sesquioxides,” J. Lumin. **87-89**, 973-975 (2000)

[Pet01] V. Peters, “Growth and Spectroscopy of Ytterbium-Doped Sesquioxides,” Dissertation, Universität Hamburg, 2001

[Pet02] V. Peters, A. Bolz, K. Petermann, and G. Huber, “Growth of high-melting sesquioxides by the heat exchanger method,” J. Cryst. Growth **237-239**, 879-883 (2002)

[Pet02b] K. Petermann, L. Fornasiero, E. Mix, and V. Peters, “High melting sesquioxides: crystal growth, spectroscopy, and laser experiments,” Optical Materials **19**, 67-71

(2002)

[Pol02] M. Pollnau, “Decorrelation of luminescent decay in energy-transfer upconversion,” J. Alloys and Compounds **341**, 5155 (2002)

[Pol98] M. Pollnau, P. J. Hardman, M. A. Kern, W. A. Clarkson, and D. C. Hanna, “Upconversion-induced heat generation and thermal lensing in Nd:YLF and Nd:YAG,” Phys. Rev. B **58**, 16076-16092 (1998)

[Por98] P. Porcher, M. C. Dos Santos, and O. Malta, “Relationship between phenomenological crystal field parameters and the crystal structure: The simple overlap model,” Phys. Chem. Chem. Phys. **1**, 397-405 (1999)

[Pro95] P. P. Pronko, S. K. Dutta, J. Squier, J. V. Rudd, D. Du and G. Mourou, “Machining of sub-micron holes using a femtosecond laser at 800 nm,” Opt. Commun. **114**, 106-110 (1995)

[Puj02] M. C. Pujol, X. Mateos, R. Solé, J. Massons, J. Gavaldà, X. Solans, F. Díaz, and M. Aguiló, “Structure, crystal growth and physical anisotropy of $KYb(WO_4)_2$, a new laser matrix,” J. Appl. Crystallogr. **35**, 108 (2002)

[Puj02b] M. C. Pujol, M. A. Bursukova, F. Güell, X. Mateos, R. Solé, Jna. Gavaldà, M. Aguiló, J.Massons, F. Díaz, P. Klopp, U. Griebner, and V. Petrov, “Growth, optical characterization, and laser operation of a stoichiometric crystal $KYb(WO_4)_2$,” Phys. Rev. B **65**, 165121 (2002)

[Puj99] M .C. Pujol, M. Rico, C. Zaldo, R. Solé, V. Nikolov, X. Solans, M. Aguiló, and F. Díaz, “Crystalline structure and optical spectroscopy of Er^{3+}-doped $KGd(WO_4)_2$ single crystals,” Appl. Phys. B **68**, 187-197 (1999)

[Puj99b] C. Pujol, M. Aguiló, F. Díaz, and C. Zaldo, “Growth and characterisation of monoclinic $KGd_{1-x}RE_x(WO_4)_2$ single crystals,” Optical Materials **13**, 33-40 (1999)

[Ram94] M. Ramaswamy-Paye and J. G. Fujimoto, “Compact dispersion-compensating geometry for Kerr-lens mode-locked femtosecond lasers,” Opt. Lett. **19**, 1765-1767 (1994)

[Ris87] W. P. Risk and W. Lenth, “Room-temperature, continuous-wave, 946-nm Nd:YAG laser pumped by laser diode arrays and intracavity frequency doubling to 473 nm,” Opt. Lett. **12**, 993-995 (1987)

[Ris88] W. P. Risk, “Modeling of longitudinally pumped solid-state lasers exhibiting reabsorption losses,” J. Opt. Soc. Am. B **5**, 1412-1423 (1995)

[Rud89] W. Rudolph and B. Wilhelmi, “Light Pulse Compression,” Hardwood Academic, London (1989)

[Sal91] B. E. A. Saleh and M. C. Teich, “Fundamentals of Photonics,” John Wiley Sons, Inc. (1991)

[Sch00] T. R. Schibli, E. R. Thoen, F. X. Kärtner, and E. P. Ippen, “Suppression of Q-switched mode locking and break-up into multiple pulses by inverse saturable inversion,” Appl. Phys. B **70**, 41-49 (2000)

[Sch03] K. I. Schaffers, J. B. Tassano, A. B. Bayramian, and R. C. Morris, “Growth of Yb:S-FAP [Yb^{3+}:$Sr_5(PO_4)_3F$] crystals for the Mercury laser,” J. Cryst. Growth **253**, 297-306

(2003)

[Sel03] R. Selvas, J. K. Sahu, I. B. Fu, J. N. Jang, J. Nilsson, A. B. Grudinin, K. H. Ylä-Jarkko, S. A. Alam, P. W. Turner, and J. Moore, "High-power, low-noise, Yb-doped, cladding-pumped, three-level fiber sources at 980 nm," Opt. Lett. **28**, 1093-1095 (2003)

[She89] M. Sheik-bahae, A. A. Said, and E. W. Van Stryland, "High-sensitivity, single-beam n_2 measurements," Opt. Lett. **14**, 955-957 (1989)

[Shi03] A. Shirakawa, K. Takaichi, H. Yagi, J-F. Bisson, J. Lu, M. Musha, K. Ueda, T. Yanagitani, T. S. Petrov, and A. A. Kaminskii, "Diode-pumped mode-locked $Yb^{3+}:Y_2O_3$ ceramic laser," Opt. Express **11**, 2911-2916 (2003), http://www.opticsexpress.org

[Sme98] L. Smentek, "Theoretical description of the spectroscopic properties of rare earth ions in crystals," Physics Reports **297**, 155-237 (1998)

[Sot99] J. M. Soto-Crespo and N. N. Akhmediev, "Multisoliton regime of pulse generation by lasers passively mode locked with a slow saturable absorber," J. Opt. Soc. Am. B **16**, 674-677 (1999)

[Spi91] C. Spielmann, F. Krausz, T. Brabec, E. Wintner, and A. J. Schmidt, "Experimental Study of Additive Pulse Mode Locking in an Nd:Glass Laser," IEEE J. Quantum Electron. **27**, 1207-1213 (1991)

[Ste00] C. Stewen, K. Contag, M. Larionov, A. Giesen, and H. Hügel, "A 1-kW CW thin disc laser," IEEE J. Selected Topics in Quantum Electr. **6**, 650-657 (2000)

[Sum94] D. S. Sumida and T. Y. Fan, "Effect of radiation trapping on fluorescence lifetime and emission cross section measurements in solid-state laser media," Opt. Lett. **19**, 1343-1345 (1994)

[Szi00] R. Szipöcs, A. Köházi-Kis, S. Lakó, P. Apai, A. P. Kovács, G. DeBell, L.Mott, A. W. Louderback, A.V. Tikhonravov, and M. K. Trubetskov, "Negative dispersion mirrors for dispersion control in femtosecond lasers: chirped dielectric mirrors and multi-cavity Gires-Tournois interferometers," Appl. Phys. B **70** [Suppl.], S51-S57 (2000)

[Tai97] T. Taira, W. M. Tulloch, and R. L. Byer, "Modeling of quasi-three-level lasers and operation of cw Yb:YAG lasers," Appl. Opt. **36**, 1867-1874 (1997)

[Tar98] G. H. M. van Tartwijk and G. P. Agrawal, "Laser instabilities: a modern perspective," Prog. Quant. Electr. **22**, 43-122 (1998)

[Tsu95] S. Tsuda, W.H. Knox, E. A. de Souza, W. Y. Jan, and J. E. Cunningham, "Low-loss intracavity AlAs/AlGaAs saturable Bragg reflector for femtosecond mode locking in solid-state lasers," Opt. Lett. **20**, 1406-1408 (1995)

[Tur03] S. K. Turitsyn, E. G. Shapiro, S. B. Medvedev, M. P. Fedoruk, and V. K. Mezentsev, "Physics and mathematics of dispersion-managed optical solitons," C. R. Physique **4**, 145-161 (2003)

[Ueh96] N. Uehara, K. Ueda, and Y. Kubota, "Spectroscopic measurements of a High-Concentration $Yb^{3+}:LiYF_4$ Crystal," Jpn. J. Appl. Phys. **35**, L499-L501 (1996)

[Via03] B. Viana, R. Gaumé, D. Vivien, D. Fournier, and J. Roger, "Prediction and measurements of thermo-mechanical and thermo-optical parameters for high power solid state lasers," in Advanced Solid State Photonics (ASSP 2003, San Antonio, USA), OSA Technical Digest, MB19-1 (2003)

[Wan00b] C. Wang, H. Zhang, X. Meng, L. Zhu, Y. T. Chow, X. Liu, R. Cheng, Z. Yang, S. Zhang, and L. Sun, "Thermal, spectroscopic properties and laser performance at 1.06 and 1.33 µm of Nd:$Ca_4YO(BO_3)_3$ and Nd:$Ca_4GdO(BO_3)_3$ crystals," J. Cryst. Growth **220**, 114-120 (2000)

[Wan99] P. Wang, J. M. Dawes, P. Dekker, H. Zhang, and X. Meng, "Spectral characterization and diode-pumped laser performance of Yb:YCOB," in OSA TOPS Vol.26, Advanced Solid-State Lasers, 631-635 (1999)

[Wan99b] P. Wang, J. M. Dawes, P. Dekker, and J. A. Piper, "Spectral properties and infrared laser performance of diode-pumped Yb:$YAl_3(BO_3)_4$," in OSA TOPS Vol.26, Advanced Solid-State Lasers, 615-617 (1999)

[Web71] M. J. Weber, "Optical properties of Yb^{3+} and Nd^{3+}-Yb^{3+} energy transfer in $YAlO_3$," Phys. Rev. B **4**, 3153-3159 (1971)

[Web99] R. Weber, B. Neuenschwander, and H. P. Weber, "Thermal effects in solid-state laser materials," Optical Materials **11**, 245-254 (1999)

[Weg95] R. T. Weg and A. Meijerink, "Cooperative Luminescence of ytterbium(III) in La_2O_3," Chem. Phys. Lett. **246**, 495-498 (1995)

[Xu03] Yongyuan Xu, Xinghong Gong, Yujin Chen, Miaoliang Huang, Zundu Luo, and Yidong Huang, "Crystal growth and optical properties of $YbAl_3(BO_3)_4$: a promising stoichiometric laser crystal," J. Cryst. Growth **252**, 241-245 (2003)

[Yan00] H. Yang, D. Shen, S. C. Tam, Y. L. Lam, J. Liu, K. Ueda, W. Xie, and J. Gu, "Femtosecond Self-Mode-Locked $La_{1-x}MgNd_xAl_{11}O_{19}$ Laser Pumped by a Laser Diode," Jpn. J. Appl. Phys. **39**, 6542-6545 (2000)

[Yan01] S. Yang, K. Lee, Z. Xu, X. Zhang, and X. Xu, "An accurate method to calculate the negative dispersion generated by prism pairs," Optics and Lasers in Engineering **36**, 381-387 (2001)

[Yan03] Q. Yang, J. Seo, S. Creekmore, D. Temple, A. Mott, N. Min, K. Yoo, S. Y. Kim, and S. Jung, "Distortions in Z-scan spectroscopy," Appl. Phys. Lett. **82**, 19-21 (2003)

[Zay99] J. J. Zayhowski, "Microchip lasers," Optical Materials **11**, 255-267 (1999)

List of symbols

a	lattice constant
$\boldsymbol{a}, \boldsymbol{b}, \boldsymbol{c}$	crystallographic axes
A	attenuation (eq. 3.77.)
	or aspect ratio
A, B, C, D	Sellmeier coefficients
α	thermal expansion coefficient
	or absorption coefficient
α_0	"one-way" absorption coefficient (neglecting reemission)
α_{eff}	effective absorption coefficient (net absorption, including reemission)
α_{max}	maximum absorption coefficient
$\mathscr{a}$	coefficient related to position-dependent pulse duration (eq. 4.19.)
$\mathscr{A}_{eff}$	effective beam area
B_{tp}	crystal field parameter related to $C_p^{(t)}$
β	inversion parameter
	or chirp parameter
$\beta_{avr(l)}$	radially averaged inversion parameter, weighted with the Gaussian intensity profile of the laser signal
$\beta_{avr(p)}$	radially averaged inversion parameter, weighted with the Gaussian intensity profile of the pump beam
$\beta_{avV(l)}$	inversion parameter averaged over the volume of the laser signal mode in the active medium, weighted with the Gaussian intensity profile of the laser signal
β_{min}	minimum value of inversion parameter required for transparency
$\mathscr{b}$	chirp parameter
c	speed of light in vacuum, $c \approx 2.998 \times 10^8$ ms^{-1}
C	specific heat per volume
C_{dop}	(relative) dopant concentration
$C_p^{(t)}$	spherical tensor of rank t for polarization p
C_r, C_ϕ	photoelastic coefficients for radial and tangential polarization
χ	material constant related to thermal conductivity
$\chi^{(1)}$	real part of first-order electric susceptibility
$\tilde{\chi}^{(1)}$	imaginary part of first-order electric susceptibility
$X^{(1)}$	first-order electric susceptibility
d_a	distance between prism apices
d_i	degeneracy of level i
D	group delay dispersion (GDD)
D_{comp}	GDD by elements for dispersion compensation
D_g	gain dispersion
D_f	filter dispersion
D_m	material GDD
δ	phase difference
	or attenuation by resonator loss (eq. 3.60.)
$\delta\lambda_{fr}$	free spectral range
$\delta\nu_{fr}$	free spectral range
Δn_T	directly temperature-dependent variation of refractive index
Δn_ε	stress-dependent variation of refractive index
$\Delta\lambda$	spectral bandwidth
$\Delta\nu_p$	spectral bandwidth of pulse (FWHM, with respect to intensity)

$\Delta\omega_p$	spectral bandwidth of pulse (FWHM, with respect to intensity)
ΔR	saturable absorption
e	Euler number, $e \approx 2{,}7182818$
E	energy **or** Young´s modulus
$\boldsymbol{E}$	electrical field strength (vector)
$E_{a,sat}$	saturation pulse-energy for absorption in saturable absorber
E_i	energy of level i
E_p	pulse energy
ε_0	vacuum permittivity, $\varepsilon_0 \approx 8.854 \times 10^{-12}$ AsV^{-1}m^{-1}
$\varepsilon_{a,sat}$	saturation parameter, not identical with saturation pulse-energy $E_{a,sat}$
ε_{sr}	relative strain of interatomic distances
$\boldsymbol{\mathcal{E}}$	electrical field strength (vector)
$\underline{\boldsymbol{\mathcal{E}}}$	slowly varying envelope of electrical field strength
f	focal length
f_{1p}	fraction of lower-multiplet population in the lower pump level, $0 \leq f_{1p} \leq 1$
f_{2p}	fraction of upper-multiplet population in the upper pump level, $0 \leq f_{2p} \leq 1$
f_{1l}	fraction of lower-multiplet population in the lower laser level, $0 \leq f_{1l} \leq 1$
f_{2l}	fraction of upper-multiplet population in the upper laser level, $0 \leq f_{2l} \leq 1$
f_r, f_ϕ	focal length (of thermal lens) for radial and tangential polarization
$F_{a,sat}$	saturation fluence of saturable absorber
F_p	pulse fluence
$\mathscr{f}$	functions containing real part of higher-order electric susceptibilities
$\breve{\mathscr{f}}$	functions containing imaginary part of higher-order electric susceptibilities
φ	angular coordinate
ϕ	angular coordinate (ϕ_i , of i-th electron) **or** instantaneous phase
g_0	"one-way" gain coefficient (gain per unit length, neglecting reabsorption)
g_{eff}	effective gain coefficient (net gain per unit length)
g_γ	normalized lineshape function for polarization γ
G	gain
G_f, G_b	forward gain, backward gain
G_p	effective gain, taking into account spectral bandwidths of pulse and gain
γ	self-phase modulation coefficient
Γ	round-trip nonlinear phase shift per power
h	Planck constant, $h \approx 6.626 \times 10^{-34}$ Js
η_q	quantum efficiency (eq. a.10.)
η_{ex}	extraction efficiency (eq. 3.83.)
η_{max}	experimental maximum value of optical-to-optical conversion efficiency η_{opt}
η_{opt}	optical-to-optical conversion efficiency with respect to the absorbed pump power (eq. 3.84.)
η_{sl}	laser slope efficiency (differential optical-to-optical conversion efficiency with respect to the absorbed pump power, eq. 3.90.)
η_{tot}	optical-to-optical conversion efficiency with respect to the incident pump power (eq. 3.85.)
I_0	incident intensity
I_{ex}	extracted intensity
$I_{ex,b}$	intensity of extracted light in backward direction only
$I_{ex,l}$	intensity of extracted light in forward direction only

I_γ	(fluorescence) intensity for polarization γ
I_l	intensity of laser signal
$I_{l,b}$	intensity of laser signal in backward direction only
$I_{l,f}$	intensity of laser signal in forward direction only
$I_{l,sat}$	saturation intensity for laser signal
I_p	intensity of pump light
$I_{p,sat}$	saturation intensity for pump light
I_t	transmitted intensity
k	Boltzmann constant, $k \approx 1.381 \text{ x } 10^{-23}$ JK^{-1} **or** wave number
$\boldsymbol{k}$	wave vector
k_0	central wave number
κ	thermal conductivity
κ_1, κ_2	values of thermal conductivity for undoped and "100% doped" host
κ_e	dielectric constant
κ_{in}	"interpolated" thermal conductivity of doped host
κ_m	relative magnetic permeability
l	mean free path length of phonons
l_a	absorption length (length where intensity has dropped to $1/e$ of its initial value)
l_f, l_g, l_{gf}	loss by additional filtering, gain-filtering, or both together
l_{tot}	total loss
L	length (of light path, crystal, etc.)
L_a, L_D, L_{SPM}	path length through medium showing absorption, dispersion, or self-phase modulation
λ	wavelength in vacuum (λ_0, central wavelength)
λ_a	wavelength of an absorption maximum
λ_{amax}	wavelength of maximum absorption
λ_c	center wavelength of saturable absorber
λ_e	wavelength of an emission maximum
λ_l or λ_{laser}	wavelength of laser signal
λ_{mf}	mean wavelength of fluorescence
λ_p or λ_{pump}	wavelength of pump light
λ_{zl}	wavelength of zero-line transition
Λ	resonator loss aside from output coupler transmission
M^2	beam quality factor
n	refractive index
n_0	linear refractive index
n_2	nonlinear refractive index referring to electrical field strength
$\underline{n}_2$	nonlinear refractive index referring to light intensity
n_c	complex refractive index
n_o, n_e	refractive index of ordinary ray and extremum of refractive index of extraordinary ray
n_m, n_g, n_p	refractive indices for light polarized parallel to the crystallo-optic axes
n_r, n_ϕ	refractive indices for radial and tangential polarization
N	active ion concentration
N_1, N_2	total population densities of lower and upper multiplet
$\boldsymbol{N_m}$, $\boldsymbol{N_g}$, $\boldsymbol{N_p}$	crystallo-optic axes
ν	frequency
ν_l	optical frequency of laser signal

ν_{rep}	pulse repetition rate
ν_p	optical frequency of pump light
ν_{poi}	Poisson´s ratio
ν_{spd}	average frequency ($h^{-1}\times$energy) of a spontaneous decay
O	operator
P_a or P_{abs}	absorbed pump power
$P_{a,sat}$	saturation power for absorption in saturable absorber
$P_{a,thr}$	absorbed pump power at the lasing threshold
P_{ex}	power extracted from the laser medium
P_{heat}	heat load (power)
P_l	intracavity power of laser signal
P_{max}	maximum power
P_{out}	output power ($P_{out,max}$, experimental maximum value of output power)
P_p	pump power
$P_{p,sat}$	saturation power for pump light absorption
$P_{p,thr}$	pump power at the lasing threshold
P_{spd}	spontaneous decay power
ψ	phase shift
$\mathcal{P}$	complex polarization vector
q	absorption coefficient of saturable absorber (q_0, unsaturated value)
q_{fin}	absorption coefficient just after the pulse has passed through the saturable absorber, before considering relaxation
Q	dissipated heat power per volume
θ	angular coordinate (θ_i, of i-th electron) **or** phase shift.
Θ_D	Debye temperature
r	radius **or** radial coordinate (r_i, of i-th electron)
R	reflectivity **or** thermal stress parameter **or** distance between ions
R_{abs}	absorption rate
R_{em}	stimulated emission rate
R_l	effective laser emission rate (net stimulated emission rate)
R_{nr}	non radiative decay rate
R_p	effective pump rate (net pump rate)
R_{rad}	fluorescence rate
R_{reabs}	reabsorption rate
R_{reem}	reemission rate
R_{spd}	spontaneous decay rate
ρ	mass density
$\sigma_{1p,2p}$,$\sigma_{2p,1p}$	individual cross sections for transition from Stark level *1p* (lower pump level) to Stark level *2p* (upper pump level) and reverse transition
$\sigma_{2l,1l}$,$\sigma_{1l,2l}$	individual cross sections for transition from Stark level *2l* (upper laser level) to Stark level *1l* (lower laser level) and reverse transition
σ_a,$\sigma_{a,\gamma}$	unsaturated absorption coefficient (for polarization γ); effective quantity, i.e. quantity that is measured for the average ion; not referring to specific Stark levels
σ_e,$\sigma_{e,\gamma}$	unsaturated emission coefficient (for polarization γ); effective quantity for the

	average ion, not referring to specific Stark levels
σ_{str}	tensile strength
t	time coordinate
t_g	group delay
t_r	retarded time coordinate
T	temperature
	or time coordinate (slow time parameter)
T_{mp}	melting point temperature
T_{OC}	output coupler transmission
T_R	round-trip period
τ	pulse duration parameter
τ_a	recovery time of saturable absorber
τ_f	fluorescence lifetime
τ_{nr}	nonradiative lifetime
τ_p	pulse duration (FWHM with respect to intensity)
τ_{rad}	radiative lifetime
$\mathcal{T}$	transmission
v	velocity of sound
v_g	group velocity
v_{ph}	phase velocity
w_a	waist size at saturable absorber
w_l	waist size of laser signal beam
w_p	waist size of pump beam
ω	frequency
Ω_f	spectral bandwidth of filter (HWHM with respect to intensity)
Ω_g	spectral bandwidth of gain (HWHM with respect to intensity)
Ω_p	spectral bandwidth of pulse (HWHM with respect to intensity)
$\boldsymbol{X_1', X_2', X_3'}$	principal axes of thermal expansion tensor
z	longitudinal coordinate
Z	partition function

List of abbreviations

AR	anti-reflective
CGLE	complex Ginzburg-Landau equation
cw	continuous-wave
fqd	fluorescence quantum defect
FWHM	full width at half maximum
GDD	group delay dispersion
GTI	Gires-Tournois interferometer
GVD	group velocity dispersion
HR	high-reflective
HWHM	half width at half maximum
KGW	$KGd(WO_4)_2$
KYbW	$KYb(WO_4)_2$
KYW	$KY(WO_4)_2$
lqd	laser quantum defect
NLSE	Nonlinear Schrödinger equation
PAM	passive amplitude modulation
Q	quality
RHS	right hand side
SESAM	semiconductor saturable absorber mirror
SPM	self-phase modulation
TDL	tapered diode laser
Ti:Sa	Ti:Sapphire
TSSG	top seeded solution growth
VCT	Vision Crystal Technology AG
WPS	weak pulse shaping

Dank

Mein herzlicher Dank gilt allen, die zum Gelingen dieser Arbeit beigetragen haben:

Herrn Prof. Dr. Thomas Elsässer, der mir die Möglichkeit gegeben hat am Max-Born-Institut interessante Forschung zu betreiben und meine Doktorarbeit betreut hat,

Herrn Dr. Uwe Griebner für die sehr gute und enge Zusammenarbeit bei den Experimenten, viele gute Diskussionen, seine Hilfsbereitschaft und insbesondere für seine Unterstützung beim Zustandekommen der vorangegangenen Seiten,

Herrn Dr. Valentin Petrov für die sehr gute und angenehme Zusammenarbeit im Labor und ebensolchen wissenschaftlichen Gedankenaustausch,

Frau Marina Friedrich für die Unterstützung bei Software und experimentellen Aufbauten,

allen Kollegen des Bereichs C2 des Max-Born-Instituts, neben den genannten vor allem den Herren Dr. Rüdiger Grunwald, Dr. Martin Leitner, Uwe Neumann, Dr. Günter Steinmeyer und Dr. Marc Wrage, für die angenehme Arbeitsatmosphäre, hilfreiche und/oder interessante Gespräche und vielfältige Unterstützung,

unserem Systemadministrator Dr. Thomas-Martin Kruel für das zuverlässige Netzwerk,

allen anderen Kollegen des Max-Born-Instituts, die dieses wissenschaftlich und menschlich reicher machen; ich habe gerne hier gearbeitet,

Herrn Dr. Todor Kirilov für die Organisation und gute Zusammenarbeit bei den Yb^{3+}-dotierten Wolframatkristallen und hilfreiche Diskussionen,

der Kristallzucht-Arbeitsgruppe der Universität Tarragona, Katalonien, besonders den Herren Prof. Dr. Francesc Díaz, Dr. Xavier Mateos, Dr. Jaume Massons und Dr. Frank Güell für die zur Verfügung gestellten hochdotierten und stöchiometrischen Wolframatkristalle, fruchtbare Konversation und ihre Gastfreundschaft,

der Vision Crystal Technology AG, Göxe, Deutschland, und ihrem Mitarbeiterteam für die zur Verfügung gestellten Yb:KGW-, Yb:KYW- und KYbW-Kristalle und für die Werksbesichtigung,

den Programmierern von Microsoft und den Schöpfern von StarOffice für zahlreiche Überraschungen in den vergangenen Monaten.

Ein besonderes Dankeschön für alles geht an meine Eltern.

Neue Yb^{3+}-dotierte Lasermaterialien und ihre Anwendung in Dauerstrich- und modengekoppelten Lasern

Zusammenfassung

Die Kombination aus Yb^{3+} als aktivem Ion und einem geeigneten Glas oder Kristall als Wirtsmaterial ergibt Lasermedien mit exzellenten optischen und mechanischen Eigenschaften. Bei Laseroszillatoren und -verstärkern, die im 1-µm-Bereich arbeiten, haben Yb^{3+}-basierte Lasermaterialien das Potential viele Nd^{3+}-basierte Materialien zu ersetzen. Dies gilt insbesondere in Systemen mittlerer bis hoher Ausgangsleistung, die für die Materialbearbeitung verwendet werden. Hier glänzen Yb^{3+}-aktivierte Medien mit hoher Lasereffizienz und relativ geringer Hitzeentwicklung. Im Falle modengekoppelter Yb^{3+}-Lasersysteme können Subpikosekunden-Pulslängen bei hoher durchschnittlicher Laserleistung erzeugt werden. Solche kurzen Pulse können z.B. die Präzision beim Laserbohren im Vergleich zu gütegeschalteten Lasersystemen verbessern und erlauben die Strukturierung von transparenten Materialien. Alle Yb^{3+}-aktivierten Lasermaterialien können mit InGaAs-Laserdioden gepumpt werden, was preiswerte, kompakte und zuverlässige Laser ermöglicht. Zu beachten ist, dass Yb^{3+}-Lasersysteme bei Raumtemperatur im quasi-drei- oder quasi-vier-Niveau-Betrieb arbeiten, d.h. dass das untere Laserniveau eine thermische Besetzung aufweist. Die Folgen sind eine Reabsorption emittierten Laserlichts und damit Verluste sowie eine erhöhte Laserschwelle. Der Reabsorptionseinfluss nimmt jedoch ab, je weiter der Laser über der Schwelle betrieben wird.

Diese Arbeit befasst sich mit zwei Gruppen neuer Yb^{3+}-basierter Laserkristalle, die im Hinblick auf die erzielbaren Lasereffizienzen am vielversprechendsten sind: Dies sind die Yb^{3+}-aktivierten monoklinen Doppelwolframate, namentlich die strukturell analogen Kristalle Yb:$KGd(WO_4)_2$ (Yb:KGW), Yb:$KY(WO_4)_2$ (Yb:KYW) und $KYb(WO_4)_2$ (KYbW), und die Yb^{3+}-dotierten Sesquioxide, repräsentiert durch ihren attraktivsten Vertreter, Yb:Sc_2O_3 (Yb:Skandia). Die herausragenden Merkmale der Wolframate sind die hohen Absorptions- und Emissions-Wirkungsquerschnitte, der mögliche sehr kleine Laserquantendefekt und im Falle von Yb:KYW und KYbW die realisierbaren sehr hohen Yb^{3+}-Konzentrationen im Kristall. Die Sesquioxide zeichnen sich außer durch gute spektroskopische Eigenschaften vor allem durch äußerst vorteilhafte thermomechanische Eigenschaften aus, z.B. hat Skandia eine um 50% höhere Wärmeleitfähigkeit verglichen mit Yttrium-Aluminium-Granat (YAG).

Der Theorieteil der Doktorarbeit behandelt die Kristallographie und die Eigenschaften Yb^{3+}-aktivierter Lasermaterialien, die Laserphysik von quasi-drei- und quasi-vier-Niveau-Lasermedien und die passive Modenkopplung. Die spektroskopischen Daten für KYbW wurden im Rahmen dieser Dissertation ermittelt, wobei die Fallstricke vermieden wurden, die mit der Messung hochabsorbierender Materialien verbunden sind. Für diesen stöchiometrischen Laserkristall ergibt sich bei einer Pumpwellenlänge von 981 nm eine extrem kurze $1/e$-Absorptionslänge von 13.3 µm. Im Experimentalteil wird das Potential von Yb^{3+}-aktivierten Wolframaten und Yb:Skandia in verschiedenen Laserkonfigurationen untersucht.

Mit niedrig Yb^{3+}-dotiertem KYW und KGW wird effizienter Dauerstrich- und modengekoppelter Laserbetrieb gezeigt. Der beste differentielle Wirkungsgrad, 68% (bezogen auf die absorbierte Pumpleistung), wird erzielt mit einem 5%-dotierten Yb:$KY(WO_4)_2$-Kristall in einem Ti:Saphir-Laser-gepumpten System. Unter Verwendung des gleichen Kristalls wird

der erste modengekoppelte Oszillator, der ein Yb^{3+}-dotiertes Wolframatmedium mit einem sättigbaren Halbleiter-Absorberspiegel (semiconductor saturable absorber mirror, SESAM) als passivem Modenkoppler kombiniert, realisiert. Die Pumpquelle ist eine neuartige Trapezlaserdiode, die eine ausgezeichnete Strahlqualität bietet (slow-axis $M^2 \approx 3$) und für eine absorbierte Pumpleistung von 1,1 W sorgt. Im solitonartigen Einzelpulsbetrieb, ergibt dies eine maximale Ausgangsleistung von 150 mW und eine minimale Pulsdauer von 101 fs. Die Femtosekunden-Laserperformance wird verglichen mit der von 5%-dotiertem Yb:KGW und 5 Gewichts-%-Yb_2O_3-dotiertem Phosphatglas im gleichen Resonator. Die ähnlichen Resultate, die mit Yb:KGW erreicht werden (maximal 120 mW, minimal 112 fs) bestätigen, dass Yb^{3+} in den verschiedenen Doppelwolframaten sehr ähnliche spektroskopische Eigenschaften besitzt. Die ähnliche Performance des Glasmediums hingegen ist ein Hinweis darauf, dass die hier verwendeten Wolframatkristalle (3 mm Dicke) dünner sein oder eine kleinere Yb^{3+}-Konzentration aufweisen sollten, um die Reabsorptionsverluste und die Laserschwelle zu verringern.

Eine optimale Strategie, die den effizienten Gebrauch von Yb^{3+}-aktivierten monoklinen Wolframaten bei Zimmertemperatur erlaubt, besteht darin, einen sehr dünnen Kristall mit sehr hoher Yb^{3+}-Konzentration in einem vollflächig stirnseitig gekühlten Laserdesign wie dem Scheibenlaser-Konzept zu verwenden, das viele Durchgänge des Pumplichts durch das aktive Medium und eine exzellente Kühlung des Mediums ermöglicht. Dies ist der Grund, warum wir 41%- bis 80%-dotiertes Yb:KYW und stöchiometrisches KYbW untersuchen. Daneben können auch andere Anwendungen, wie z.B. Mikrochip-Laser, von den sehr hohen Absorptions- und Verstärkungskoeffizienten dieser Kristalle profitieren. Wichtige Aspekte der Untersuchungen sind, ob hohe Yb^{3+}-Konzentrationen in Wolframat-Wirtsmedien eine gute optische Kristallqualität erlauben und ob das Problem der Hitze, die in den relativ kleinen aktiven Volumina hochdotierter Kristalle entsteht, bewältigt werden kann. Dies wird in dieser Arbeit gezeigt. Zum ersten Mal gelingt es, Lasertätigkeit von Wolframaten mit einer Yb^{3+}-Konzentration wesentlich über 20% und schließlich, mit einem 125-µm-dünnen KYbW-Kristall, den Dauerstrichbetrieb eines stöchiometrischen Yb-Lasermaterials zu erreichen. Thermische Probleme sind jedoch nicht zu übersehen; der Dauerstrich-Laserbetrieb erfordert eine vollflächige stirnseitige Kühlung des Kristalls und optisches Pumpen im langwelligen Teil des Absorptionsspektrums (oberhalb der mittleren Fluoreszenzwellenlänge). Durch langwelliges Pumpen eines KYbW-Laserkristalls erzielen wir auch den nach unserem Wissen kleinsten Laserquantendefekt, der jemals für einen Laserkristall beobachtet wurde, 1.6%. KYbW wird sich noch besser für Laserkonzepte wie den Scheibenlaser eignen, wenn dünnere Medien als hier (ideal wären 10-20 µm Dicke) oder Kompositmedien (Yb^{3+}-aktiviertes und undotiertes Material) zur Verfügung stehen.

Mit Yb:Skandia erreichen wir in allen untersuchten Laserkonfigurationen hohe Effizienzen. Ein 0,7%-Yb^{3+}-dotierter Kristall kommt in einem Dauerstrich-System unter Verwendung eines Ti:Saphir-Pumplasers zum Einsatz. Der differentielle Wirkungsgrad beträgt 65%. Mit dem gleichen Kristall zeigen wir nach unserem Wissen erstmals modengekoppelten Betrieb eines $Yb:Sc_2O_3$-Lasers und, allgemeiner, eines Oszillators mit einem Sesquioxid-Laserkristall. Im Pikosekunden-Betrieb mit dem Ti:Saphir-Pumplaser, d.h. bei Modenkopplung ohne solitonenartige Pulsformung, wird ein Effenzienzrekord für modengekoppelte Laser mit einem kristallinen aktiven Medium aufgestellt, 47% Konversionseffizienz (bezogen auf die absorbierte Pumpleistung) bei 820 mW Ausgangsleistung und einem differentiellen Wirkungsgrad von 54%. Zusätzliche Dispersionskompensation durch Prismen führt zu solitonartigen Pulsen mit einer Dauer von 230 fs bei 540 mW Ausgangsleistung (30% Wirkungsgrad) bei einem differentiellen Wirkungsgrad von 35%. Verwendung der dispersionskompensierten Kavität in Verbindung mit der Trapezlaserdiode, die ebenfalls in den modenkoppelten Wolframatlaser-Experimenten zum Einsatz kommt, führt auch zu einer ähnlichen Leistungsausbeute wie in diesen Experimenten, d.h. zum 130 mW Laserleistung bei 1 W Pumpleistung. Die minimale Pulslänge beträgt 255 fs und ist damit etwas länger verglichen mit Yb:KYW and Yb:KGW, was eine Folge des schmaleren Verstärkungsspektrums von Yb:Skandia ist.

Unsere Resultate sind sehr vielversprechend, obwohl die Lasermedien, die in dieser Arbeit verwendet werden, keineswegs optimal sind (sie sind generell zu lang mit Blick auf Reabsorptionsverluste; bei den Kristallen mit hoher Yb^{3+}-Konzentration stören evtl. auch Verunreinigungen). Für die Zukunft kann man vermuten, dass Yb^{3+}-dotierte Wolframat- und Sesquioxidkristalle in vielen kommerziellen Lasern mittlerer bis hoher Leistung zu finden sein werden, vorzugsweise wenn Modenkopplung gefordert ist. Gleichwohl sollten folgende Hinweise beachtet werden:

Mehr als andere Yb-Lasermaterialien profitieren Yb^{3+}-aktivierte Wolframate von Pumpquellen mit hoher Brillianz und sie sollten daher mit solchen kombiniert werden. Die Kristalle arbeiten am besten in stirnseitig gekühlten Systemen wie dem Scheibenlaser. Auf Grund der ähnlichen Radien von Y^{3+} und Yb^{3+} ist KYW der bessere Wirtskristall verglichen mit KGW, wenn höhere Dotierungsgrade realisiert werden sollen. Die beste Kristallqualität bietet jedoch das stöchiometrische Material KYbW. Sc_2O_3 ist ein ausgezeichnetes Wirtsmaterial für niedrige Yb^{3+}-Konzentrationen, d.h. bis zu etwa 1% Dotierung. Oberhalb dieses Wertes verschlechtert der Größenunterschied von Sc^{3+} und Yb^{3+} zunehmend die Kristallqualität und auch die thermische Leitfähigkeit wird signifikant reduziert. In diesem Fall können die spektroskopisch leicht unterlegenen, analogen Sesquioxide Lu_2O_3 and Y_2O_3, sofern ihre Zucht noch verbessert werden kann, vorzuziehen sein.

Publikationen, die im Zusammenhang mit dieser Dissertation erfolgten

Journalbeiträge

P. Klopp, V. Petrov, U. Griebner, G. Erbert, “Passively mode-locked Yb:KYW laser pumped by a tapered diode laser”, Opt. Express 10, S. 108-113 (2002)

M. C. Pujol, M. A. Bursukova, F. Güell, X. Mateos, R. Solé, J. Gavalda, M. Aguiló, J. Massons, F. Diaz, P. Klopp, U. Griebner, V. Petrov, “Growth, optical characterization and laser operation of a new stoichiometric crystal $KYb(WO_4)_2$”, Phys. Rev. B65, 165121 (2002)

P. Klopp, U. Griebner, V. Petrov, X. Mateos, M. A. Bursukova, M. C. Pujol, R. Solé, J. Gavalda, M. Aguiló, F. Güell, J. Massons, T. Kirilov, F. Diaz, “Laser operation of a new stoichiometric crystal $KYb(WO_4)_2$”, Appl. Phys. B 74, S. 185-189 (2002)

P. Klopp , V. Petrov, U. Griebner, V. Nesterenko, V. Nikolov, M. Marinov, M. A. Bursukova, M. Galan, “Continuous-wave lasing of a stoichiometric Yb laser material: $KYb(WO_4)_2$”, Opt. Lett. 28, S. 322-324 (2003)

P. Klopp , V. Petrov, U. Griebner, “Potassium Ytterbium Tungstate Provides the Smallest Laser Quantum Defect”, Jpn. J. Appl. Phys. 42, S. L246 -L248 (2003)

P. Klopp, V. Petrov, U. Griebner, K. Petermann, V. Peters, G. Erbert, “Highly-efficient mode-locked $Yb:Sc_2O_3$ laser”, Opt. Lett. 29, S. 391-393 (2004)

Konferenzbeiträge

P. Klopp, G. Erbert, U. Griebner, “Passively mode-locked laser performance of Yb:KGW and Yb:KYW”, DPG Frühjahrstagung Quantenoptik, Berlin, 02.-06.04.2001, in Verhandlungen der Deutschen Physikalischen Gesellschaft 5/2001, postdeadline paper (2001)

P. Klopp, U. Griebner, V. Petrov, G. Erbert, “Femtosecond Yb:KGW laser pumped by a compact high brightness diode laser”, CLEO/Europe - EQEC Focus Meetings 2001, Progress in Solid State Lasers, München, 18.-22.06.2001, Conference Digest, S. 31 (2002)

P. Klopp, U. Griebner, V. Petrov, X. Mateos, M. A. Bursukova, M. C. Pujol, F. Güell, R. Solé, J. Gavaldà, M. Aguiló, J. Massons, T. Kirilov, F. Diaz, “Lasing of Yb^{3+} in a new stoichiometric double tungstate”, Conference on Lasers and Electro-Optics, in OSA Trends in Optics and Photonics (TOPS) Vol. 73 bzw. OSA Technical Digest, Postconference Edition (Optical Society of America, Washington DC, 2002), S. 29-30 (2002)

M. C. Pujol, M. A. Bursukova, F. Güell, X. Mateos, R. Solé, Jna. Gavaldà, M. Aguiló, J. Massons, T. Kirilov, F. Diaz, P. Klopp, U. Griebner, V. Petrov, “Growth and optical characterization of a new stoichiometric monoclinic laser crystal $KYb(WO_4)_2$”, Conference on Lasers and Electro-Optics, in OSA TOPS Vol. 73 bzw. OSA Technical Digest, Postconference Edition, S. 499-500 (2002)

P. Klopp, V. Petrov, U. Griebner, V. Nikolov, V. Nesterenko, T. Kirilov, “Continuous wave lasing of Yb^{3+} in a stoichiometric double tungstate”, Photonics West 2003, San José, California, in Proceedings of the SPIE vol.4968, S. 46-53 (2003)

P. Klopp, U. Griebner, V. Petrov, K. Petermann and V. Peters, “Highly-efficient mode-locked Yb:Sc_2O_3 laser”, Advanced Solid-State Photonics (ASSP 2003), San Antonio, USA, OSA Technical Digest, paper TuA7, S. 154-157 (2003)

P. Klopp ,U. Griebner and V. Petrov, “$KYb(WO_4)_2$ provides the smallest laser quantum defect”, Conference on Quantum Electronics and Laser Scene Conference (CLEO’03), OSA Technical Digest, paper CWG-3, S. 153 (2003)

P. Klopp, U. Griebner, V. Petrov, K. Petermann and V. Peters, “Highly-efficient mode-locked Yb:Sc_2O_3 laser”, CLEO’03, OSA Technical Digest, paper CWG-1, S. 151 (2003)

P. Klopp, U. Griebner, V. Petrov, V. Nesterenko, V. Nikolov, M. Marinov, M. Bursukova, M. Galan, “Room temperature cw lasing of stoichiometric $KYb(WO_4)_2$”, CLEO/Europe - EQEC 2003, München, 22.-27.6.2003, Europhysics Conference Abstract Vol. 27E, paper CA6-1 (2003)

Lebenslauf

Persönliche Daten

Name	Peter Klopp
Geburtsdatum	14.12.1968
Geburtsort	Wiesbaden
Nationalität	deutsch
E-Mail	peter.klopp@berlin.de

Ausbildung und beruflicher Werdegang

08/1999-05/2006	Max-Born-Institut für Nichtlineare Optik und Kurzzeitspektroskopie, Berlin; Promotion in Physik
04/1998-02/1999	Lambda Physik GmbH, Göttingen; Forschung und Entwicklung, “Diode-Pumped Solid State Lasers”
1990-1997	Johannes Gutenberg-Universität, Mainz; Studium der Physik, Diplomarbeit “Aufbau eines Festköper-Lasersystems für die Resonanzionisations-Massenspektroskopie am Plutonium”
1988-1990	Orthopädische Klinik der Inneren Mission, Bad Schwalbach; Zivildienst
1977-1988	Gesamtschule Obere Aar in Taunusstein
1975-1977	Schelmengrabenschule in Wiesbaden

Versicherung

Hiermit erkläre ich, die Dissertation selbstständig und nur unter Verwendung der angegebenen Hilfen und Hilfsmittel angefertigt zu haben. Ich habe mich anderwärts nicht um einen Doktorgrad beworben und besitze einen entsprechenden Doktorgrad nicht. Ich erkläre die Kenntnisnahme der dem Verfahren zu Grunde liegenden Promotionsordnung der Mathematisch-Naturwissenschaftlichen Fakultät der Humboldt-Universität zu Berlin.